# Ultracold Molecular Plasma

by

Markus Schulz-Weiling

A THESIS SUBMITTED IN PARTIAL FULFILLMENT OF
THE REQUIREMENTS FOR THE DEGREE OF

DOCTOR OF PHILOSOPHY

in

The Faculty of Graduate and Postdoctoral Studies

(Physics)

THE UNIVERSITY OF BRITISH COLUMBIA

(Vancouver)

August 2017

# Abstract

The conditions afforded by a skimmed free-jet expansion intersected by two laser pulses, driving resonant transitions in nitric oxide, determine the phase-space volume of a dense molecular Rydberg ensemble. Spontaneous avalanche to plasma within this system leads to the development of two macroscopic domains. These domains are clearly distinguished by their polarizability as well as their locality within the plasma. The first domain appears at the system core, is polarized by fields exceeding 500 mV/cm and displays an ambipolar expansion character suggestive of initial electron temperatures exceeding ∼150 Kelvin. The second domain travels with the velocity of the supersonic beam and is robust to the application of several hundred V/cm pulses. It is further distinguished through the apparent arrest of relaxation channels, annealing the domain over a millisecond or more in a state far from thermal equilibrium. Both domains are linked via the spontaneous breaking of ellipsoidal symmetry to form bifurcating arrested volumes.

# Lay summary

Plasma is the fourth state of matter next to solid, fluid and gas. Physical systems can transition between states of matter when energy is added or removed. Plasmas form when neutral matter obtains enough energy to break into charged subatomic components - into ions and electrons.

Plasma particles carry charge and can sense each other over distance, giving raise to collective behaviour. Such dynamic systems, when prepared far from thermal equilibrium, must redistribute their energy along all accessible channels on a short timescale.

Our group studies the evolution of plasma in an exotic regime. We observe unexpected system behaviour and the arrest of energy redistribution for uncharacteristic durations, suggesting new physics. We seek to understand these dynamics on the microscopic scale.

# Preface

This thesis is the result of a collaborative research effort in the lab of Professor Ed Grant at the University of British Columbia. My involvement in this lab dates back to the year 2009 and consists of an undergraduate research project, my thesis project for the degree 'Diplomphysiker' at the University of Freiburg as well as my PhD program. My work in this research group, prior to enrolling into the PhD program in January 2012, led to the following publications:

- H. Sadeghi, M. Schulz-Weiling, J.P. Morrison, J.C.H. Yui, N. Saquet, C.J. Rennick and E.R. Grant. *Molecular ion-electron recombination in an expanding ultracold neutral plasma of $NO^+$*
  Phys. Chem. Chem. Phys.: 13(42):18872-9 (2011)

- N. Saquet, J.P. Morrison, M. Schulz-Weiling, H. Sadeghi, J.C.H. Yui, C.J. Rennick and E.R. Grant. *On the formation and decay of a molecular ultracold plasma*
  J. Phys. B: At. Mol. Opt. Phys.: 44 184015 (2011)

- C.J. Rennick, N. Saquet, J.P. Morrison, J. Ortega-Arroyo, P. Godin, L. Fu, M. Schulz-Weiling and E.R. Grant. *Dissociative recombination and the decay of a molecular ultracold plasma*
  J. Phys.: Conf. Ser.:  300 012005 (2011)

- M. Schulz-Weiling. *Expansion dynamics of a non-spherical ultracold plasma in a supersonic molecular beam*
  Diplomarbeit (diploma thesis) - Faculty of Mathematics and Physics Albert-Ludwigs-Universität Freiburg (2011)

In the following, I list six published articles reporting results from research work over the course of my PhD program. I state my relative contributions:

- (1) H. Sadeghi, A. Kruyen, J. Gurian, J. Morrison, M. Schulz-Weiling, N. Saquet, C.J. Rennick and E.R. Grant. *Dissociation and the development of spatial correlation in a molecular ultracold plasma*
  Phys. Rev. Lett.: **21**;112(7):075001 (2013)
  Contributed technical lab support and took part in discussions as well as the writing process.

- (2) J. Hung, H. Sadeghi, M. Schulz-Weiling and E.R. Grant. *The evolution from Rydberg gas to Plasma in an Atomic Beam of Xe*
  J. Phys. B: At. Mol. Opt. Phys.: **47** 155301 (2014)
  Converted our experimental setup to prepare a xenon plasma. Data collection and analysis was done by J. Hung and H. Sadeghi. Contributed to discussions and writeup.

- (3) M. Schulz-Weiling and E.R. Grant. *Three-dimensional imaging of the ultracold plasma formed in a supersonic molecular beam*
  AIP Conf. Proc. 1668, 050002 (2015)
  Developed new detector and collected all data published in this article. Contributed key points of the interpretation. Creation of the manuscript was a combined effort of the authors.

- (4) M. Schulz-Weiling and E.R. Grant. *Quantum State Control of Ultracold Plasma Fission*
  J. Phys. B: At. Mol. Opt. Phys. **49** (2016) 064009 (9pp) (2016)
  Collected all data published in this article. Contributed key points of the interpretation. Creation of the manuscript was a combined effort of the authors.

- (5) M. Schulz-Weiling, H. Sadeghi, J. Hung and E.R. Grant. *On the evolution of the phase-space distributions of a non-spherical molecular ultracold plasma in a supersonic beam*
  J. Phys. B: At. Mol. Opt. Phys. 49 193001 (2016)

This article is the expression of my multi-year effort to provide a more solid foundation to our supersonic beam apparatus, which led to my discussion of our system in lower geometry. I incorporated results from my diploma thesis. The 3D hydrodynamic shell model computation is based on a 1D model by H. Sadeghi for a spherical plasma. My co-authors provided editing.

- (6) R. Haenel, M. Schulz-Weiling, J. Sous, H. Sadeghi, M. Agigh, L. Melo, J. S. Keller and E. R. Grant. *Arrested relaxation in an isolated molecular ultracold plasma*
  Accepted for publication in Physics Review A (July 2017)
  Contributed central experimental results. Creation of manuscript by Ed Grant. Contributed to data interpretation and provided editing.

Chapter 4 in Part I of my thesis represents a literature review of plasma physics and has appeared in a similar form in my diploma thesis. Chapters 5, 6 and 8 have appeared in comparable format in publication reference (5). The coupled-rate-equation model discussed in Chapter 7 was previously developed by J. Morrison and N. Saquet, J. Hung and H. Sadeghi. My colleagues were kind enough to share their code and allow me to develop their method. Chapter 10 takes results from reference (3) and draws on our discussion in reference (6). Chapter 11, likewise, borrows from the discussion in reference (6).

# Table of Contents

# Appendices

# List of Tables

# List of Figures

# List of Abbreviations

In order of appearance:

| | |
|---|---|
| UNP | ultracold neutral plasma |
| MOT | magneto-optical trap |
| DIH | disorder-induced heating |
| UMP | ultracold molecular plasma |
| NO | nitric oxide |
| N | nitrogen |
| O | oxigen |
| IP | ionization potential |
| RD | radiative decay |
| PD | predissociation |
| PQN | principal quantum number |
| TBR | three body recombination |
| DR | dissociative recombination |
| FI | field ionization |
| He | helium |
| REMPI | resonance enhanced multi-photon ionization |
| CCD | charged coupled device |
| MCP | multichannel plate |
| FWHM | full width at half maximum |
| Ry | Rydberg |
| ODE | ordinary differential equation |
| ZEKE | zero electron kinetic energy |
| FMP | front mounting plate |
| SFI | selective field ionization |
| ITO | indium tin xide |
| grnd. | electrical ground |
| ICD | interatomic (intermolecular) Coulombic decay |

# List of Symbols

Over the course of this thesis, I will often designate the three dimensions in space by subscript $k=x,y,z$. Subscripts $\alpha = i, e$ refer to ions and electrons, respectively. The boldface typeset indicates a vector. Due to the wealth of variables in this document, I use subcategories spectroscopic symbol and global symbol.

**Spectroscopic variables:**

| | |
|---|---|
| **L** | total orbital angular momentum |
| $\boldsymbol{\ell}$ | orbital angular momentum |
| $M_L$ | projection of **L** on molecular axis |
| $\Lambda$ | absolute of $M_L$ |
| $\Sigma, \Pi, \Delta, ...$ | spectroscopic numbering |
| $\sigma, \pi, \delta, ...$ | spectroscopic numbering |
| $s, p, d, ...$ | spectroscopic numbering |
| **S** | total spin |
| **s** | spin |
| $M_S$ | projection of **S** on molecular axis |
| $\Sigma$ | absolute of $M_S$ |
| **J** | total angular momentum |
| $\Omega$ | total electric angular momentum projection on molecular axis |
| **N** | angular momentum of nucleus |
| **R** | angular momentum of nucleus in Hund's case d) |
| $F_1, F_2$ | spectroscopic labels |
| $P, p$ | transition $\Delta J/\Delta K = +1$ |

| | |
|---|---:|
| $Q,\, q$ | transition $\Delta J/\Delta K = 0$ |
| $R,\, r$ | transition $\Delta J/\Delta K = $ -1 |
| $\omega$ | photon classifier |
| $B_\nu$ | rotational constant |

**Global variables:**

| | |
|---|---:|
| $\Gamma$ | Coulomb coupling parameter |
| $e$ | electron (elementary charge) |
| e | Euler's number |
| $\pi$ | mathematical constant $\pi$ |
| $\epsilon_0$ | Vacuum permitivity |
| $a_{ws}$ | Wigner-Seitz radius |
| $k_B$ | Boltzmann constant |
| $T$ | Temperature |
| $h$ | Planck constant |
| $\hbar$ | reduced Planck constant |
| $\nabla$ | nabla - vector differential operator |
| $M,\, m$ | mass |
| $\mu$ | reduced mass |
| $x,\, y,\, z$ | spatial dimensions |
| **r** | position vector |
| $t$ | time |
| $r,\, R$ | radius |
| $\Psi$ | wave function |
| $W$ | energy |
| $n$ | principal quantum number |
| $R_\infty$ | Rydberg constant |
| $Ry$ | Rydberg energy |
| $\delta_\ell$ | quantum defect |
| $k$ | rate constant |
| $\tau$ | life time |
| $a_0$ | Bohr radius |

| | |
|---|---|
| $\rho$ | Density |
| $E$ | electric field |
| $P$ | pressure |
| $\mathbf{u}$ | mean velocity |
| $v$ | velocity |
| $\phi$ | electric potential |
| $Q, q$ | electric charge |
| $\delta(\mathbf{r})$ | delta function |
| $\lambda_D$ | Debye length |
| $f$ | particle distribution function |
| $F$ | force |
| $N$ | particle number |
| $b$ | impact parameter |
| $\tilde{\sigma}$ | cross section |
| $\mathcal{F}$ | flux |
| $[P]$ | stress tensor |
| $\gamma$ | hydrodynamic velocity parameter |
| $\sigma$ | Gaussian width |
| $C_p$ | heat capacity at const. pressure |
| R | gas constant |
| $\gamma_h$ | heat capacity ratio |
| g | gravitational constant |
| $h$ | enthalpy per unit mass |
| $a$ | isentropic sound speed |
| $\mathcal{M}$ | mach number |
| $D$ | nozzle diameter |
| $Z$ | collision rate |
| $\tilde{f}$ | probability distribution |
| $\Phi$ | total flow |
| $l$ | length |
| $\tilde{Z}_r$ | partition function |
| $\tilde{P}$ | power |
| $I$ | intensity |

| | |
|---|---|
| $\mathcal{E}(r)$ | Erlang distribution function |
| $f_P$ | Penning fraction |
| $C^{cut}$ | cut-off condition |
| $\Delta$ | width, change in a variable |
| # | number |
| $V$ | volume |
| G1, G2, G3 | grids within experimental apparatus holding potential |
| P1, P2 | plates within experimental apparatus holding potential |
| C1, C2, C3 | cyllinders within experimental apparatus holding potential |

# Acknowledgements

I would like to express my profound gratitude to Professor Edward Grant, for having been much more than my research supervisor, but a mentor throughout my journey at UBC.

I further like to acknowledge the help of all whom I had the privilege of calling colleagues: visiting professor James Keller; post doctoral fellows Chris Rennick, Nicolas Saquet and Josh Gurian; my fellow students Jonathan Morrison, Hossein Sadeghi, Mahyad Aghigh, Rommel Oliveira, Luke Melo, Jaimie Ortega-Arroyo, Paul Godin, Julian Yiu, Anneke Kruyen, Jachin Hung, Chelsea Cayabab and Rafael Haenel.

A special thanks to the Department of Chemistry Electronics and Machine Shops for all their help.

Thank you all for six happy and fulfilled years in Vancouver!

# Dedication

To my parents.

# Chapter 1

# General introduction

**Plasma**, also referred to as the fourth aggregate state, is by far the most common state of visible matter in the universe. It exists in hot surroundings and is created by ionizing collisions between particles or by high energy radiation fields in interstellar space.

The field of plasma physics was founded in the early 20th century when isolated researchers developed an interest in ionized gas phenomena. Early research focused on the effects of ionospheric plasma on long-range short-wave radio propagation and gaseous electron tubes in the pre-semiconductor era of electronics. In the 1950s, plasma physics became a central field of interest in the large-scale research efforts to produce fusion energy. This goal has been pursued ever since, nowadays in multi-national research facilities like ITER (International Thermonuclear Experimental Reactor). Other important research efforts that build on the field of plasma physics include solar- and astrophysics, as well as combustion engine and propulsion technology. Plasmas appear in technical applications such as metal manufacturing, surface treatments, lithography and plasma display panels. In the near future, advances in medical research could replace the unbeloved dentist drill by a painless plasma plume [45]. Because of their great importance in astrophysics and fundamental sciences, as well as modern technology, plasmas have for some time been of great interest to researchers.

Two central quantities by which plasmas can be characterized are temperature and density. This is illustrated in Figure 1.1, where a variety of natural and artificial plasmas are displayed. A distinction can be made between thermal plasmas ($\Gamma < 1$) and Coulomb correlated plasmas ($\Gamma > 1$), where $\Gamma$ denotes the so called **Coulomb coupling** parameter, which is
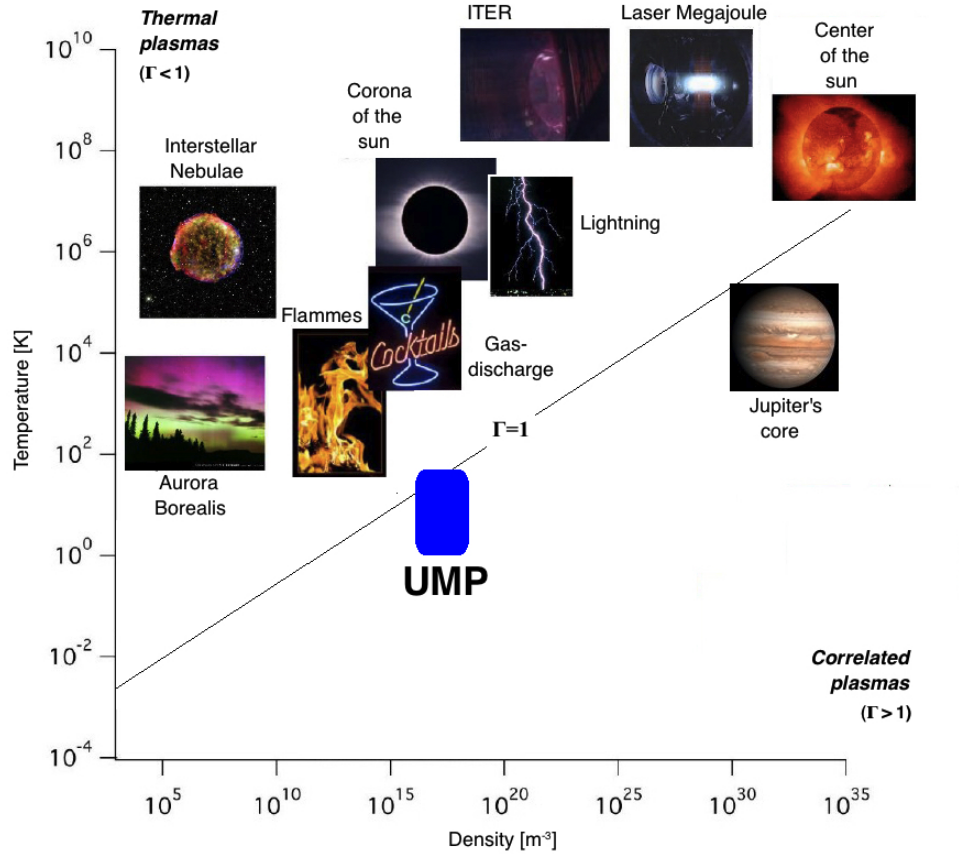
Figure 1.1: **Overview of the occurrence of neutral plasmas** - Some examples for neutral plasmas are shown at their respective position in the density-temperature diagram. The scaling is double-logarithmic. The $\Gamma = 1$ line separates thermal plasmas from plasmas in the correlated regime.

determined by the dimensionless ratio

$$\Gamma = \frac{e^2/4\pi\epsilon_0 a_{ws}}{k_B T}.$$

Here, $e$ is the electron charge, and $a_{ws}$ is the Wigner-Seitz radius, which relates to the particle density $\rho$ by $4/3\pi a_{ws}^3 = 1/\rho$. The condition $\Gamma > 1$ refers to a change in plasma behaviour, when densities and temperatures

of the charged particles reach regimes where the average electrostatic potential energy exceeds the average thermal energy and correlation effects occur. For example, plasmas with $\Gamma > 1$ can form liquid-like states and negative-pressure environments [54, 56], and highly correlated plasmas at $\Gamma \approx 180$ have even been predicted to undergo phase transitions to form body-centered-cubic crystals [25], which was later experimentally observed [16]. Effects like these presumably occur to some degree in the core of Jovian-type planets, stars and laser implosion experiments [39].

For some time now, researchers have tried to achieve high correlation in experimental plasma systems. Systems with solid-like particle distributions are impractical, as their ionization, while remaining in the correlated temperature frame, is difficult to achieve. Due to this, experimentalists focused their attention on cold, low-density gases. One of the earliest approaches to experimentally study plasma in the correlated regime was in a cryogenic afterglow experiment at an initial gas temperature of 4.2 K, electron temperature of 10 K and density of $\sim 10^{24}$ m$^{-3}$ [21].

More recently, a new means of creating and studying **ultracold neutral plasma** (UNP) in a laboratory was introduced by Rolston and coworkers in an experiment at NIST in 1999 [42]. Rolston's experiment combined the cooling power of a magneto-optical trap (MOT) with a narrow-band laser ionization to create a plasma, which was colder than any formerly observed.

His experiment demonstrated that a sample of metastable xenon atoms, held at a density as high as $2 \cdot 10^9$ cm$^{-3}$ and cooled to $\sim 10$ $\mu$K, when photo ionized, would subsequently evolved to form a plasma. This plasma has the special feature that, because of the very slow ion motion, the initial amount of electron kinetic energy is only determined by the tuning of the ionizing laser, i.e. by the difference between photon energy and binding potential. It is therefore not necessary to heat the whole system to achieve collisional ionization, as the narrow-band laser deposits energy right into the free electron kinetic energy bath. While the newly formed ions carry on with the momentum of the former neutrals, the electrons initially obtain only the

excess energy of the laser. Such systems, being created far from a state of equilibrium, exhibit surprisingly long life times. In his experiment, Rolston observed a lifetime of $\sim 100~\mu$s and demonstrated that initial plasma electron temperatures as low as 10 mK were achievable. This is considerably lower than any cold plasma occurring in nature. This fact, together with the method of creation, led Rolston to name his system an 'ultracold neutral plasma'.

Subsequent experiments extended this method to a variety of different atoms, such as strontium [55], rubidium [88], calcium [18] and caesium [69]. Latter experiment with caesium also showed that ultracold plasmas can form spontaneously from dense ultracold Rydberg ensombles.

UNPs facilitate ideal tabletop experiments for the study of many-body systems with strong inter-particle forces. For example, studying these systems can help astro-physicists to better understand the dynamics of star-clusters [17]. Naturally, Coulomb correlation became a central topic in UNP research.

The goal of achieving high orders of correlation in tabletop experiments, however, received a set-back with the discovery of disorder-induced heating (DIH) in UNPs [44]. DIH takes place in the first moments after plasma formation. It describes the release of potential energy of the spatially uncorrelated ion distribution into thermal motion, thus limiting ion equilibrium temperatures to several degree Kelvin [43].

In 2008, our research group demonstrated that it is possible to create an **ultracold molecular plasma** (UMP) from a $\sim 1$ K cold molecular Rydberg gas of nitric oxide [50]. We form this ensemble by intersecting a supersonic molecular beam with laser light, driving resonant transitions in nitric oxide to populate a high-Rydberg state. This Rydberg ensemble spontaneously transitions to plasma. We named our system ultracold in reference to the field of ultracold neutral plasmas. Our experiment showed that, by utilizing the beam method, it is possible to create ultracold plasma with initial den-

sities three orders of magnitude larger than those created in MOT systems. Higher densities yield, as seen in the definition of the Coulomb coupling parameter, $\Gamma$, higher correlations. Additionally, our approach enables us to perform research on many-body molecular plasma systems, which is scarcely possible in MOT systems. Here, new processes like two-body electron-cation dissociative recombination appear on the scene, which are able to contribute relaxation channels which do not exist in MOT plasmas [66, 71].

The UMP we create in the laboratory shows surprising characteristics. We observe the spontaneous breaking of symmetry of the developing ensemble and the arrest of plasma relaxation dynamics with a subcomponent of the system, expressed through a lack in signal decay and thermally driven expansion. What are the fundamental microscopic mechanisms leading to this unexpected behaviour? Could this be an effect of Coulomb coupling? I will pursue these and other question over the course of this thesis.

I have composed my thesis in four parts. Part I - *Fundamentals*, will review nitric oxide spectroscopy as well as Rydberg and plasma theory - all three are central concepts in UMP physics. Part II - *Formation of a molecular Rydberg ensemble*, will introduce our experiment. I will put an emphasis on the discussion of the physics of supersonic beam systems, which is central to characterizing the initial state of our system. This part will conclude with a statement of the initial phase-space distribution function of our Rydberg ensemble. Part III - *Theory work*, will take a theoretical approach to discuss the internal conversion of Rydberg gas to plasma and its subsequent expansion. Part IV - *Experimental work*, will introduce our means of plasma detection and discuss our observations within the framework of Parts I through III.

# Part I

# Fundamentals

In this first part of my thesis, I will review some concepts fundamental to our field of research. In our experiment, we cool nitric oxide in a supersonic jet. Two-resonant photon transitions drive ground-state molecules into the high-Rydberg manifold. Internal conversion of the Rydberg ensemble forms an ultracold molecular plasma.

Chapter 2 will discuss the spectroscopic properties of nitric oxide (NO). Following that, Chapter 3 reviews the fundamental features of Rydberg systems and their interaction with external perturbers. Chapter 4 will introduce important concepts of plasma theory and discuss some of their implications to UNP research. Subsequent parts of my thesis will frequently draw on the knowledge base derived over the following pages.

# Chapter 2

# Spectroscopy of nitric oxide

The following is a brief introduction into the spectroscopic properties of nitric oxide.[1] In our experiment, we excite NO from the X ground state via the intermediate A-state into the high Rydberg manifold. I will limit this discussion to these quantum states. Vibrations do not play a role in our experiment and are not discussed. Neither is the effect of nuclear spin. I follow the notation in Herzberg [32].

The motion of electrons in a diatomic molecule takes place within the cylindrical field of force set by the intermolecular axis. A precession of total electronic orbital angular momentum (without spin), $\mathbf{L} = \sum_i \boldsymbol{\ell}_i$, takes place about this axis. Only the projection of $\mathbf{L}$ on the molecular axis, with components $M_L(\hbar/2\pi)$, is a constant of motion. $M_L$ can take values $M_L = L, L-1, L-2, ..., -L$. Projection states differing only in the sign of $M_L$ have the same energy. Since $L$ is not a good quantum number for molecules, the following notation has been established:

$$\Lambda = |M_L| = 0, 1, 2, ..., L = \Sigma, \Pi, \Delta, \Phi, ... \tag{2.1}$$

The representative numbering of $\Lambda$ through Greek capital letters is analogous to the mode of designation for atoms. $\Pi, \Delta, \Phi, ...$ states are doubly degenerate as $\Lambda = |\pm M_L|$. States $\Lambda = \Sigma$ are non-degenerate.

The spin states of the individual electrons form a total spin $\mathbf{S} = \sum_i \mathbf{s}_i$. In $\Sigma$ states and in absence of external fields or rotation, $\mathbf{S}$ is uncoupled from the molecular axis. For states $\Lambda \neq 0$, precession of $\mathbf{L}$ about the molecular axis

---

[1]Excerpted from Herzberg's *Spectra of Diatomic Molecules* [32], Brown et. al. *Chemistry: The Central Science* [12] and Abraham's review paper on nitric oxide spectroscopy [10].

(a) Hund's Case (a)    (b) Hund's Case (b)    (c) Hund's Case (d)
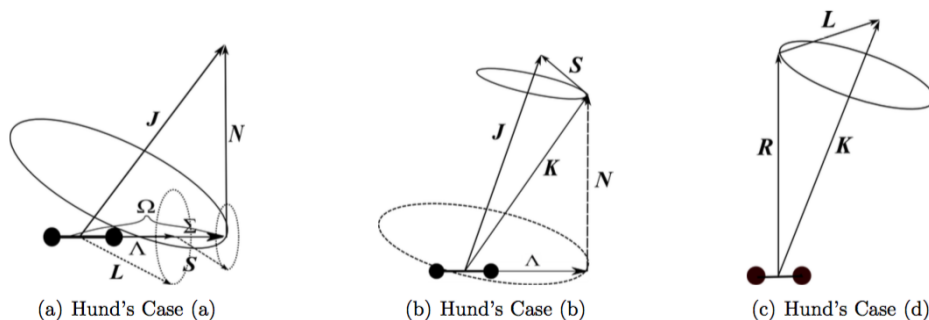
Figure 2.1: **Hund's cases: Coupling of rotation and electronic motion** - **J** is the total angular momentum, **N** is the angular momentum of the nuclear rotation. **K** is the total angular momentum apart from spin. **L** is the total electronic orbital angular momentum and $\Lambda$ it's projection on the molecular axis. **S** is the total electronic spin and $\Sigma$ it's projection on the molecular axis. In Hund's case (d), **N** becomes **R**, a good quantum number. (Figure (c) does not show the coupling of **S** and **K** to **J**.) Credit: J.P. Morrison

causes an internal magnetic field in the same direction. This in turn causes **S** to precess about the molecular axis with constant components $M_S(\hbar/2\pi)$. The notation,

$$\Sigma = M_S = S, S - 1, S - 2, ..., -S \tag{2.2}$$

has been established. The total electronic angular momentum about the intermolecular axis is called $\Omega$. It is obtained by addition of $\Lambda$ and $\Sigma$.

$$\Omega = |\Lambda + \Sigma| \tag{2.3}$$

Angular momentum caused by nuclear rotation of the molecular core is represented through quantum vector **N**. There is no quantum number associated with **N**. The total angular momentum of the system - combination of electron spin, electronic orbital angular momentum and nuclear rotation - is always designated **J**. Different classifications for different modes of coupling for **J** were first introduced by Hund. Figure 2.1 shows Hund's cases (a), (b) and (d), which play a role in our experiment.

9

**Hund's case (a)** assumes that the interaction of nuclear rotation with the electronic motion $\Omega$ is weak. Thus, **J**, constant in magnitude and direction, is a resultant formed by the nutation of $\Omega$ and **N** about **J**. A different way of understanding Hund's case (a), is that the precession of **L** and **S** about the internuclear axis is much faster than above mentioned nutation.

In **Hund's case (b)**, the electronic spin **S** is only very weakly coupled to the molecular axis. This is the case when $\Lambda = 0$ (absence of internal magnetic field) or even if $\Lambda \neq 0$ in the case of particularly light molecules. Thus, $\Omega$ is not defined. Now, $\Lambda$ (if nonzero) and **N** together form the resultant **K**.

$$K = \Lambda, \Lambda + 1, \Lambda + 2, ... \tag{2.4}$$

is the total angular momentum apart from spin. **K** and **S** together form resultant **J**.

$$J = (K + S), (K + S - 1), (K + S - 2), ..., |K - S| \tag{2.5}$$

**Hund's case (d)** refers to the case where the coupling between **L** and the nuclear axis is very weak while that between **L** and the nuclear rotation is strong. This is usually the case for molecular high Rydberg states. Here, the angular momentum of nuclear rotation is called **R** (rather than **N**) and has magnitude $\sqrt{R(R+1)}\hbar/2\pi$. Possible values for **R** are 0, 1, 2, ... . Vector addition of **R** and **L** yield **K**, which can have values:

$$K = (R + L), (R + L - 1), (R + L - 2), ..., |R - L| \tag{2.6}$$

The angular moments **K** and **S** together form total angular momentum **J**. In general (except for K<S), each level with a given K consist of 2S+1 subcomponents.

**Nitric oxide** has a total of fifteen electrons and forms an electronic ground state in the $(1\sigma)^2(2\sigma)^2(3\sigma)^2(4\sigma)^2(5\sigma)^2(1\pi)^4(2\pi)^1$ configuration, as shown in Figure 2.2. NO has eleven valence electrons but only the $\pi^*_{2p_x}$ electron is unpaired. Thus, total orbital angular momentum projection is
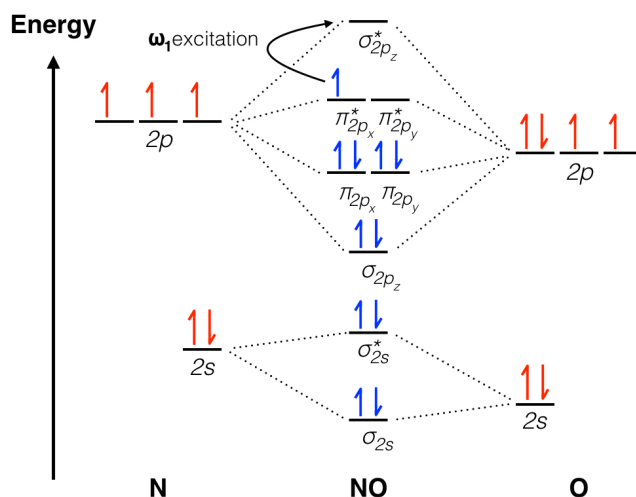
Figure 2.2: **NO molecular orbital diagram** - Only the open shell electron levels are displayed. The excitation pathway for $\omega_1$ photons is indicated.

$\Lambda = 1$ and total spin is $\mathbf{S} = 1/2$. The NO ground state is (mostly) Hund's case (a). Spin-orbit interaction yields a multiplet $\Omega = \Lambda + \Sigma = 3/2, 1/2$. The notation for the resulting states are:

$$^2\Pi_{3/2} \qquad \text{and} \qquad ^2\Pi_{1/2}$$

Figure 2.3 shows the NO level diagram and our excitation pathway. As typical for Hund's case (a), spin-orbit splitting between $\Omega = 3/2$ and $\Omega = 1/2$ is large compared to the rotational spacing. As mentioned previously, levels with $\Lambda \neq 0$ are double degenerate. Interactions between nuclear rotation and $\mathbf{L}$ causes this degeneracy to lift and is called $\Lambda$-type doubling. As a result, each J value splits into two components. Designations e and f label the rotationless parity as positive and negative, respectively.

The first excited state in NO has the configuration $(1\sigma)^2(2\sigma)^2(3\sigma)^2(4\sigma)^2$ $(5\sigma)^2(1\pi)^4(6\sigma)^1$ and corresponds to a $^2\Sigma$ electronic state. Since $\Lambda = 0$, this state is Hund's case (b). For S=1/2 the multiplicity is 2. Similar to above case, molecular rotation induces a small internal magnetic field which splits

the spin degeneracy. The spectroscopic labels $F_1(K)$ and $F_2(K)$ refer to components with J=K+1/2 and J=K-1/2, respectively.

For any electric dipole transition, the following selection rules apply:

$$\Delta J = 0, \pm 1, \text{ with the restriction } J = 0 \Rightarrow J = 0$$

$$\text{Parity:} \quad \text{only } pos \rightleftharpoons neg$$

$$\Delta S = 0$$

The first two rules are rigorous. A very cold (<1K) spectrum of the NO X to A-state transitions consists of four lines:

$pQ_{11}(1/2):$     $J" = 1/2, K" = 1, F1f \Rightarrow J' = 1/2, K' = 0, F1e$

$qR_{11}(1/2):$     $J" = 1/2, K" = 1, F1e \Rightarrow J' = 3/2, K' = 1, F1e$

$qQ_{21}(1/2):$     $J" = 1/2, K" = 1, F1e \Rightarrow J' = 1/2, K' = 1, F2f$

$rR_{21}(1/2):$     $J" = 1/2, K" = 1, F1f \Rightarrow J' = 3/2, K' = 2, F2f$

Transitions are designated P, Q, R for changes in J of +1, 0 , -1; p, q, r for changes in K. The subscripts 11 (or 21) label transitions to F1 (or F2) from F1.

In our experiment, we tune laser $\omega_1$ to the $qQ_{11}(1/2)$ transition ($\sim$226nm) to populate the rovibronic ground-state of the NO A-state. Subsequent photon absorption of $\omega_2$ light populates the high-Rydberg manifold between principal quantum numbers 35 to 80. The ionic core of such Rydberg molecules has configuration $(1\sigma)^2(2\sigma)^2(3\sigma)^2(4\sigma)^2(5\sigma)^2(1\pi)^4$ and corresponds to $^1\Sigma$.
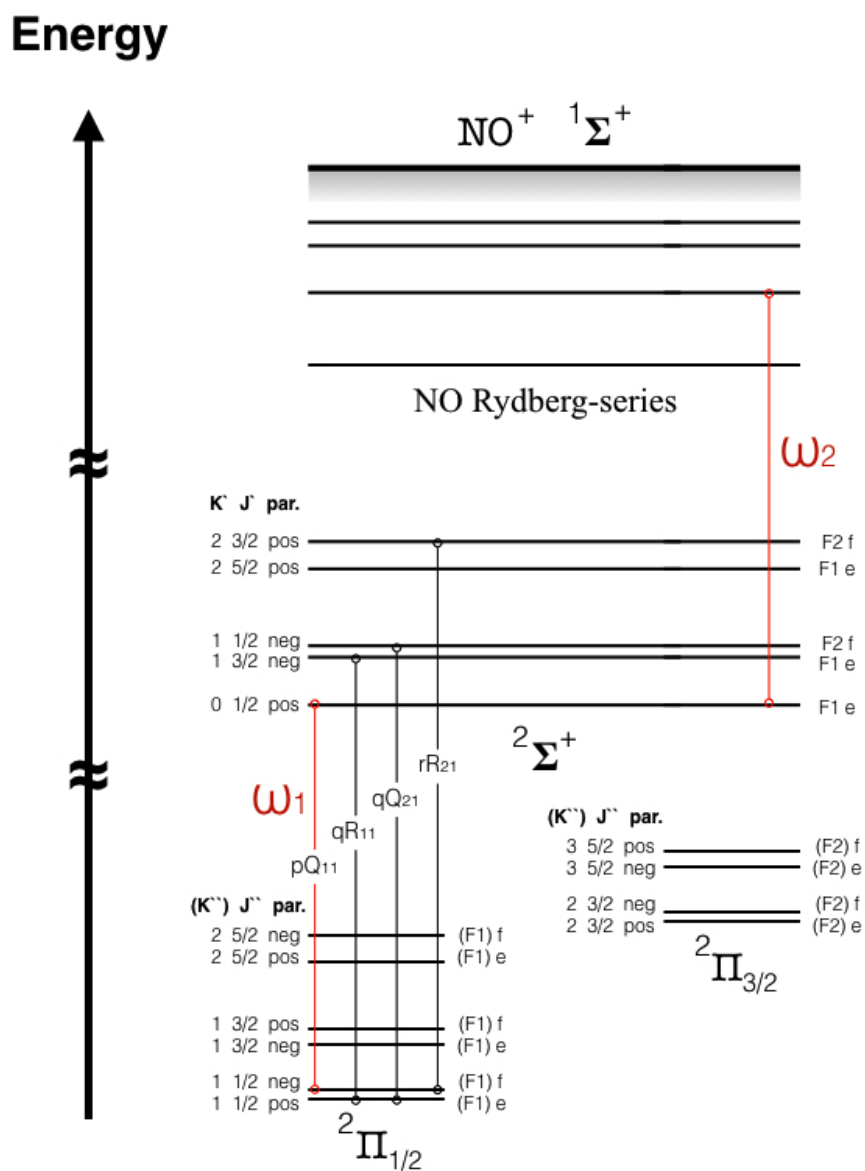
Figure 2.3: **NO level diagram for X, A and Ry-states and transitions A←X, Ry←A.** - Labeling information for energy levels and transitions are found in the text.

# Chapter 3

# Rydberg physics

The physical description of highly excited valence electron of an atom or molecule can be approximated through hydrogen wave functions. This is possible because the electric field of the system core, as seen from greater distance, is shielded through the inner electrons such that it looks similar to that experienced by the electron in the hydrogen atom. Highly excited systems, for which this is the case, are referred to as Rydberg atoms or molecules. They have special characteristics like an increased response to electric or magnetic fields as well as long radiative lifetimes.

## 3.1   Rydberg molecules

To first order, a Rydberg system is identical with atomic hydrogen, whose time-independent Schrödinger equation in the absence of external fields is:

$$\left(-\frac{\hbar^2\nabla^2}{2m_e} - \frac{e^2}{4\pi\epsilon_0 r}\right)\Psi(r,\theta,\phi) = E\Psi(r,\theta,\phi) \tag{3.1}$$

Here, $\nabla$ is the gradient operator, $\hbar$ is the reduced Plank constant $\hbar = h/2\pi$, $m_e$ is the rest mass of the electron, $\epsilon_0$ is the vacuum permittivity and $r$ is the Rydberg electron radial distance from the system core. Eq. 3.1 is best solved in spherical coordinates (see for example [19]), yielding the well known hydrogen wave function $\Psi_{n\ell m}$ and quantized energies:

$$W_n = -\frac{m_e^2 e^4}{8\epsilon_0^2 h^2}\frac{1}{n^2} = -\frac{Ry}{n^2} \tag{3.2}$$

Ry is the Rydberg unit of energy $(1Ry = hcR_\infty)$ and $n$ is called the principal quantum number. The angular momentum quantum number $\ell = 0, 1, ..., n-1$

in wave function $\Psi_{n\ell m}$ determines the magnitude of angular momentum of the Rydberg electron and magnetic quantum number $m = -\ell, ..., \ell$ it's projection (on an arbitrary z-axis).

Only Rydberg systems with high values for $n$ and $\ell$ are well represented by Eq. (3.1). Low angular momentum states, however, can penetrate and polarize the electronic shell structure of the ionic core. Here, the Rydberg electron experiences a larger positive force from the system core when it's wave function penetrates the inner electronic shells. Such states tend to be closer bound and the Rydberg electron has reduced energy. To account for this, a parameter called quantum defect was introduced through which an effective quantum number, $\nu \equiv n - \delta_\ell$, is defined. The quantum defect depends on angular momentum $\ell$. For nitric oxide, $\delta_\ell$ takes values of $\delta_s = 1.21$, $\delta_p = 0.73$, $\delta_d = -0.05$ and $\delta_{\ell > 3} \leq 0.01$ [11]. Thus, the Rydberg system energy spectrum becomes,

$$W_n^{Ryd} = W_{IP} - \frac{Ry}{(n - \delta_\ell)^2}, \tag{3.3}$$

where $W_{IP}$ is the ionization threshold of the respective atom or molecule.

Based on the solution of Eq. (3.1), many properties of Rydberg systems can be derived. Table 3.1 summarizes some important trends with regard to principal quantum number scaling. A detailed discussion of Rydberg physics is found in [28].

| Property | $n$-dependence |
|---|---|
| Binding energy | $n^{-2}$ |
| Energy between adjacent n states | $n^{-3}$ |
| Orbital radius | $n^2$ |
| Geometric cross section | $n^4$ |
| Polarizability | $n^7$ |
| Dipole moment | $n^2$ |
| Radiative lifetime | $n^3$ |

Table 3.1: Some general properties of Rydberg atoms

## 3.2 Dynamic processes in dense Rydberg gases

The study of dynamic processes in dense Rydberg gasses has been a 'hot topic' in our laboratory over the recent years. We were in particular interested in creating a model which could accurately describe the internal conversion of a dense Rydberg gas into a plasma. These efforts were first led by my colleagues Nicolas Saquet and Jonathan Morrison [52, 77]. They were further developed by Jachin Hung and Hossein Sadeghi [38] and more recently myself. The following shall serve as an introduction into the topic.

**Angular momentum mixing**

The properties of Rydberg molecules like dipole moment and predissociation lifetime are strongly dependent on the angular momentum state of the molecule. Rydberg molecules created within our experiment are subject to a number of interactions with their environment. Prominent perturbers are stray-fields, black-body-radiation and collisions with neutrals, ions and electrons. The result of these interactions is a statistical mixture of the nearly degenerate angular momentum-state manifolds. This greatly dilutes the core-penetrating low-l angular momentum states and boosts Rydberg lifetimes by typically an order of magnitude. For Rydberg states in NO, this effect has been observed and studied by [11, 87]. For our system, we expect l-mixing on a sub-nanosecond timescale.

**Lifetimes of Rydberg states**

There are two processes by which diatomic Rydberg molecules decay in the absence of a collision partner, radiative decay and predissociation:

$$M^* \xrightarrow{k_{RD}} M_X \qquad M^* \xrightarrow{k_{PD}} A + B \qquad (3.4)$$

$M^*$ is the Rydberg molecule, $M_X$ is the molecule in the ground state and A/B are atomic systems. NO Rydberg states decay primarily by predissociation [65]. Here, the Rydberg electron collides with the many-electron molecular core, leading to an internal transition of the molecule to an unstable

excited state. The molecule dissociates predominantly into neutral atoms. Excess energy goes into the motion of these fragments. The frequency of such collisions scales with the Bohr frequency and core penetration depends strongly on electron angular momentum $\ell$. Murgu et. al. [53] have collected the $\ell$-dependent rate coefficients for NO in atomic units:

Table 3.2: Predissociation rates for NO (atomic units)

| | |
|---|---|
| $k_s$ | $1.4 \cdot 10^{-2}/(2\pi n^3)$ |
| $k_p$ | $4.6 \cdot 10^{-2}/(2\pi n^3)$ |
| $k_d$ | $2.9 \cdot 10^{-2}/(2\pi n^3)$ |
| $k_f$ | $1.2 \cdot 10^{-3}/(2\pi n^3)$ |
| $k_{\ell>3}$ | $3 \cdot 10^{-5}/(2\pi n^3)$ |

Here, I have set $k_{\ell>3} = k_g$. As discussed previously, we expect angular momentum mixing on a sub-nanosecond timescale. Assuming equipartition of states over available quantum levels $m_\ell$ yields a rate constant for the predissociation of NO Rydberg molecule with PQN $n$:

$$k_{PD}(n) = \frac{\sum_\ell (2\ell + 1)k_\ell}{n^2} \frac{4.13 \cdot 10^{16}\mathrm{s}^{-1}}{2\pi n^3} \tag{3.5}$$

The first term accounts for the statistical weight of $\ell$-levels. Using Equation (3.5), Table 3.3 computes several values for the predissociation lifetime, $\tau_n = 1/k_{PD}(n)$, of NO Rydberg states.

**Penning ionization**

Penning ionization is an ionization process between two neutral atoms or molecules. Applied to our experiment, it refers to a dipole-dipole interaction between two neighbouring Rydberg molecules, which results in the ionization of one partner and the de-excitation of the other to a lower energy state. It's symbolic representation is:

$$M^*(n_0, \ell) + M^*(n_0, \ell) \longrightarrow M^+ + M^*(n\text{'}, \ell\text{'}) + e^- \tag{3.6}$$
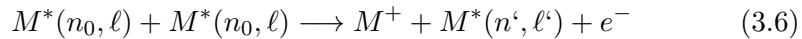
Table 3.3: Predissociation lifetimes $\tau_n$ for NO

| | |
|---|---|
| $\tau_{10}$ | 0.05 ns |
| $\tau_{20}$ | 1.54 ns |
| $\tau_{30}$ | 11.1 ns |
| $\tau_{40}$ | 44.1 ns |
| $\tau_{50}$ | 125 ns |
| $\tau_{60}$ | 286 ns |
| $\tau_{70}$ | 565 ns |
| $\tau_{80}$ | 1.00 $\mu$s |
| $\tau_{90}$ | 1.64 $\mu$s |

Here, $M^+$ is the molecular ion and $e^-$ a free electron. $(n_0, \ell)$ and $(n', \ell')$ are principal quantum number and angular momentum for initial and final states, respectively.

A theoretical study by Robicheaux [67] investigated the Penning process between two cold Rydberg atoms using a classical trajectory Monte Carlo method. The simulation was conducted for a fully mixed $\ell$-manifold. An ionization probability of 90% within 800 Rydberg periods was found for collision partners separated by less than $1.8 \cdot 2n^2 a_0$. Here, $a_0$ is the Bohr radius. He found that in such interaction the deactivated partner, $M^*(n', \ell')$, would transition to a distribution state $n' \propto n^5$ and $n'_{max} = n_0/\sqrt{2}$ due to energy conservation.

**Charged particle collisions with Rydberg molecules**

As discussed above, dense Rydberg gasses can achieve a level of ionization via Penning interactions. This, in turn, leads to new dynamics between the remaining Rydberg states and Penning ions and electrons. The three most prominent examples, valid for both atomic and molecular Rydberg systems, are:

**Impact ionizing collisions** between a free electron and a Rydberg

system. In such collisions the free electron transfers kinetic energy to the bound Rydberg electron, leading to ionization. $n_i$ is the initial principal quantum number.

$$M^*(n_i) + e^- \xrightarrow{k_{ion}} M^+ + e^- + e^- \tag{3.7}$$
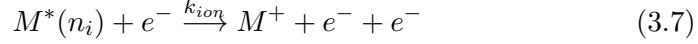
**Three body recombination** (TBR) is the reverse process of the electron-Rydberg ionizing collision. Here, two free electron and an ion interact, yielding to the capture of one electron by the ion. A new Rydberg state is formed and the excess energy is carried away by the second electron. $n_f$ is the final principal quantum number.

$$M^+ + e^- + e^- \xrightarrow{k_{TBR}} M^*(n_f) + e^- \tag{3.8}$$
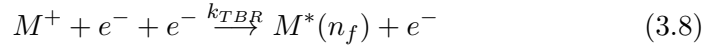
**n-changing collisions** between free electron and bound Rydberg states. In such interaction, the free electron either gains or looses energy, leaving the Rydberg system behind in lower or higher n-state, respectively.

$$M^*(n_i) + e^- \xrightarrow{k_{n_i,n_f}} M^*(n_f) + e^- \tag{3.9}$$
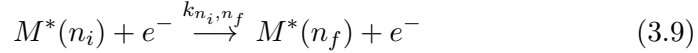
A theoretical study of these three interactions was done by Mensbach and Keck [46] and more recently further refined by Pohl et. al. [64]. The following rate coefficients $k_{ion}$, $k_{TBR}$ and $k_{n_i,n_f}$ were obtained from fits to Monte Carlo simulation data:

$$k_{ion}(n_i) = \frac{11(Ry/k_BT)^{1/2}k_0 e^{-\epsilon_i}}{\epsilon_i^{7/3} + 4.38\epsilon_i^{1.72} + 1.32\epsilon_i}$$

$$k_{TBR}(n_f) = \frac{11(Ry/k_BT)^{1/2}k_0 e^{-\epsilon_f}}{\epsilon_f^{7/3} + 4.38\epsilon_f^{1.72} + 1.32\epsilon_f}n_f^2\Lambda^3\rho_e e^{\epsilon_f}$$

$$k_{n_i,n_f} = k_0\frac{\epsilon_i^{5/2}\epsilon_f^{3/2}}{\epsilon_>^{5/2}}e^{-(\epsilon_i-\epsilon_<)}\left(\frac{22}{(\epsilon_> + 0.9)^{7/3}} + \frac{9/2}{\epsilon_>^{5/2}\Delta\epsilon^{4/3}}\right) \tag{3.10}$$

19

Here, $k_0 = e^4/(k_B T \sqrt{m_e Ry})$, $\epsilon_{i/f} = Ry/n_{i/f}^2 k_B T$, $\Delta\epsilon = |\epsilon_f - \epsilon_i|$, $\epsilon_> = max(\epsilon_i, \epsilon_f)$, $\epsilon_< = min(\epsilon_i, \epsilon_f)$ and $\Lambda = \sqrt{h^2/2\pi m_e k_B T}$ is the thermal de Broglie wavelength. $\rho_e$ is the electron density, $m_e$ the electron mass and $k_B$ is the Boltzmann constant.

There is one more important electron-Rydberg interaction that applies only to the case of molecular Rydberg states. An atomic Rydberg ion colliding with a free electron cannot recombine (radiationless) in a two-body process due to energy conservation.[2] Molecules, however, have more internal degrees of freedom and are equipped to absorb energy. Thus, a molecular ion can bind a free electron in a two-body collision. This typically leads to an internal transition of the now neutral molecule to an unstable excited state. The result is molecular dissociation. This process is called **dissociative recombination** (DR). For nitric oxide, it is represented by:

$$NO^+ + e^- \xrightarrow{k_{DR}} N^* + O^* \tag{3.11}$$
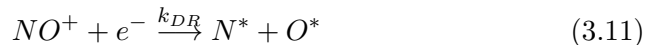
Here, $N^*$ and $O^*$ are neutral nitrogen and oxygen in a possible state of excitation. The rate constant, $k_{DR}$, has been thoroughly characterized by scattering theory calculations and experimental measurements [81]. We use:

$$k_{DR} = 6 \times 10^{-6} \, T_e^{-1/2} \, \frac{\sqrt{\mathrm{K}} \cdot \mathrm{cm}^3}{\mathrm{s}} \tag{3.12}$$

## 3.3   Field ionization of Rydberg molecules

Characteristic for Rydberg systems is the relatively loosely-bound valence electron, which is susceptible to field ionization for fields of typically a few hundred Volts per cm. In a classical model, ionization occurs when an external electric field lowers the potential barrier of a bound electron enough for the electron to escape.

The hydrogen potential along $\hat{z}$, for a system perturbed by an uniform

---

[2]The cross-section for recombination accompanied by photon emission is negligible in dense plasma.
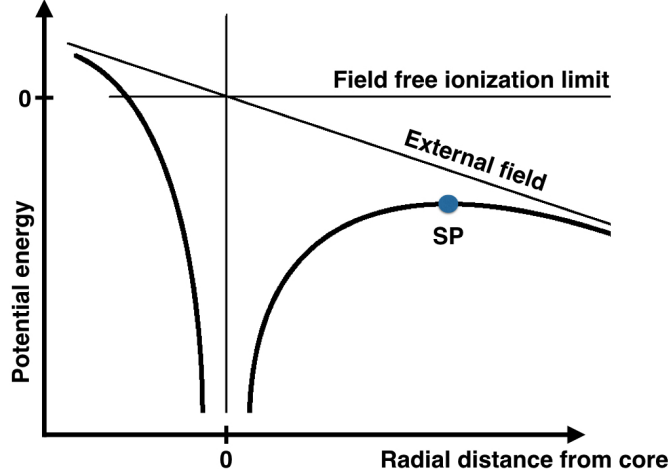
Figure 3.1: **Classical field ionization of a Rydberg atom**

external field $\mathbf{E} = -E\hat{z}$, becomes:

$$W(z) = -\frac{\zeta}{z} - Eze \qquad \text{where } \zeta = \frac{e^2}{4\pi\epsilon_0} \tag{3.13}$$

This potential has a saddle point at $z_{sp} = \sqrt{\zeta/Ee}$ with a reduced binding energy $W(z_{sp}) = -2\sqrt{\zeta Ee}$. When this energy reduction becomes larger than the classical binding energy, $W_B = -Ry/n^2$, the system ionizes. Setting these two energy values equal yields the value $E_{FI}$ for the field strength required to field ionize Rydberg electron with principal quantum number n:

$$E_{FI} = \frac{W_B^2}{4\zeta e} = \frac{Ry^2}{4\zeta en^4} \tag{3.14}$$

Eq. 3.14 states the classical ionization limit for atomic hydrogen without considering the Stark effect. The Stark effect describes the shifting of energy levels as a consequence of external electric fields. For Rydberg systems, these shifts can be significant due to their large dipole moments. It turns

out that, other than expected, red, or down shifted, Stark states ionize near the classical ionization limit while blue, or upshifted, states only ionize at higher fields.[28] It is possible to express the increase in binding energy of extreme red, high-$n$ Stark states due to the linear stark effect via $W_B^{Stark} = \sqrt{16/9}W_B$. Thus, Eq. 3.14 becomes:

$$E_{FI}^{Stark} = \frac{4Ry^2}{9\zeta en^4} \tag{3.15}$$

I rewrite above equation in terms of binding energy, expressed in wavenumbers, and field, expressed in V/cm, and obtain:

$$W_B[\text{cm}^{-1}] = 4.59 \cdot \sqrt{E[\text{V/cm}]} \tag{3.16}$$

# Chapter 4

# Plasma theory

This chapter aims to give an introduction into plasma theory. One goal of this thesis is to obtain a formalism linking the microscopic properties of our plasma system to macroscopic observables. We can only approximate our real system values and it is important to keep track of and understand all the assumptions that are necessary to derive a theoretical kinetic representation of our system.

For this reason, the first part of this chapter will review some general relations in plasma theory. Important concepts like the Debye length and quasi-neutrality, as well as plasma kinetic theory will be introduced. Section 4.2 will derive a theory framework on which I will draw in Part III of my thesis to model our system. Section 4.3 examines the applicability of 'classical' plasma theory in UNPs.

## 4.1 Introduction to plasma theory[1]

It is important to note that not all ionized gases can be called a plasma, because there is always some degree of ionization in any gas.[2] F. F. Chen defines a plasma as "*a quasineutral gas of charged and neutral particles which exhibits collective behaviour*".[15] To understand this definition, it is important to examine what is meant by 'collective behaviour' and 'quasi-neutrality'.

---

[1]For a more extensive account, it is referred to [7], [15] or [29].

[2]The Saha equation gives the amount of ionization to be expected in a gas in thermal equilibrium. For ordinary air at room temperature the fractional ionization is $\frac{\rho_{ionized}}{\rho_{neutral}} = 10^{-122}$ (see [15]).
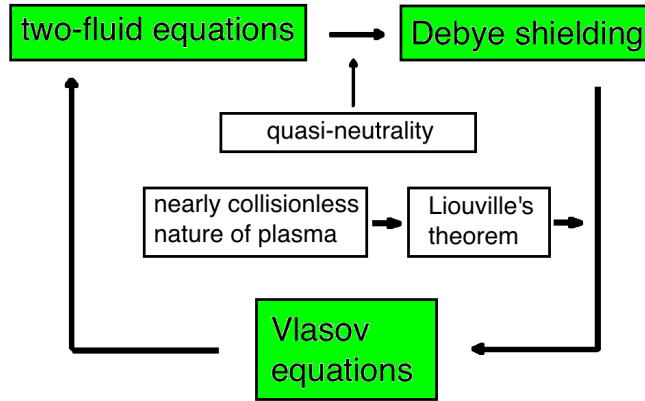
Figure 4.1: **Concept of circular logic on which plasma theory is based**

The following analysis will show that plasma theory can be based on a concept of circular logic. One can start by requiring quasi-neutrality and by approximating the plasma as a fluid, and subsequently derive the concept of 'Debye shielding' based on those assumptions. Debye shielding in turn can be used to show that a plasma will act to remain in a quasineutral state and that it can be described in a fluid approximation. I will investigate this more closely in the following.

**Debye shielding**

Consider a finite-temperature plasma consisting of a statistically large number of electrons and ions, distributed uniformly and having temperatures, $T_e$ and $T_i$, respectively. Plasma species do not need to be in thermal equilibrium with each other, they are, however, usually assumed to be equilibrated within one species. Each species, henceforth denoted as $\alpha$, can be regarded as a fluid[3] with density $\rho_\alpha$, pressure $P_\alpha = \rho_\alpha k_B T_\alpha$ and a mean velocity $\mathbf{u}_\alpha$.

---

[3]The fluid approximation is a description in which particles move on streamlines as determined by an electric mean field and a pressure gradient. It only holds for a nearly collisionless plasma where collisions may be neglected to first order. Origin and quality of this assumption will be discussed shortly.

The fluid equation of motion for each species is

$$m_\alpha \frac{d\mathbf{u}_\alpha}{dt} = q_\alpha \mathbf{E} - \frac{1}{\rho_\alpha} \nabla P_\alpha, \qquad (4.1)$$

where $m_\alpha$ and $q_\alpha$ are the particle mass and charge and $\mathbf{E}$ is the electric field. The given plasma is now subjected to a 'very slow' perturbation so that the following assumptions hold: the inertial term $d/dt$ is negligible as the perturbation is 'very slow'; inductive electric fields are negligible so that $\mathbf{E} \approx -\nabla \phi$, where $\phi$ is the electric potential; the plasma species remain in thermal equilibrium. With this, Eq.(4.1) reduces to

$$0 \approx -\rho_\alpha q_\alpha \nabla \phi - k_B T_\alpha \nabla \rho_\alpha, \qquad (4.2)$$

which can be solved to yield

$$\rho_\alpha = \rho_{\alpha 0} \cdot exp(-q_\alpha \phi / k_B T_\alpha), \qquad (4.3)$$

where $\rho_{\alpha 0}$ is a constant. Suppose that the discussed perturbation originates from a single additional test particle with charge, $q_T$, that is slowly inserted into the initially unperturbed, spatially uniform, neutral plasma (i.e. $\phi(t = 0) = 0$). The origin of the coordinate system shall be incident with the test particle. Upon insertion, particles with the same charge as the test particle will be slightly repelled and particles with the opposite charge slightly attracted. These slight displacements will result in a small, non-zero potential which will be determined by the superposition of the test particle potential with the potential of the plasma particles that have moved. The response of plasma particles towards the test particle is called shielding or screening, because the displacements reduce the effectiveness of the test particle field. The change in $\phi$ is calculated using Poisson's equation, where the cloud contribution is self-consistently represented by Eq.(4.3). Thus, Poisson's equation is given by:

$$\nabla^2 \phi(\mathbf{r}) = -\frac{1}{\epsilon_0} [q_T \delta(\mathbf{r}) + q_i \rho_i(\mathbf{r}) + q_e \rho_e(\mathbf{r})] \qquad (4.4)$$

The perturbation due to a single test particle is assumed to be small so that $|q_\alpha \phi| \ll k_B T_\alpha$, in which case Eq.(4.3) becomes $\rho_\alpha / \rho_{\alpha 0} = 1 - q_\alpha \phi / k_B T_\alpha$ and therefore:

$$\nabla^2 \phi(\mathbf{r}) = -\frac{1}{\epsilon_0}[q_T \delta(\mathbf{r}) + (1 - \frac{q_e \phi(\mathbf{r})}{k_B T_e})\rho_{e0} q_e + (1 - \frac{q_i \phi(\mathbf{r})}{k_B T_i})\rho_{i0} q_i] \qquad (4.5)$$

The assumption of initial neutrality means that $\rho_{e0} q_e + \rho_{i0} q_i = 0$, and above equation reduces to

$$\nabla^2 \phi(\mathbf{r}) - \frac{1}{\lambda_D^2}\phi(\mathbf{r}) = -\frac{q_T}{\epsilon_0}\delta(\mathbf{r}), \qquad (4.6)$$

where the effective Debye length is defined as

$$\frac{1}{\lambda_D^2} = \sum_\alpha \frac{1}{\lambda_{D,\alpha}^2} \qquad (4.7)$$

and the species Debye length is:

$$\lambda_{D,\alpha}^2 = \frac{\epsilon_0 k_B T_\alpha}{\rho_{\alpha 0} q_\alpha^2} \qquad (4.8)$$

Equation (4.6) can be solved to give

$$\phi(\mathbf{r}) = \frac{q_T}{4\pi\epsilon_0 r}e^{-r/\lambda_D}, \qquad (4.9)$$

which has the general form of a Yukawa potential but is in this context commonly referred to as Debye-Hückel potential. For $r \ll \lambda_D$ this potential is identical to the potential of the test particle in vacuum. For $r \gg \lambda_D$ the potential $\phi(\mathbf{r})$ approaches zero because the test charge is completely screened by the surrounding charged particle cloud. With this, $\lambda_D$ can be seen as the spherical distance at which the shielding by the plasma cloud lessens the particles potential by the factor 1/e.

It is important to realize that the test particle could be any given particle in the plasma and therefore, Eq.(4.9) is the time-averaged effective potential of any selected particle in the plasma system.

This analysis is based on the assumption that there is a macroscopically large number of shielding particles in the cloud. Therefore, one requires that the system is much larger than one Debye length and that there is a statistically large number of particles in each Debye sphere, i.e. one requires that

$$\frac{4}{3}\pi \lambda_D^3 \cdot \rho_0 \gg 1. \tag{4.10}$$

**Quasi-neutrality**

One of the initial conditions required in the derivation of Debye shielding was the condition of quasi-neutrality. In the moment of ionization, every plasma system is quasineutral. The above requirement means that the ion and electron densities remain approximately equal, i.e. that $\rho_e \approx \rho_i = \rho$ for all times. It is possible to show that quasi-neutrality is indeed a good approximation for systems with a Debye length much smaller than the system size.

Consider an initially neutral plasma with temperature $T_e$ and calculate the largest radius $r_{max}$ of a sphere that could spontaneously become depleted of electrons due to electron thermal motion.[4] Optimal depletion means that the electrons have a velocity distribution, such that they all leave the sphere radially and come to a rest on the sphere's surface, before they are pulled back in by the positive field of the ionic charge. One way to calculate the energy stored in this artificial system is by determining the energy in the electrostatic field that is produced by the ions. This electrostatic energy was initially zero and only exists due to the developed charge separation. It must be equivalent to the work done by the electrons.

The energy density of an electric field, $\mathbf{E}$, is $\epsilon_0 E^2/2$. The ion charge density in a sphere of radius $r$ is $Q = 4\pi\rho e r^3/3$ and the electric field at radius $r$ is $E_r = Q/4\pi\epsilon_0 r^2 = \rho e r/3\epsilon_0$. The ionic electrostatic field energy in

---

[4]In this calculation, ion motion is neglected and the ions are approximately represented by a uniform background charge. This is a valid approximation, because the electron mobility vastly exceeds that of the ions due to the large mass ratio.

the electron-depleted sphere of radius $r_{max}$ is thus:

$$W = \int_0^{r_{max}} \frac{\epsilon_0 E_r^2}{2} 4\pi r^2 dr = \pi r_{max}^5 \frac{2\rho^2 e^2}{45\epsilon_0} \tag{4.11}$$

The initial electron thermal kinetic energy was:

$$W_{kinetic} = \frac{3}{2}\rho k_B T_e \cdot \frac{4}{3}\pi r_{max}^3 \tag{4.12}$$

Equating energies yields

$$r_{max}^2 = 45\frac{\epsilon_0 k_B T_e}{n_e e^2} \qquad or \qquad r_{max} \approx 7\lambda_D. \tag{4.13}$$

This quick analysis shows that it is theoretically possible for a plasma of temperature $T_e$ to evolve into a state where a volume $4/3\pi(7\lambda_D)^3$ spontaneously loses all its electrons. Since the initial conditions for this to happen are statistically extremely improbable, expected regions of non-neutrality are much smaller and unlikely to exceed one Debye length. Thus, an initially quasineutral plasma with a microscopic Debye length remains quasineutral.

**Kinetic theory and Vlasov's equation**

A good description of ultracold plasmas can be obtained by kinetic theory with the introduction of the phase space distribution function $f_\alpha(\mathbf{x}, \mathbf{v}, t)$. This function describes how particles are distributed in both physical and velocity space. The number density of particles of species $\alpha$ in physical space is defined by

$$\rho_\alpha(\mathbf{r}, t) = \int f_\alpha(\mathbf{r}, \mathbf{v}, t)d\mathbf{v}, \tag{4.14}$$

and the mean (fluid) velocity of the particles is given by:

$$\mathbf{u}_\alpha(\mathbf{r}, t) = \frac{1}{\rho_\alpha(\mathbf{r}, t)} \int \mathbf{v} f_\alpha(\mathbf{r}, \mathbf{v}, t)d\mathbf{v} \tag{4.15}$$

In both equations the integrals range from $-\infty$ to $+\infty$.

To follow the evolution of a system with a known initial distribution function, one needs to obtain an equation that describes the changes to this function as time progresses. This can be done by invoking Liouville's theorem. The theorem asserts that the phase-space density is constant along the trajectories of the system - that is that the number of particles, as one follows a group of particle through phase-space, is constant with time.

The theorem holds for conservative systems within a Hamiltonian formalism, and for **collisionless** particles that share the same Hamiltonian function. It is not applicable for systems of different species but can be used for each species separately. The constraint of a 'conservative system' means that if the system undergoes any series of changes, and is then brought back (in any manner) to its original state, then the whole work done is zero.

The basic idea behind this theorem relies on an interesting feature of phase-space. For a conservative Hamiltonian system, a pair of simple relations completely determines particle evolution:

$$\frac{d\mathbf{r}}{dt} = \mathbf{v} \qquad\qquad \frac{d\mathbf{v}}{dt} = \frac{\mathbf{F}}{m} \tag{4.16}$$

Knowing a particle's starting point in phase-space predefines its whole trajectory. Liouville's theorem is based on the fact that phase-space trajectories of independent particles do not intersect. If two trajectories intersect at one point, then that point represents a starting point for the further development of these trajectories. Both trajectories would then develop the same way - in both directions in time - in that case they would not be intersecting, but identical.

Consider a single particle on a trajectory in phase-space, and define an infinitesimal vicinity around this particle at a point $t_0$ in time. As time advances, one can follow this particle and all other particles that started in this infinitesimal volume. All particles in this volume share similar initial conditions and will be subjected to identical forces - they will stay close

together as time evolves. Due to the fact that phase-space trajectories don't intersect, it is impossible that a trajectory - once in this volume - leaves it, because this would mean that it would have to intersect with a trajectory on the volume surface. Therefore, the number or density of particles in the vicinity of one point, which is moving in phase-space according to the equation of motion, is constant in time.

To enforce this theorem in three-dimensional phase-space, one must ensure the conservation of the total number of particles,

$$N = \int f(\mathbf{r}, \mathbf{v}, t) d\mathbf{r} d\mathbf{v}, \tag{4.17}$$

within a phase-space volume element. This is done by invoking that the total time derivative must vanish:

$$0 = \frac{dN}{dt} = \int (\frac{\partial f}{\partial t} + \frac{\partial f}{\partial \mathbf{r}} \frac{\partial \mathbf{r}}{\partial t} + \frac{\partial f}{\partial \mathbf{v}} \frac{\partial \mathbf{v}}{\partial t}) d\mathbf{r} d\mathbf{v} \tag{4.18}$$

The above equation must hold for every volume element in phase-space, therefore:

$$\frac{\partial f}{\partial t} + \frac{\partial f}{\partial \mathbf{r}} \frac{\partial \mathbf{r}}{\partial t} + \frac{\partial f}{\partial \mathbf{v}} \frac{\partial \mathbf{v}}{\partial t} = 0 \tag{4.19}$$

It is easy to rewrite this equation by implementing the equations of motion, Eq. (4.16), which yields

$$\frac{\partial f}{\partial t} + \mathbf{v} \cdot \frac{\partial f}{\partial \mathbf{r}} + \frac{\mathbf{F}}{m} \cdot \frac{\partial f}{\partial \mathbf{v}} = 0, . \tag{4.20}$$

Equation (4.20) is called the 'Vlasov equation' after A. A. Vlasov who was the first to formulate it in this form.

If one continues to investigate kinetic theory, one can show that fluid theory, as it was used to derive the Debye screening length, can be found as a specialization of the above formalism. More specifically, the plasma fluid equation of motion, Eq. (4.1), is obtained by taking the first moment of Eq.

(4.20), i.e.:

$$\int \mathbf{v}[\frac{\partial f}{\partial t} + \mathbf{v} \cdot \frac{\partial f}{\partial \mathbf{r}} + \frac{\mathbf{F}}{m} \cdot \frac{\partial f}{\partial \mathbf{v}}]d\mathbf{v} = 0$$

$$\Rightarrow \quad m_\alpha \frac{d\mathbf{u}_\alpha}{dt} = q_\alpha \mathbf{E} - \frac{1}{\rho_\alpha}\nabla P_\alpha \tag{4.21}$$

In this, the circle of reasoning closes as fluid theory and quasi-neutrality can now be used to introduce the Debye length.

In the above discussion of plasma theory, the fact that particle collisions seem forbidden in the kinetic theory approach was set aside. Is it in fact reasonable to introduce Liouville's theorem to describe the evolution of a plasma system?

**Collisionless plasma?**

The kinetic theory approach is based on Liouville's theorem for collisionless particles. Why is it that collisions threaten the validity of this theorem?

Figure 4.2 shows the trajectories of two (neutral) particles in one-dimensional phase-space. $t_1$, $t_2$, $t_3$ are subsequent steps in time. Both particles have an initially positive velocity, however one of the particles is moving much faster. At $t = t_2$ the faster particle bumps into the slower, thereby transferring kinetic energy. The collision results in a sudden change in the velocity of both particles that can be regarded as an end of the phase-space trajectory at one point (annihilation) and the creation of a new one at a different point (creation). This corrupts the conservation of phase-space volume and therefore Liouville's theorem.

For charged particle systems, one can argue that collisions that result in an apparent annihilation of a phase-space trajectory are infrequent enough so that they can be neglected.

Consider a classical many-body system of plasma particles where the electrostatic forces, $\mathbf{F}_{\alpha,p}$, upon which the various charged particles $p$ react, are known. These forces change the particle trajectories in phase-space.
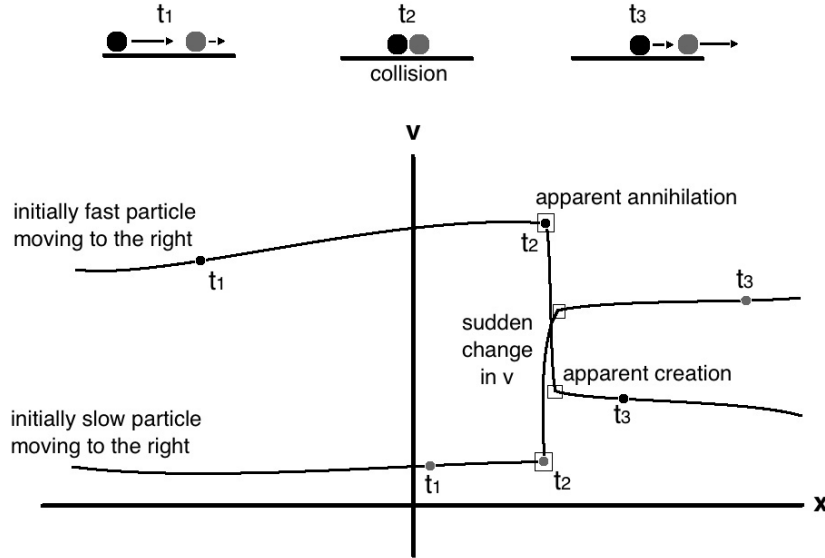
Figure 4.2: **Collision in phase-space** - Two particles collide in one-dimensional phase-space. $t_1$, $t_2$, $t_3$ are subsequent time steps. As a result of the collision, both particles assume new trajectories which can be seen as the annihilation of the old and the creation of a new respective trajectory.

They are in general composed of a macroscopic, or slowly varying part, together with a microscopic, or rapidly varying part due to short-range inter-particle forces, i.e. collisions. This first part is termed macroscopic because it will be approximately the same for all particles occupying the same region in phase-space. The fundamental assumption of the kinetic theory approach is that the macroscopic forces are dominant over the microscopic and phase-space volume is approximately conserved.

To examine this statement, one can consider the change to the path of a test particle of charge $q_T$ and mass $m_T$, as it is injected with velocity $\mathbf{v}_T$ into the plasma. This test particle will undergo a number of random collisions with the plasma particles, thereby altering its momentum and energy. The

intensity of a collision can be characterized by the deflection angle $\theta$, which is given by

$$tan(\theta/2) = \frac{q_T q_\alpha}{4\pi\epsilon_0 b\mu v_{rel}^2},\tag{4.22}$$

with reference to the Rutherford scattering problem in the center-of-mass frame. Here, $\mu^{-1} = m_T^{-1} + m_\alpha^{-1}$ is the reduced mass, $b$ is the impact parameter, $v_{rel}$ is the initial relative velocity between the test particle and the plasma particle in the respective scattering event and $q_\alpha$ and $m_\alpha$ denote the charge and mass of the latter.

To differentiate between macroscopic and microscopic exertion of influence onto the test particle, it is common to separate scattering events into two groups: small-angle collisions where $\theta < \pi/2$ and large-angle collisions where $\pi/2 \leq \theta \leq \pi$. The impact parameter of a $\pi/2$ collision can be found using Eq. (4.22):

$$b_{\pi/2} = \frac{q_T q_\alpha}{4\pi\epsilon_0 \mu v_{rel}^2}\tag{4.23}$$

Figure 4.3 shows an example for a $\pi/2$ scattering event and a small-angle scattering event with respective cross-sections. The total cross section for all large-angle scattering events is:

$$\tilde{\sigma}_{large} \approx \pi b_{\pi/2}^2 = \pi(\frac{q_T q_\alpha}{4\pi\epsilon_0 \mu v_{rel}^2})^2\tag{4.24}$$

Grazing (small-angle) collisions occur much more frequently but with less of an impact on the test particle. To compare the respective cumulative effect of small- and large-angle collisions, it is possible to construct an effective small-angle collision cross-section.

For this, the first step is to sum over a number of small-angle deflections and calculate at which point the cumulative effect is equivalent to a large-angle deflection, i.e.:

$$\theta_{large}^2 \simeq \pi^2/4 \overset{!}{=} \sum_{i=1}^{N} \theta_{i,small}^2 = \mathcal{F}t^* \cdot \int_{b_{\pi/2}}^{\lambda_D} 2\pi b[\theta(b)]^2 db\tag{4.25}$$
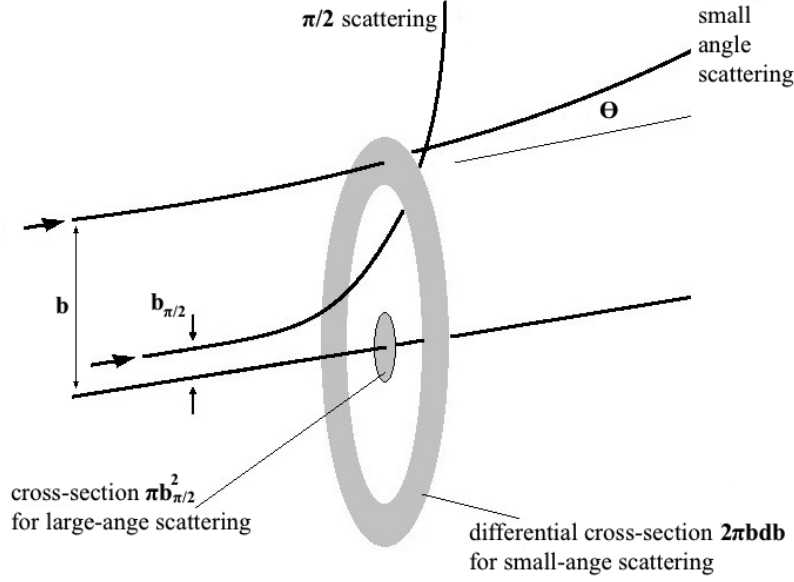
Figure 4.3: **Differential scattering cross-section for large and small deflections** - Large-angle scattering events only occur for impact parameters smaller than $b_{\pi/2}$, i.e. for initial trajectories crossing trough the inner circle area.

$2\pi bdb$ is the circle area between $b$ and $db$. $\theta(b)$ is the deflection at impact parameter $b$ according to Eq.(4.22). With this, the integration distinguishes between differential cross-sections at different impact parameters. $\mathcal{F} = \rho_P v_{rel}$ is the apparent flux of particles where $\rho_P$ is the plasma density. $t^*$ is the unknown variable in above equation and has dimension of time. The lower integration limit is the impact parameter limit for large-angle collisions, $b_{\pi/2}$, and the upper limit is the Debye length since particles further away are screened.

Solving Eq.(4.25) for $t^*$ gives the time needed by small-angle collisions to achieve the cumulated effect of one ($\pi/2$) large-angle collision. At the same time, $t^{-1} = \tilde{\sigma}\mathcal{F}$ (cross-section times particle flux), can be seen as the rate at which collisions occur. With this, Eq.(4.25) can be rearranged to give, $\tilde{\sigma}^*$, the cross-section for cumulative grazing collisions that are equivalent to

a large-angle scattering event:

$$\tilde{\sigma}^* = \int_{b_{\pi/2}}^{\lambda_D} 8\pi^{-1} b \left( \frac{q_T q_P}{2\pi\epsilon_0 \mu v_{rel}^2 b} \right)^2 db \approx \pi ln \left( \frac{\lambda_D}{b_{\pi/2}} \right) \tilde{\sigma}_{large} \tag{4.26}$$

With this equation, it becomes apparent that if $\lambda_D \gg b_{\pi/2}$, then the path of the plasma particles is mostly determined by the cumulative effects of macroscopic particle interactions rather than by head-on collisions. This is what was meant by 'collective behavior'. For systems in which above conditions apply, it is possible to neglect large-angle perturbation by short-range particle interactions and employ Liouville's theorem as an approximation of the system.[5]

The requirement $\lambda_D \gg b_{\pi/2}$ can be rearranged to give $6\pi\rho\lambda_D^3 \gg 1$, which is similar to the condition found in 4.1. Introducing the Coulomb coupling parameter,

$$\Gamma = \frac{e^2/4\pi\epsilon_0 a_{ws}}{k_B T}, \qquad \text{where} \qquad a_{ws} = (3/4\pi\rho)^{1/3} \tag{4.27}$$

is the Wiegner-Seitz radius that gives the average distance between particles, the very same relation can be written as:

$$\frac{\sqrt{3}}{2\Gamma^{3/2}} \gg 1 \tag{4.28}$$

Collisionless plasma theory therefore requires that $\Gamma \ll 1$. It is in fact the breakdown of standard plasma theory and the lack of an adequate description of correlated many-body systems, which makes UNPs so intriguing. This will be discussed further in section 4.3.1.

Returning to the previous analysis, one can conclude that plasma kinetic theory does not follow each particle on its complicated path through space

---

[5]Choosing $\pi/2$ as the deflection angle that separates macroscopic from microscopic interactions seems somewhat arbitrary. This, however, is of no consequence as the logarithmic dependence in Eq. (4.26) makes any choice of similar order basically equivalent in the final result.

but instead averages over the region where binary collisions occur and then treats a particle and its immediate surroundings as subject to an overall collective mean-field that is created by plasma particles positioned further away.

Instead of knowing the exact location of all $N = N_e + N_i$ particles in six-dimensional phase-space by solving $6N$ equations (4.16), it is the requirement of $\sqrt{3/4}/\Gamma^{3/2} \gg 1$ that allows for the employment of a statistical treatment by utilizing $\rho$, $\mathbf{u}_\alpha$ and $T_\alpha$.[6]

## 4.2  Dynamics in two-species neutral plasmas

Within the collisionless approximation, this section establishes a formalism that allows us to model the expansion and decay of a non-spherical plasma system into vacuum. We wish to extend above analysis, represented by Vlasov's equation, Eq. (4.20), to a dissociating plasma. The evolution of such system is described by the Boltzmann equation, a generalization of Vlasov's equation, formulated to include dissociative recombination (DR) of electrons and ions:

$$\frac{\partial f_\alpha}{\partial t} + \mathbf{v} \cdot \frac{\partial f_\alpha}{\partial \mathbf{r}} - m_\alpha^{-1} \frac{\partial f_\alpha}{\partial \mathbf{v}} q_\alpha \frac{\partial \phi(\mathbf{r})}{\partial \mathbf{r}} = \left( \frac{\partial f_\alpha}{\partial t} \right)_{DR} \tag{4.29}$$

Here, $m_\alpha$ and $q_\alpha$ designate once more the mass and charge of particle species $\alpha = e, i$, for electrons and ions respectively. The force term from Eq. (4.20) is expressed via the electrostatic potential $\phi(\mathbf{r})$:

$$\mathbf{F} = -q_\alpha \frac{\partial \phi(\mathbf{r})}{\partial \mathbf{r}} \tag{4.30}$$

---

[6]A more rigorous discussion of the kinetic theory of plasmas starts with a classical Hamiltonian to derive a general form of Liouville's equation for the N-particle phase-space density. It is possible to obtain a hierarchy of density functions (BBGKY-Hierarchy - after Bogolyubov, Born, Green, Kirkwood and Yvon) through integration. The one-particle phase-space probability function $f_\alpha$ is obtained through neglecting of higher orders in this hierarchy.

### 4.2.1 Moments of the Boltzmann equation

I begin my analysis with the zeroth and first moments of the Boltzmann equation. To calculate the zeroth moment of Eq. (4.29), I integrate over $d\mathbf{v}$:

$$\int \frac{\partial f_\alpha}{\partial t} d\mathbf{v} + \int \mathbf{v} \frac{\partial f_\alpha}{\partial \mathbf{r}} d\mathbf{v} - \int m_\alpha^{-1} \frac{\partial f_\alpha}{\partial \mathbf{v}} q_\alpha \frac{\partial \phi(\mathbf{r})}{\partial \mathbf{r}} d\mathbf{v} = \int \left( \frac{\partial f_\alpha}{\partial t} \right)_{DR} d\mathbf{v} \quad (4.31)$$

The first integral,

$$\int \frac{\partial f_\alpha}{\partial t} d\mathbf{v} = \frac{\partial}{\partial t} \int f_\alpha d\mathbf{v} = \frac{\partial \rho}{\partial t}, \quad (4.32)$$

is reduced to the density as the time derivative is placed in front of the integral. I apply quasineutrality, i.e. $\rho_e \approx \rho_i \equiv \rho$, in the last step.

The second term can be rearranged to give

$$\int \mathbf{v} \frac{\partial f_\alpha}{\partial \mathbf{r}} d\mathbf{v} = \frac{\partial}{\partial \mathbf{r}} \int \mathbf{v} f_\alpha d\mathbf{v} = \frac{\partial}{\partial \mathbf{r}} (\rho \mathbf{u}_\alpha), \quad \text{where} \quad \mathbf{u}_\alpha = \frac{\int \mathbf{v} f_\alpha d\mathbf{v}}{\int f_\alpha d\mathbf{v}}. \quad (4.33)$$

I rearrange the last integrand on the left side using the divergence theorem:

$$- \int m_\alpha^{-1} \frac{\partial f_\alpha}{\partial \mathbf{v}} q_\alpha \frac{\partial \phi}{\partial \mathbf{r}} d\mathbf{v} = - \frac{q_\alpha}{m_\alpha} \frac{\partial \phi}{\partial \mathbf{r}} \int \frac{\partial}{\partial \mathbf{v}} f_\alpha d\mathbf{v} = - \frac{q_\alpha}{m_\alpha} \frac{\partial \phi}{\partial \mathbf{r}} \underbrace{\int_{S_v}^{v=\infty} f_\alpha d^2 v}_{=0}$$

$$(4.34)$$

This term vanishes as the phase-space density is zero for $v \to \infty$. The right-hand side of Eq. (4.31) can be evaluated to give:

$$\int \left( \frac{\partial f_\alpha}{\partial t} \right)_{DR} d\mathbf{v} = \left( \frac{\partial \rho}{\partial t} \right)_{DR} = -k_{DR} \cdot \rho^2 \quad (4.35)$$

Here, in the first step, I integrate the phase space distribution function over velocity to obtain the variation of density with time, equivalent to the right hand side of Eq. (4.31). The second step accounts for the fact that dissociative recombination is a second order kinetic process, dependent on the product of the (equal) ion and electron densities. $k_{DR}$ is the electron-ion dissociative recombination rate constant. With this, the zeroth order

moment of the Boltzmann equation becomes the equation of continuity:

$$\frac{\partial \rho}{\partial t} + \frac{\partial}{\partial \mathbf{r}}(\rho \mathbf{u}_\alpha) + k_{DR} \cdot \rho^2 = 0 \qquad (4.36)$$

To find the first moment of the Boltzmann equation I multiply Eq. (4.29) by $m_\alpha \mathbf{v}$, and integrate over $d\mathbf{v}$. I obtain:

$$m_\alpha \int \mathbf{v} \frac{\partial f_\alpha}{\partial t} d\mathbf{v} + m_\alpha \int \mathbf{v}(\mathbf{v}\frac{\partial f_\alpha}{\partial \mathbf{r}}) d\mathbf{v} - q_\alpha \int \mathbf{v}\frac{\partial \phi}{\partial \mathbf{r}}\frac{\partial f_\alpha}{\partial \mathbf{v}} d\mathbf{v} = \int m_\alpha \mathbf{v} \left(\frac{\partial f_\alpha}{\partial t}\right)_{DR} d\mathbf{v} \qquad (4.37)$$

The first term can be rewritten as

$$m_\alpha \int \mathbf{v} \frac{\partial f_\alpha}{\partial t} d\mathbf{v} = m_\alpha \frac{\partial}{\partial t}(\rho \mathbf{u}_\alpha) = m_\alpha \frac{\partial \rho}{\partial t}\mathbf{u}_\alpha + m_\alpha \rho \frac{\partial \mathbf{u}_\alpha}{\partial t}, \qquad (4.38)$$

where $\mathbf{u}_\alpha = \rho^{-1} \int \mathbf{v} f_\alpha d\mathbf{v}$ is the local hydrodynamic velocity. The third term of Eq. (4.37), integrated by parts, yields:

$$q_\alpha \int \mathbf{v}\frac{\partial \phi}{\partial \mathbf{r}}\frac{\partial f_\alpha}{\partial \mathbf{v}} d\mathbf{v} = q_\alpha \frac{\partial \phi}{\partial \mathbf{r}} \int \mathbf{v}\frac{\partial f_\alpha}{\partial \mathbf{v}} d\mathbf{v} = -q_\alpha \frac{\partial \phi}{\partial \mathbf{r}} \int f_\alpha d\mathbf{v} = -q_\alpha \frac{\partial \phi}{\partial \mathbf{r}}\rho \quad (4.39)$$

Now, I restructure the second integral of Eq.(4.37) to give:

$$\int \mathbf{v}(\mathbf{v}\frac{\partial f_\alpha}{\partial \mathbf{r}}) d\mathbf{v} = \frac{\partial}{\partial \mathbf{r}} \int \mathbf{v}\mathbf{v} f_\alpha d\mathbf{v} = \frac{\partial}{\partial \mathbf{r}}(\rho \overline{\mathbf{v}\mathbf{v}}) \qquad (4.40)$$

Here, we use the fact that $\mathbf{v}$ is an independent variable in phase space. The over-bar indicates an averaged quantity. The last equality holds because the average of a quantity is $1/\rho$ times its weighted integral. I can now separate the velocity, $\mathbf{v}$, into two parts, the average (fluid) velocity and a thermal velocity:

$$\mathbf{v} = \mathbf{u}_\alpha + (\mathbf{v} - \mathbf{u}_\alpha) \qquad (4.41)$$

$$\Rightarrow \frac{\partial}{\partial \mathbf{r}}(\rho \overline{\mathbf{v}\mathbf{v}}) = \frac{\partial}{\partial \mathbf{r}}(\rho \mathbf{u}_\alpha \mathbf{u}_\alpha) + \frac{\partial}{\partial \mathbf{r}}(\rho \overline{(\mathbf{v} - \mathbf{u}_\alpha)(\mathbf{v} - \mathbf{u}_\alpha)}) + 2\frac{\partial}{\partial \mathbf{r}}(\rho \mathbf{u}_\alpha \overline{(\mathbf{v} - \mathbf{u}_\alpha)}) \qquad (4.42)$$

The fluid velocity $\mathbf{u}_\alpha$ is already an averaged quantity and the average of the local thermal velocity $\overline{(\mathbf{v} - \mathbf{u}_\alpha)}$ is zero, so the last term vanishes. The

quantity $m_\alpha \rho \overline{(\mathbf{v} - \mathbf{u}_\alpha)(\mathbf{v} - \mathbf{u}_\alpha)}$ is precisely defined as the stress tensor [15]

$$[\mathbf{P}]_\alpha = m_\alpha \rho \overline{(\mathbf{v} - \mathbf{u})(\mathbf{v} - \mathbf{u})} = m_\alpha \rho \int \{(\mathbf{v} - \mathbf{u}_\alpha) \otimes (\mathbf{v} - \mathbf{u}_\alpha)\} f_\alpha d\mathbf{v}, \quad (4.43)$$

where $\mathbf{a} \otimes \mathbf{b}$ indicates the dyadic product of two vectors $\mathbf{a}$ and $\mathbf{b}$. The remaining term in Eq.(4.42) can be written as

$$\frac{\partial}{\partial \mathbf{r}}(\rho \mathbf{u}_\alpha \mathbf{u}_\alpha) = \mathbf{u}_\alpha \frac{\partial}{\partial \mathbf{r}}(\rho \mathbf{u}_\alpha) + \rho \mathbf{u}_\alpha \frac{\partial \mathbf{u}_\alpha}{\partial \mathbf{r}} = -\mathbf{u}_\alpha \frac{\partial \rho}{\partial t} - \mathbf{u}_\alpha k_{DR} \cdot \rho^2 + \rho \mathbf{u}_\alpha \frac{\partial \mathbf{u}_\alpha}{\partial \mathbf{r}},$$
$$(4.44)$$

where I use the first moment, the equation of continuity. The right hand side in Eq. (4.37) yields:

$$\int m_\alpha \mathbf{v} \left(\frac{\partial f_\alpha}{\partial t}\right)_{DR} d\mathbf{v} = m_\alpha \left(\frac{\partial \rho}{\partial t}\right)_{DR} \mathbf{u}_\alpha + \rho m_\alpha \left(\frac{\partial \mathbf{u}_\alpha}{\partial t}\right)_{DR} = -\mathbf{u}_\alpha k_{DR} \cdot \rho^2$$
$$(4.45)$$

Step one is once more equivalent to the first part on the right-hand side of Eq. (4.37). The last step uses Eq. (4.35), and the fact that electron-ion recombination does not impose a force on the system as charge and global momentum are conserved.

Collecting these results, I now express Eq.(4.37) in a form that considers electrons and ions separately. The first moment of the Boltzmann equation gives:

$$m_e \rho \frac{\partial \mathbf{u}_e}{\partial t} + m_e \rho \mathbf{u}_e \frac{\partial \mathbf{u}_e}{\partial \mathbf{r}} + \frac{\partial}{\partial \mathbf{r}}[\mathbf{P}]_e - e \frac{\partial \phi}{\partial \mathbf{r}} \rho = 0 \qquad (4.46)$$

$$m_i \rho \frac{\partial \mathbf{u}_i}{\partial t} + m_i \rho \mathbf{u}_i \frac{\partial \mathbf{u}_i}{\partial \mathbf{r}} + \frac{\partial}{\partial \mathbf{r}}[\mathbf{P}]_i + e \frac{\partial \phi}{\partial \mathbf{r}} \rho = 0 \qquad (4.47)$$

### 4.2.2 Quasineutrality

Equations (4.36), (4.46) and (4.47) represent the Boltzmann equation in a restructured form. They describe how particles must act upon pressure and field gradients to conserve phase-space volume. My goal is to express the electrostatic potential, $\phi$, by means other than Poisson's equation [41]. By

subtracting Eq.(4.47) from Eq.(4.46) and rearranging the result, I find [61]:

$$e\frac{\partial \phi}{\partial \mathbf{r}} = \frac{\frac{\partial \mathbf{u}_e}{\partial t} - \frac{\partial \mathbf{u}_i}{\partial t} + \mathbf{u}_e \frac{\partial \mathbf{u}_e}{\partial \mathbf{r}} - \mathbf{u}_i \frac{\partial \mathbf{u}_i}{\partial \mathbf{r}}}{1/m_e + 1/m_i} + \frac{\frac{\partial}{\partial \mathbf{r}} \left( \frac{[\mathbf{P}]_e}{m_e} - \frac{[\mathbf{P}]_i}{m_i} \right)}{\rho/m_e + \rho/m_i} \qquad (4.48)$$

This is equivalent to Poisson's equation. The first term on the right-hand side of this equation describes the charge separation in the plasma. Differences between electron and ion densities and charge currents give rise to this term. The second term describes the effect of the thermal pressure on the particle densities.

Once more, I apply the quasi-neutrality condition and allow for electron relaxation. Owing to the much smaller electron mass, the electron distribution function relaxes on a much shorter time scale than the characteristic rate at which the ion density changes. This, in combination with quasi-neutrality, allows me to write the change of electron velocity in time and space as $\frac{\partial \mathbf{u}_e}{\partial t} \approx \frac{\partial \mathbf{u}_i}{\partial t}$ and $\frac{\partial \mathbf{u}_e}{\partial \mathbf{r}} \approx \frac{\partial \mathbf{u}_i}{\partial \mathbf{r}}$. On these grounds, the first term in Eq.(4.48) can be neglected with respect to the the second. The expression for the electrostatic potential $\phi$ becomes:

$$e\frac{\partial \phi}{\partial \mathbf{r}} \approx \frac{\frac{\partial}{\partial \mathbf{r}} \left( \frac{[\mathbf{P}]_e}{m_e} - \frac{[\mathbf{P}]_i}{m_i} \right)}{\rho/m_e + \rho/m_i} \qquad (4.49)$$

### 4.2.3 Equilibration

In later Chapters of this work, I will derive the phase-space distribution function for the plasma formed in our experiment. I will find, that the precursor plasma volume travelling within our skimmed supersonic molecular beam develops distinct velocity in the dimensions perpendicular and parallel to the direction of propagation, characterized by $T_\perp$, ($T_x$ and $T_y$) and $T_\parallel$ ($T_z$). Upon ionization, these temperatures refer to $NO^+$ velocity distributions in the plasma. To first order, we can neglect the collisional coupling of ion motion over orthogonal axes.

This does not apply to the electron velocity distribution. The electrons in the plasma volume move with a speed on the order of $\sim 10^4 \mu m/\mu s$ and undergo a very large number of collisions. They certainly possess the means

to transfer kinetic energy between coordinate axes directions. In the following, I develop a treatment incorporating complete equilibration of the free electrons.

I begin by taking a closer look at the pressure tensor. For the special case of a Maxwellian velocity distribution, drifting at a given velocity **u**, the off-diagonal elements of the pressure tensor vanish and one obtains the simple expression [15]:

$$[\mathbf{P}]_\alpha = \begin{bmatrix} \rho_\alpha k_B T_{\alpha,x} & 0 & 0 \\ 0 & \rho_\alpha k_B T_{\alpha,y} & 0 \\ 0 & 0 & \rho_\alpha k_B T_{\alpha,z} \end{bmatrix}$$

I want to find a simplified expression for the electric field in Eq.(4.49). To incorporate electronic equilibration, I recognize that the electron and ion temperatures in a typical ultracold plasma system differ by no more than two orders of magnitude, while $m_i > 50\,000 \cdot m_e$. This leads to the final expression for the electrostatic potential [43]:

$$e\frac{\partial \phi}{\partial \mathbf{r}} \approx \frac{\frac{\partial}{\partial \mathbf{r}}\left(\frac{[\mathbf{P}]_e}{m_e} - \frac{[\mathbf{P}]_i}{m_i}\right)}{\rho/m_e + \rho/m_i} \approx \frac{\frac{\partial}{\partial \mathbf{r}}\left(\frac{[\mathbf{P}]_e}{m_e}\right)}{\rho/m_e} \approx k_B T_e \rho^{-1} \frac{\partial \rho}{\partial \mathbf{r}} \tag{4.50}$$

In the third step, as mentioned before, I account for electron-electron collisions by the assumption of instant equilibration between the very fast electrons.

It is interesting to note that with Eq.(4.50), I reduce the term that couples the moments of the Boltzmann equation to a simple expression that depends only on the density distribution and the electron temperature. The ion-electron coupling remains governed by the requirement of quasi-neutrality. As seen in Eq.(4.50), the electrostatic force that drives the plasma expansion is determined only by the electronic thermal energy and the normalized density gradient. This simple form is only possible because the Maxwellian velocity distribution allows for a fluid treatment and the unwinding of the pressure tensor.

A full description of the system requires one final expression. Eqs. (4.46)

and (4.47) express the first moment of the Boltzmann equation in terms of the newly found electrostatic field, Eq. (4.50), separated into its coordinates:

$$m_e \rho \frac{\partial \mathbf{u}_e}{\partial t} + m_e \rho \mathbf{u}_e \frac{\partial \mathbf{u}_e}{\partial \mathbf{r}} = 0 \qquad (4.51)$$

$$m_i \rho \frac{\partial u_k}{\partial t} + m_i \rho u_k \frac{\partial u_k}{\partial r_k} + k_B \frac{\partial \rho}{\partial r_k}(T_e + T_{i,k}) = 0, \qquad (4.52)$$

where I recognize the Maxwellian nature of the ion temperature (with $T_{i,x} = T_{i,y} = 0$) and deem possible contributions of $\partial_r T_i$ negligible. The subscript $k = x, y, z$ stands for the different Cartesian coordinates. I find that the electron velocities are unaffected by density gradients and are only coupled to ions through quasi-neutrality while ion motion evolves according to plasma shape.

### 4.2.4 Global energy

To explicitly recognize the equilibration of the electron thermal energy over the coordinate axes, I set $T_{e,x}(t) = T_{e,y}(t) = T_{e,z}(t) \equiv T_e(t)$. For future reference, I require an expression for the total energy of the system, $W_{tot} = W_{kin} + W_{pot}$. The macroscopic electric potential energy, $W_{pot}$, is negligible in a classical plasma, where the Coulomb correlation parameter, $\Gamma = q^2/4\pi\epsilon_0 a_{ws} k_B T \ll 1$. Electrons and ions shield each other as long as the approximation of quasi-neutrality holds. Lacking a formalism to deal explicitly with a strongly coupled plasma, I treat the system as uncorrelated and neglect $W_{pot}$. Thus, I represent the total energy by:

$$W_{tot} = W_{kin}^{thermal} + W_{kin}^{hydrodynamic} =$$

$$\frac{3}{2} N k_B T_e(t) + \sum_k \frac{1}{2} N k_B T_{i,k}(t) + \sum_p \frac{1}{2} m_i \mathbf{u}_p^2 \qquad (4.53)$$

where the second term sums contributions to the ion kinetic energy over the three coordinate axes, $k = x, y, z$ and $N \equiv N_e = N_i$ represents the number

of particles of each species. $\mathbf{u}_p$ is the hydrodynamic velocity of ion $p$. The equation above neglects the hydrodynamic velocity of the electrons owing to their small mass. Recalling that self-similarity requires a hydrodynamic velocity parameter, $\gamma_k = u_k/r_k = \dot\sigma_k/\sigma_k$, the third term rearranges to give:

$$\sum_p \frac{1}{2}m_i\mathbf{u}_p^2 = \frac{1}{2}m_i\sum_k\sum_p u_{p,k}^2 = \frac{1}{2}m_i\sum_k \int \gamma_k^2 r_k^2 \rho_i \; d\mathbf{r}$$

$$= \frac{1}{2}m_i\sum_k \int \gamma_k^2 r_k^2 \rho_{i,0}\exp\left(-\frac{r_k^2}{2\sigma_k^2}\right)\exp\left(-\frac{r_{k'}^2}{2\sigma_{k'}^2}\right)\exp\left(-\frac{r_{k''}^2}{2\sigma_{k''}^2}\right) \; d\mathbf{r}$$

$$= \frac{1}{2}m_i\sum_k 2\pi\sigma_{k'}\sigma_{k''}\gamma_k^2\rho_{i,0}\cdot\underbrace{\int r_k^2\exp\left(-\frac{r_k^2}{2\sigma_k^2}\right)\; dr_k}_{=\sqrt{2\pi}\sigma_k^3} = \frac{1}{2}m_iN\sum_k\gamma_k^2\sigma_k^2$$

$$(4.54)$$

To solve this equation, I reduce it to a Gauss integral using integration by parts. In the last step I recognize that,

$$N = (2\pi)^{3/2}\sigma_x\sigma_y\sigma_z\rho_0. \tag{4.55}$$

The expression for the total energy then becomes:

$$W_{tot} = \frac{3}{2}Nk_BT_e(t) + \frac{1}{2}N\sum_k\left[k_BT_{i,k}(t) + m_i\dot\sigma_k^2\right] \tag{4.56}$$

The total energy of the plasma changes over time owing to dissociative recombination and energy transfer between plasma ions and Rydberg molecules by resonant charge exchange. For present purposes, I neglect the latter. This then leads to a balance of temperature decrease and hydrodynamic velocity increase, such that $dW = (\partial W/\partial N)dN$ [70], that is:

$$\frac{dW_{tot}}{dt} = \frac{1}{2}k_B\dot N\left[3T_e(t) + \sum_k T_{i,k}(t)\right] + \frac{1}{2}m_i\dot N\sum_k\dot\sigma_k^2 \tag{4.57}$$

Taking the total time derivative of Eq. (4.56) gives:

$$\frac{dW_{tot}}{dt} = \frac{1}{2}k_B \left[ \dot{N} \left( 3T_e(t) + \sum_k T_{i,k}(t) \right) + N \left( 3\dot{T}_e(t) + \sum_k \dot{T}_{i,k}(t) \right) \right]$$

$$+ \frac{1}{2}m_i \left[ \dot{N} \sum_k \dot{\sigma} v_k^2 + 2N \sum_k \dot{\sigma}_k \ddot{\sigma}_k \right] \tag{4.58}$$

Equating (4.58) and (4.57), yields an expression for the time derivative of temperature:

$$\left[ 3\dot{T}_e(t) + \sum_k \dot{T}_{i,k}(t) \right] = -2\frac{m_i}{k_B} \sum_k \dot{\sigma}_k \ddot{\sigma}_k \tag{4.59}$$

I will return to these important equations of plasma theory when I begin to construct computation models for our UNP in Part III.

## 4.3  Plasma theory applied to UNPs

Having derived the fundamental concepts and equations of plasma theory, I wish to discuss the special case of ultracold neutral plasma within the framework of plasma theory.

### 4.3.1  Kinetic theory in molecular ultracold plasma

It is important to state that the description of our system proceeds only in the classical regime, despite the very low temperatures of ultracold plasma systems. The term 'ultracold' is meant to separate the field of ultracold neutral plasma from the field of 'cold plasma', in which electron temperatures still range to typically $10^3$ degree Kelvin. We use it to show the close resemblance of our molecular system to UNPs.

Over the course of this work, it will be shown that our initial charged particle densities are in the range of $10^{12}$ cm$^{-3}$ and our electron and ion temperatures are larger than one Kelvin. Assuming spherical coordinates, our density predicts an electronic Fermi temperature,

$$T_F = \frac{\hbar^2}{2m_e k_B}(3\pi^2 \rho_e)^{2/3}, \tag{4.60}$$

of 4.2 mK, orders of magnitude below the estimated system temperature. Based on this quick analysis, I will base the description of our system kinetics solely on classical mechanics.

Most plasma systems are accurately described by a fluid theory. This approximation allows for a description of all relevant dependent variables, such as density, fluid velocity and pressure as functions of space and time only. This simplified treatment becomes possible because within the fluid approximation velocity distributions are implicitly assumed to be Maxwellian about some mean. The need to know each particle velocity is replaced by an overall temperature. The development of a Maxwellian distribution, however, implies the particles can transfer energy and therefore equilibrate their kinetic energies on a timescale that is short compared to the time at which we observe the system. This is obviously not the case for an expansion of a small plasma volume into vacuum. In fact, we enter a regime where it becomes problematic to refer to a system temperature or for the case of ions even a species temperature at all.

By now, it has become apparent that the Coulomb coupling parameter $\Gamma$ plays an important role in plasma systems. $\Gamma$ itself only depends on the density, $\rho$, and on the temperature $T$.

To determine $\Gamma$, we must rely on indirect measurements and predictions. The system density and ion temperature can be estimated through analysis of the molecular beam. Later in this work, an 'electron temperature' value will be obtained from a direct fit of the solution of Vlasov's equation to the time-dependent plasma width as well as through computation models.

But is it justified to employ Boltzmann's equation? And can our system even be referred to as a plasma? Following the analysis of Section 4.1, it is feasible to set $\Gamma = 0.3$ as an upper limit for a thermal plasma. This is because:

$$\Gamma = 0.3 \qquad \Rightarrow \qquad \frac{\tilde{\sigma}^*}{\tilde{\sigma}_{large}} \approx \pi \cdot ln(\frac{\sqrt{3}}{2\Gamma^{3/2}}) \approx 5 \qquad (4.61)$$

45

$\Gamma = 0.3$ means that the path of a plasma particle is governed five times stronger by the collective field than by large-angle collisions and allows the approximate treatment of collisionless kinetic theory for thermal plasmas.

We have pushed our experimental system into a regime where the concepts derived for thermal plasmas, together with Chen's definition (see 4.1), begin to fail. $\Gamma \geq 0.3$ does however not mean that the concepts of Debye screening or quasi-neutrality become unsound. One has to remember that these concepts were derived in a density frame as opposed to a particle frame. High Coulomb correlation simply means that the average particle distance exceeds the classical Debye length and this can lead to new effects. Ultra-cold Plasma researchers therefore settle for a less strict definition of plasma and only require that the Debye length of the system is much smaller than the system itself.

In our research, we are bound for now to approximate our system, however cautious, through thermal plasma concepts. This approach is encouraged by our experimental results, as our system exhibits prominent plasma characteristics. For example, we have subjected our plasma volume to a pulsed electric field of an amplitude as low as 3 $V/cm$, which is far smaller than that required to field-ionize the Rydberg state into which the system was initially excited [50]. This field is able to extract a small signal of electrons. Pulses of amplitudes as high as 200 $V/cm$, however, fail to destroy the plasma signal. These observations can be interpreted as follows: the system exhibits a loosely-bound surface charge of electrons, at the same time a Debye screening length much smaller than the diameter of the plasma is shielding the system core. This is strong evidence of plasma behaviour.

I conclude that it is possible to refer to our system as a plasma. In lack of a more suitable theory, I will use Boltzmann's equation as a first approximation to describe our plasma. This is done in full knowledge that it might not extend to properly describe all aspects to our system.

### 4.3.2 Correlation effects

In the following, I will give an example how the onset of correlation might change the nature of a plasma. The following model uses Debye-Hückel theory as described by Murillo [54].[7]

To employ this theory, one assumes an infinite electron plasma in a neutralizing and uniform ionic background with density $\rho$.[8] The origin of the coordinate system shall be fixed onto one electron. Spherical symmetry of the particle distribution is assumed. The description of this system through the one-dimensional Poisson equation and the assumption of a linearized Boltzmann distribution yields the Debye-Hückel potential,

$$\phi(r) = \frac{e}{4\pi\epsilon_0} \cdot \frac{e^{-r/\lambda_D}}{r},\qquad(4.62)$$

where the Debye length is given by $\lambda_D = \sqrt{\epsilon_0 k_B T_e / e^2 \rho}$, as before. The derivation is analog to Section 4.1. The Debye-Hückel potential is an interpolation between the exact solutions at $r = 0$ and $r \to \infty$. Using Eq. (4.62), one can now calculate the potential felt by each particle, excluding its own charge:

$$lim_{r \to 0} \left[ \phi(r) - \frac{e}{4\pi\epsilon_0 r} \right] = -\frac{e}{4\pi\epsilon_0 \lambda_D}\qquad(4.63)$$

The right-hand side of above equation states the energy between one particle and the remainder of the plasma. Summation over all $N$ free electrons (without double counting) gives a factor of $N/2$ and the total energy becomes:

$$W_{DH} = \frac{3}{2} N k_B T_e - \frac{N}{2} \frac{e^2}{4\pi\epsilon_0 \lambda_D} = \frac{3}{2} N k_B T_e \left( 1 - \frac{1}{\sqrt{3}} \Gamma_e^{3/2} \right),\qquad(4.64)$$

Eq. (4.64) shows that a decrease in the total energy can occur as a result

---

[7]In this reference, Debye-Hückel theory is derived in the cgs-system. For conformity, this discussion was transferred into mks-units.

[8]A study by T. Pohl showed ion correlation to have an negligible effect on plasma expansion ([63]).

of correlations. This reduction is due to interactions of the electrons with the opposite-signed background. Debye theory provides an easy access to the complex attributes of correlated plasmas. Above findings conform qualitatively with the observed Wigner crystallization of highly coupled plasmas [25]. The quantitative effect of linearization of Boltzmann's equation in the derivation of the Debye-Hückel potential (cf. 4.1), which turns the potential into an interpolation between the exact solutions at $r = 0$ and $r \to \infty$, on the quality of Eq. (4.64) is difficult to assess.

### 4.3.3   Disorder induced heating

In the introduction to my thesis, I have already eluded to the fact that disorder-induced heating is an important mechanism in UNP research. Researchers in our field strive to create highly correlated plasma in the laboratory. MOT plasmas, prepared at densities of $\rho \approx 1 \cdot 10^9$ cm$^{-3}$ and low initial ion and electron temperatures, T$_i$=10 $\mu$K and T$_e$=0.1 K, seemed ideal to achieve high levels of correlation, $\Gamma_i \approx 2.7 \cdot 10^6$ and $\Gamma_e \approx 27$. Kuzmin and O'Neil [44], however, point out that these initial temperature values are mere measures of initial particle kinetic energy and not equilibrium temperatures. Molecular-dynamics simulation supported by experimental data [85] show rapid ion heating in MOT plasmas during equilibration over the first 250 ns after plasma formation. The origin of this heating is the fact that UNPs are created from a gas of spatially uncorrelated atoms. During the early evolution of the plasma, the charged particles move towards equilibrium positions, transferring potential energy into (thermal) kinetic energy. A crude first-order approach to estimate the energy released into the thermal bath during equilibration is found by equating thermal energy and the Coulomb interaction between neighbouring ions [43]:

$$k_B T_{DIH} \approx \frac{e^2}{4\pi\epsilon_0 a_{ws}}$$
(4.65)

For above example system, T$_{DIH}$ becomes $\sim 2.7$ K yielding a value $\Gamma \approx 1$.

Molecular ultracold plasma is also formed by excitation of an uncorrelated gas. Application of above model yields heating on the order of $T_{DIH}$=27 K for initial plasma densities of $\rho = 1 \cdot 10^{12}$ cm$^{-3}$. We argue that the Penning ionization process at our densities yields a degree of pre-correlation [71]. This process selects for pairs of excited molecules close together. The deactivated Penning partners predissociate, depleting the leading edge of the distribution of nearest-neighbor distances. I will return to the process of DIH in Part IV.

# Part II

# Formation of a molecular Rydberg ensemble

In order to form an ultracold neutral plasma (UNP) in the laboratory, one requires a cold and dense ensemble of atoms or molecules and a laser excitation pathway to bound or continuum states near the ionization limit. Within our research field, the use of magneto-optical traps (MOTs) to cool atomic ensembles has become the method of choice. Our approach differs, in that we form a UNP within the expansion of a supersonic beam.

A supersonic molecular beam presents a dynamic experimental environment, in which gas expanding from a high-pressure reservoir attains a sub-Kelvin temperature in a local frame that moves with relatively high velocity in the laboratory. This differs substantially from the conditions encountered after laser cooling of a gas of atoms in a MOT. The supersonic beam environment yields two distinct advantages for the study of ultracold plasma physics: Charge-particle densities in beams can exceed those attainable in a MOT by orders of magnitude. This medium can also support the formation of molecular ultracold plasmas, introducing interesting and potentially important new degrees of freedom that govern the dynamics of their evolution.

Charged particle density distributions play a fundamental role in defining the properties of a plasma system. The initial state of the excitation volume sampled when forming a plasma in a molecular beam depends on a set of complex conditions underlying the expansion. This complicates the initial phase-space distribution of a beam plasma, whereas the excitation of an atomic gas trapped in a MOT yields a well defined plasma phase-space distribution, in which initial density and ion temperature follow from simple analysis of the trapping potential. The beam plasma, while allowing for straightforward detection, requires a more sophisticated characterization of initial conditions. For example, few experimental methods exist that can provide an accurate absolute measure of either neutral or ion densities.

This part of my thesis provides an analysis that addresses this apparent disadvantage. In the following, I characterize the initial phase-space distribution function of a molecular Rydberg ensemble within the lower symmetry

geometry formed by the intersection of lasers and molecular beam. This ensemble is the precursor of our UNP, and thus of fundamental importance to our work.

Chapter 5 will discuss the physics of our supersonic molecular beam in detail. Chapter 6 considers the laser excitation of cold NO in the jet and combines the findings of Part II to state a distribution function for NO Rydberg states in our experiment.

# Chapter 5

# Molecular Beam Gas Dynamics

In this chapter, I construct a theoretical description of the molecular beam that depends solely upon the measured reservoir gas pressure and the known system dimensions. This discussion is vital because it defines the important characteristics of a nozzle expansion that allow its characterization in phase-space. In some cases, I compare predictions to values measured by experiment. I argue that the good agreement obtained in those cases for which a comparison is possible, confirms the essential accuracy of the hydrodynamic model presented below.

## 5.1 Experimental setup overview

Figure 5.1 gives a bird-view schematic of our experimental setup. Our experiment table top is 4 by 10 feet and supports a high vacuum chamber pumped down to a vacuum pressure of $\sim 10^{-8}$ torr. The chamber contains a supersonic-beam apparatus, consisting of nozzle and skimmer, as discussed in the next section. Horizontal viewports on the chamber allow us to intersect the molecular beam in between two detection plates (optional) with laser light.

The laser light consists of two coincident nano-second light pulses, $\omega_1$ and $\omega_2$ (cf. Chapter 2). Both originate from pumped dye laser and are frequency doubled. The intensity of $\omega_1$-light is attenuated via a set of Glan-Thompson polarizer. We take great care to optimize the shape of $\omega_1$ with a $50\mu m$-aperture spatial filter, before sending it on to the chamber. A dichroic merges $\omega_1$ and $\omega_2$ prior to transit through the viewports.
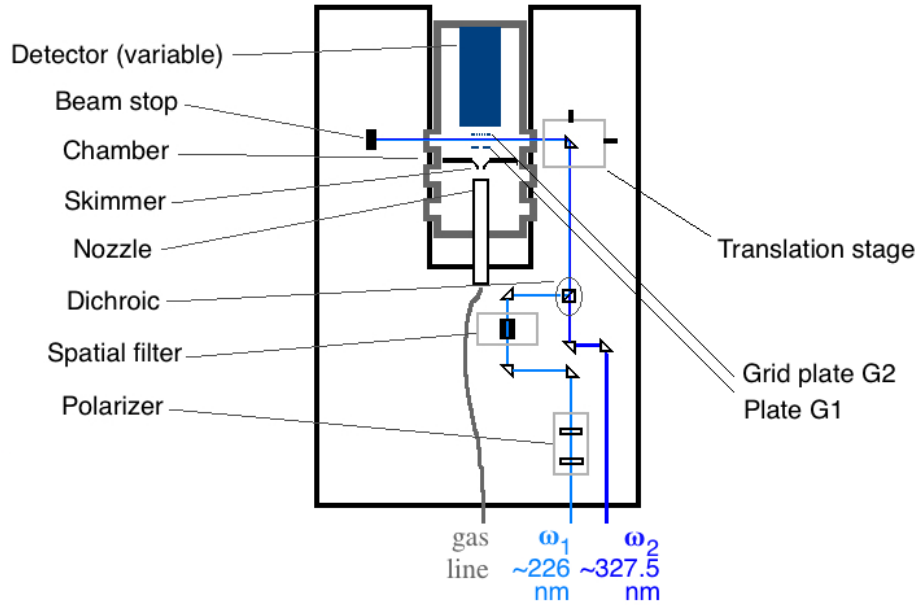
Figure 5.1: **Bird-view schematic of our experiment table**

A more complete account of the dimensions and components (incl. light sources) of our experimental setup can be found in Appendix A.

## 5.2 The supersonic beam

A supersonic beam apparatus typically consists of a gas reservoir, an evacuated chamber and a nozzle, through which the gas enters the evacuated space. As the gas flows into the vacuum, isentropic expansion transforms random thermal energy into directed laboratory kinetic energy, and the jet cools in the moving frame. Provided that the ratio between reservoir pressure, $P_0$, and background chamber-gas pressure, $P_b$, exceeds a certain critical value, the flow becomes supersonic [83]. This is crucial for a simple description of the beam. An experimental chamber cannot have infinite dimensions, and the beam must encounter obstacles as it expands. Information about

these boundary conditions travel back to the source of the jet by the means of pressure waves, which propagate at the local speed of sound, and force the beam to adjust. This information, however, cannot reach the part of the beam that propagates with a supersonic velocity. Atoms and molecules advancing with higher velocity sweep away back-reflected pressure waves. This collision forms a shock front that defines a region of supersonic gas velocity known as the zone of silence. This is illustrated this on the left-hand side in Figure 5.2.
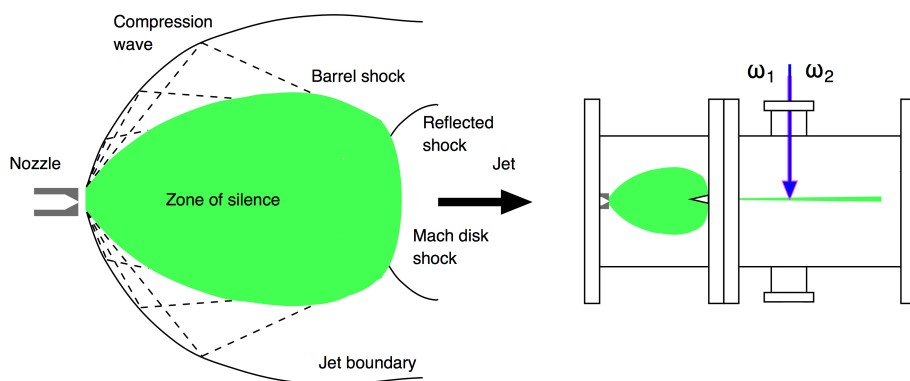


Figure 5.2: **Continuum free-jet expansion** - Left: A schematic sketch showing the regions of an unobstructed supersonic gas expansion from a converging nozzle (adapted from: [83]). Right: Schematic of our high vacuum chamber with indicated supersonic molecular beam.

A high-vacuum molecular beam system usually employs two chambers, a source chamber and an experimental chamber, which are separated by a differential wall fitted with a skimmer. This arrangement creates a narrow beam that propagates in the low background pressure of the experimental chamber. The skimmer orifice forms this beam by sampling the supersonic flow region. Particles within it experience no effect of the downstream conditions, so their theoretical description follows that of an unobstructed expansion. In our experimental system, all processes of interest take place in a differentially pumped experimental chamber within this zone of free expansion.

## 5.3 Gas properties

A gas reservoir held at a pressure of 500 kPa supplies an expansion mixture of nitric oxide (NO) seeded at a ratio of 1:10 in helium. The pumping capacity of the vacuum system substantially exceeds the flow of gas produced by the pulsed nozzle operating with an orifice diameter of 500 $\mu$m and an opening interval of 400 $\mu$s. I therefore assume that the gas establishes a stagnation point in this reservoir, at which the overall particle velocity relative to the reservoir wall is zero. At this point, the supply gas has a stagnation pressure, $P_0$, equal to the release pressure, and a stagnation temperature, $T_0$, equal to room temperature.

Turbomolecular pumps, attached to both chambers, maintain a vacuum in the apparatus. With the pulsed beam running at a frequency of 10 Hz, we measure a source chamber background pressure of $P_b \approx 0.001$ Pa.

While the use of helium as a carrier gas increases the beam velocity and improves cooling, it also adds complexity to the hydrodynamic description of the system. Real gas mixtures present complications, and it is customary to introduce simplifications. Thus, I will assume an ideal gas mixture at all points in the beam, and neglect the very small effects of diffusive separation, non-continuum velocity slip and temperature slip.

At a temperature of 293 K, nitric oxide has a constant pressure molar heat capacity of $C_p^{NO} = 29.88$ J mol$^{-1}$ K$^{-1}$, very close to 7/2 R, where R is the gas constant [1]. This state quantity changes with the cooling of the beam as the number of thermally accessible rotational levels decreases. The population of higher rotational levels in nitric oxide collapses at a characteristic rotational temperature of $\sim T_{rot}^{NO} = 2.46$ K, reducing the heat capacity to 5/2 R [33]. The gas reaches this phase-transition at a point in the expansion, where the vast majority of collisions has already taken place. Additionaly, NO accounts for only 10% of the mixture. Accordingly, I simplify the model by fixing $C_p^{NO}$ to its room temperature value. The mass of nitric oxide is $m_{NO} = 30.006$ g/mol. Helium has a heat capacity of 12.471 J K$^{-1}$ mol $^{-1}$ and a mass of $m_{He} = 4.0026$ g/mol.

As an ideal gas mixture, I can describe the expanding mixture of He and

NO in terms of its mean mass $\overline{M}$, mean heat capacity $\overline{C}_p$ and mean heat capacity ratio $\overline{\gamma}_h$, given respectively by:

$$\overline{M} = \sum_i X_i m_i = 0.9 \cdot m_{He} + 0.1 \cdot m_{NO} = 6.603 \ \frac{\text{g}}{\text{mol}} \tag{5.1}$$

$$\overline{C}_p = \sum_i X_i C_{p_i}^{mol} = 21.7 \ \frac{\text{J}}{\text{mol} \cdot \text{K}} \tag{5.2}$$

$$\overline{\gamma}_h = (1 - \text{R}/\overline{C}_p)^{-1} = 1.62 \tag{5.3}$$

$X_i$ is the particle fraction, where $i$ represents NO or He. Table 5.1 summarizes the state properties of the stagnation mixture.

Table 5.1: State properties of the seeded supersonic expansion stagnation mixture

| | |
|---|---|
| Temperature, $T_0$ | 293 K |
| Pressure, $P_0$ | 500 kPa |
| Nozzle diameter | 0.5 mm |
| Skimmer diameter | 1 mm |
| heat capacity ratio, $\overline{\gamma}_h$ | 1.62 |

## 5.4 Continuum free-jet expansion

I now derive the equations for the flow variables for a gas mixture with the above state properties, within the continuum free-jet approximation. In this approximation, the particle jet is considered to be stationary, adiabatic and compressible. All state properties below refer to those of the ideal mixture, as defined above.

The opening of the nozzle forms a pulsed beam. However, the duration of this pulse exceeds the time required for the leading edge of the jet to cross the dimensions of the chamber. Such conditions satisfy the continuum beam approximation, so I can assume stationary flow [83].

Neglecting the effects of viscosity and shock waves, which is a good

approximation in the zone of silence, I can model the isentropic flow using Bernoulli's equation [76]:

$$g \cdot y + \frac{u^2}{2} + h = const. \qquad \text{(per unit mass)} \qquad (5.4)$$

Here, $u$ is the fluid flow speed at a point on a streamline, $g$ is the gravitational acceleration, $y$ is the elevation and $h$ is the enthalpy per unit mass. If the flow is irrotational, i.e. $\nabla \times \mathbf{u} = 0$, the constant in Eq. (5.4) has the same value for all streamlines (homoentropic flow). For our short times and low densities and small spatial length scales, gravitational effects are completely negligible. Thus, I simplify Eq. (5.4) to yield:

$$\frac{u^2}{2} + h = const. \qquad (5.5)$$

For an infinitesimal variation,

$$d(\frac{u^2}{2}) + dh = d(\frac{u^2}{2}) + \frac{\mathrm{R}}{m} \frac{\gamma_h}{\gamma_h - 1} dT = 0, \qquad (5.6)$$

in which I represent $dh$ for an ideal gas by,

$$dh = C_p dT = \frac{\mathrm{R}}{m} \frac{\gamma_h}{\gamma_h - 1} dT \qquad (5.7)$$

Integrating Eq.(5.6) between distinct points of the flow field, i.e. from the stagnation point $(P_0, \rho_0, T_0, u_0)$ to $(P, \rho, T, u)$, yields:

$$\frac{u^2}{2} + \frac{\mathrm{R}}{m} \frac{\gamma_h}{\gamma_h - 1} T = \frac{u_0^2}{2} + \frac{\mathrm{R}}{m} \frac{\gamma_h}{\gamma_h - 1} T_0 = const. \qquad (5.8)$$

Introducing the isentropic sound speed $a = \sqrt{(dP/d\rho)_0} = \sqrt{\frac{\gamma_h \mathrm{R} T}{M}}$, which is defined as the propagation of a small disturbance where $M$ is the molar mass of the gas, I rewrite Eq (5.8),

$$\frac{u^2}{2} + \frac{a^2}{\gamma_h - 1} = \frac{u_0^2}{2} + \frac{a_0^2}{\gamma_h - 1} = const., \qquad (5.9)$$

where $a_0 = \sqrt{\frac{\gamma_h R T_0}{M}}$. I define the Mach number, $\mathcal{M} = u/a$, and recognize that $\mathcal{M}_0 = 0$ at the stagnation point. Now rearranging Eq. (5.9) yields the sonic velocity, $a$:

$$a = \frac{a_0}{(1 + \frac{\gamma_h - 1}{2} \mathcal{M}^2)^{1/2}} \tag{5.10}$$

As $a \propto T^{1/2}$, I can write

$$T = \frac{T_0}{(1 + \frac{\gamma_h - 1}{2} \mathcal{M}^2)}, \tag{5.11}$$

and, applying the Poisson adiabatic equations of state, $\frac{P}{P_0} = (\frac{T}{T_0})^{\frac{\gamma_h}{\gamma_h - 1}}$ and $\frac{\rho}{\rho_0} = (\frac{T}{T_0})^{\frac{1}{\gamma_h - 1}}$, Eq. (5.11) yields an equation of state for the local pressure:

$$P = \frac{P_0}{(1 + \frac{\gamma_h - 1}{2} \mathcal{M}^2)^{\frac{\gamma_h}{\gamma_h - 1}}} \tag{5.12}$$

I can define particle number density, $\rho$, simply in terms of the ideal gas equation of state:

$$\rho = \frac{N}{V} = \frac{P}{k_B T}, \tag{5.13}$$

and, returning to the hydrodynamic beam velocity $\mathbf{u}$, I write:

$$|\mathbf{u}| = \mathcal{M} \cdot a = \frac{\mathcal{M} \cdot a_0}{(1 + \frac{\gamma_h - 1}{2} \mathcal{M}^2)^{1/2}} \tag{5.14}$$

For the maximum beam velocity, I find:

$$u_{max} = \lim_{\mathcal{M} \to \infty} |\mathbf{u}| = \lim_{\mathcal{M} \to \infty} \frac{a_0}{(\frac{1}{\mathcal{M}^2} + \frac{\gamma_h - 1}{2})^{1/2}} = a_0 \sqrt{\frac{2}{\gamma_h - 1}} \tag{5.15}$$

.

Eqs. (5.11-5.14) represent the hydrodynamic flow equations that characterize the expansion. Using parameter values defined above by $T_0$, $\overline{\gamma}_h$ and $\overline{M}$ in Table 5.1, Eq. (5.15) yields a theoretical quantity, $a_0 = 773$ m/s for the speed of sound at the nozzle. The speed of sound subsequently drops as the beam cools. The gas exiting the nozzle quickly accelerates to approach

a center-line beam velocity of $u_{max} = 1387$ m/s.

A photodiode monitoring the rising edge of the $\omega_1$ laser pulse triggers data acquisition. The time between this start pulse and the signal waveform produced when the illuminated volume reaches the detector yields a time of flight over a known distance, and thus determines the velocity of the beam. Present conditions yield an experimental velocity of $u_{max}^{exp} = 1447 \pm 30$ m/s.

The difference of $\sim 4.5\%$ between the measured and predicted velocity very likely arises from a deviation in the commercially prepared gas mixture from its nominal 1:10 NO to He composition. It could be said that the velocity determined in this way provides an exceedingly accurate *in situ* measure of expansion gas mixture composition. Other factors such as source temperature variation, a more precise accounting of the rotational energy release from the relaxation of the NO heat capacity, or NO–He speed differentials arising from velocity slip have far less consequence. I therefore maintain that the correspondence between predicted and measured molecular beam velocity assures the reliability with which this hydrodynamic picture determines other properties of this free-jet expansion.

Returning to the flow equations, Eqs.(5.11 - 5.14), it is important to notice that I can account for all four thermodynamic quantities at any point of any streamline in terms of the local Mach number $\mathcal{M}$.

## 5.5 The method of characteristics

I proceed now to employ the approximations introduced above to describe the supersonic flow in the skimmed expansion starting with the following set of fluid mechanics equations [84, 91].

$$\text{Conservation of mass:} \quad \nabla(\rho \cdot \mathbf{u}) = 0 \tag{5.16}$$

$$\text{Conservation of momentum:} \quad \rho \mathbf{u} \cdot \nabla \mathbf{u} = -\nabla P \tag{5.17}$$

$$\text{Conservation of energy:} \quad h_0 = const. \tag{5.18}$$

$$\text{Equation of state:} \quad P = \rho \frac{\text{R}}{M} T \tag{5.19}$$

$$\text{Thermal equation of state:} \quad dh = C_p dT \tag{5.20}$$

Substituting $\mathcal{M}\mathbf{a}$ for $\mathbf{u}$, yields a set of hyperbolic partial differential equations for a supersonic flow that can be solved numerically by the method of characteristics.

This approach determines particular curves in space along which the component equations of the partial differential equations can be combined to yield ordinary differential equations. Ashkenas and Sherman [4, 57], provide a function that accurately fits the variation of the Mach number, within the zone of silence as a function of the nozzle distance $z$ for $\mathcal{M} > 5.5$:

$$\mathcal{M} = A\left(\frac{z - z_0}{D}\right)^{\gamma_h - 1} - \frac{1}{2}\left(\frac{\gamma_h + 1}{\gamma_h - 1}\right) / [A\left(\frac{z - z_0}{D}\right)^{\gamma_h - 1}], \tag{5.21}$$

The quantity $z$ measures the distance from the nozzle orifice along the centreline of the beam. $D$ is the nozzle exit diameter and constants A and $z_0$ are fitting parameters obtained numerically. The heat capacity ratio of our expansion, $\overline{\gamma}_h = 1.62$ conforms closely with that of pure helium, $\gamma_h = 1.67$, for which Ashkenas and Sherman find $z_0/D = 0.075$ and A $= 3.26$. I adopt these parameter values as an approximation, and solve the hydrodynamic flow equations, Eqs.(5.11 - 5.14), for points along the centerline of the beam.

Figure 5.3 plots results of this calculation. Here I express $T$, $\rho$ and $P$ as quantities in proportion to their values at the stagnation point and give $u$ as a fraction of its long-distance limit $u_{max}$. Note that the beam velocity reaches its maximum within a travel distance of $\sim 1$ mm, accompanied by rapid declines in gas temperature, density and pressure.

## 5.6   Non-equilibrium effects

The foregoing derivations describe an idealized gas that maintains energy equilibration over all levels. Energy transfer takes place by means of particle-particle collisions. I have already shown that the temperature and the particle density of the beam both decrease, as the gas expands into the source chamber. It is instructive to examine how this process affects the collision frequency and the completeness of energy equilibration.
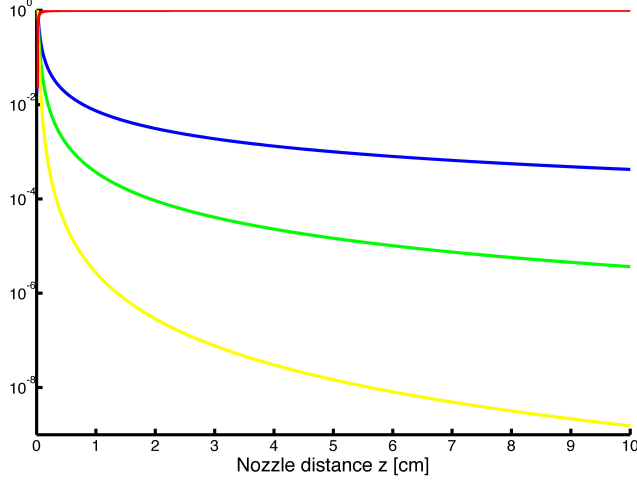
Figure 5.3: **Thermodynamic values for the hydrodynamic flow** - Red line = $u/u_{max}$; blue line = $T/T_0$; green line = $\rho/\rho_0$; yellow line = $P/P_0$ (or from top to bottom)

To assess this in reasonable detail, I calculate the mean-number of hard-sphere, two-body collisions for a particle at a specific point along the centreline flight path. In the following description, I determine the collision number applying an approximation, in which gas particles are represented by spheres of radius $r_0$. As helium is the chief constituent of the gas, I assume that $r_0$ equals the distance, at which the Lennard-Jones potential for helium atoms,

$$W = 4\epsilon\{(\frac{\tilde{\sigma}_{LJ}}{r})^{12} - (\frac{\tilde{\sigma}_{LJ}}{r})^6\}, \tag{5.22}$$

becomes repulsive. This occurs at $r_0 = 2.64$ Å [59] and yields a hard-sphere cross section, $\tilde{\sigma}_{He} = \pi r_0^2 = 21.9$ Å$^2$.

This calculation focuses on a single particle that travels with the velocity $\mathbf{v}_2$ across a group of particles that all have the same velocity $\mathbf{v}_1$. I place the origin of the coordinate system at the center of the test particle. This particle now sees the other particles as a group travelling with a relative velocity, $v_{rel} = |\mathbf{v}_1 - \mathbf{v}_2|$. Among those particles, ones that have centres

that pass through a circle area of diameter $d = 2r_0$, that lies at the center of the coordinate system and is perpendicular to $\mathbf{v}_{rel}$, collide with the test particle. This gives rise to a collision frequency,

$$Z_c^{v_1,v_2} = \pi d^2 v_{rel} \rho, \tag{5.23}$$

where $\rho$ is the gas number density. Eq. (5.23) neglects the fact that other particles can transfer momentum to the test particle, thereby changing $\mathbf{v}_1$ and thus $\mathbf{v}_{rel}$. I can account for this by a statistical approach. To do this, I assume that a collision changes $\mathbf{v}_2$ into $\mathbf{v}_2'$, and that $\mathbf{v}_2'$ is determined by a Maxwellian probability distribution $\tilde{f}$. Additionally, I want to allow groups of particles with different velocities $\mathbf{v}_1$ to take part in the collision. $\mathbf{v}_1$ shall also be sampled from a Maxwell-Boltzmann distribution. Assuming spherical coordinates, the $z$-axis being coincident with $\mathbf{v}_2$, I find the mean-magnitude of the relative velocity to be:

$$< v_{rel} > = \int \int \sqrt{v_1^2 + v_2^2 - 2v_1 v_2 cos\theta} \tilde{f}(v_1) \tilde{f}(v_2) \, d\mathbf{v}_1 d\mathbf{v}_2 \tag{5.24}$$

A solution to this integral is,

$$< v_{rel} > = \sqrt{\frac{16\mathrm{R}T}{\pi M}} = \sqrt{2} < v >, \tag{5.25}$$

where $< v >$ is defined as [76]:

$$< v > = \frac{\int_0^\infty v \tilde{f}(v) dv}{\int_0^\infty \tilde{f}(v) dv} \tag{5.26}$$

For temperature $T(z)$ and density $\rho(z)$, I find the two-body mean-collision rate per unit time as:

$$Z_c(z) = 16 \, \tilde{\sigma}_{He} \sqrt{\frac{RT(z)}{\pi \overline{M}}} \rho(z) \tag{5.27}$$

For example, the collision rate $Z_c(z)$ at the entrance orifice of a skimmer at $z = 3.5$ cm distance from the nozzle, is $\sim 175\,000$ collisions per second.

I transform this characteristic property of the expansion to define a quantity with greater utility. Let $Z_c dt$ represent the number of collisions undergone by one particle during the time-interval $dt$. The distance that is traveled by the particle during this time interval is $dz = v(z)dt$. Therefore, $Z_c(z)/v(z)dz$ represents the number of collisions experienced by a particle that travels the infinitesimal distance between $z$ and $dz$. With this, I calculate the number of remaining collisions, $Z_r$, that a particle at a given point $z$ will experience until it reaches infinity:

$$Z_r(z) = \int_z^\infty \frac{Z_c(z')}{v(z')} dz' \tag{5.28}$$
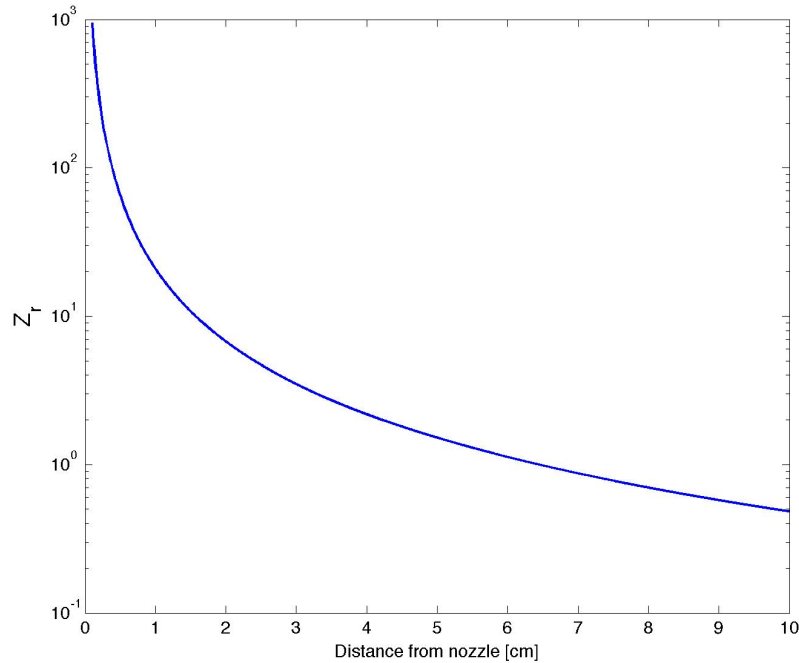


Figure 5.4: **Two-body collision number -** Mean-number of collisions experienced by a molecule at point z as it travels from z to infinity

Figure 5.4 shows that $Z_r(z)$ decreases drastically over the course of the

expansion. Near the nozzle, each particle takes part in hundreds of collisions, but after only $1 - 2$ cm of flight, collisions become much less frequent. This is the region where the rotational heat bath, determined by the occupation of the rotational energy states which depends on $T_{rot}$, decouples from the translational temperature bath, described through $T_{trans}$.

This decoupling occurs because energy does not transfer between the rotational states of two colliding molecules in every single collision. Typical rotational collision numbers, i.e. the mean-number of collisions a molecule undergoes before changing rotational state, is known to be about 5-20 for $N_2$ and $O_2$ [13]. Assuming a comparable number for NO, which has similar mass and size, I estimate from Fig. 5.4, that molecules in the beam stop exchanging rotational energy at a distance of about 0.6 cm to 1.3 cm after the nozzle. Comparing this with Fig. 5.3 yields a temperature of roughly $1.6 - 4.1$ K in this region.

In summary: we can expect a quantity that relates to the rotational temperature, as determined by the Boltzmann population of rotational energy levels, to decouple (or freeze out) from the still-falling equilibrium translational temperature at $1.6 - 4.1$ K.

Our experimental setup allows a facile measurement of the rotational temperature via the spectrum of the $X^2\Pi \leftarrow A^2\Sigma^+$ transition. Figure 5.5 compares theoretical predictions[9] for the temperature-dependent A-state spectrum with a plot of a $\omega_1$ $1+1'$ REMPI scan. We find that the calculated temperature for rotational freezing accords very well with that measured by the $1 + 1'$ REMPI scan. This is an important result as we can conclude that the overall beam temperature reaches $\sim 2.5$ K, at a point where each particle experiences an average of a dozen more collisions. These remaining collisions, while not likely to further relax rotational energy, continue to cool the translational temperature of the beam. Thus, we can expect $T_{rot} \gg T_{trans}$.

Not only do the rotations freeze out, but we also expect that the particle translational temperature itself will stop declining and separate from the

---

[9]We employ *PGOPHER, a Program for Simulating Rotational Structure, C. M. Western, University of Bristol, http://pgopher.chm.bris.ac.uk*
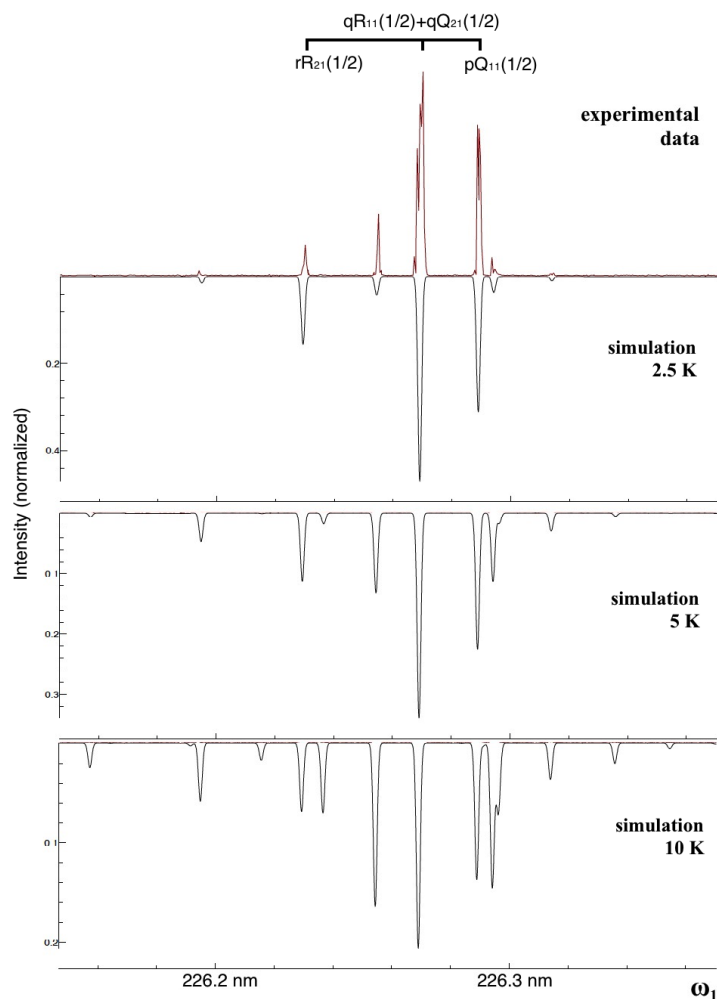
Figure 5.5: **Rotational temperature of nitric oxcide** - The uppermost curve shows data from a typical 1+1' REMPI scan of the transition spectrum between the $^2\Pi_{1/2}$ ground state and the $A^2\Sigma^+$ first excited state in NO. The data was recorded by intersecting the molecular beam with a tuneable laser, 7.5 cm downstream of the skimmer, and accelerating freed electrons towards a MCP detector. The inverted plots beneath are theoretical predictions for above transition spectra for different rotational populations of the molecular states. For better comparison, three theoretical predictions with temperatures of 2.5 K, 5 K and 10 K are given.

calculated equilibrium temperature at a point, where collisions begin to completely cease. I will discuss this in the following section.

The above description of hard-sphere collisions and temperature decoupling from equilibrium mechanics represents a crude approximation of the processes in a real pulsed supersonic molecular beam system. Without such simplification, it is very hard to make statements about the exact region of freezing and its extent. However, it is not as much the location of the freezing surface but the understanding of this process that will be important for the following sections.

## 5.7 Sudden freeze and point-source approximation

In this part of the molecular beam description, I derive an expression for the density distribution of the gas particles after the point of skimming. I begin by introducing two approximations that enable this calculation.

The last section argues that the closing of equilibration channels cause the translational temperature to freeze when particles cease to collide. This is a continuous process. But, as a simplification, I shall introduce the sudden freeze approximation [3]. This model will assume the existence of a discrete freezing surface across all streamlines. Upstream of this surface, I will describe the translational temperature by equilibrium mechanics, and assume the temperature downstream to be frozen. I will further assume that this surface is located at the entrance of the skimmer.[10] Particles that pass through the skimmer orifice continue to travel in a free flow with the over-all velocity, $\mathbf{u}$, and relative velocities, $\mathbf{v} - \mathbf{u}$, which I determine from the calculated beam temperature at the skimmer entrance. At this point, we need not further consider the properties of He, as its role of buffer gas ceases with the end of particle collisions.

---

[10]This approximation is necessary to obtain a simple solution for the particle density distribution in the experimental chamber. Earlier calculations predict that $\sim 2$ collisions remain on average for a particle once it passes the skimmer at a distance of $\sim 3$ cm from the nozzle (cf. Figure 5.4). I neglect these remaining collisions in following discussion.

To further simplify the calculations, I also assume that all particles enter the experimental chamber originating from a single point, coincident with the centre of the skimmer entrance. This so-called point-source approximation [76] holds as long as we concern ourselves with planes at distance $l$, where $l$ is much larger than the diameter of the skimmer.

I start this description at the point of skimming at $z_{skimmer} = z_s$. As a reminder, this is the freezing surface where equilibrium flow merges into free molecular flow and the gas past this point is determined by the previously calculated (and now frozen) values for $T(z_s)$ and $\rho(z_s)$, where I multiply our previous density by 0.1 and only consider NO. The particle velocities are approximated by a Maxwell-Boltzmann distribution function which is normalized to the beam density:

$$\tilde{f}(\mathbf{v}) = \rho_s \left( \frac{m}{2\pi k_B T_s} \right)^{3/2} e^{-\frac{m}{2k_B T_s}(\mathbf{v}-\mathbf{u})^2}, \tag{5.29}$$

Here:

$$\rho_s = \rho(z_s) = \int \tilde{f}(\mathbf{v}) d\mathbf{v} \qquad \mathbf{u} = <\mathbf{v}> = \rho_s^{-1} \int \mathbf{v} \tilde{f}(\mathbf{v}) d\mathbf{v} \tag{5.30}$$

$$T_s = T(z_s) = \frac{2}{3k_B} \int \frac{m}{2} |\mathbf{v} - \mathbf{u}|^2 \tilde{f}(\mathbf{v}) d\mathbf{v} \tag{5.31}$$

It is possible to split the velocity $\mathbf{v}$ into a component parallel to the beam centerline, $\mathbf{v}_\parallel$, and a component in the perpendicular direction $\mathbf{v}_\perp$.

$$\mathbf{v} - \mathbf{u} = \mathbf{v}_\parallel - \mathbf{u} + \mathbf{v}_\perp \tag{5.32}$$

$$\Rightarrow (\mathbf{v} - \mathbf{u})^2 = u^2 \{ (\frac{v_\parallel}{u} - 1)^2 + \frac{v_\perp^2}{u^2} \} \tag{5.33}$$

This definition allows me to separate the distribution function into parallel and perpendicular components where,

$$\tilde{f}(v_\parallel, v_\perp) = \rho_s \tilde{f}_\parallel \tilde{f}_\perp, \tag{5.34}$$

in which:

$$\tilde{f}_{\parallel} = (\frac{m}{2\pi k_B T_s})^{1/2} e^{-\frac{mu^2}{2k_B T_s}(v_{\parallel}/u-1)^2} = \frac{S_s}{u\sqrt{\pi}\mathcal{F}} e^{-S_s^2(v_{\parallel}/u-1)^2}$$

$$\tilde{f}_{\perp} = (\frac{m}{2\pi k_B T_s}) e^{-\frac{mu^2}{2k_B T_s}(v_{\perp}/u)^2} = \frac{S_s^2}{u^2\pi} e^{-S_s^2(v_{\perp}/u)^2}$$

$$S_s = u/\sqrt{2k_B T_s/m}$$

Molecules at the entrance of the skimmer now contribute to the total density, $n_s$, with velocity components $v_{\parallel}$ and $v_{\perp}$, in the intervals $(v_{\parallel}, v_{\parallel} + dv_{\parallel})$ and $(v_{\perp}, v_{\perp} + dv_{\perp})$ as,

$$d^3\rho_s = \tilde{f}(v_{\parallel}, v_{\perp})dv_{\parallel}d^2v_{\perp} \tag{5.35}$$

I write the intensity (or flux density) differential in the velocity components at the skimmer as:

$$d^3\mathcal{F} = v_{\parallel}d^3\rho_s = v_{\parallel}\rho_s\tilde{f}_{\parallel}dv_{\parallel}\tilde{f}_{\perp}d^2v_{\perp} \tag{5.36}$$

The intensity differential in the sole component $v_{\parallel}$ is

$$d\mathcal{F} = v_{\parallel}\rho_s\tilde{f}_{\parallel}dv_{\parallel}\int_{-\infty}^{\infty}\int_{-\infty}^{\infty}\tilde{f}_{\perp}d^2v_{\perp} = v_{\parallel}\rho_s\tilde{f}_{\parallel}dv_{\parallel}, \tag{5.37}$$

and the total flux density per area and along the beam line, follows as,

$$\mathcal{F} = \int_0^{\infty} d\mathcal{F} = \frac{\rho_s^2 S_s^2}{\pi}\{\frac{e^{-S_s^2}}{2S_s^2} + \frac{\sqrt{\pi}}{2S_s}(1 + erf(S_s))\} \tag{5.38}$$

Appendix G.1 of reference [76] solves this integral. The total flow through the skimmer of area A is now:

$$\Phi_s = A \cdot \mathcal{F} \tag{5.39}$$

I next derive an expression for the density distribution past the skimmer. For this, I must define a new set of coordinates $\theta, l, r, \chi$ according to Figure 5.6. In these coordinates, I find
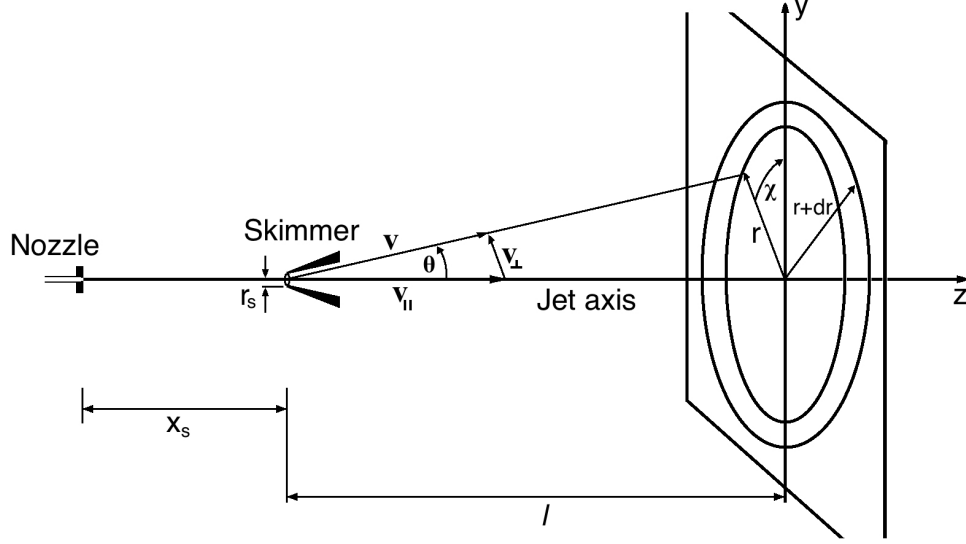
Figure 5.6: **Geometry, used in the calculation of $\mathcal{F}(r, l)$**

$$d^3v = dv_\| d^2v_\perp = dv_\| v_\perp dv_\perp d\chi = (\frac{rdr}{l^2})v_\|^2 dv_\| d\chi, \qquad (5.40)$$

where I use $v_\perp = v_\| \tan(\theta) \approx v_\| r/l$. It follows that

$$d^3\rho_s = \tilde{f}(v_\|, v_\perp)d^3v = \rho_s \tilde{f}_\|(v_\|)\tilde{f}_\perp(v_\|, r)\frac{rdrd\chi}{l^2}v_\|^2 d^2v_\|, \qquad (5.41)$$

where:

$$\tilde{f}_\perp(v_\|, r) = \frac{S_s^2}{\pi u^2}e^{-S_s^2(\frac{v_\| r}{ul})^2} \qquad (5.42)$$

The flow rate differential in the variables $v_\|, r$ and $\chi$ must conform with the flow rate at the point of skimming. In the new coordinates, this is given by:

$$d^3\Phi_s = Av_\| d^3\rho_s = A\tilde{f}_\| \tilde{f}_\perp n_s \frac{rdrd\chi}{l^2}v_\|^3 dv_\| \qquad (5.43)$$

The total flow across the part of the $\pi$-plane (see fig.5.6), which lies between $r$ and $dr$, is obtained by integrating over $\chi$. From cylindrical symmetry, it

follows that $d^2\Phi_s = \int_0^{2\pi} d^3\Phi_s = 2\pi d^3\Phi_s$. With this:

$$\frac{d^2\Phi_s}{2\pi r dr} = A\rho_s \tilde{f}_\parallel \tilde{f}_\perp l^{-2} v_\parallel^3 dv_\parallel = d\mathcal{F}(r,l) \tag{5.44}$$

The above expression represents the flux density of particles through a circular element between $r$ and $r+dr$ that lies in a plain orthogonal to $z$ and at distance $l$ from the skimmer. The integration of this expression [76] yields the desired density distribution:

$$\mathcal{F}(r,l) = \frac{A\rho_s u}{2\pi^{3/2} l^2 S_s} e^{-\eta^2 \xi^2} (1+\eta^2)^{-2} \{\sqrt{\pi}\xi(\xi^2+3/2)(1+erf(\xi))+e^{-\xi^2}(1+\xi^2)\} \tag{5.45}$$

Here $\eta = r/l$ and $\xi = S_s(1+\eta^2)^{-1/2}$. $\mathcal{F}(r,l)$ has the dimension of cm$^{-2}$ s$^{-1}$. To convert flow into density, I divide by the velocity $v_\parallel$. Plotting the result, using the molecular beam parameters given above and choosing a distance $l$ from the skimmer much greater than its diameter, indicates the Gaussian nature of this function.

My analysis shows that I can approximate $\mathcal{F}(r,l)/v_\parallel$ by a Gaussian if I am willing to accept an error on the order of 1%:

$$\rho_l^{Gauss}(r) = \rho_l^0 \cdot e^{\frac{r^2}{2\sigma_l^2}}, \tag{5.46}$$

Here, constants, $\rho_l^0$ and $\sigma_l$, depend on parameters that I obtain numerically by fitting to $\mathcal{F}(r,l)/v_\parallel$. This yields a very simple mathematical form for the NO density distribution.

Let us compare these findings with experimental observation. Figure 5.7 displays a measurement made by collecting the signal produced by a neutral particle beam incident on an imaging detector mounted 468 mm downstream from the skimmer.[11] This measurement uses a nozzle-skimmer distance of 35 mm. Considering these flight parameters, together with the stagnation reservoir properties listed in Table 5.1 in the collision model of Section 5.6, I predict a temperature of 0.46 K at the point of skimming.

---

[11] A full description of the detector employed in this experiment can be found in Appendix A.
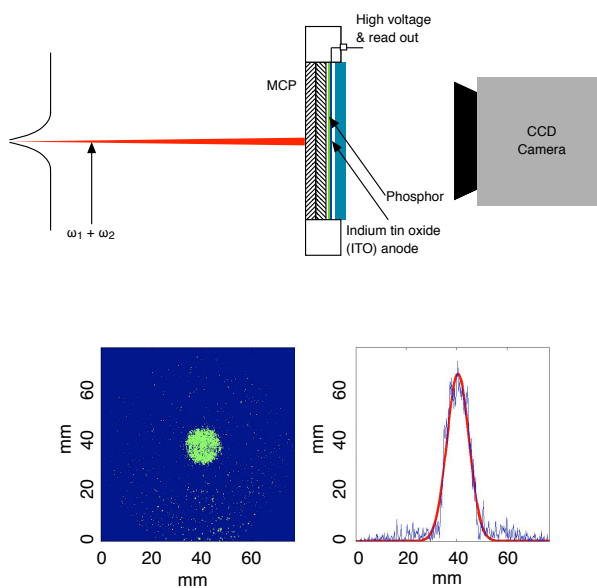
Figure 5.7: **Top:** Experimental setup for the imaging of the molecular jet. The jet enters the experiment chamber through the skimmer and impacts on a MCP stack after a free-flight of 468mm. Free electrons are created, multiplied and viewed as photons by a CCD camera. **Bottom-Left:** CCD response of molecular beam impacting on phosphor screen detector (at a distance of 468mm from the skimmer) without laser light present; **Bottom-Right:** Vertical summation over image pixel and fit, fitted Gaussian width is 4.35mm.

Upon passing through the skimmer, a particle in the beam has an average of 2.7 collisions left on its way to infinity, which I neglect in this analysis. For above conditions, I predict a beam width of 3.8 mm at the detector which is 13% narrower than the measured width of Figure 5.7.

From the experimentally measured width, we can estimate that the NO particles impacting the detector in Figure 5.7 have a temperature of 0.6 K in the moving frame as they pass through the skimmer. Given the number of assumptions in this analysis, this correspondence between calculated and measured properties of the beam suggest that the model presented here reflects the important aspects of the beam physics and yields a good description of the system employed in these experiments.

## 5.8   Phase-space distribution of nitric oxide

As a final step, I calculate the velocity distribution of the beam particles at a distance $l$ beyond the skimmer. Here, I assume that the beam propagates in a continuous fashion along the $z$-axis and, after the skimmer orifice collisions are no longer present.

Considering a moving-frame coordinate system that travels with the beam velocity $u_\parallel$, I expect that the particles in the experimental chamber within this frame conserve their Maxwellian velocity distribution, owing to the absence of collisions. Note in particular that fast particles, i.e. particles with velocities that originate in the wings of the distribution, leave the volume sooner than slower particles. As fast particles leave a volume element along $z$, fast particles from the leading and trailing volume elements enter and the overall velocity distribution, and with it $T_z = T_{parallel}$, remains the same along the $z$-axis.

A different situation describes the velocity distribution perpendicular to the beam centreline. In the point-source approximation, a particle stream of intensity $\Phi_s$ enters the experimental chamber. In the same moving frame as above, faster particles quickly deviate from the centreline and exit a given volume element sooner than slower moving particles. To a first approximation, the position of a particle within a plane in $x$-$y$ coordinates directly

Figure 5.8: **Left:** Random distribution of 10,000 particles in an area corresponding to the skimmer orifice. Each particle has x and y velocity components sampled from a Mexwell-Boltzmann distribution of 0.6 K. **Middle:** The same distribution evolved over a flight-time corresponding to the distance skimmer-detector. Each particle-trajectory originates from the particle point of origin within the red circle, i.e. all trajectories are outward. **Right:** Radial plot and fit of evolved density distribution (middle). I obtain a Gaussian width of ∼4.53 mm (cf. Figure 5.7).

depends its initial velocity component, $v_\perp$. This is illustrated in Figure 5.8 and holds for distances much larger than the skimmer diameter.

I can assign each point in space a hydrodynamic velocity, $u_\perp(\mathbf{r})$, given by

$$u_\perp(\mathbf{r}) = u_\perp(l, r_\perp) = \frac{r_\perp}{\text{time to reach } l} = \frac{r_\perp}{\frac{l}{u_\parallel}}, \qquad (5.47)$$

which represents the velocity directed away from the centerline. If a particle is found at point $\mathbf{r}$, it must exhibit the velocity $u_\perp(\mathbf{r})$.

This analysis does not mean that the Maxwellian distribution is lost. It means that the velocity spread for all particles in any x-y-plane is just the same as it was at the point of skimming. The velocity at an infinitely small volume and at an arbitrary point $\mathbf{r}$ (after the skimmer and within the point-source approximation), however, is just $u_\perp$. The temperature $T_\perp(\mathbf{r})$, i.e. the width of the velocity distribution perpendicular to the stream line and at point $\mathbf{r}$ in the experimental chamber, quickly approaches zero owing to this mechanism.

I thus write an expression for the phase-space density of the NO particles in the volume of a thin plane-perpendicular section at a distance $l$ from the skimmer as:

$$f_l^{NO}(\mathbf{r}, \mathbf{v}) = \rho_l^0 \cdot \exp(\frac{r_\perp^2}{2\sigma_l^2}) \cdot \exp(-\frac{m_{NO}(v_\parallel - u_\parallel)}{2k_B T_\parallel}) \cdot \delta(v_\perp - u_\perp(l, r_\perp)) \quad (5.48)$$

# Chapter 6

# The Rydberg ensemble

## 6.1 Excitation process

The last chapter has developed a description of nitric oxide molecules seeded in a supersonic molecular beam of helium. In the chapter to follow, I utilize the characteristics of this beam to obtain the initial plasma particle phase-space distribution functions.

The spectroscopic characteristics of Nitric oxide have been discussed at length in Chapter 2. To estimate the initial density of a photoprepared Rydberg gas, I begin by calculating the fraction of NO molecules that populate the lowest lying rotational ground state level, from which the excitation process originates.

In Hunds case (a), the $J''$ levels of $^2\Pi$ NO split into manifolds of $\Omega = \frac{1}{2}$ ($F_1$) and $\Omega = \frac{3}{2}$ ($F_2$), separated by the spin-orbit splitting, which for this system is about 119.8 cm$^{-1}$ [1]. Rotational cooling in the supersonic expansion relaxes population to the lowest few levels of the $F_1$ manifold. To a good approximation, the rotational energy of levels in the $^2\Pi_{1/2}$ manifold increases as:

$$W_{rot}(N'') = B_v N''(N'' + 1) \tag{6.1}$$

where $B_v = 1.67$ cm$^{-1}$ [1].[12]

Statistical thermodynamics relates the fractional populations in these

---

[12]The NO X-state is described (mostly) though Hund's case a). I use notation $N$ to describe the molecular core rotation despite the fact that $N$ is not a good quantum number.

levels to the local rotational temperature,

$$P(N'') = \frac{2(2N'' + 1)e^{-W_{rot}(N'')/k_B T}}{\tilde{Z}_r} \tag{6.2}$$

where

$$\tilde{Z}_r = \sum_{N''} 2(2N'' + 1)e^{-W_{rot}(N'')/k_B T}. \tag{6.3}$$

Under molecular beam conditions, the partition function sum extends over only a few levels of $F_1$. The factor of two in the degeneracy reflects Λ-doubling of the rotational levels in the Π state into positive and negative parity components.

The foregoing molecular beam model as well as our general experimental experience accord with a rotational temperature range from $T_R = 1.5$ to 4 K. Over this range, the predicted fractions of the NO population occupying $F_1$ levels with angular momentum of the nuclear rotation of $N'' = 0$ and 1 vary as follows.

Table 6.1: Fractional population in $F_1$ rotational states of $^2\Pi$ NO as a function of rotational temperature in the molecular beam

| $T_R$ | $N'' = 0$ | $N'' = 1$ |
|---|---|---|
| 1.6 K | 0.87 | 0.13 |
| 2.5 K | 0.68 | 0.30 |
| 4.1 K | 0.48 | 0.44 |

In most cases, we find spectroscopically measured intensities consistent with $T_R \approx 2.5$ K. At this rotational temperature, 68 percent of the nitric oxide in the illumination volume occupies the rotational ground state. Half of these molecules have the (-) parity required for a dipole-allowed transition to the rotational level $N' = 0$ of the A $^2\Sigma^+$ $v' = 0$ state that represents the first step of our excitation sequence (cf. Figure 2.3).

Thus, we tune the output, $\omega_1$, of the first of two dye lasers to ∼226 nm, which excites the (-) parity component of the ground state NO X $^2\Pi_{\frac{1}{2}}$ $J'' = 1/2$ molecules to the $J' = 1/2$ (+) level of the A $^2\Sigma^+$ $v' = 0$ state via
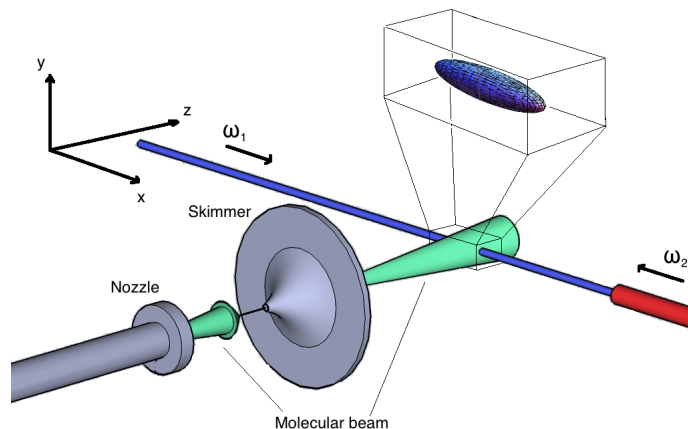
Figure 6.1: **Creation of a NO Rydberg ellipsoid -** The gas mixture of NO and He exits the nozzle and cools as it expands into the vacuum. Only the coldest part of the beam passes the skimmer. This part slightly expands as it continues, which is due to the remaining thermal motion of the gas particles. It is overlapped by two counter-propagating lasers that create an ellipsoid of NO Rydberg molecules which continues to travel with the molecular beam.

the $pQ_{11}(1/2)$ transition. A second laser, $\omega_2$, tuned to a wavelength in the interval between 327 nm and 330 nm, drives this population to a single, high lying NO Rydberg level of principal quantum number, $n$, in the range between 30 and 80, selected from manifolds of Rydberg states, all with total angular momentum neglecting spin of $K = 1$. The short predissociation lifetimes of all other accessible Rydberg states in practice limits this process to the $nf$ series.[13] The two-colour, laser-crossed molecular beam intersection forms an ellipsoidal excitation volume schematically diagrammed in Figure 6.1.

To calculate the A-state density distribution within this ellipsoid, I assume that the molecular beam expands to a negligible degree over the width of the illuminated region in $z$. The mathematical form of the A-state distri-

---

[13]This is further discussed in Chapter 9.2.1.

bution then follows through convolution of cylindrical molecular beam and cylindrical laser geometry:

$$\rho_{A-state}(x,y,z) = \rho^0_{A-state} \cdot \exp\left(-\frac{x^2}{2\sigma^2_{NO}} - \frac{y^2}{2\sigma^2_{NO}} - \frac{y^2}{2\sigma^2_{\omega_1}} - \frac{z^2}{2\sigma^2_{\omega_1}}\right)$$

$$= \rho^0_{A-state} \cdot \exp\left(-\frac{x^2}{2\sigma^2_x} - \frac{y^2}{2\sigma^2_y} - \frac{z^2}{2\sigma^2_z}\right)$$

$$\text{where} \quad \sigma_x = \sigma_{NO}, \quad \sigma_y = \sqrt{\frac{\sigma^2_{NO} \cdot \sigma^2_{\omega_1}}{\sigma^2_{NO} + \sigma^2_{\omega_1}}}, \quad \sigma_z = \sigma_{\omega_1}$$

(6.4)

I now endeavour to estimate the A-state peak density $\rho^0_{A-state}$. The 1+1 REMPI spectrum of NO presents a set of transitions. Choosing the ground-to-ground rovibronic NO X-A resonance, we decrease the $\omega_1$ laser intensity by means of two polarizers. We do this to minimize contributions from hot electrons produced by 2-$\omega_1$-photon ionization. For most experiments, we offset the polarizer by $\sim 50$ degrees, which yields an $\omega_1$ intensity of 1.75 $\mu$J per pulse. Assuming a perfect Gaussian laser shape, I can calculate the peak intensity of the beam from the average laser power, $\tilde{P}$:

$$\tilde{P} = I_{peak} \cdot \int \exp\left(-\frac{y^2}{2\sigma^2}\right) dy \int \exp\left(-\frac{z^2}{2\sigma^2}\right) dz = I_{peak} \cdot 2\pi\sigma^2$$

$$\Rightarrow I_{peak} = \frac{\tilde{P}}{2\pi\sigma^2}$$

(6.5)

I take the Gaussian rms-width of the laser intensity distribution to be $\sigma_1 \approx 0.2$ mm, as determined from razor-blade tomography. For a single pulse of 10 ns, the peak power is $I_{peak} = 0.7$ mW/cm$^2$. From this photon flux, I calculate the density of molecules excited to the NO A-state, $\rho_{A-state}$, by:

$$\rho_{A-state} = \rho_{GS} \cdot \chi_{abs} \cdot \mathcal{F}$$

(6.6)

$$\mathcal{F} = I_{peak} \cdot E_\gamma^{-1}$$

Here, $\mathcal{F}$ is the photon-flux and $\rho_{GS}$ is the ground state density at the

centre of the spatial distribution. $\chi_{abs}$ is the photon absorption cross-section. The energy of a 226 nm photon is $W_\gamma = hc/\lambda = 8.79 \cdot 10^{-19}$ J. Based on measurements of Bethke [9], Hippler and Pfab estimate $5 \cdot 10^{-16}$ cm$^2$ as the effective cross-section of a typical rovibronic transition of the $\gamma(0,0)$ band for NO in a comparable experiment [34]. I will adopt this value. For a photon flux of $7.9 \cdot 10^{22}$ s$^{-1}$ cm$^{-2}$, Eq. (6.6) calculates an A-state density of,

$$\rho_{A-state} = \rho_{GS} \cdot 0.4 \tag{6.7}$$

The factor 0.4 approaches saturation and I employ a simple rate equation model to account for this. I also introduce an ionization channel through $\tilde{\sigma}_{ion}$, representing the cross-section for one-photon ionization from the A-state. This cross-section was measured by Zacharias, Schmiedl and Welge to be $\tilde{\sigma}_{ion} = 7 \cdot 10^{-19}$ cm$^{-2}$ for 266 nm light [30], and I approximate this value to hold for our transition. I solve the following set of equations numerically,

$$\frac{dN_{es}}{dt} = \tilde{\sigma}_{abs} \cdot N_{gs} \cdot F \tag{6.8}$$

$$\frac{dN_{ion}}{dt} = \tilde{\sigma}_{ion} \cdot N_{es} \cdot F, \tag{6.9}$$

where $N_{gs}$, $N_{es}$ and $N_{ion}$ are the number of molecules in the transition ground state, excited state and ionized state respectively.

The A-state population, exterior to the point of maximal intensity, is assumed to depend linearly on the laser intensity. The overlap of the low intensity, Gaussian $\omega_1$-laser profile and the Gaussian NO density distribution within the molecular beam creates a prolate ellipsoid of A-state NO molecules. The $\omega_2$ laser is much stronger in intensity, saturating the transition from the A-state into the Rydberg level. Furthermore, since the FWHM of $\omega_2$ has about 3 times that of $\omega_1$, the spatial Rydberg density is determined by $\omega_1$ alone and matches the ellipsoidal distribution of initial A-state population.

## 6.2    Phase-space distribution of the Rydberg ensemble

I now summarize the results from above discussion. For this purpose, I consider a setup with a 2.5 cm nozzle-skimmer distance and at 7.5 cm skimmer-laser distance. The model above (Chapter 5) predicts a beam temperature at the skimmer of 0.7 K, with a remaining collision number of 4.7. By the point of laser-overlap, the beam will have developed a Gaussian width of 750 $\mu$m with a peak density of $1.62 \cdot 10^{14}$ cm$^{-3}$ NO molecules.

Let us put these last values into context. Section 5.7 develops a method to determine the density distribution of NO within the experimental chamber. A prediction using this method underestimates apparent beam temperature by 13% compared to the quantity we determine experimentally (cf. Figure 5.7). Thus, we ought to view 0.7 K as a lower bound for the actual beam temperature. Figure 6.2 details typical variations in NO density and distribution width as a function of beam temperature. We can see that underestimating temperature to a small extent leads to a small overestimate in density and small underestimate in width. For the purpose of this tutorial, I will continue with the theoretical values derived above.

At an assumed $\omega_1$ laser intensity of 1.75 $\mu$J and a Gaussian laser width of 0.2 mm I calculate an A-state peak density of $1.5 \cdot 10^{13}$ cm$^{-3}$ and an ion number of $5 \cdot 10^9$ cm$^{-3}$ produced in the first excitation step. Saturation of the $\omega_2$ transition promotes half of the A-state density to Rydberg molecules.

I will now generalize the phase space distribution of the Rydberg gas. Here, I include provision for the conversion of thermal energy into radial

streaming motion.

$$f_{Ry}(\mathbf{r}, \mathbf{v}) \approx \rho_{Ry} \cdot \exp\left(-\frac{m_{NO}(v_x - \gamma_x \cdot x)^2}{2k_B T_x} - \frac{x^2}{2\sigma_x^2}\right)$$
$$\cdot \exp\left(-\frac{m_{NO}(v_y - \gamma_y \cdot y)^2}{2k_B T_y} - \frac{y^2}{2\sigma_y^2}\right) \quad (6.10)$$
$$\cdot \exp\left(-\frac{m_{NO}(v_z - \gamma_z \cdot z)^2}{2k_B T_z} - \frac{z^2}{2\sigma_z^2}\right)$$

The above equation recognizes the linear dependence in the hydrodynamic velocity (cf. Eqs. (5.47) and (7.11)) and writes $u_k(l, k) = \gamma_k \cdot k$, where I use the hydrodynamic velocity parameter $\gamma_k$.

I set initial conditions according to the discussion above, where: $T_z = 0.7$ K, and $T_y = T_x \approx 0$ K (as a result of the point source approximation). $\sigma_x = \sigma_{NO} = 0.75$ mm while $\sigma_z = \sigma_{\omega_1} = 0.2$ mm. Eq. (6.4) yields the value $\sigma_y = 0.193$ mm for $\sigma_{NO} = 0.75$ and $\sigma_{\omega_1} = 0.2$ mm. I elect to simplify the following consideration by treating our plasma as cylindrically symmetric, i.e. $\sigma_y = \sigma_z \approx 0.2$ mm.
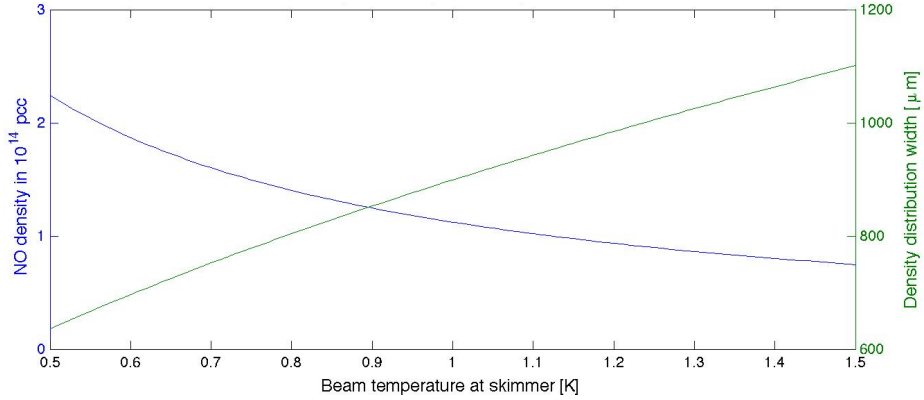


Figure 6.2: **Plot of peak density vs. Gaussian beam width** as a function of beam temperature for a system with 2.5 cm nozzle-skimmer distance and at a point 7.5 cm downstream from the skimmer. For a temperature of 0.7 K, the graph yields a density of $1.62 \cdot 10^{14}$ cm$^{-3}$ NO molecules at a Gaussian width of 750 $\mu$m.

I derive a value for each $\dot{\sigma}_k$ by considering the rate of expansion about the respective $k$-axis. At the instant of Rydberg formation, the distribution of ion velocities in $z$ has a width determined by $T_z$ and a first moment of zero. Thus, the initial ensemble has no expansion velocity about $z$ in the moving frame, $\dot{\sigma}_z(t = 0) = 0$. The quantities, $\dot{\sigma}_x(t = 0)$ and $\dot{\sigma}_y(t = 0)$ have nonzero values owing to the small underlying divergence of the molecular beam. I obtain $\sigma_x^0 = \sigma_l$ from Eq. (5.46) and use the relation

$$\frac{l}{v_{\parallel}} = \frac{\sigma_x^0}{\dot{\sigma}_x} \tag{6.11}$$

to obtain $\dot{\sigma}_x$ and similarly $\dot{\sigma}_y$ as:

$$\dot{\sigma}_y(t) = \frac{\sigma_y^0}{\sigma_x^0} \cdot \dot{\sigma}_x(t) \tag{6.12}$$

The initial hydrodynamic velocity parameter is defined by $\gamma_k(t) = \dot{\sigma}_k(t)/\sigma_k(t)$. Table 7.1 summarizes the initial conditions of our Rydberg ensomble as laser

Table 6.2: Initial conditions imposed on Rydberg molecule position and momentum based on underlying molecular beam and excitation scheme. Below values in combination with equation 6.10 give a full account of the phase-space distribution of our Rydberg ensemble.

| Rydberg ensemble initial conditions | |
| --- | --- |
| $\sigma_x$ | 750 $\mu$m |
| $\sigma_y$ | 200 $\mu$m |
| $\sigma_z$ | 200 $\mu$m |
| $\gamma_x$ | 0.0193 $\mu$s$^{-1}$ |
| $\gamma_y$ | 0.0193 $\mu$s$^{-1}$ |
| $\gamma_z$ | 0 $\mu$s$^{-1}$ |
| $T_x$ | $\sim$0 K |
| $T_y$ | $\sim$0 K |
| $T_z$ | 0.7 K |
| $\rho_{Ry}$ | $7.5 \cdot 10^{12}$ cm$^{-3}$ |

excitation has concluded. The initial peak density of Rydberg states, $\rho_{Ry}$,

should be understood as an upper boundary, as it was derived for an ideal system.

# Part III

# Theory work

The previous part of my thesis developed the hydrodynamics of supersonic expansion in terms of the functional characteristics of a differentially pumped molecular beam apparatus. I characterized the Rydberg gas phase-space volume created by the convolution of laser and molecular beam distribution functions. Chapter 6.2 concluded with a statement of the phase-space distribution function of the Rydberg ensemble formed in our experiment.

Over the course of part III, I will consider the evolution of this Rydberg ensemble in time. This will be done in two steps. Chapter 7 will discuss the internal conversion of our Rydberg gas to plasma via Penning ionization and electron-Rydberg collisional avalanche. As I will show, this plasma formation process is reaching a quasi-equilibrium on a nano-second timescale. The chapter will conclude stating the initial state of the phase-space distribution of plasma ions and electrons. Following this, Chapter 8 will shift timescales to consider ambipolar expansion and decay of the plasma ensemble over tens of micro-second.

While seeking to take full account of the spatial asymmetry and chemical reactivity encountered in the molecular beam ultracold plasma, I will stop short of considering the effects of Coulomb correlation. Ion and electron densities and temperatures, estimated by gauging the model developed below against the results consistently produced by molecular beam ultracold plasma experiments, point to plasma evolution through a regime of strong coupling. The means by which the plasma reaches such conditions and the effect of strong coupling on plasma observables remains to be addressed. The toolset described in the following provides a solid, zeroth-order platform from which to consider the evolution to a state of strong coupling under the non-spherical, reactive conditions of the molecular beam ultracold plasma.

Chapter 7 will deploy a computational method originally derived by Jonathan Morrison and Nicolas Saquet [79], and later developed by Jachin Hung and Hossein Sadeghi [37], all previous members of my research group. Similarly, Chapter 8 deploys a method first developed by Hossein Sadeghi for

a high-symmetry plasma in the absence of thermal or hydrodynamic motion of the ions [70]. I have developed both methods further. I am grateful to my colleagues for sharing their code and wish to acknowledge their contribution to the following two chapters.

# Chapter 7

# Early-time dynamics in an UNP

At a distance of 7.5 cm beyond the skimmer, where our lasers cross the molecular beam, the thermal energy of the nitric oxide in the beam has largely relaxed to become directional kinetic energy and collisions have ceased (cf. Chapter 5). This changes after the laser pulses, $\omega_1$ and $\omega_2$ excite about 10 percent of this population to form a Rydberg gas. A nitric oxide molecule, excited to a high lying Rydberg state, let us say, $n_0 = 50$, has an electronic orbital diameter of $2n_0^2 a_0$, in this case approximately 260 nm.

At the core of the Rydberg ellipsoid, where the initial Rydberg gas density is as high as $\rho_0 \sim 10^{12}$ cm$^{-3}$, the mean distance between excited molecules is defined by a Wigner-Seitz radius, $(3/4\pi\rho_0)^{1/3} = a_{ws}$ of $\sim 500$ nm. As a consequence of overlapping Rydberg orbitals, we can expect that in our experiment, plasma formation is fundamentally linked to Penning ionization.

According to Raubicheaux (cf. Section 3.2), Rydberg atoms as close together as $1.8 \cdot 2n^2 a_0$ ionize in 90% of the cases in less than 800 Rydberg cycles. For example, by exciting into $n_0 = 50$, 800 Rydberg periods require $2\pi n^3 \approx 15$ ns (atomic units). Thus, plasma formation in dense Rydberg systems is a nano-second process.

An ionized Rydberg molecule will continue to move with the velocity of the former neutral. Movement of NO$^*$ and NO$^+$ is based on two concepts.

Along the z-axis, molecules have mean velocity components according to the thermal spread $v = \sqrt{k_B T_{beam}/m_{NO}} \approx 14$ nm/ns. At the same time, molecules, sitting for example at a radial distance of one standard deviation, $\sigma_x$, from the molecular beam centre line, have a radial velocity component of $v_\perp = \sigma_x \cdot \gamma_x = 14$ nm/ns. Overall, molecular movement on a nano-second timescale is very slow compared to the inter-particle distance. Based on this analysis, I will neglect NO core movement in a first-order approximation, as I consider plasma formation at the nano-second timescale.

## 7.1 Plasma evolution from a Rydberg gas

The following model is based on the concepts of Penning ionization and charged particle collisions with Rydberg molecules. These concepts, along with the respective rate coefficients were discussed in Chapter 3.

**Penning ionization**

Let us consider a uniform Rydberg gas of density $\rho_{Ry}^0$. In order to find the number of Penning partners within a critical distance of $r_c = 1.8 \cdot 2n_0^2 a_0$, one can consult the density-dependent Erlang distribution of nearest neighbour distances:

$$d\mathcal{E}(r) = 4\pi \rho_{Ry}^0 r^2 e^{-\frac{4\pi}{3}\rho_{Ry}^0 r^3} dr \tag{7.1}$$

For densities as high as $10^{12}$ $cm^{-3}$, an appreciable fraction of NO* molecules falls within the critical distance, where Penning ionization occurs spontaneously. To gauge the fraction of molecules, termed $f_P$, that form pairs separated by critical distance, $r_c$, I integrate Eq. 7.1.

$$f_P = \int_0^{r_c} d\mathcal{E}(r) = 1 - e^{-\frac{4\pi}{3}\rho_{Ry}r_c^3} \tag{7.2}$$

From this number, I estimate the density of Penning electrons:

$$\rho_e^0 = f_P \cdot \rho_{Ry} \cdot 1/2 \cdot 0.9 \tag{7.3}$$

The factor, $1/2$, accounts for the fact that a Penning interaction involving two Rydberg molecules produces one Penning electron and one deactivated Rydberg state. I multiply by 0.9 to comply with Raubichaux's 90% ionization. The principal quantum numbers of deactivated Penning partners $(\sum_i \rho_{Ry,i}^{deac} = \rho_e)$ distribute in proportionality to $n^5$ over states with $n$ from the ground state to $n_0/\sqrt{2}$, the highest final state in an interaction that transfers sufficient energy to ionize a molecule in state $n_0$. The drop in Penning partner binding energy determines the Penning electron temperature. The density of unaltered Rydberg states after Penning ionization is:

$$\rho_{Ry}^{unaltered} = (1 - f_P \cdot 0.9) \cdot \rho_{Ry} \qquad (7.4)$$

At a Rydberg density of $\rho_{Ry}^0 = 10^{12}\ cm^{-3}$ and for $n_0 = 50$, the Penning process supports as much as 16% electron-ion pair formation. The first Penning electrons escape from the gas volume. This creates a net positive space charge that begins to trap the remaining electrons. The escape of electrons ceases as soon as the depth of the trapping potential becomes equal to the electron kinetic energy. It is possible to estimate the number of escaping electrons, by calculating the excess charge that is required to trap electrons of thermal energy $3/2 k_B T_e$, within a Gaussian sphere of dimension $\sigma$ [17]:

$$N_i - N_e = \frac{3}{2} k_B T_e \sigma \frac{4\pi\epsilon_0}{e^2} \sqrt{\frac{\pi}{2}} = 2250 \ \ll N_i, \qquad (7.5)$$

for $\sigma = 200\ \mu$m and an electron temperature of 100 $K$ (this temperature conforms with results found later in this chapter). I find that the small fraction of $\ll 1$ % lost electrons can account for a trapping potential which is strong enough to confine the remainder and leads to a good approximation of quasi-neutrality for our plasma.

I assume that the velocities of the trapped electrons equilibrate instantly on the timescale of the experiment to define a time-evolving global electron temperature with an initial value $T_e^0$. The magnitude of this value follows

from energy conservation in the Penning process:

$$T_e^0 = \left( -\frac{Ry}{n_0^2}\rho_{Ry} + \frac{Ry}{n_0^2}\rho_{Ry}^{unaltered} + \sum_n \frac{Ry}{n^2}\rho_{Ry,n}^{deac} \right) / \left( \frac{3}{2}\rho_e^0 k_B \right) \qquad (7.6)$$

For above values, I find an initial electron temperature of $T_e^0 \approx 40$ K.

The electron and ion densities, the Rydberg distribution as well as the electron temperature serve as seed conditions for the evolution of our Rydberg system to plasma.

**Ionization avalanche**

Evolution to plasma proceeds in a dynamically complex sequence of events. Fast-moving Penning electrons impact isolated Rydberg molecules to start a collisional ionization cascade. For densities formed by saturated $\omega_1$ and $\omega_2$ transitions in the core of the Rydberg gas ellipsoid, the processes of Penning ionization and avalanche occur on the same timescale as laser excitation. To simplify the present description, I neglect any coupling between the dynamics of photoexcitation, Penning ionization and electron-impact avalanche.

Above discussion allows me to find post-Penning process vaules $\rho_{Ry}^{unaltered}$, $\rho_{Ry,n}^{deac}$, $\rho_e^0$ and $T_e^0$ for initial conditions $\rho_{Ry}^0$ and $n_0$. I now compile $\rho_{Ry}^{unaltered}$ and values $\rho_{Ry,n}^{deac}$ into a new array $\rho_n^0 = \rho(n, t = 0)$. Eqs. (7.7, 7.8) and Eq. (7.10) construct a rate equation model for the evolution of atomic Rydberg gas to plasma, incorporating the processes and rate coefficients introduced in Section 3.2:

$$\frac{d}{dt}\rho_n = -k_{ion}(n)\rho_n\rho_e + k_{tbr}(n)\rho_e^3 + \sum_{n_i \neq n} k(n_i, n)\rho_{n_i}\rho_e - \sum_{n_f \neq n} k(n, n_f)\rho_n\rho_e$$

$$(7.7)$$

$$\frac{d}{dt}\rho_e = \sum_n k_{ion}(n)\rho_n\rho_e - \sum_n k_{tbr}(n)\rho_e^3 \qquad (7.8)$$

Please note that $\rho_i = \rho_e$ in the quasi-neutral approximation. The evolution

of the electron temperature follows from energy conservation:

$$\frac{3}{2}k_B T_e \rho_e - Ry \sum_n \frac{\rho_n}{n^2} - W_{tot}(t) = 0 \qquad (7.9)$$

The derivative of above equation yields:

$$\frac{d}{dt}T_e = \left( \sum_n Ry \frac{\dot{\rho}_n}{n^2} - 1.5 k_B T_e \dot{\rho}_e \right) / (1.5 k_B \rho_e) \qquad (7.10)$$

For above computation, array $\rho_n$ is in principal infinite as $n = 1, ..., \infty$. I constrict accessible values of n to an interval between $n_{min}$ and $n_{max}$. Intuitively, one should set $n_{min} = 1$. Low-n Rydberg states, however, are most likely to decay via predissociation (see Table 3.3) or radiative decay. A possibility to account for low-n decay in a first-order approach is to set $n_{min} > 1$ and implement a decay path $M^*(n \leq n_{min}) \Rightarrow M_{deac}$ in the computation. Here, $M_{deac}$ refers to either the ground state or a dissociated state of the molecule, in either case a state no longer taking part in the system dynamics. Neither radiative decay nor predissociation influence the electron temperature and Eq. 7.10 remains unaltered. To improve the speed of computation, I elect not to consider dissociative recombination as a decay mechanism in the early time dynamics simulation. This approximation yields an acceptable error for evolution times $\ll 1\mu s$.

Morrison et. al. [52] have studied the effect of boundary conditions for plasma formation in NO and determined $n_{min} = 10$ as adequate. They set boundary $n_{max} = [\sqrt{Ry/k_B T_e}]$ according to the thermal energy of electrons. The square brackets indicate a rounded value. I will adopt these boundaries in the following.

## 7.2 Simulation results

In this section, I will discuss ionization avalanche computation results for several values of $\rho_{Ry}^0$ and $n_0$. As previously, I begin with $\rho_{Ry}^0 = 1 \cdot 10^{12} \; cm^{-3}$

and $n_0 = 50$.

## Rydberg manyfold decay

Figure 7.1 displays the evolution of n-level density with time. The top-left bar diagram shows the Rydberg manifold right after the Penning process. Of the initial Rydberg density $\rho_{Ry}^0$ in level n=50, 16% has been ionized and the same fraction was de-excited to levels below n=36. 68% of Particles do not take part in the Penning process and remain in level n=50.

As time progresses, n-changing electron-Rydberg collisions fan out the initial distribution. In these interactions, a hop to a neighboring state is more likely than to a state further away. A general trend of the Rydberg manifold down towards low-n states becomes apparent as $k_{n,n-1} > k_{n,n+1}$.

There are three loss mechanisms of Rydberg density considered in our model. The first is electron impact ionization. The second is via level-hopping to $n_{max}$ at which point the Rydberg state is considered ionized. And the third is level-hopping to $n < n_{min}$ and decay to an inactive state (ground state or dissociated state). Repopulation is possible through three-body-recombination. The evolution of the Rydberg manifold is largely completed after 100 ns.

## Electron temperature and density evolution

Figure 7.2 shows the evolution of Rydberg density and temperature. Starting with the Penning temperature of $\sim 40$ K, the system initially cools over the first nanosecond. This is due to cold electrons entering the distribution via level-hopping to $n_{max}$ and subsequent ionization. This ionization process ceases after the first few nanoseconds and is the main source of free electrons and ions.

The cascade of the Rydberg manifold down to low-n states is releasing lots of thermal energy to the electrons. After the initial quench in temperature, the electrons heat rapidly to a temperature approaching $\sim 200$ K. The heating slows as the bulk of the Rydberg manifold reaches $n_{min}$ and decays (at $\sim 20$ ns - see Figure 7.1). Slower heating via electron-Rydberg collisions
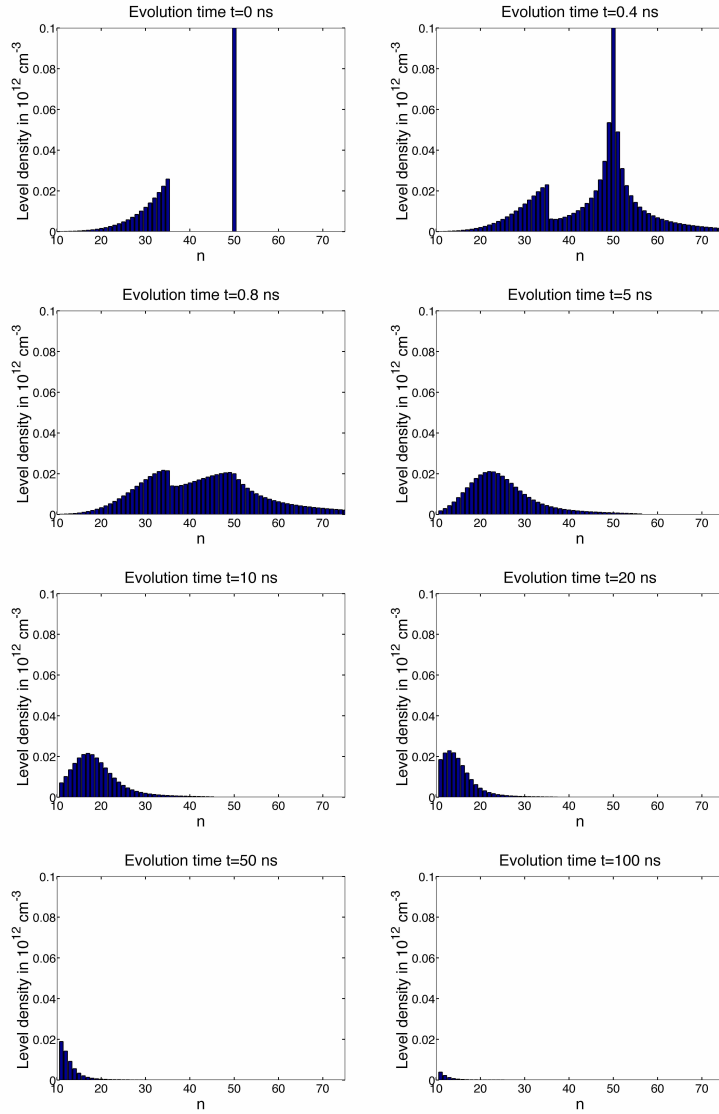
Figure 7.1: **Density distribution over n-levels -** The top-left figure shows the n-level distribution after the Penning process for $\rho_{Ry}^0 = 1 \cdot 10^{12} \ cm^{-3}$ and $n_0 = 50$. State $n=50$ has been cut off, its value being $\rho_{n=50}(t=0) = 0.67 \cdot 10^{12} \ cm^{-3}$.
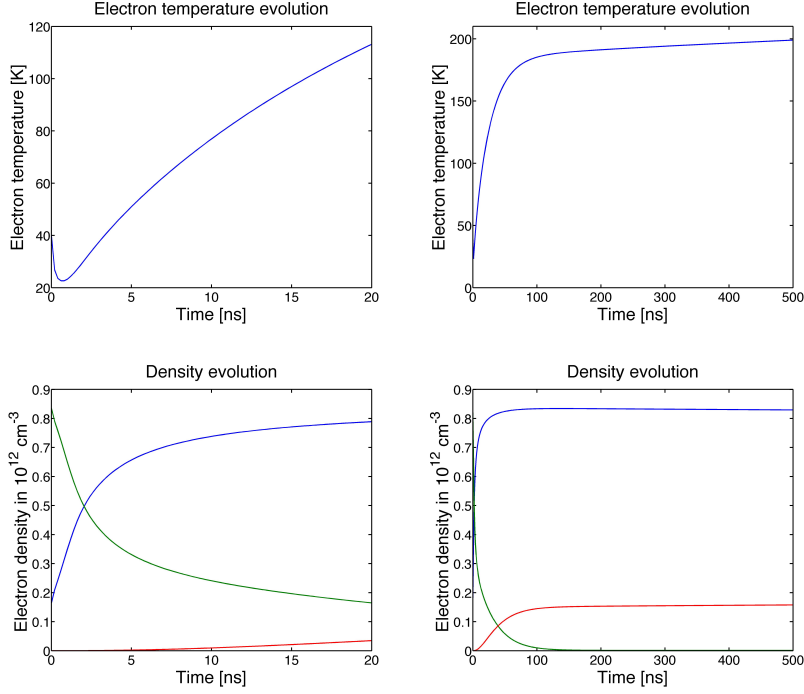
Figure 7.2: **Evolution of electron temperature and density -** The figures show the identical dataset as Figure 7.1, with the left-hand figures displaying an expanded timescale. The density plots show electron, total Rydberg and deactivated neutral densities (blue, green, red).

continues to take place up to $\sim 1$ $\mu s$ evolution, until all low-n levels have decayed via $n_{nim}$.

**Evolution at different densities and PQNs**

Figure 7.3 extends the previous computation to values $n_0 = 40$, 50, 60 and different initial densities $\rho_{Ry}^0 = 1,0.9,...,0.1 \cdot 10^{12}$ $cm^{-3}$. Several trends are apparent in the graphs:

- For the same PQN value, normalized electron densities approach the same upper limit.
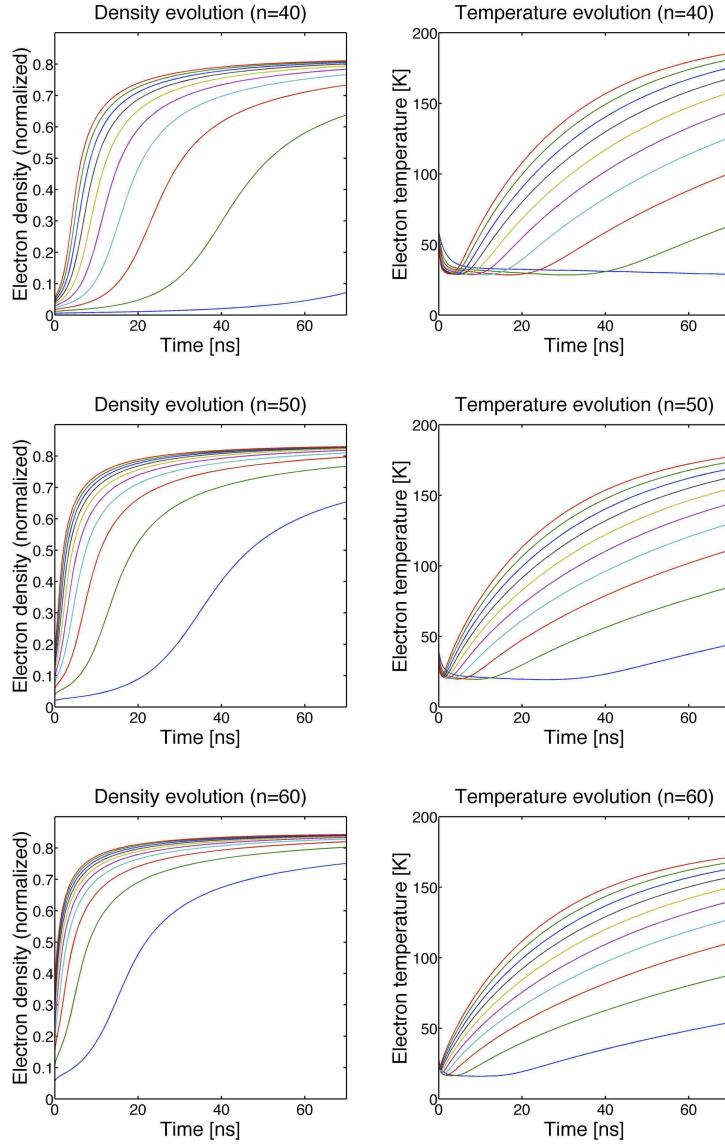
Figure 7.3: **Electron density and temperature evolution** for states $n$=40, 50, 60 and initial density $\rho_{Ry} = 1$, 0.9, 0.8,...,0.1·$10^{12}$ $cm^{-3}$ (for each figure top to bottom).

- The lower the initial Rydberg density, the lower the initial electron density and in turn the longer the decay of the Rydberg manifold (i.e. plasma formation).

- Plasmas formed from larger PQNs have a larger Penning fraction and thus higher initial electron density. They avalanche faster than plasmas formed at the same density but lower PQN.

For the evolution of electron density in time the following holds: The main growth in density is briefly delayed until the level-hopping Rydberg manifold reaches $n_{max}$. The growth later ceases as the bulk of the manifold decays to lower n-levels. This defines a point of inversion, POI, of the density evolution. POI is mathematically well defined and I will consider its double value as the plasma rise time, $t_{rise} = 2 \cdot t_{POI}$. This coincides with $\sim 90\%$ total ionization and shall serve as a measure for the time it takes for a Rydberg system to evolve to plasma. Figure 7.4 displays rise times for plasmas formed at different $\rho^0_{Ry}$ and PQN.

**Ionization avalanche for our experimental conditions**

Our research group has developed above formalism to simulate the early time dynamics in an ultracold neutral plasma. I will now use this model to derive the initial plasma properties for our experimental system, that is for $\rho^0_{Ry} = 7.5 \cdot 10^{12} \ cm^{-3}$. In the following, I will consider the case of laser excitation to Rydberg state $n_0 = 50$.

The phase-space distribution of the Rydberg ensemble formed in our experiment was summarized in Section 6.2, Table 6.2. The formed plasma occupies the extent of the former Rydberg volume. I set $\sigma_{Ry,k} = \sigma_{i,k}$ based on the fact that different density values achieve the same fractional ionization for a given PQN (cf. Figure 7.3). From quasi neutrality it follows that $\rho_i = \rho_e = \rho$ and $\sigma_{i,k} = \sigma_{e,k} = \sigma_k$. The ions are created with the velocity vectors of the former neutrals ($\gamma_{Ry,k} = \gamma_{i,k}$ and $T_{Ry,k} = T_{i,k}$).

In this model, electrons are assumed to thermalize instantaneously. They do not take on any hydrodynamic velocity characteristics and are fully described in momentum space by electron temperature $T_e$. For values of
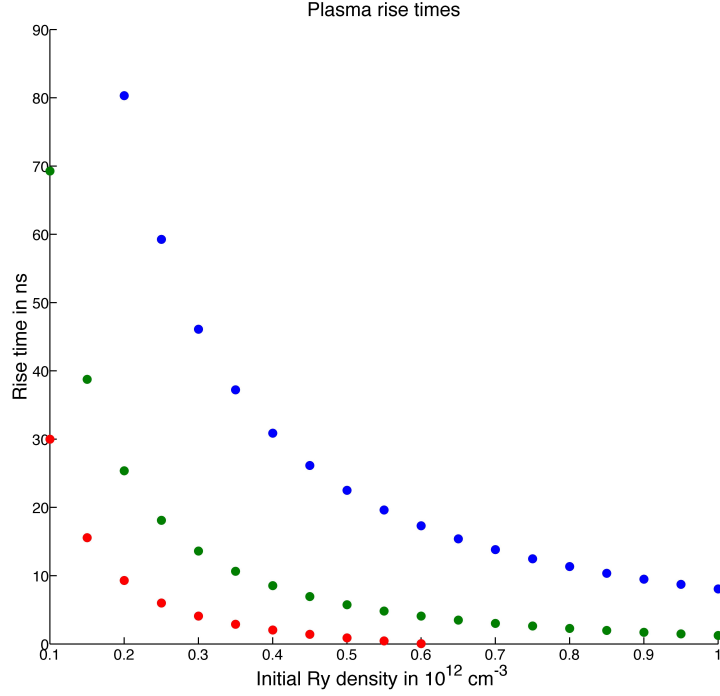
Figure 7.4: **Plasma avalanche times** for states $n$=40, 50, 60 (blue, green, red or top to bottom) and varying initial density $\rho_{Ry}^0$.

$\rho_{Ry}^0 = 7.5 \cdot 10^{12} \ cm^{-3}$ and $n_0 =$50, I find $\rho_e \approx 6 \cdot 10^{12} \ cm^{-3}$, $T_e$ appoching $\sim$ 200 K and $t_{rise} \approx 1$ ns. All results are sumerized in table 7.1.

Once more, the initial electron density should be understood as an order of magnitude estimate based on the predicted Rydberg density. I reformulate Eq. 6.10, the phase-space distribution function of the Rydberg ensemble, to yield the distribution function for plasma electrons and ions.

Table 7.1: Initial conditions imposed on plasma particle position and momentum based on underlying molecular beam and excitation scheme. Below values in combination with equation 7.11 give a full account of the phase-space distribution of our plasma.

| Plasma initial conditions | |
|---|---|
| $\sigma_x$ | 750 $\mu$m |
| $\sigma_y$ | 200 $\mu$m |
| $\sigma_z$ | 200 $\mu$m |
| $\gamma_{i,x}$ | 0.0193 $\mu$s$^{-1}$ |
| $\gamma_{i,y}$ | 0.0193 $\mu$s$^{-1}$ |
| $\gamma_{i,z}$ | 0 $\mu$s$^{-1}$ |
| $T_{i,x}$ | 0 K |
| $T_{i,y}$ | 0 K |
| $T_{i,z}$ | 0.7 K |
| $n_0$ | 50 |
| $\rho_{Ry}^0$ | $7.5 \cdot 10^{12}$ cm$^{-3}$ |
| $\gamma_{e,k}(0)$ | 0 $\mu$s$^{-1}$ |
| $\rho$ | $\sim 6 \cdot 10^{12}$ cm$^{-3}$ |
| $T_e$ | $\sim$200 K |

$$
\begin{aligned}
f_i(\mathbf{r}, \mathbf{v}, t) = {}& \rho \cdot \delta(v_x - \gamma_{i,x}) \delta(v_y - \gamma_{i,y}) \\
& \cdot \exp\left( -\frac{m_{NO}(v_z)^2}{2k_B T_{i,z}} - \frac{x^2}{2\sigma_x^2} - \frac{y^2}{2\sigma_y^2} - \frac{z^2}{2\sigma_z^2} \right) \\
f_e(\mathbf{r}, \mathbf{v}, t) = {}& \rho \cdot \exp\left( -\frac{m_e}{2k_B T_e}(v_x^2 + v_y^2 + v_z^2) \right) \\
& \cdot \exp\left( -\frac{x^2}{2\sigma_x^2} - \frac{y^2}{2\sigma_y^2} - \frac{z^2}{2\sigma_z^2} \right)
\end{aligned}
\tag{7.11}
$$

Note that the thermal velocity distribution in x and y has collapsed to a delta-function for $T_{i,k} \longrightarrow 0$.

The next section details a hydrodynamic approach to simulate the long-time phase-space evolution of a plasma with the charged-particle distribution functions described above.

# Chapter 8

# Long-time dynamics in an UNP

In our experiment, we form a plasma with phase-space distribution resembling Eq. 7.11, at initial conditions, Table 7.1. The last section discussed the process of plasma formation at sub-microsecond timescales and for fixed molecular core positions. I now shift gears and will study the evolution of plasma including expansion for timescales up to tens of microseconds. For this purpose, I will **reset the time origin** (value t=0). In the following $t_0$ refers to the point in time at which the previous section ended, the point where the formation of plasma is complete.

Section 8.1 will derive an analytic expression for the expansion of a non-dissociating plasma into vacuum. Section 8.2 will extend this discussion to derive a computation model for plasma expansion under the influence of dissociative recombination. Simulation results will be discussed in Section 8.3.

## 8.1  Analytic solution to plasma expansion

One can describe the free expansion of a non-dissociating plasma in simple terms via the Vlasov equations. Setting the right-hand side of the Boltzmann equation, Eq. (4.29), to zero, I obtain the electron and ion Vlasov equations as:

$$\frac{\partial f_e}{\partial t} + \mathbf{v}\frac{\partial f_e}{\partial \mathbf{r}} + m_e^{-1}\frac{\partial f_e}{\partial \mathbf{v}}e\frac{\partial \phi}{\partial \mathbf{r}} = 0, \tag{8.1}$$

$$\frac{\partial f_i}{\partial t} + \mathbf{v}\frac{\partial f_i}{\partial \mathbf{r}} - m_i^{-1}\frac{\partial f_i}{\partial \mathbf{v}}e\frac{\partial \phi}{\partial \mathbf{r}} = 0 \tag{8.2}$$

Dorozhkina and Semenov have derived an exact self-similar solution of the three-dimensional Vlasov equations, Eqs. (8.1) and (8.2), for electrons and ions with self-consistent electric fields,

$$e\frac{\partial \phi}{\partial \mathbf{r}} = k_B T_e \rho^{-1} \frac{\partial \rho}{\partial \mathbf{r}},\tag{8.3}$$

as in Eq. (4.50). The result describes how a spatially localized plasma volume expands into vacuum in the quasi-neutral approximation. Their solution yields [23, 24]:

$$f_i \propto \exp\left(-\sum_k \frac{r_k^2}{2\sigma_k^2(t)}\right) \exp\left(-\sum_k \frac{m_i(v_k - \gamma_k(t)r_k)^2}{2k_B T_{i,k}(t)}\right)\tag{8.4}$$

$$f_e \propto \exp\left(-\sum_k \frac{r_k^2}{2\sigma_k^2(t)}\right) \exp\left(-\sum_k \frac{m_e(v_k - \gamma_k(t)r_k)^2}{2k_B T_{e,k}(t)}\right)\tag{8.5}$$

Temperatures, rms-radii and the hydrodynamic velocity parameters within this solution satisfy,

$$T_{\alpha,k}(t) = T_{\alpha,k}(0) \cdot \frac{\sigma_k^2(0)}{\sigma_k^2(t)} \qquad \gamma_k(t) = \frac{\dot{\sigma}_k(t)}{\sigma_k(t)}$$

$$\sigma_k^2(t) = (\sigma_k(0) + \dot{\sigma}_k(0)t)^2 + c_k^2 t^2 \qquad c_k^2 = \frac{k_B}{m_i}(T_{e,k}(0) + T_{i,k}(0))\tag{8.6}$$

using once again, the condition that $m_i \gg m_e$.

Eqs. (8.4) and (8.5) conform with the initial conditions of the molecular beam plasma system. However, a closer look at Eqs. (8.6), reveals that this description fails to include a means to transfer energy between the coordinates axes of the system. I introduce coupling between these coordinates once again by explicitly recognizing rapid electron equilibration, i.e. $T_{e,x}(t) = T_{e,y}(t) = T_{e,z}(t) \equiv T_e(t)$.

I combine the equation of continuity, Eq. (4.36), for $k_{DR} = 0$, with Eqs. (8.6), the first moment of Boltzmann's equation (Eq. 4.52) and the previously found expression for the total energy (Eq. 4.56). This, for the special case of a Gaussian density distribution, leads to a set of ten ordinary

differential equations that include electronic equilibration and accurately approximate the Gaussian ellipsoidal plasma in the case of absence of a loss mechanism [43]:

$$\dot{\sigma}_k(t) = \sigma_k(t)\gamma_k(t) \qquad \dot{\gamma}_k(t) = \frac{k_B(T_e(t) + T_{i,k}(t))}{m_i\sigma_k(t)} - \gamma_k^2(t)$$

$$\dot{T}_e(t) = -\frac{2}{3}T_e(t)\sum_k \gamma_k(t) \qquad \dot{T}_{i,k}(t) = -2\gamma_k(t)T_{i,k}(t) \qquad (8.7)$$

Note that the initial temperature of the molecular beam detailed in Table 7.1, $T_{i,x}(t)$ and $T_{i,y}(t)$, start out at 0 K and remain so throughout the expansion. $T_{i,z}(t)$ begins at 0.7 K and falls. Terms linking $T_e(t)$ with the evolution of $\gamma_x(t)$, $\gamma_y(t)$ and $\gamma_z(t)$ couple electron thermal energy into all three dimensions of the expansion.

In the following section, I will derive a model that incorporates expansion under the influence of particle loss, in our case dissociative recombination. Above set of rate equation, derived analytically, will be useful to test the more complex computational method.

## 8.2 Expansion under the influence of dissociative recombination
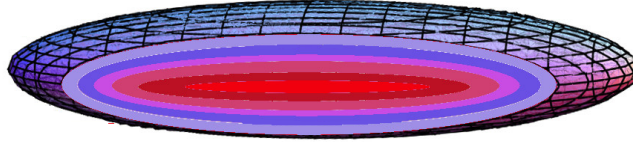


Figure 8.1: **Illustration of plasma in the shell picture**

The presence of DR precludes an exact self-similar solution of the corresponding Boltzmann equations. So, I numerically model the expansion of the system with reference to a set of equal density surfaces, leading to a

shell or onion model description. This is illustrated in Figure 8.1.

I follow the discussions in [73] and [70], extending the analysis from cylindrical and spherical symmetry to model an ellipsoidal plasma with finite initial ion temperatures and radial velocities. The shells in this plasma model expand on account of initial hydrodynamic velocities as well as the ambipolar conversion of electronic and ionic temperatures into directional kinetic energy. The charged particle number per shell changes only due to DR. Three body recombination to Rydberg states and subsequent predissociation only plays a minor role in the long-term evolution of plasma and is in the following neglected.

**Initial conditions:**

To define the initial conditions of this model, I first establish a global region of interest by introducing a computational cut-off, $C^{cut}$, found by multiplying the Gaussian rms-width along each axis by 5, $C_k^{cut} = \sigma_k^0 \cdot 5$. The initial shell width follows from division of $C^{cut}$ by the number of shells, $\Delta_k^{shell} = C_k^{cut}/\#^{shell}$. The surface of the $j$-th shell is now defined by

$$\frac{r_x^2}{(R_{x,j}^0)^2} + \frac{r_y^2}{(R_{y,j}^0)^2} + \frac{r_z^2}{(R_{z,j}^0)^2} = 1, \tag{8.8}$$

where the semi-principal axis lengths are defined as $R_{k,j}^0 = j \cdot \Delta_k^{shell}$. I determine the density of shell $j$ by evaluating,

$$\rho_j^0 = \rho_0^{peak} \exp\left(-\frac{(R_{k,j}^0)^2}{2 \cdot \sigma_k^0}\right), \tag{8.9}$$

using the same prescription for each axis $k = x, y, z$. The initial hydrodynamic velocity components of each shell are determined by $u_{k,j}^0 = R_{k,j}^0 \cdot \gamma_k^0$. I find the shell volume using,

$$V_j = \frac{4}{3}\pi \left[\prod_k R_{k,j} - \prod_k R_{k,j-1}\right], \tag{8.10}$$

determining the initial number of ions by $N_j^0 = \rho_j^0 \cdot V_j^0$. The initial conditions, for the system of differential equations I intend to solve include,

$$N_j^0, R_{x,j}^0, R_{y,j}^0, R_{z,j}^0, u_{x,j}^0, u_{y,j}^0, u_{z,j}^0, T_{i,x}(0), T_{i,y}(0), T_{i,z}(0), T_e(0), \qquad (8.11)$$

where subscripts $j$ point to an array of size $\#^{shell}$.

**Differential equations:**

My ODE integrator advances the system in steps starting from the initial conditions defined by Eq. (8.11). After each step, Eq. (8.10) determines the new volume of each shell, $j$, and $\rho_j = N_j/V_j$ yields the corresponding density. Dissociative recombination reduces the number of ions in the $j^{\text{th}}$ shell according to Eq. (4.36) expressed as:

$$\frac{\partial N_j}{\partial t} = -k_{DR} \cdot N_j^2/V_j \qquad (8.12)$$

The radius and volume of each shell evolves in time according to the hydrodynamic velocity of the ions:

$$\frac{\partial R_{k,j}(t)}{\partial t} = u_{k,j}(t) \qquad (8.13)$$

Equation (4.52) formulated for a uniform $u_k(r_k)$ within each shell, $j$, describes the temporal development of the hydrodynamic velocity in each case:

$$\frac{\partial u_{k,j}}{\partial t} = \frac{k_B}{m_i \rho_j} \frac{\partial \rho_j}{\partial r_k} \cdot (T_e + T_{i,k}) \qquad (8.14)$$

Eq. (8.14) defines two important characteristics of these shell-model expansion dynamics. First, note that the change in velocity in any coordinate direction depends on the corresponding density gradient, $\partial_r \rho$. This gradient varies with axis direction according to initial conditions. However, the quantity $\partial_r \rho_j$ changes smoothly, moving from one major axis to another on any arbitrary shell. Thus, I can represent the force as it changes the ellipsoidal shape of any shell $j$ by the gradients, $\partial_r \rho_j$, determined at the principal axis

positions $R_{k,j}$ from evolving plots of $\rho_k$ versus $r$ in each axis direction.

Note that Eq. (8.14) also holds that the electron and ion temperatures combine to drive the expansion. Energy conservation gives rise to the same effect in the Vlasov case, where it appears in the time variation of temperature, Eq. (4.59), and in the analytic solution for the time dependence of $\gamma_k$, Eq. (8.7). While this description fully couples the electron temperature in three dimensions, I allow the ion temperature to act as an energy reservoir for expansion only according to its initial coordinate axis distribution, $T_{i,x}(0) = T_{i,y}(0) = 0$ and $T_{i,z}(0) = 0.7$ K.

I rewrite Eq. (4.59) as it reflects the conversion of electron and ion thermal energy to hydrodynamic ion radial expansion energy.

$$\left[ 3\frac{\partial T_e}{\partial t} + \sum_k \frac{\partial T_{i,k}}{\partial t} \right] = -\frac{2m_i}{k_B \sum_j N_j} \sum_{k,j} N_j u_{k,j} \frac{\partial u_{k,j}}{\partial t} \tag{8.15}$$

Here, I have translated Eq. (4.59) into the shell picture by realizing that in this frame, the hydrodynamic energy represented by Eq. (4.54) becomes:

$$1/2 m_i N \sum_k \gamma_k^2 \sigma_k^2 \Rightarrow 1/2 m_i \sum_{k,j} N_j u_{k,j}^2 \tag{8.16}$$

Secondly, I assume that the ion thermal energy contribution to the hydrodynamic expansion energy is in proportion to its contribution to the thermal sum. Thus, I gauge the thermal relaxation of electrons and ions in each degree of freedom by:

$$\frac{\partial T_e}{\partial t} = -\frac{T_e}{T_e + 1/3 \sum_k T_{i,k}} \frac{1}{3} \left[ \frac{2m_i}{k_B \sum_j N_j} \sum_{k,j} N_j u_{k,j} \frac{\partial u_{k,j}}{\partial t} \right] \tag{8.17}$$

$$\frac{\partial T_{i,k}}{\partial t} = -\frac{T_{i,k}}{T_e + T_{i,k}} \left[ \frac{2m_i}{k_B \sum_j N_j} \sum_{k,j} N_j u_{k,j} \frac{\partial u_{k,j}}{\partial t} \right] \tag{8.18}$$

In summary, Eqs. (8.12), (8.13), (8.14), (8.17) and (8.18) represent a complete set of differential equations modelling the evolution of plasma

undergoing DR, based on initial condition (8.11).

## 8.3 Simulation results

**Spherical expansion and the effect of dissociative recombination**

I begin by applying the 3D shell model methodology described above to simulate the self-similar expansion hydrodynamics of a spherical Gaussian nitric oxide plasma, for which I can compare the numerical results with corresponding analytical solutions. To represent the free expansion of this test plasma, I choose an initial Gaussian width of $\sigma_x = \sigma_y = \sigma_z = 200 \ \mu$m, and set the initial charged particle density to $\rho_e^0 = \rho_i^0 = \rho_0 = 6 \cdot 10^{12} \ \text{cm}^{-3}$.

I wish to develop an intuition for the behaviour of plasma to different electron temperature values. The upper three panels in Figure 8.2 show the shell model evolution of Gaussian radial density distributions of a nitric oxide plasmas with three selected electron temperatures, $T_e = 5, 20, 100$ K. These model plasmas lose no ions to dissociative recombination, and the shell-model solution conforms exactly with the time-dependent Gaussian solutions of the Vlasov equations.

Note that in the representation of Figure 8.2, expansion appears most evidently in the transfer of charged particles from the comparatively small volume of the plasma core to occupy the much larger and much lower density plasma domain at larger $r$. This dispersion of $\text{NO}^+$ plasma mass occurs much faster at higher temperature. On the scale of the initial peak density, the charge distribution spreads to become barely observable after 3 $\mu$s for $T_e = 100$ K. Experimental observations of nitric oxide plasma evolution show evidence of a peaked electron signal reflecting a spatially localized plasma even after hundreds of microseconds [50, 73, 78].

The lower frames of Figure 8.2 compares the shell model evolution of a plasma that undergoes dissociative recombination described by a rate constant (cf. Section 3.2):

$$k_{DR} = 6 \cdot 10^{-6} T_e^{-1/2} \ \text{cm}^3 \ \text{s}^{-1}, \tag{8.19}$$
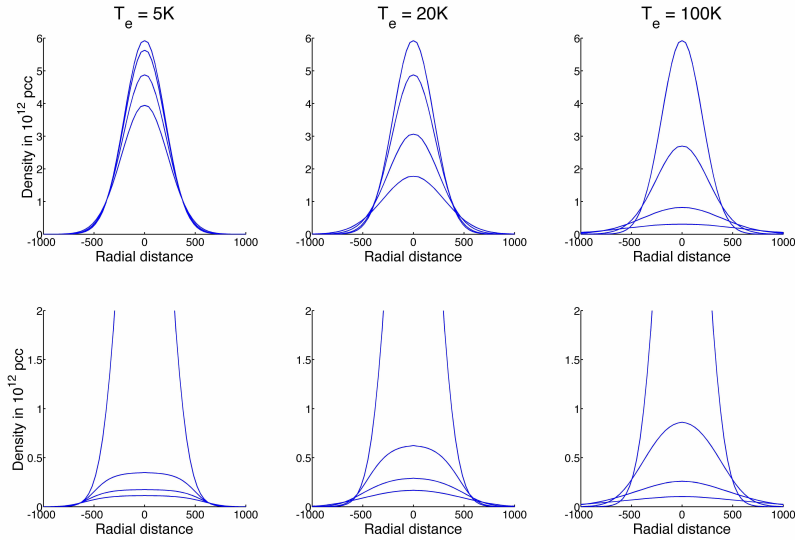
Figure 8.2: **Plasma density** along the z-axis for a spherical system for initial electron temperatures of $T_e$ = 5, 20, 100 K. Each figure shows the early evolution of plasma for time steps of 0, 1, 2 and 3 $\mu$s (top to bottom curves). The top figures display simulation results for a system without DR, the bottom simulations include DR.

In the presence of dissociative recombination, an initially Gaussian plasma departs from a state of self-similar expansion. At low electron temperature in particular, the rapid recombination of $NO^+$ with electrons in the dense centre of the plasma flattens the core of the spatial distribution. This change readily appears in a plot of density as a function of radial distance, $r$. Figure 8.3 shows that by flattening the distribution function at its core, DR significantly retards the rate at which the shell with an initial radius of $1\sigma$ expands.

However, as suggested above, an overwhelming majority of the electrons in the plasma sphere occupy the sizeable volume at larger $r$. Here, dissociative recombination proceeds at a rate that is slow compared with expansion. As evident in Figure 8.3, DR has a much smaller effect on the rate at which radial velocity grows in the shell at $3\sigma$. In an apparatus that collects
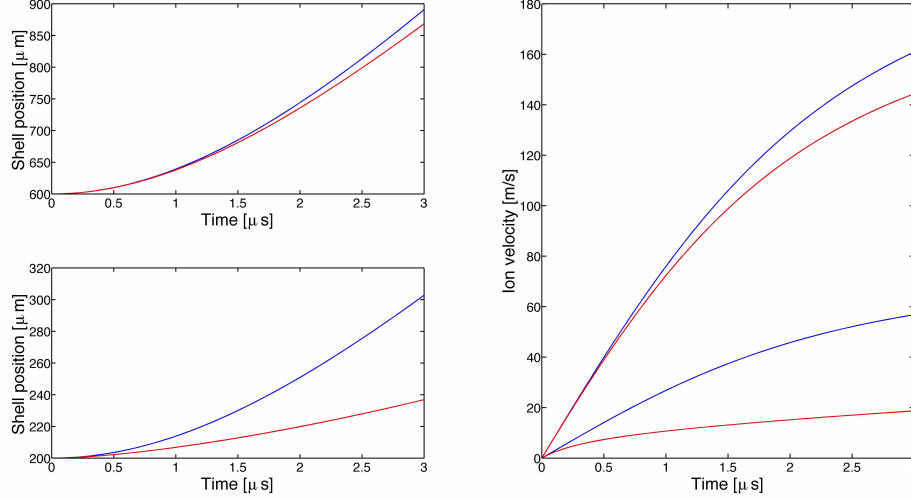
Figure 8.3: **Shell positions and shell velocities** of shells with initial radii of $1\sigma$ and $3\sigma$ with (red) and without (blue) DR in an ultracold plasma with $T_e = 20$ K plasma.

electrons released as a spherical plasma transits a perpendicular grid, the self-similar hydrodynamics of this Gaussian tail obscures the experimental observation of retarded expansion in the core, if present [70].

Figure 8.2, shows how the effect of DR diminishes substantially at higher electron temperature. Generally speaking, the rate of plasma expansion provides a reliable gauge of electron temperature, while the rate at which DR causes plasma decay depends both on electron temperature and local density. In the absence of DR, a Gaussian plasma of a given radius expands at the same rate regardless of its overall density.

**Effect of thermal velocity components of the molecular beam**

The molecular beam hydrodynamics model developed in Section 7.2 describes the intrinsic divergence of the plasma volume in $x$ and $y$ owing to the initial conditions of the molecular beam. This divergence adds slightly to the radial expansion of a spherical plasma measured in those coordinate

108

dimensions. Similarly, though the illuminated volume has no hydrodynamic divergence in the $z$ dimension, the molecules move back and forth along the axis of propagation with the residual translational temperature of the supersonic expansion, $T_\parallel$, and this affects the rate of expansion measured in $z$.
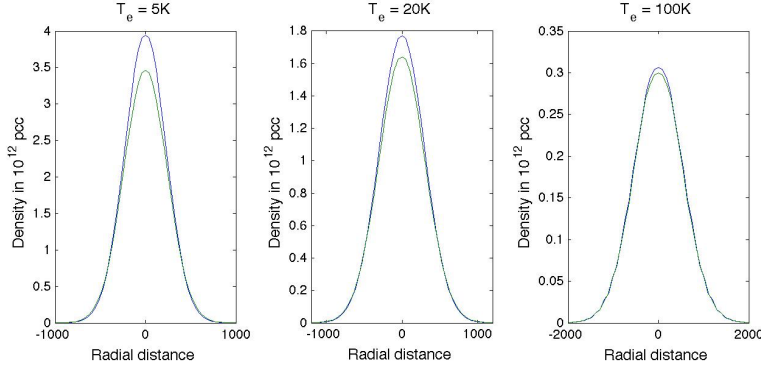


Figure 8.4: **Plasma density** along the z-axis for a spherical system without DR at time t $= 3\,\mu$s. Upper curves: without initial hydrodynamic expansion. Lower curves: with $\gamma_k(0) = 0.0193\ \mu\text{s}^{-1}$ .

Examining the plasma dimensions at an evolution time of 3 $\mu$s and at electron temperatures of 5, 20 and 100 K, I find that the plasma created with initial divergence expands just a bit faster. Figure 8.4 displays the density distributions of spherical plasmas without DR for cases that assume no initial hydrodynamic divergence, compared with plasma expansions that begin under conditions of $\gamma_k(0) = 0.0193\ \mu\text{s}^{-1}$, for $k = x, y$, and longitudinal ($z$-axis) temperature, $T_\parallel = 0.7$ K, all as described in Table 7.1. Initial divergence increases the expansion rate, but the net effect is very small. The initial values of $\gamma_k(0)$ reflect a gas temperature of 0.7 K at the point of skimming. The effect produced is barely discernible when the electron temperatures exceeds a few degrees Kelvin.

A similar situation exists if I treat the ions as an energy bath with a translational temperature determined by the temperature of the NO precursor in the beam. Any such energy must stream into expansion. However,

for large $T_e$ compared to $T_i$ resulting effect is very small. Overall, I conclude that the effect of ion thermal motion on the hydrodynamics of our molecular beam plasma are negligible for any $T_e \gg 0.7$K.

## Non-spherical expansion, including the effect of dissociative recombination

I finally consider the shell-model expansion of an ellipsoidal plasma volume with DR, compared with that of one without DR, described both by shell model and analytically. Figure 8.5 details the shell model expansion of a plasma volume that begins with $\sigma_x = 750$ $\mu$m and $\sigma_y = \sigma_z = 200$ $\mu$m and an electron temperature of 50 K, with and without DR. On the left, we see the self-similar expansion of shells at 1 and 3 $\sigma$, compared with the Vlasov description (cf. Section 8.1) of expansion in the long and short axes of the Gaussian ellipsoid.
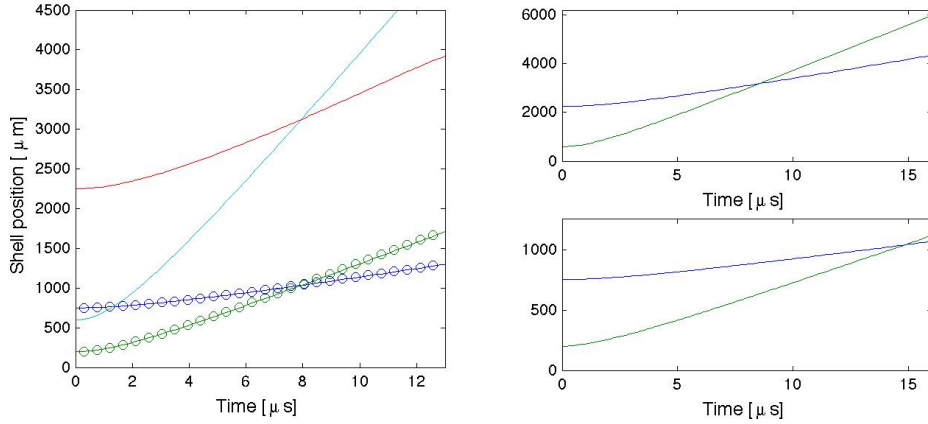


Figure 8.5: **Shell position** of 50 K electron temperature plasma with initial widths of $\sigma_x = 750$ $\mu$m and $\sigma_y = \sigma_z = 200$ $\mu$m. Left: shells with initial radii of $1\sigma$ and $3\sigma$ along $x$ and $y/z$ axes for the self-similar case. (the locus of circles underlying the shell-model result plot values obtained using Eq. (8.7)) Right bottom: evolution of $1\sigma$ shells along $x$ and $y/z$ axes for a dissociating system. Right top: evolution of $3\sigma$ shells along $x$ and $y/z$ axes for a dissociating system.

Figure 8.5 makes an important prediction. The higher density gradients along $y$ and $z$ cause more thermal energy flow into the expansion along these coordinates. In the self-similar case on the left, the Gaussian width in the short-axis coordinate directions, $y$ and $z$ overtakes that in the long-axis direction, $x$ after 8 $\mu$s. By this point, ion acceleration has ceased and the expansion has become ballistic. The plasma volume proceeds from prolate to become spherical at this point and then evolves further as an oblate ellipsoid. In the absence of DR, all shells cross this point at the same time; the expansion remains self-similar.

On the right, we see the effect of DR, which occurs mainly in the high-density core of the plasma. The flattening of the spatial distribution retards expansion in the core, and with reduced radial velocity, the shell representing a $1\sigma$ ion density becomes spherical at a much later time, $\sim$15 $\mu$s. The $3\sigma$ shell, with a spatial distribution that is much less affected by DR expands with long- and short-axis ballistic velocities much like the self-similar example.

# Part IV

# Experimental work

In Part II of my thesis, I introduced the components involved in preparing the initial state of our system under study. This discussion led to a description of the phase-space distribution function of the molecular Rydberg ensemble formed in our experimental apparatus. Chapter 7 in Part III introduced a rate equation model detailing the internal conversion of a dense Rydberg gas to plasma. Following this, Chapter 8 developed a simulation model suited to the expansion hydrodynamics of a plasma with the initial conditions of our experiment. Therein, dissociative recombination competes with ambipolar expansion to shape the charged particle distribution. Electron temperature regulates rate processes in both, plasma formation and evolution.

The application of Boltzmann's equation, as discussed in Section 4.3.1 and applied in Chapter 8, is applicable to systems with a Coulomb coupling parameter $\Gamma < 0.3$. For a charged particle density of $\rho = 1 \cdot 10^{12}$ cm$^{-3}$, a coupling of $\Gamma < 0.3$ or $\Gamma > 1$ is achieved for temperatures T>90 K and T<27 K, respectively. Based on the analysis of plasma formation in Chapter 7, we expect our system to establish initial electron and ion temperatures of $T_e^0 \approx$200 K and $T_i^0 \approx$1 K. These values yield $\Gamma_e^0 \approx 0.13$ and $\Gamma_i^0 \approx 27$. The effects of disorder-induced heating, as discussed in Section 4.3.3, have so far not been considered. DIH is expected to further limit $\Gamma_i$ to values close to one. Overall, the approximate description of our plasma system through Boltzmann's equation, represented by the shell expansion model developed in Chapter 8, seems feasible.

We are an experimental group and have studied ultracold molecular plasma in the laboratory for the past ten years. We have developed previously discussed theoretical framework and computational methods to aid us in the interpretation of our experimental results. A full conceptual understanding of our system should lead to the convergence of theory models and experimental data. So far, this has not been the case. The search for the root of this discrepancy lies at the centre of Part IV.

In the following, I will introduce our schemes of plasma detection and discuss our observations. Chapter 9 will introduce our first generation of detectors and discuss our observations of plasma evolution in 1D. Chapter 10 will introduce our new 3D tomographic imaging machine - the *PlasmaTV*. The development of this new detector has been the central task of my PhD. I have elected to split considerations in Chapters 9 and 10 with reference to our knowledge-base before and after the introduction of the PlasmaTV. This will highlight the paradigm-shift brought about by this new method of studying plasma. Chapter 11, with the title 'Arrested relaxation', will conclude my thesis. Here, I collect the findings of this thesis and speculate on future research avenues.

# Chapter 9

# Plasma detection in 1D

## 9.1 The ZEKE and moving-grid detectors

Our research group began work in the field of ultracold neutral plasmas in 2006. Our original experiments were performed with a ZEKE (Zero Electron Kinetik Energy) spectrometer with modified potentials. This apparatus is shown in Figure 9.1 and consists of three grid plates, G1 to G3, a stack of MCPs and an anode. Typical operation voltages are listed in Table 9.1.

As detailed in Part II of this thesis, we create a molecular Rydberg volume that moves within a supersonic beam expansion. Laser excitation takes place in the relatively field free region between G1 and G2. The Rydberg volume, as it travels, has a few microseconds time to evolve before reaching detection grid G2. Upon transition through G2, this volume encounters a forward-potential, typically >100 V/cm, which extracts loosely bound electrons and accelerates them towards the stack of 2.54 cm diameter MCPs. Here, impacting electrons are multiplied at a total gain of $1 \cdot 10^7$ and col-

| Element | Voltage |
|---|---|
| G1 | variable |
| G2 | grnd. |
| G3 | 100V |
| MCP front | 200V |
| MCP middle | 1200V |
| MCP back | 2200V |
| Anode | 2400V |

Table 9.1: This table details typical voltages applied to the components of the ZEKE detector - see Figure 9.1
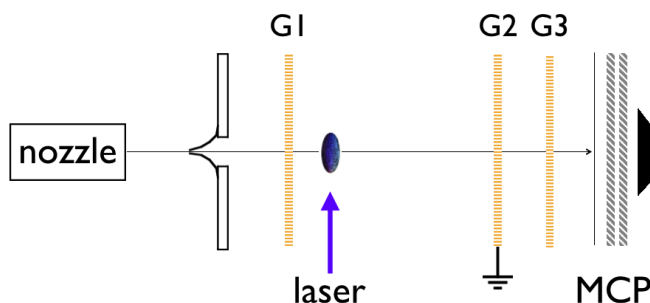
Figure 9.1: **Schematic of our 1D detection scheme -** The molecular beam enters from the left along the center-line of the detector. It passes through a fine grid plate G1. As the jet traverses the distance between plates G1 and G2, it is intersected with a nano-second laser pulse. The excited volume continues to travel with the molecular beam to reach detection grid G2. G1 and G2 are grounded, G3 holds a positive voltage. Upon transit through grid G2, the system encounters an electric field that accelerates negatively charged particles towards a MCP detector. The charge impact is amplified and read out via a detector anode.

lected at the anode. A capacitive output coupler monitors the supply of voltage to the anode and allows us to view time-resolved charge impact as an oscilloscope trace. Transit time of our excited volume through G2 is on the order of one microsecond. For the purpose of our experiments, electron extraction and detection are instantaneous.

In 2009, we introduced a new detector that has since been at the centre of our experimental work.[14] This detector is based on the ZEKE spectrometer with the added feature, that the plane of detection can move up and down the streamline of the molecular beam. This is achieved by means of a bellows-isolated linear actuator driven by an animatics integrated SM23165D Smart Motor. The detector assembly travels on 1/2 inch mounting rods via linear bearings along a range of $\sim$ 10 cm. By moving the

---

[14]Design and construction of this new detector was spearheaded by Chis Rennick, at the time a post-doctoral fellow in our group. A more complete account of the design and operation of ZEKE and moving-grid detectors can be found in [26, 49].
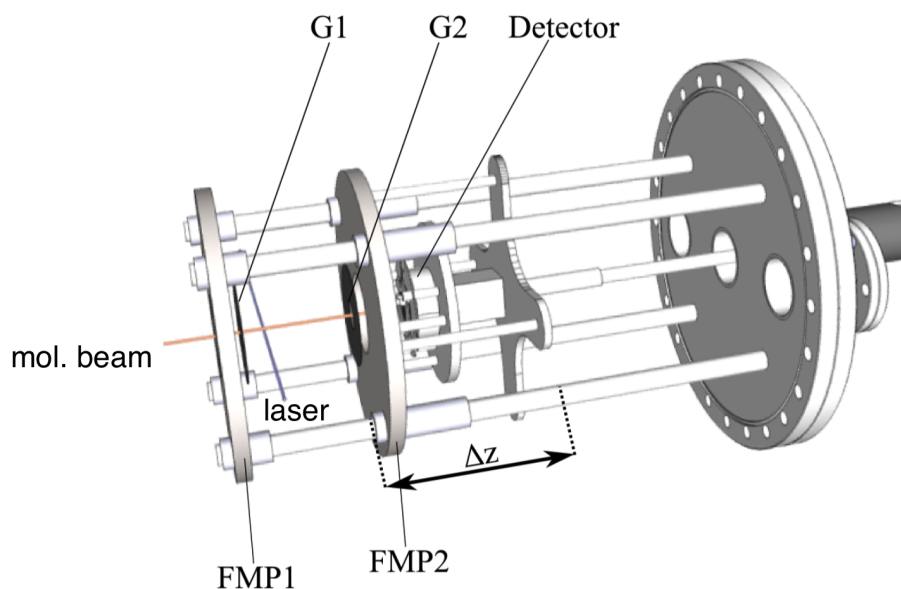
Figure 9.2: **E-drawing of the moving-grid detector -** The detector is mounted on the 10" diameter backflange of our vacuum chamber. FMP1 and FMP2 represent front-mounting plate 1 and 2, respectively. Detection is analogous to the ZEKE scheme in Figure 9.1. The entire detection carriage, including G2, FMP2, MCPs and anode can be translated along the z-dimension, thus varying the time after which the laser excited volume transits detection grid G2.

detector up and down the molecular jet streamline, we vary the duration over which the excited volume can evolve prior to detection at G2.

## 9.2 Observations and discussion

Over the following pages, I will discuss key observations through use of our 1D detection systems.

### 9.2.1 Rydberg spectrum

As discussed in Chapter 6.2, we prepare a cigar-shaped Rydberg volume, moving with the velocity of our molecular beam. The experiment is prepared according to Part II, yielding initial conditions stated in Table 6.2. The detector voltages conform with table 9.1, with grid G1 on ground.

Nitric oxide spectroscopy was reviewed in Chapter 2. We populate NO quantum-states near the ionization continuum through double-resonant laser excitation. When calibrating our laser system, we first set $\omega_2$ to $\sim 321\ nm$ and $\omega_1$ to $\sim 226\ nm$. One $\omega_1$ and one $\omega_2$ photon combined are energetic enough to ionize the NO ground state. We ensure that neither of the two laser beams in itself is able to multi-photon-ionize our sample by observing the detector response as we vary the intensity of one laser while the other is blocked. Following this, we scan for the desired intermediate transition between rotational ground state and rovibronic excited state by 1+1' resonance enhanced multi photon ionization (REMPI) signal analysis with $\omega_1$.[15] Excitation, by means of an intermediate state, boosts the creation of ions and we obtain a transition spectrum between the $X^2\Pi_{1/2}$ ground state and the $A^2\Sigma^+$ first excited state of NO. We apply a small forward bias between the plate G1 and grid G2 to collect the liberated electrons.

We tune to the pQ$_{11}$(1/2)-line, representing the transition between the lowest rovibronic level of the NO ground state and the lowest rovibronic level of the A-state, to select $A^2\Sigma^+$ ($\nu' = 0\ K' = 0\ J' = 1/2$) as the intermediate state of the excitation process.

With $\omega_1$ fixed to populate this state, we next reduce the $\omega_2$-photon energy below the ionization potential, replace the forward bias between G1 and G2 with a reverse bias of $\sim 500$ mV/cm and scan $\omega_2$ for a Rydberg resonances.

A typical resonance signal, as we observe it on the oscilloscope, is displayed in Figure 9.3. We see an electron prompt peak after $\sim 250$ ns, originating from Penning ionized electrons that leave the illuminated volume

---

[15]This was displayed in Figure 5.5.
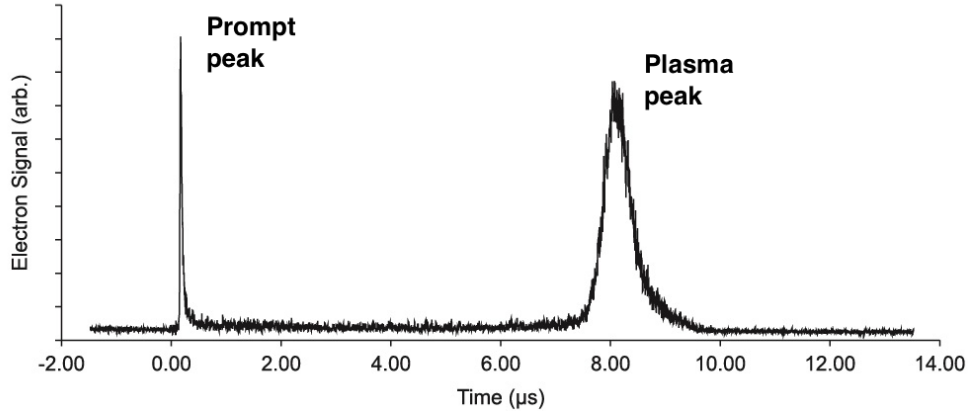
Figure 9.3: **Typical plasma signal observed by ZEKE or moving-grid detector** - Laser excitation take place in the field-free region between grids G1 and G2. We excite to $n_0$=50. The first peak at $\sim 200$ ns represents prompt electrons that are created during the plasma formation process. The second peak at $\sim 8$ $\mu$s gauges the charge density and the spatial dimensions of the plasma volume as it traverses grid G2.

shortly after the process of laser excitation (cf. Chapter 7). These prompt electrons leave a small charge imbalance behind. In a first-order model, this imbalance traps the remaining electrons and forces them to travel with the slow ionic volume. We observe an impact signal that is measured as the illuminated volume transits G2, $\sim 8$ $\mu$s after excitation. At this point, the quasi-free electrons are extracted by the electric field between G2 and G3 and accelerated towards the MCP.

Having obtained a signal, we integrate over the plasma peak (second peak) as we scan our Rydberg state distribution ($\omega_2$-scan). This is shown in Figure 9.4. We average ten shots before taking a step of 0.001 nm in $\omega_2$-wavelength. The x-scale is vacuum-corrected. We record the peak positions of the Rydberg series. Least-square fit of the Rydberg formula (Eq. 3.3 for a series of PQNs) to the measured series allows us to assign IP and quantum defect to the series as well as the principal quantum number to each peak.

119
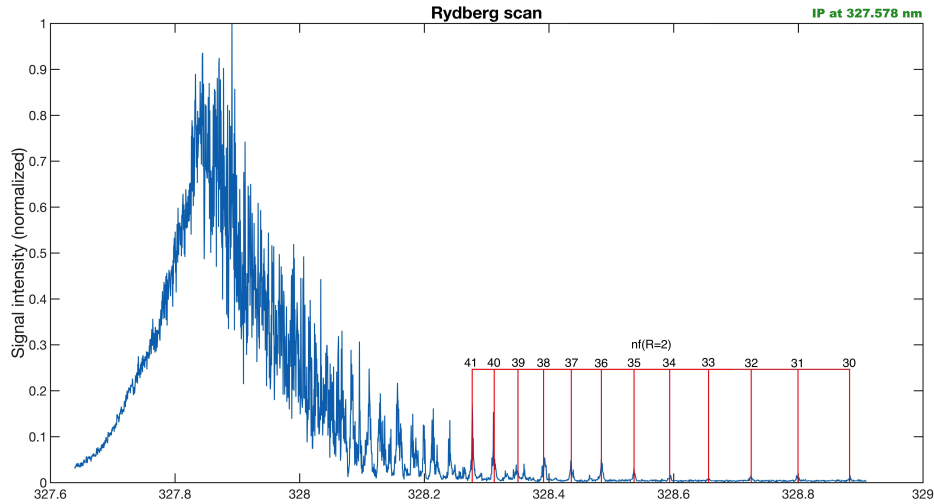
Figure 9.4: **Resonance in the plasma signal observed scanning** $\omega_2$ - The (late peak) plasma signal is averaged over one second and then integrated to yield an intensity measure. This signal is recorded as $\omega_2$ is scanned with a step-size of 0.001 nm. The assigned peaks correspond to the $nf$-Rydberg series which converges to the rotational level, $N^+ = 2$, in the $^1\Sigma^+$ vibrational ground state of $NO^+$. The ionization potential is expected to be at $\sim 327.58$ nm.

**Discussion**

There are two curiosities found in the data displayed in Figure 9.4: First: The observed Rydberg spectrum is toward higher wavelength dominated by one series. The extrapolated ionization potential of this series confirms with the $N^+ = 2$ rotational level of the $^1\Sigma^+$ vibrational ground state of $NO^+$. Second: Toward lower wavelength, the signal response rises, reflecting an increase in state density, combined with more efficient avalanche to plasma, moderated by a declining electronic transition moment. The resonance peaks at wavelength $\omega_2$=327.85 nm, which lies $\sim$0.3 nm below the IP in photon energy space. The signal decays quickly for higher energies.

The shape of our spectrum is by no means obvious and we have only recently understood the underlying dynamics. I will delay their discussion until Chapter 10.

A discussion of the dominance in $f$-series requires further spectroscopic considerations. As discussed in Chapter 2, Rydberg states conform with Hund's case (d). The A-state is Hund's case (b). In both states, K, the total angular momentum apart from spin, is a good quantum number and selection rule,

$$\Delta K = 0, \pm 1,$$

applies. For any dipole-transitions, the selection rule $\Delta J = 0, \pm 1$ holds rigorously. The total angular momentum of the A-state is $J = K + S = 0 + 1/2 = 1/2$. The transition $K{=}0 \longrightarrow K{=}0$ is forbidden because of selection rule $\Delta S{=}0$ and the fact that the absorption of one photon must change the angular momentum by one unit of $\hbar$. Thus, the populated Rydberg state must have values $J = 3/2$ or $1/2$, $K{=}1$ and $S{=}1/2$. Table 9.2 lists possible combinations of angular momentum coupling for accessible Rydberg states.

Selection rules alone cannot explain the dominance of the $f$-wave in Figure 9.4. The reason is two-fold: Dixit et. al. [22] have conducted a theoretical study of the rotational branching ratios in the resonance-enhanced multiphoton ionization of NO via the A-state. The valence electron of the A-state, due to interactions with the non-spherical molecular potential, is not excited into a p-wave, as expected for the atomic case, but into a state of coupled $\ell$-waves. Their results show that $p$- and $f$-waves dominate in this coupled state based on shape-resonance.

A look at Table 9.2 reveals that $p$-waves approach $NO^+$ in either $R{=}0$ or $R{=}2$ core states. $f$-waves approach $NO^+$ in Rydberg molecule core states $R{=}2$ or $4$.[16] Performing pulsed field ionization experiments in a similar setup to ours, Vrakking and Lee [87] found that the dominante Rydberg series in

---

[16]Note, that the Rydberg system is described in Hund's case d), the ion, however, in Hund's case b). In accordance with Herzberg's notation, I will refer to the molecular core rotation with variable $R$ for the Rydberg system and variable $N$ for the ion.

Table 9.2: Possible angular momentum coupling for Rydberg states populated from the ground rovibronic level of the NO A-state.

| $J$ | $=$ | $R$ | $+$ | $L$ | $+$ | $S$ | character |
|-----|-----|-----|-----|-----|-----|-----|-----------|
| 1/2 | | 1 | | 0 | | -1/2 | $s$-wave |
| 1/2 | | 0 | | 1 | | -1/2 | $p$-wave |
| 1/2 | | 2 | | -1 | | -1/2 | $p$-wave |
| 1/2 | | -1 | | 2 | | -1/2 | $d$-wave |
| 1/2 | | 3 | | -2 | | -1/2 | $d$-wave |
| 1/2 | | -2 | | 3 | | -1/2 | $f$-wave |
| 1/2 | | 4 | | -3 | | -1/2 | $f$-wave |
| 1/2 | | -3 | | 4 | | -1/2 | $g$-wave |
| 1/2 | | 5 | | -4 | | -1/2 | $g$-wave |
| | | | | -etc- | | | |
| 3/2 | | 1 | | 0 | | +1/2 | $s$-wave |
| 3/2 | | 0 | | 1 | | +1/2 | $p$-wave |
| 3/2 | | 2 | | -1 | | +1/2 | $p$-wave |
| 3/2 | | -1 | | 2 | | +1/2 | $d$-wave |
| 3/2 | | 3 | | -2 | | +1/2 | $d$-wave |
| 3/2 | | -2 | | 3 | | +1/2 | $f$-wave |
| 3/2 | | 4 | | -3 | | +1/2 | $f$-wave |
| 3/2 | | -3 | | 4 | | +1/2 | $g$-wave |
| 3/2 | | 5 | | -4 | | +1/2 | $g$-wave |
| 3/2 | | -4 | | 5 | | +1/2 | $h$-wave |
| | | | | -etc- | | | |

NO (excited from the A-state) are $np(R = 0)$, converging to 30,522.443 cm$^{-1}$, and $nf(R = 2)$, converging to 30,534.394 cm$^{-1}$. Their results agree well with our findings.

The $p$-series only begins to emerge for energies higher $36f(R = 2)$. As discussed in Chapter 7, internal conversion of Rydberg gas to plasma takes several nanoseconds. For long wavelengths, collisional cross-sections of Rydberg molecules become small and conversion to plasma takes longer. But the lifetimes of the $\ell$-waves are very short for states $\ell < 3$. For example, before the onset of $\ell$-mixing, states excited to $n$=50 have lifetimes $\tau_{50}^s = 1.36$ ns, $\tau_{50}^p = 0.41$ ns, $\tau_{50}^d = 0.56$ ns and $\tau_{50}^f = 15.8$ ns (cf. Table 3.2). This explains

the absence of the *p*-series for longer wavelength.

### 9.2.2 Plasma formation

The operation principle of our detector can make it hard for us to differ between the signal response of a plasma transiting G2, from that of a Rydberg volume. In the case of a plasma, electrons bound by the ionic space charge are extracted by the field between G2 and G3 and swept into the detector. In the case of the Rydberg gas, and for sufficiently strong voltage on G3, field-ionization removes electrons upon transit through G2 and sweeps them into the detector. The effective signal is similar.

There are two indicators in Figure 9.3 which lead us to believe that we are indeed observing a plasma: 1) The prompt peak appearance is unjustified in case of a Rydberg gas. 2) The lifetime of $\sim$8 $\mu$s is unjustified for a Rydberg gas prepared at $n <$100 (see Section 3.2). In the following, I will discuss an experiment which serves as further proof of concept for plasma formation as discussed in Chapter 7.

Figure 9.5 displays the electron signal as a function of electric field obtained by applying a voltage ramp in between grids G1 and G2. Our Rydberg gas was prepared in the following way: Laser $\omega_1$ has $\sim 8$ $\mu$J power and we determined for this dataset a FWHM of 2.57 mm via razor-blade-tomography (Gaussian width of $\sigma_{\omega_1} = 1.1$ mm (no teslescope on $\omega_1$)). For the measurement we closed an iris on $\omega_1$ to a diameter of 1.7 mm, only allowing the maximum intensity through. This created a cylinder of A-state molecules in the molecular beam with only one dimension (x-axis) being Gaussian and the other two dimension approximately constant in density. Based on the laser width and power, I calculate an A-state peak density of $3.11 \cdot 10^{12}$ cm$^{-3}$ (cf. Chapter 6.1).

Laser $\omega_2$ has $\sim 2$ mJ power and a FWHM of $\sim 3$ mm, much larger than $\omega_1$. We allow for a 200 ns delay between lasers $\omega_1$ and $\omega_2$ (approximate NO life-time) to reduce the Rydberg gas density by a factor of $\sim$1/e [40]. Assuming saturation of $\omega_2$, we expect to populate a Rydberg state peak

density of $5.7 \cdot 10^{11}$ cm$^{-3}$ (or mean density of $\sim 2.6 \cdot 10^{11}$ cm$^{-3}$).[17]

$\omega_2$ is tuned to prepare this Rydberg ensemble in state $50f(R = 2)$. We observe the system response to a 3 kV field ramp (forward-bias detection of electrons). The first 1/3 of the ramp is approximately linear and reaches 1 kV after $\sim$500 ns. The distance between G1 and G2 is set to $\sim$4.55 cm using the moving-grid detector. Figure 9.5 shows the response of the illuminated volume to the linear ramp from field-strength 0 to 200 V/cm. The six different figures represent delays in the application of the field of 10, 200, 400, ..., 1000 ns (accuracy $\sim \pm 10$ ns). Each (time-delay) figure compiles 3000 single-measurements, sorted vertically in the post-data-analysis by total electron yield.

**Discussion**

The first thing we notice in viewing Figure 9.5 is a variation in response despite constant experimental conditions. This is caused by the interplay between molecular beam and lasers, which prepares the Rydberg ensemble in each measurement with slight variations in shape and density. Denser systems have a higher electron yield. Our sorting of the 3000 measurements by electron yield creates a contour-plot with increasing density along the y-axis. I assume that the densities in Figure 9.5 are distributed around a mean value. The horizontal traces displayed near the middle of the y-axis should correspond closely to this mean. I refrain from labeling this axis as I expect a non-linear spread around the mean density.

Our analysis of this data is straightforward. Electrons pulled off the illuminated volume at low field strength indicate the presence of a weakly-bound plasma surface-charge. Electron signal at higher fields represents field ionization of Rydberg states.

---

[17]In a Gaussian distribution, 50% of particles sit within a distance of $1.26\sigma$ from the centre. At this distance, the density has a value of $\sim$0.45 times the peak density.
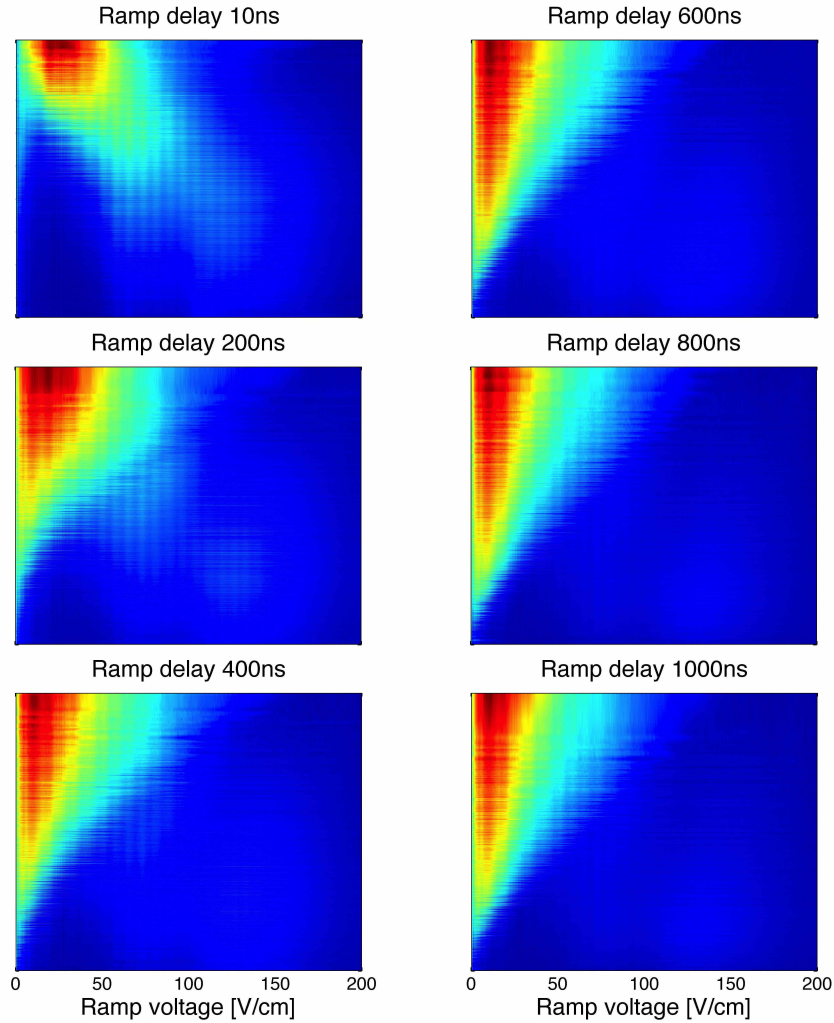
Figure 9.5: **Field ionization by a linear voltage ramp** - Our Rydberg ensemble is prepared at $n_0$=50. We measure the system response to a linear voltage ramp (forward-bias for electrons) between G1 and G2. The field is raised from 0 to $\sim$200 V/cm in $\sim$400 ns. Each figure displays 3000 single-measurements in a contour plot, sorted according to total electron yield. The application of the ramp is systematically delayed by steps of $\sim$200 ns. Overall, we observe the transition of Rydberg gas to plasma.

Our measurements at 10 ns ramp-delay displays two distinct Rydberg features with an onset near ramp voltages E≈62 V/cm and E≈114 V/cm. Based on the discussion in the last section, we expect to predominantly excite Rydberg states in the $np(R = 0)$- and $nf(R = 2)$-series. A quick spectroscopic calculation shows that our $\omega_2$-photons which populate Rydberg state $50f(R = 2)$ also populate $59p(R = 0)$. $E$=114 V/cm conforms with the minimum field necessary to diabatically ionize $50f$-Rydberg states to NO$^+(N = 2)$. Here, I used the following relation:

$$4.12 \cdot \sqrt{E} = \frac{Ry}{(n - \delta_l)^2} \tag{9.1}$$

Eq. 9.1 derives from Eq. 3.16. The factor 4.12 is a fitted parameter and replaces the hydrogenic factor 4.59 from Eq. 3.16 [26]. $E$ is in V/cm and $Ry$=109737.3 cm$^{-1}$. $E$=62 V/cm confirms with the field necessary to ionize the $59p$-state approaching NO$^+(N = 0)$.

In studying this data at a 10 ns ramp-delay, we note that for a fraction of runs ($\sim$ 20%), clear plasma character can already be observed. As we increase the delay between $\omega_2$ and application of the ramp, the transition from Rydberg to plasma moves down the y-axis to lower densities. Overall, this behaviour agrees very well with our plasma rise-time model for a spread of initial densities, as discussed in Chapter 7. The data clearly displays the transition of a Rydberg gas to plasma.

I wish to derive an estimate of the initial Rydberg densities in this data. In other words, at which time-delay display ramp-traces at medium y-axis hight (mean of density distribution) over 50% plasma characteristics. While these traces show clear Rydberg character for an early ramp, a very crude visual analysis shows that plasma character becomes dominant after $\sim$200 ns.

Let's compare this value to a theoretical prediction. Applying the computational model from Chapter 7, I find that $t_{rise}$ ≈200 ns for $n_0$=50 confirms with a mean density of $\rho_0^{Ry} = 5 \cdot 10^{10}$ cm$^{-3}$ (or peak density of $\sim 1 \cdot 10^{11}$

cm$^{-3}$).

Traces in the high-density region of the data appear to have transformed to plasma on the nanosecond timescale. This is typical for initial Rydberg densities of $\sim 1 \cdot 10^{12}$ cm$^{-3}$. Overall, I estimate that the data displayed in Figure 9.5 is spread over two orders of magnitude in peak density from $\sim 1 \cdot 10^{10}$ cm$^{-3}$ to $\sim 1 \cdot 10^{12}$ cm$^{-3}$ with a mean at $\sim 1 \cdot 10^{11}$ cm$^{-3}$. For typical measurements with coincident laser excitation, i.e. no dealy between $\omega_1$ and $\omega_2$, I expect values multiplied by the Euler factor.

Another approach for analyzing this data-set is displayed in Figure 9.6. Here, I compute the total signal of each of the 3000 traces for each of the 6 time-delays. I sort the resulting totals into bins and display the evolution of signal distribution over time-steps 10, 200, 400, ..., 1000 ns. The blue curve in Figure 9.6 (10 ns-delay) shows an approximately normal distribution skewed slightly to lower total electron signal. One can understand this in the following way: For each run, our experiment prepares a Rydberg volume with a density sampled from a distribution with a mean and a spread. The interplay of molecular beam and lasers are responsible for this shot-to-shot variation. Even during the population of Rydberg states through $\omega_2$, higher order processes begin to take place. Penning ionization, dissociative recombination and electron-Rydberg collisions are second order processes in density and constitute a loss-mechanism for signal electrons. At a given $\omega_1 - \omega_2$ delay, Rydberg systems formed at higher density sustain higher-rate second and third-order loss processes. These processes deplete the fraction of traces with large total signal, yielding the observed skew of the distribution to lower total signal.

Overall, the ramp-field delay data discussed in this section agrees very well with the theoretical concepts developed in Chapter 7.
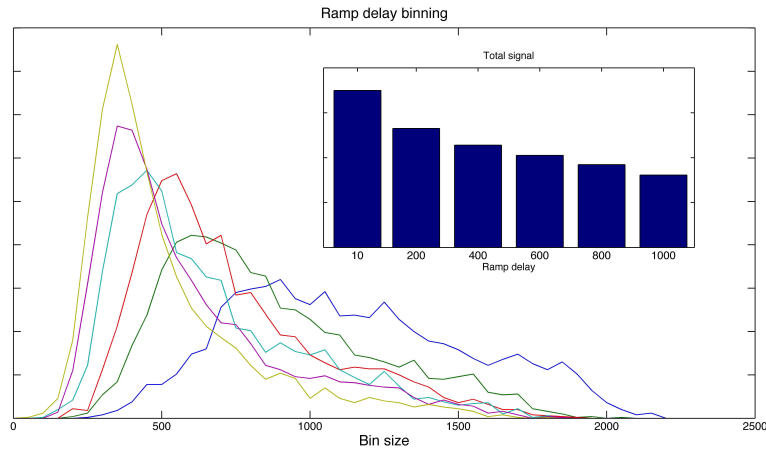
Figure 9.6: **Summation and binning of ramp-delay data** - Each curve represents one of the ramp delays. I integrate over each of the 3000 oscilloscope traces and sort the resulting total into bins. The 10ns-delay data (blue) appears closest to a normal distribution while 200, 400, ..., 1000 ns delays (green, red, ..., yellow) move progressively closer to low count. This progression illustrates the second-order plasma decay due to DR. The top-right corner bar plot illustrates the total loss of signal over the first microsecond evolution.

Moving-grid detector data set (n=50)
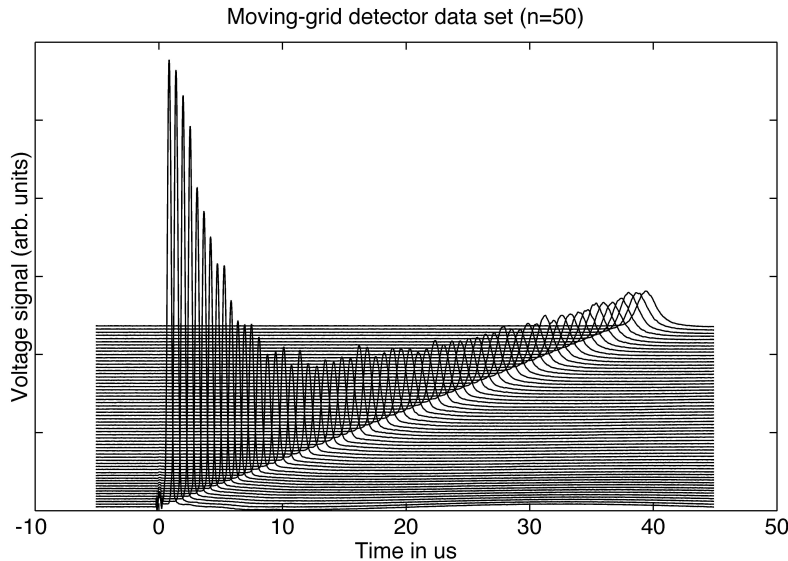


Figure 9.7: **Evolution of the plasma peak -** Plasma waveform captured by the moving-grid detector as a function of flight time. The system is prepared in the $n_0$=50 Rydberg state. G1 holds a +2V positive charge to deflect the prompt peak (line at $t$=0). The different traces are vertically offset for better clarity. The Figure shows how the plasma expand and decay, as it evolves in time.

### 9.2.3   Plasma expansion and decay in 1D

So far, our discussion was restricted to experiments with a fixed distance between the point of laser excitation and the detection grid G2. In the following, I will introduce a dataset won through use of the moving-grid detector.

The experiment is once more prepared according in initial conditions in Table 6.2. The detector voltages conform with Table 9.1, with a potential of +1.2 V on grid G1. $\omega_2$ is fixed to populate the $n$=50 Rydberg level. The created plasma is now characterized by the shape of the plasma peak. We are interested in the change of its shape, as the plasma evolves in time.

We bring our movable detector close to the region of illumination and start a scan in which only the detector position, relative to the region of

plasma formation, is varied. Figure 9.7 displays the change of the plasma signal as the detector is moved along the stream line of the molecular beam. This allows the plasma an evolution timespan between $\sim 1.5$ $\mu s$ and $\sim 40$ $\mu s$. The separate signal traces are averaged over 10 shots and have been vertically offset for clarity. The small positive voltage on G1 reduces the prompt peak, as initial electrons are pulled away from the detector.

**Discussion**

Two immediate observations can be drawn from Figure 9.7: (1) As the plasma evolves in time, it decays as indicated by the decline in plasma peak amplitude. (2) During its evolution, the plasma expands as indicated by the increase in signal width.

A closer study of the data reveals that the individual traces agree remarkably well with Gaussian waveforms:

$$I_{I_0,\sigma}(z) = I_0 \cdot exp\left(-\frac{z^2}{2\sigma^2}\right) \tag{9.2}$$

To aid the characterization of this data, I fit Eq. 9.2 to the signal traces and extract fitting parameters $I_0$ and $\sigma$. The relative area of the plasma signal is $A = \sqrt{2\pi}I_0\sigma$. I obtain 95% confidence bounds for $I_0$ and $\sigma$ through my fitting routine. The error of area A is obtained using error propagation. The results of this characterization is displayed in Figure 9.8.

Our data displays the broadening of the plasma to five times it's initial z-width over 40 $\mu$s evolution. The evolution can be separated into two regions, before and after the $\sim$10 $\mu$s mark. As discussed in Chapters 4, 7 and 8, our plasma forms from a dense Rydberg gas via internal conversion on a nanosecond timescale. In its initial state, the electrons carry almost all the kinetic energy of the system. In their attempt to leave the plasma, they pull on the ions and thus transfer energy into the radial motion of the ions. This mechanism is called ambiploar expansion and continues until the
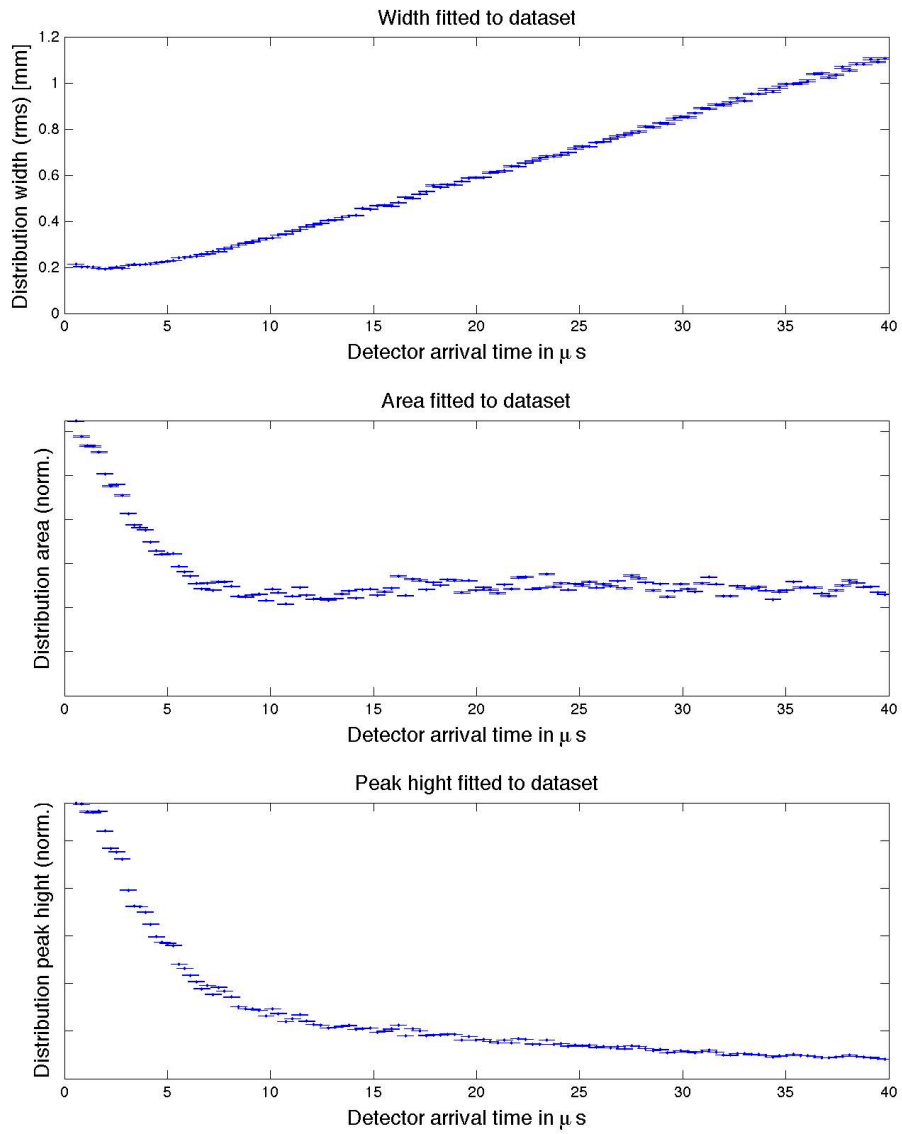
Figure 9.8: **Plasma evolution characterized through Gaussian fits - We** characterize our dataset through Gaussian fitting parameter: width $\sigma$ (top), area A (middle), peak hight $I_0$ (bottom). Displayed error bars represent 95% confidence bounds.

system kinetic energy is almost entirely captured within the radial motion of ions. The top graph in Figure 9.8 shows the acceleration of ions typical for ambipolar expansion. After $\sim$10 $\mu$s, the acceleration stops and the expansion becomes ballistic. In our data, we observe the decrease of the distribution peak hight to become linear as well as a levelling out of the distribution area around this point.

**The self-similar Vlasov picture**

Next, I will conduct a comparative study of theory and experimental results. I wish to compare our experimental observations with simulation results based on the formalism developed in Part III in order to draw some important conclusions.

I begin by comparing our experimental data to a non-dissociating plasma expansion in the self-similar Vlasov picture, as given by Eqs. 8.7. I use initial conditions from Table 7.1, leaving the electron temperature as a loose fitting parameter in order to reproduce our data. This is done in Figure 9.9. I find that our experimental expansion curve is closely reproduced by setting the initial electron temperature to $T_e(0){=}1.9$ K. This is in strong contrast to our expected temperature value, $T_e(0) \approx$200 K, which was based on molecular dynamics calculation (see Section 7.2).

The observation of this unexpectedly slow expansion of beam plasma reaches as far back as our first experiments. Our search for the root of this dramatic mismatch between theory prediction and experimental observation has been going on for many years. MOT plasmas do not seem to exhibit this behaviour, leading us to suspect that the molecular nature of our system might be the root of the very slow expansion. The primary characteristic of molecular compared to atomic plasma is dissociative recombination. I developed the expansion model discussed in Section 8.2 in order to allow for a direct comparison between molecular plasma theory and our experimental data.
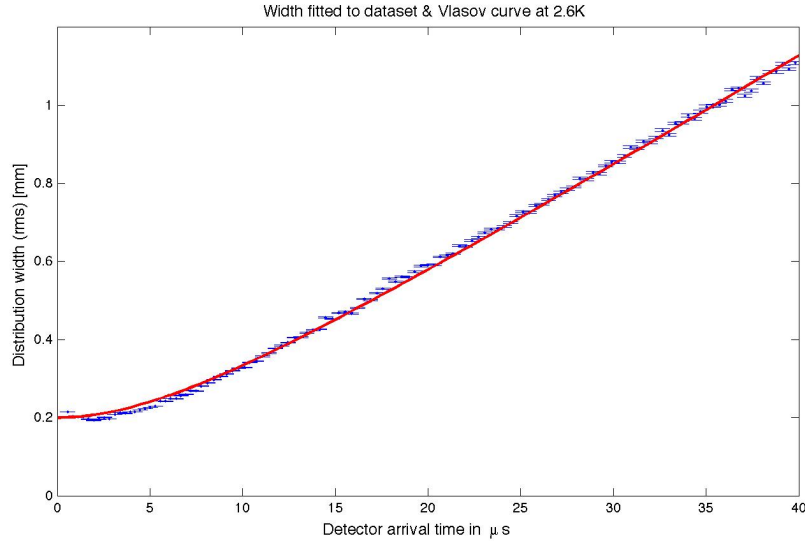
Figure 9.9: **Comparison of experiment and simulation results:** experimental data points as in Figure9.8; self-similar non-spherical Vlasov curve (cf. Eq. (8.7)) for initial conditions from table 7.1 and 1.9 K electron temperature.

## Plasma expansion under the influence of dissociative recombination

I wish to compare simulation results from my dissociating shell model to our experimental data curve. To do so, I first need to take a closer look at the method by which our detector collects plasma information. One weakness of our current detection scheme is that our detector only extracts relative charged particle density measurements along the z-dimension while it integrates over x and y (cf. Figure 9.10). This represents a loss of information and complicates comparison between data and simulation.

I can illustrate this effect by asking, what response a plasma sphere of constant density, sent through our detector, would create. This sphere is
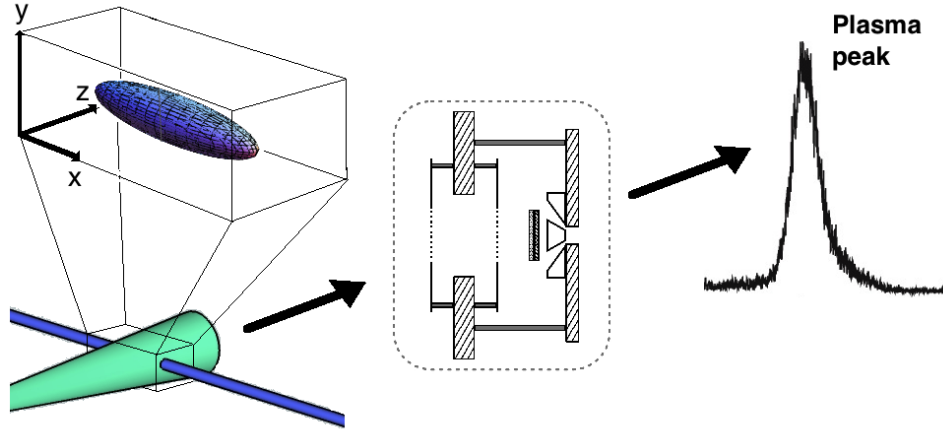
Figure 9.10: **Our detection scheme:** As our plasma volume transits the detection grid, a forward bias extracts electrons and accelerates them onto the MCP. Our oscilloscope trace, as collected by a metal anode, is one-dimensional and represents the flow of electrons through the x-y-plane at the detector entrance grid.

defined as:

$$\rho(r) = \begin{cases} \rho_0 & \text{for r} \leq 1 \\ 0 & \text{for r} > 1 \end{cases} \tag{9.3}$$

As this sphere passes into our detector, the entrance grid works as a sampler of charge. For a unitary density sphere, the obtained signal at any point in time is given by the convolution of sphere and grid. As seen in Figure 9.11, this is a circle area with radius $R = \sqrt{1 - z^2}$, z being the distance from the centre of the plasma. The response of the detector is now given by

$$Response \propto \rho_0 \pi \times R^2 = \rho_0 \pi \times (1 - z^2) \tag{9.4}$$

This example illustrates how a spherical object of unitary density is turned into a quadratic signal and helps us understand our detector response. Above, I compared our experimental data to a self-similar expansion. In this, I took advantage of the fact that we measure along a symmetry axis
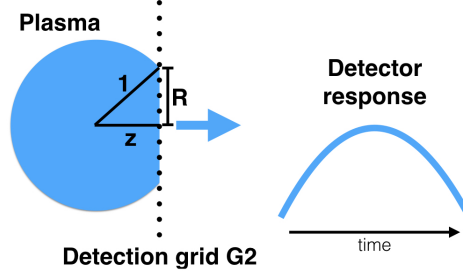
Figure 9.11: **Detector response to a unitary plasma sphere**

and that a Gaussian density distribution, integrated over two dimensions, remains Gaussian. This is not the case for a dissociating plasma.

To obtain a means to compare and draw conclusions from calculations, I simulate our detector response for 3D shell model data in a way comparable to the unitary density sphere example. The output of my 3D shell model simulation yields shell densities $\rho_j(t)$, shell positions $R_{k,j}(t)$, shell velocities $u_{k,j}(t)$ and electron temperature $T_e(t)$ for shells $j$ at time-step $t$ and along dimension $k = x, y, z$.

I select a single time-step $t$ and fit a 'SmoothingSpline' to density over shell positions to reconstruct full density information for our charged particle distribution. Next, I define segments of equal distance, $Z_{1,..,m,..,M}$ starting at $Z_1 = 0$, along the positive z-axis (for an ellipsoidal centred coordinate system). I compute $\rho(Z_m)$ and subsequently find $X_m$ and $Y_m$ for which $\rho(X_m) = \rho(Y_m) = \rho(Z_m)$. This defines a new shell system of arbitrary exactness.

The $Z_m$'s will serve me as bins for a particle count. Bin $m$ is defined to sit in between two planes, both parallel to the x-y-plane, at position $Z_m$ and $Z_{m+1}$. I want to count the particles within each bin to reconstruct our detector response. My $m$ shell surfaces are now defined as:

$$\frac{x^2}{X_m^2} + \frac{y^2}{Y_m^2} + \frac{z^2}{Z_m^2} = 1 \tag{9.5}$$

135

I want to find the intercept of my shells with the planes at positions $Z_m$. I select a single $m$ and find the intercept of shells $n = m + 1, .., M$ as ellipses given through:

$$\frac{x^2}{X_n^2} + \frac{y^2}{Y_n^2} = 1 - \frac{Z_m^2}{Z_n^2} \tag{9.6}$$

The individual ellipses are fully defined through their major and minor radii:

$$x_{m,n} = \sqrt{X_n^2 \cdot \left(1 - \frac{Z_m^2}{Z_n^2}\right)} \tag{9.7}$$

$$y_{m,n} = \sqrt{Y_n^2 \cdot \left(1 - \frac{Z_m^2}{Z_n^2}\right)} \tag{9.8}$$

I can now construct the area between two consecutive ellipses as

$$A_{m,n} = \pi \cdot (x_{m,n} \cdot y_{m,n} - x_{m,n-1} \cdot y_{m,n-1}), \tag{9.9}$$

from which I calculate the the number of particles within bin $m$ as

$$N_m = \sum_n A_{m,n} \cdot \rho(Z_n) \cdot \Delta, \tag{9.10}$$

where $\Delta$ is the bin width, i.e. the distance between $Z_m$ and $Z_{m+1}$. Completing this process for all bins results in a half peak, which when mirrored, represents the response of our detector to a system obtained by the 3D shell model.

I now apply my detector simulation formalism to 3D shell model data and compare the result to experimental data. In a first step, I consider the first $\sim 1$ $\mu$s of evolution of a 2 K electron temperature dissociating plasma prepared at a peak density of $\rho = 6 \cdot 10^{12}$ cm$^{-3}$.[18] Figure 9.12 displays the density distribution along z for my dissociating shell model plasma for four

---

[18]This density conforms with the theory prediction from Chapter 7. As seen in Subsection 9.2.2, indirect plasma density measurements fall short of this value by an order of magnitude. Nonetheless, I will begin my discussion with the case of a high-density plasma to draw some important conclusions.

time steps in the early evolution of the system. I have chosen a time at which expansion is still at an acceleration state while DR is highly dominant in the core of the plasma. Dissociation is proportional to $\rho^2$ and $T_e^{-1/2}$ (cf. Eqs. 8.12 and 8.19). One can see how the initially Gaussian distribution flattens at the peak and evolves away from the Gaussian form. The flattening of the peaks is accompanied by a fall in peak density from initially $\sim 6 \cdot 10^{12}$ cm$^{-3}$ down to $\sim 0.2 \cdot 10^{12}$ cm$^{-3}$ within the first $1\mu$s. The lower graphs in Figure
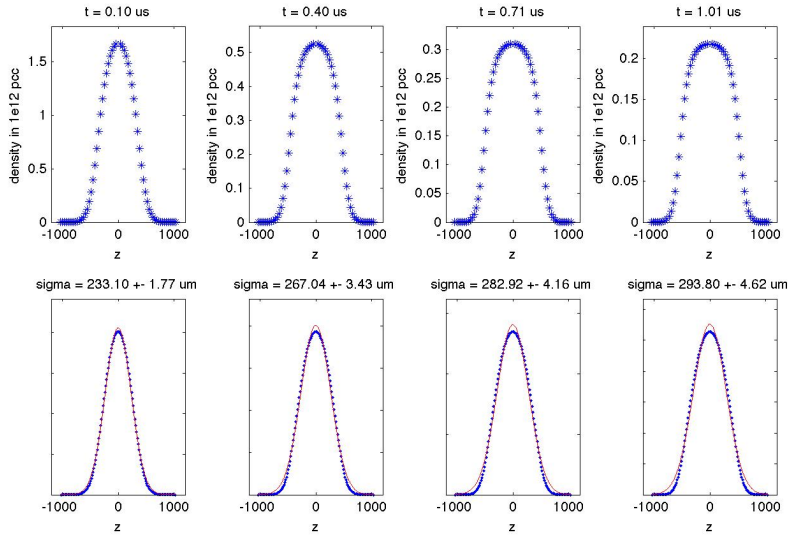


Figure 9.12: **Density evolution and corresponding detector response over the first $\mu$s:** I have simulated our system using my shell model formalism and initial condition based on Table 7.1. The initial electron temperature was set to 2 K. Above figures show the evolution in charged particle density along z. Figures below correspond to the expected detector response (Gaussian fits included).

9.12 represent the traces I would expect to see on the oscilloscope, if plasmas as simulated by the shell model formalism would pass into our detector. One can observe that the flat distribution heads vanish as the detector model integrates simulated plasma slices over x and y. There is a simple explanation to this as illustrated on a spherical shell plasma undergoing DR: the flat-

137

tening of the density distribution is due to the $\rho^2$-dependence of dissociative recombination. As it turns out, the part of the plasma most affected by DR lies within the $1\sigma$ radius of the density distribution but contains less than 20% of the total particle number. The plasma wings, however, remain near-Gaussian and constitute the bulk of charges. Our method of detection integrates over plasma slices and we are unable to discern core-dissociation without further tools.

I fit Gaussian curves to my simulated detector response in order to make these DR effects more visible. One can note in particular, that the plasma width grows over the first 1 $\mu$s in steps of 34, 15, 11 $\mu$m, i.e. apparent growth slows down. This is counterintuitive as one would have expected ambipolar expansion to accelerate the system. As it turns out, this apparent initial expansion is a remnant of DR, which flattens our density distribution leaving our detector response slightly non-Gaussian. This misleads our fitting routine towards observing an increase in width while ambipolar expansion only begins to accelerate the system. Figure 9.13 illustrates this effect more clearly by comparing the apparent detector width of dissociating shell plasmas at temperatures of 15, 7.5 and 1.9 K over a lifetime of 35 $\mu$s. The black curve on top of the data points represents shell model calculations with DR deactivated and serves as a test for the accuracy of the simulation rutine.

Figure 9.13 discourages the notion that DR could be the origin for the very slow expansion in our experimental data. Our riddle persists. The overall expansion of our system, that is the slope of a line through the data points in Figure 9.13, places our initial electron temperature at about $\sim$2 K. Such low temperature, however, would cause DR to reshape our detector response and become visible through deviation from Gaussian form as indicated by the accelerated growth right after plasma formation as well as larger error bars. We observe neither in our experimental data.

One possible explanation remains within the framework constructed in Chapter 8. In the following, I will explore the possibility of an initial plasma
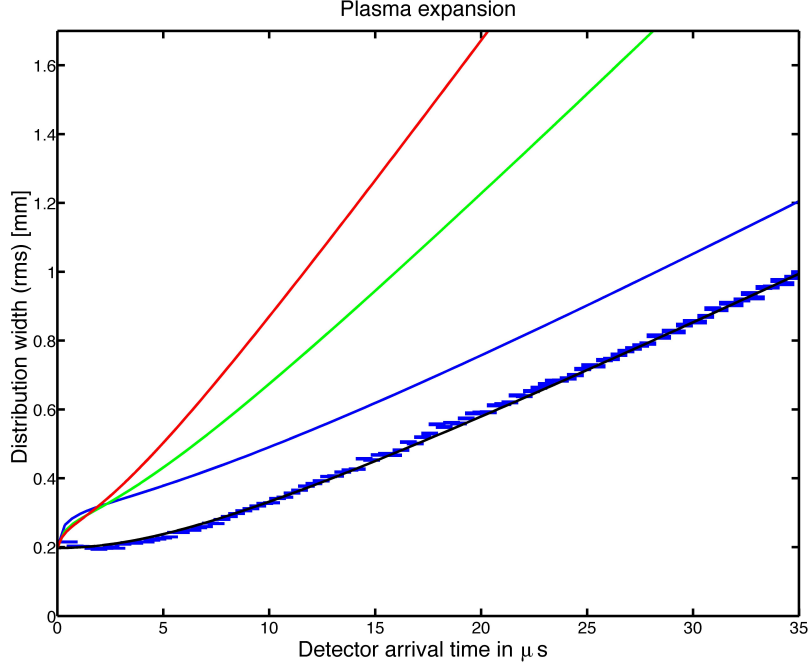
Figure 9.13: **Comparison of experiment and simulation results:** Top to bottom - detection simulation for dissociating plasma with initial conditions from table 7.1 and 15, 7.5 and 1.9 K initial electron temperature. The black curve represents 3D shell model data without DR at 1.9 K electron temperature. It serves as proof of accuracy for the computation. Experimental data points taken from Figure 9.8.

density much lower than $1 \cdot 10^{12}$ cm$^{-3}$. As DR is a second-order process in plasma density, low initial densities could explain our failure to observe it in our data. I will fix the initial electron temperature in my computation to $T_e(0) =$1.9 K and consider different initial density values $\rho(0) = 1 \cdot 10^{10}$, $1 \cdot 10^{11}$, $1 \cdot 10^{12}$ cm$^{-3}$. Figure 9.14 compares the expected width and area evolution for this computation to the experiment data.

Studying the shape progression of the expansion curves in Figure 9.14, it becomes apparent that system peak densities lower than $1 \cdot 10^{10}$ cm$^{-3}$ are able to reproduce our experimental results even under the influence of DR.
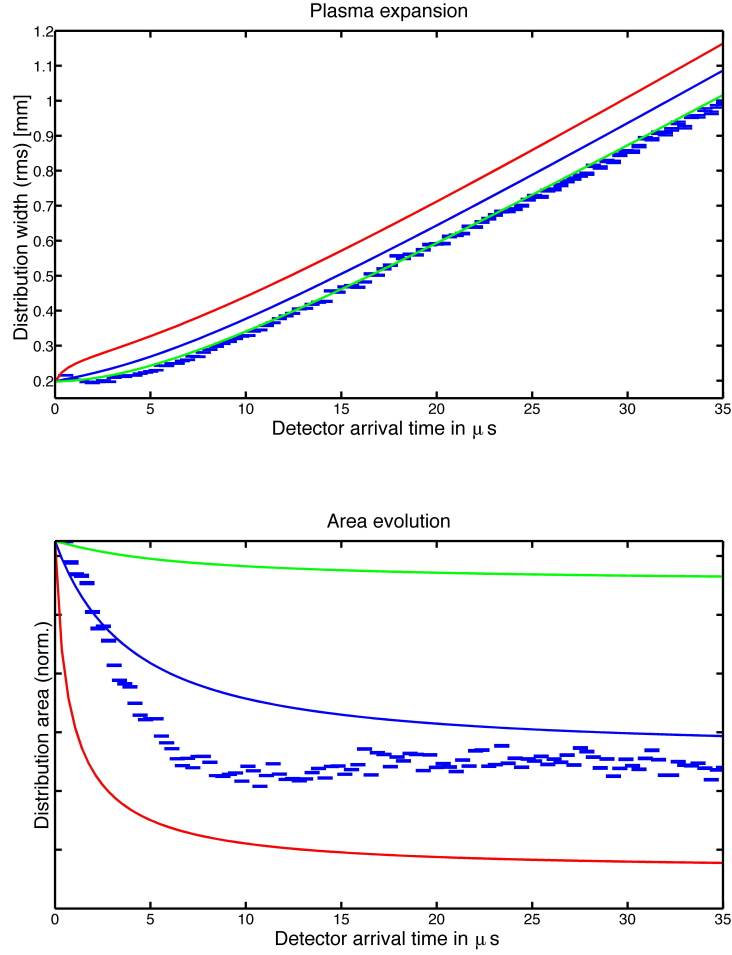
Figure 9.14: **Comparison of experiment and simulation results -** Computation results for $T_e(0)$=1.9 K and densities $\rho(0) = 1 \cdot 10^{10}$, $1 \cdot 10^{11}$, $1 \cdot 10^{12}$ cm$^{-3}$ (green, blue, red) compared to experimental data from Figure 9.8. Top: Evolution of distribution width along z. Bottom: Evolution of area measured along z.

However, a look at the area evolution for the low density system simulations shows vast disagreement from the experimental results.

In summary, I must conclude that the theoretical model developed in Chapter 8 is unable to reproduce our experimental results, likely due to a systematic error in our assumptions.

## 9.3   Chapter summary

Over the course of Chapter 9, I introduced our 1D detection scheme. In Section 9.2.1, I discussed an experiment in which we excited a molecular volume via the NO A-state to the high-Rydberg manifold. We allowed this volume to travel with the supersonic beam towards detection grid G2 and observed the following:

- Our illuminated volume travels with the velocity of the molecular beam and generates signal at our detector for specific $\omega_2$-energies.

- A spectroscopic analysis shows that the resonant $\omega_2$-energies conform with the NO $nf(R = 2)$- and $np(R = 0)$-Rydberg energies.

- Signal was observed down to PQNs of $30f(R = 2)$ and $39p(R = 0)$. This we understand in the following way: Plasma formation is fuelled by the Penning process. This process depends on Rydberg orbital size ($\propto n^2$) and lifetime of Rydberg states. $nf$-Rydberg states live much longer than $np$-states.

Section 9.2.2 discussed selective field ionization measurements performed on our illuminated volume. The volume was prepared in Rydberg level $50f(R = 2)$. A field-ramp was applied at different $\omega_2$ to ramp time delays. I found that:

- Our $\omega_2$-laser populates degenerate Rydberg states $50f(R = 2)$ and $59p(R = 0)$. We observe two dominant Rydberg features in our SFI map conforming with these two state binding energies.

- Our SFI map tracks the conversion of the illuminated volume from Rydberg gas to plasma. I was able to confirm our conceptual understanding of plasma formation, as discussed in Chapter 7. A quantitative analysis put the Rydberg volume under study at an initial density of $1 \cdot 10^{11} \text{cm}^{-3}$.

- Thus, typical Rydberg systems formed without $\omega_1$ to $\omega_2$ time-delay form at $\sim 2.7 \cdot 10^{11} \text{cm}^{-3}$.

Lastly, Section 9.2.3 discussed expansion data obtained with our moving-grid detector. Once again, the system was prepared in state $50f/59p$. My discussion of this dataset yields the following results:

- We are able to observe the system evolution over a timespan of up to $45\mu$s.

- Our results show a system with a rapid decay of $\sim 60\%$ of its charge carriers over the first $\sim 5\mu$s of evolution. Afterwards, decay appears deactivated.

- The plasma exhibits a very slow expansion characteristic, suggesting initial electron temperatures of only $\sim 2$ K based on conversion of initial electron temperature to radial ballistic ion motion during ambipolar expansion.

While we were able to learn a great deal about our experimental system, several fundamental questions remain. I summarize these in the following:

- In Section 9.2.1, I could not explain the fact that the plasma resonance peaks $\sim 0.3$ nm prior to reaching the $nf(R=2)$ ionization energy.

- Molecular dynamics calculations for the process of plasma formation predicted equilibrium electron temperatures on the order of $\sim 200$ K (cf. Chapter 7). An indirect temperature measurement through expansion velocity obtained a value of $\sim 2$ K. Based on the findings in this chapter, I cannot explain the mismatch.

- The decay of our plasma does not conform with expectations. The expected flattening of the plasma density distribution due to DR was not observed. The shut off is too abrupt.

There seems to be a link between the latter two open questions which adds insight towards finding a solution. One can argue, that the absence of DR points towards a further contradiction in initial electron temperature. The low electron temperature causes DR to appear prominently in our simulation ($k_{DR} \propto \sqrt{T_e}$). Hot electrons are fast and not so easily captured by the NO ion. Thus, we have two indications for the presence of hot electrons and it seems prudent to consider other mechanisms of energy dissipation which might explain the observed slow expansion despite hot initial electrons.

As discussed in Section 9.2.3, our 1D detectors integrate plasma distribution in y and z, which constitutes a loss of information. The search for this unknown energy dissipation mechanism fuelled the development of our new 3D plasma detector, discussed in the next chapter.

# Chapter 10

# Plasma detection in 3D

In the following, I will introduce our new 3D imaging detector, which has acquired the name 'PlasmaTV' within our research group. With this detector, we employ direct imaging to observe the dynamics of plasma expansion in $x$, $y$ and $z$. Our findings provide evidence for surprising new channels of energy disposal that operate in the particular geometry of our laser-crossed molecular beam plasma apparatus.

## 10.1  The plasma-tv detector

The key component of our new detector is a Chevron Model 3075FM detector assembly by *BURLE ELECTRO-OPTICS INCORPORATED*. This assembly consists of an 8 inch vacuum flange with a fiberoptic window of 76.7 mm diameter at its center. Stacked on the vacuum side of the window sits an indium tin oxide (ITO) layer with a phosphor coating. Mounted in parallel to this fiberoptic phosphor screen, and with a few millimetre distance, are two Microchannel plates (MCPs). The active area of this detector has a 75mm diameter. A schematic of it is shown in Figure 10.1.

Charged particles impacting on the MCPs create an electron cascade within the channels. This cascade exits the MCPs at the back and is accelerated towards the ITO anode. Typical voltages are MCPin = -200 V to +200 V, MCPout = MCPin + 1.8 kV and Anode = MCPout + 2 kV. The electron cascade impacts on the phosphor, causing luminescence. We record the spatial information of such charged particle impacts using a CCD camera. Additionally, we are able to record the temporal information via a capacitive output coupler, much like we do with our 1D detectors (cf. Chap-

ter 9).[19]

Our vacuum chamber is equipped with magnetic mu-metal shielding, fitted to the inside diameter of the chamber walls. Similar to previous experiments, we illuminate a volume of the molecular beam 150 mm after the skimmer and employ our *BURLE* detector in one of three configurations (cf. Figure 10.1):

- a) We mount the detector onto a 10" to 8" zero-length-adapter, which closes our vacuum chamber. This creates an unobstructed flightpath of our molecular beam within the experiment chamber. The distance between skimmer tip and detector measures 468mm in this configuration. We detect particle impact on the MCP.

- b) We use the previous configuration but add an 11" vacuum chamber extension, which allows for a total distance of 747 mm between skimmer and detection plane.

- c) We employ an array of vertical grids (G1, G2) combined with an electronic lensing system (plates and cylinders: P1, P2, C1, C2, C3) as displayed in Figures 10.1, c and 10.2. In this setup, we form our Rydberg volume between plates G1 and G2. The volume travels only a short distance (max. 21mm) towards detection grid G2. Upon transit through G2, loosely bound electrons are extracted by a forward potential (typically formed by 1kV on plate P2). Extracted electrons continue on a trajectory towards the *BURLE* detector. The electronic lensing system is set to recreate a true image of the charge distribution at the detection plane G2, with a magnification factor of typically 10 to 25.[20]

---

[19]We detect an image that represents our systems density distribution in $x/y$ while integrating over $z$. Simultaneously, we collect the charge impact on the detector to obtain information of the density distribution in $z$ while integrating over $x/y$. Please note, that the obtained 3D distribution only approximates the full density information, as this integration process incorporates a loss of information.

[20]The initial design of this electron optics array was done by Nicolas Saquet, at the time a post-doctoral researcher in our lab.
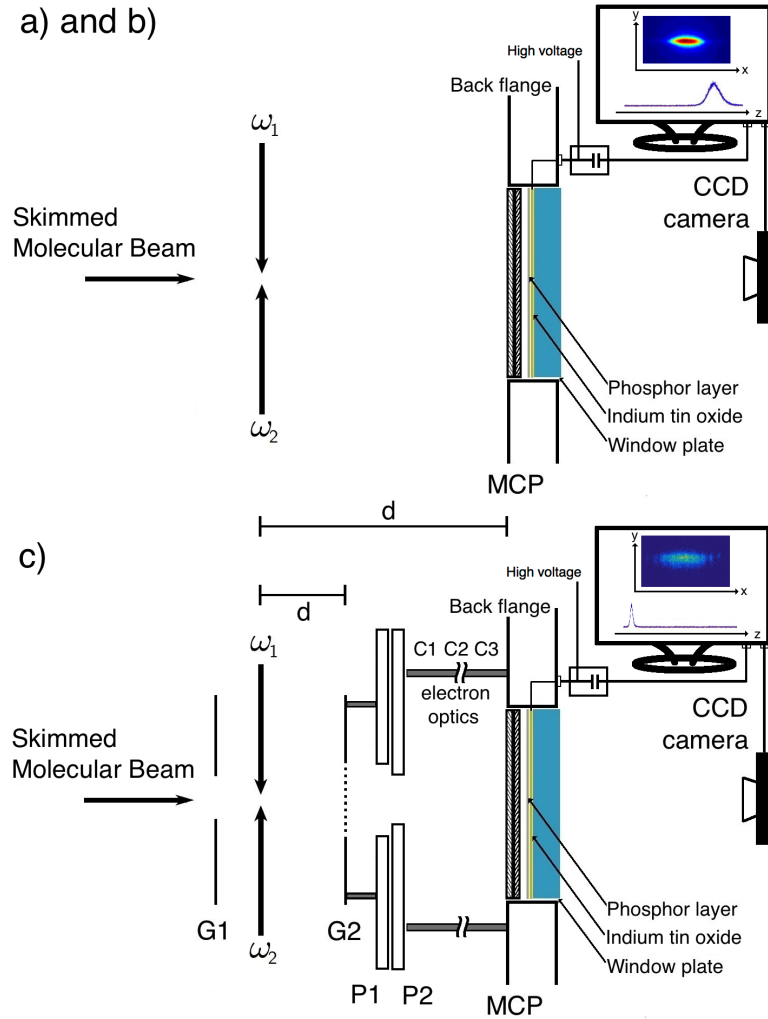
Figure 10.1: **Schematic of plasma-tv detector in different configurations -** The *BURLE* detector is mounted at the back of our vacuum chamber. It consists of a set of MCPs and a fiberoptic phosphor screen. The trajectory of our skimmed molecular beam is normal to the plane of detection (MCPs). We record timing and x/y position of particle impact on the MCPs. In configuration a), the distance d between laser and MCPs is 453 mm. Configuration b) extends this distance to d=732 mm. Configuration c) shortens the free flight distance of the illuminated volume to d<21 mm. Here, detection grid G2 extracts spatial information of plasma electrons (see text).

146
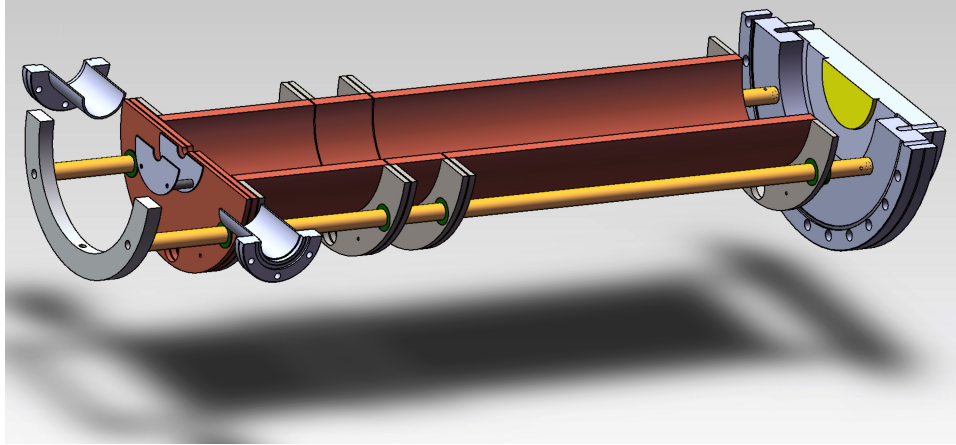
Figure 10.2: **Schematic of plasma-tv detector in configuration c) -** This figure shows an e-drawing of our electronic lens system. The molecular beam enters from the left. Vacuum chamber viewports allow for laser access between plates G1 and G2. The illuminated volume transits G2 and loosely bound electrons are accelerated towards the MCP detector at the end of the chamber.

The design and work with configuration c) is more complex compared to configurations a) and b). We based the dimensions of the electronic lens array on simulations performed with the SimIon software. Typical voltages of configuration c) are listed in Table 10.1. Figure 10.3 shows an instructive display of particle trajectories within the lens array. The detector is set to project a magnified real image, of the charge distribution transiting G2, onto the MCPs.

Figure 10.4 gives an example of the working of our new detector. We place a CCD camera in the back of our vacuum chamber and adjust distance and angle until the image is focussed on the fiberoptic window of the *BURLE* detector. The known window plate dimensions allow us to compute the in focus CCD pixel width. For measurements, we put a blackout around camera and detector and view the lighting-up of the phosphor screen due to charged particle impact on the MCPs. The right-hand side of Figure 10.4 shows the camera capture for an electron burst created between G1 and G2. For this

147
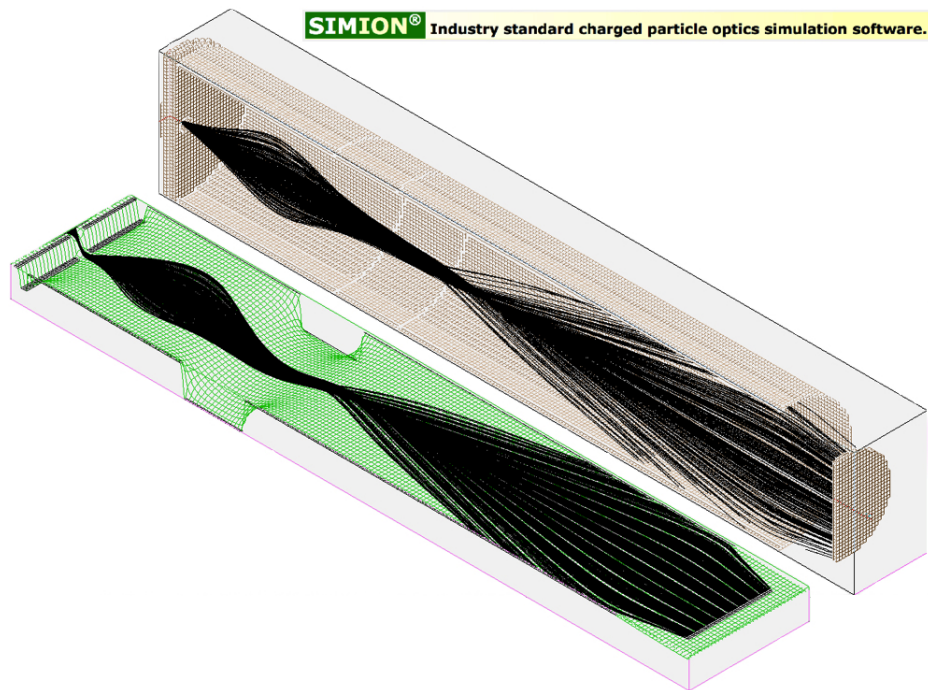
Figure 10.3: **Charged particle trajectories within electrostatic lens array -** This figure was created with the aid of SimIon. It shows charged particle trajectories in real-space (top) as well as potential energy space (bottom) for detector voltages in Table 10.1. The detector is set to project a magnified real image of the charge distribution transiting G2 onto the MCPs.

| Element | Voltage |
|---|---|
| G1 | variable |
| G2 | grnd. |
| P1 | 20 V |
| P2 | 1 kV |
| C1 | grnd. |
| C2 | 2 kV |
| C3 | 50 V |
| MCP front | 200 V |
| MCP back | 2 kV |
| Anode | 4 kV |

Table 10.1: This table details typical voltages applied to the components of the PlasmaTV detector - see Figures 10.1, c and 10.2

image, applied voltages conform with Table 10.1 and -300 V on G1. We observe magnification of the detection grid G2 of a factor 25.

## 10.2 Observations and discussion

The following three subsections will discuss our findings employing the PlasmaTV detector in configurations a), b) and c). Sections 10.2.1 and 10.2.2 closely follow recently published work, references [80, 82]. Recent qualitative results obtained through use of our new detector in configuration c) will be discussed in Section 10.2.3.

### 10.2.1 Plasma bifurcation

**Experimental**

Experimental data discussed in this chapter was won by preparing a Rydberg ensemble as discussed in Part II of my thesis. Laser pulses $\omega_1$ and $\omega_2$ cross the molecular beam at a position 143 mm beyond the skimmer, corresponding to a detection chamber flight time of $t = 100$ $\mu$s. The hydrodynamics of the skimmed supersonic expansion yield a beam at this point with a Gaussian radial distribution about its propagation axis that has a FWHM of 3.2

149
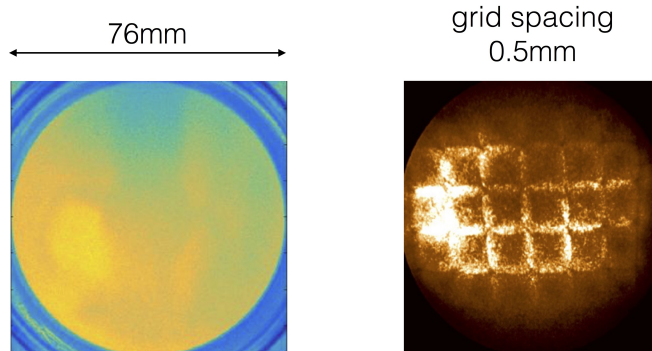
Figure 10.4: **Example image PlasmaTV detector -** The left-hand image shows the phosphor screen as seen by our CCD camera, mounted in the back of the vacuum chamber. In the right-hand image, we've placed a blackout around CCD camera and detector. The image shows the lighting-up of the phosphor screen, as we create a free electron flux through grid G2. Magnification amounts to a factor of $\sim 25$.

mm and a peak density of NO of $2.43 \times 10^{13}$ cm$^{-3}$. The molecules have a velocity spread parallel to the beam defined by a longitudinal temperature, $T_\parallel = 0.6$ K. Phase-space cooling reduces the perpendicular temperature by an amount proportional to the divergence, defined by $r_\perp = v_\perp t$.

The fraction of NO molecules excited to the A-state varies linearly with $\omega_1$ laser pulse energy. A rotatable Glan-Taylor polarizer and spatial filter in the optical train of $\omega_1$ form a beam with a variable pulse energy between 1.75 and 4.24 $\mu$J. Assuming a saturated $\omega_2$ transition, we estimate that the corresponding initial average density of the resulting Rydberg gas varies from $3 \times 10^{11}$cm$^{-3}$ to approximately $7 \times 10^{11}$ cm$^{-3}$.

After the skimmer, the molecular beam travels without obstruction to reach the detector, as diagrammed in Figure 10.1. Interchangeable 10 inch diameter conflat flange tubes determine the total, field-free, skimmer-to-detector flight distance. The use of a short tube section defines a distance of 468 mm (configuration a). The longer section affords an experimental chamber flight distance of 747 mm (configuration b).

This plasma flies freely to impact the grounded input face of the MCP stack. To determine the width of this signal in $z$, we apply 1.8 kV to the back if the detector, bias the ITO anode to a potential of 4.3 kV and record an oscilloscope trace reflecting the number of electrons incident on the $x, y$ plane of the detector as a function of time. The nozzle opens at a frequency of 10 Hz for a duration of 300 $\mu$s. The camera records images of the $x, y$ distribution of electrons integrated in $z$ by collecting photons for 30 ms following each laser shot. Both camera images and oscilloscope traces discussed in this section represent averages of 250 shots.

**Results:**

**Spatial Distribution of Charge in the Ultracold Plasma as a Function of Rydberg Gas Principal Quantum Number**
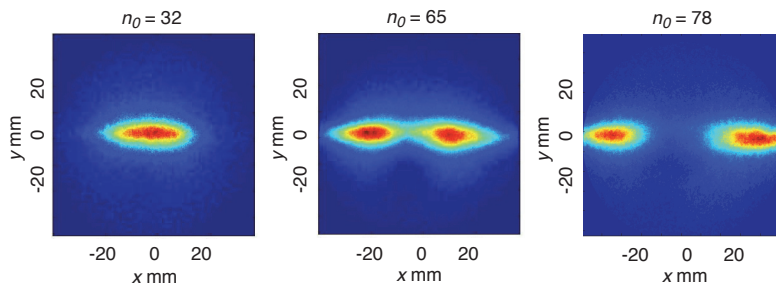


Figure 10.5: **Detector response recorded after preparing the Rydberg gas volumes** with the following set of approximate initial densities and selected initial principal quantum number: (left) $3 \times 10^{11}$ cm$^{-3}$ and $n_0 = 32$, (centre) $3 \times 10^{11}$ cm$^{-3}$ and $n_0 = 65$, (right) $7 \times 10^{11}$ cm$^{-3}$ and $n_0 = 78$. Here, we have positioned the detector at the longer flight distance measured as 747 mm from the skimmer wall, yielding a flight time in all cases of 420 $\mu$s after laser excitation. All figures represent averages over 250 CCD images.

Figure 10.5 shows $x, y$ particle density distribution detector images recorded after preparing Rydberg gas volumes with initial principal quantum numbers, $n_0 = 32$, $n_0 = 65$ and $n_0 = 78$ in the $f$ series. We allow these volumes

151
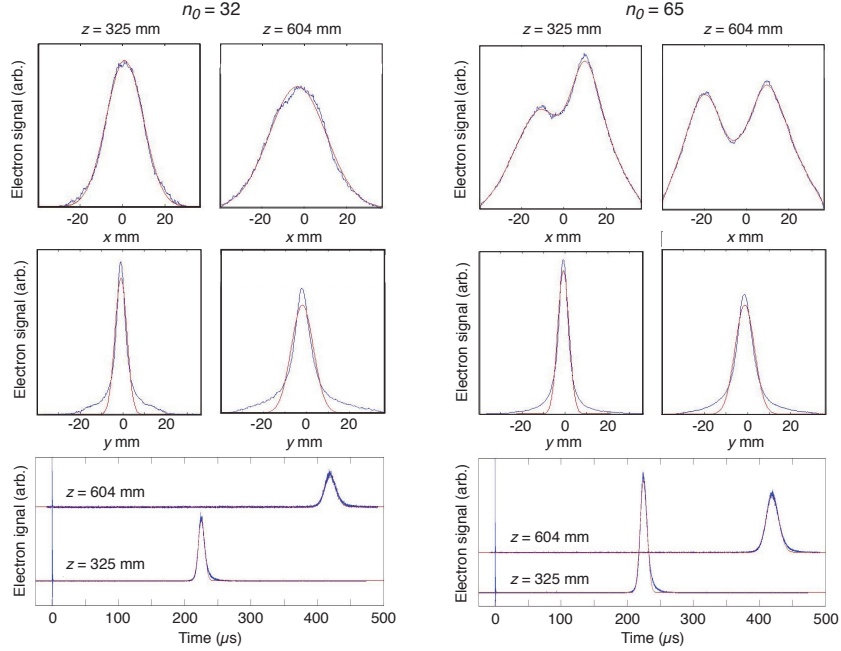
Figure 10.6: **Distributions of electron density in** $x, y$ **and** $z$ following excitation to Rydberg gasses with initial principal quantum numbers of $n_0 = 32$ and $n_0 = 65$ and propagation over the distances indicated from the point of laser interaction to the detector plane. (top) Distribution of the electron density over the horizontal cross-beam coordinate $x$, integrated in $y$ and $z$. (centre) Distribution of the electron density over the vertical cross-beam coordinate $y$, integrated in $x$ and $z$. (bottom) Distribution of the electron density over the molecular beam propagation coordinate $z$, integrated in $x$ and $y$, displayed as the waveform of the detector anode signal as a function of time. Smooth red curves represent Gaussian ($y$ and $z$) or sum of Gaussian ($x$) fits.

to propagate a distance of 604 mm from the point of laser interaction. The $n_0 = 32$ and $n_0 = 65$ images were collected with the $\omega_1$ attenuating polarizer set to 50°. This affords a laser pulse energy of 1.75 $\mu$J, well below the threshold for saturating the initial $X^2\Pi$ to A $^2\Sigma^+$ transition. For the purposes of obtaining the $n_0 = 78$ image in Figure 10.5, we set the polarizer to 0°, yielding a laser pulse energy of 4.24 $\mu$J which nearly saturates the $\omega_1$

transition.

When these illuminated volumes strike the detector, they produce images that differ in shape from the Gaussian radial distribution of the molecular beam in several important ways. The laser intersects the molecular beam to form a prolate ellipsoid. We can determine the size of this initial ellipsoid from the measured radial profiles of $\omega_1$ and the molecular beam at the point of intersection. Comparing the dimensions of this volume to the distributions in Figure 10.5, we can determine that the excited density diverges faster than a correspondingly marked volume of the unperturbed molecular beam.

Figure 10.6 plots distributions of electron density in $x, y$ and $z$ obtained for $n_0 = 32$ and $n_0 = 65$ measured after propagation distances of 325 and 604 mm. Note for $n_0 = 32$, the charge distribution in the $x$ dimension exceeds the neutral beam divergence by more than a factor of two. The expansion of the $n_0 = 32$ image in the $\Delta y$ coordinate increases faster than the calculated divergence of an element of the core of the molecular beam marked to have the initial 1 mm FWHM $y$ dimension of the $\omega_1$ laser beam. The width of the charge distribution measured along the axis of propagation, $z$, grows faster than $\Delta y$. Note as well that the distribution evolves in $y$ to exhibit an accelerated, non-Gaussian tail.

For $n_0 = 65$, the plasma evolves in $y$ much like it does for $n_0 = 32$, showing again non-Gaussian tails in the expansion along $\pm y$. Note, however, that the distribution extends over a much wider distance in $x$, and exhibits a distinctive low-density hole in the centre, on the axis of the molecular beam. Table 10.2 details the measured widths in $x, y$ and $z$ following short and long flight paths for $n_0 = 32$ and 65.

Gaussian waveforms fit to the anode current signals in Figures 10.6 establish arrival time differences for long and short flightpaths of 194.1 $\mu$s for $n_0 = 32$ and 194.9 $\mu$s for $n_0 = 65$. The average of this flight time difference divided by the distance difference of 279 mm yields a beam velocity, $v_{beam}$=1434 m s$^{-1}$. With this beam velocity, the difference in the $x$ separation of the density maxima measured for $n_0 = 65$ determines that the lobes

Table 10.2: Experimental measures of FWHM in $x, y$ and $z$ dimensions for excited volumes striking the imaging detector following short (unprimed) and long (primed) flight times, as derived from Gaussian fits to intensity distributions pictured in Figure 10.6. All values are expressed in mm. Note that we can determine unperturbed $\Delta x_0 = 10.25$ and $\Delta y_0 = 3.3$, from the short flight path divergence of the beam, marked simply by its intersection with $\omega_1$. We further predict $\Delta z_0 = 6.9$ based on the z-dimension thermal velocity of 'marked' molecules as well as $\omega_1$-laser size. We convert the temporal widths in $z$ and $z'$ to spatial widths using $v_{beam}$.

|            | $\Delta x$ | $\Delta y$ | $\Delta z$ | $\Delta x'$ | $\Delta y'$ | $\Delta z'$ |
|------------|------------|------------|------------|-------------|-------------|-------------|
| $n_0 = 32$ | 20.42      | 6.25       | 16.08      | 31.71       | 12.14       | 28.77       |
| $n_0 = 65$ | -          | 6.17       | 17.72      | -           | 10.61       | 32.12       |

in these charge density images separate with a $\pm x$ velocity of 74 m s$^{-1}$.

The cross-beam, $\Delta x$ expansion of the prolate excitation volume varies systematically with the Rydberg gas initial principal quantum number chosen by tuning $\omega_2$. Figure 10.7 plots normalized distributions of the electron signal as a function of $x$ for selected $nf(2)$ principal quantum numbers from 28 to 78, all recorded with an $\omega_1$ pulse energy of 1.75 $\mu$J.

Contour plots corresponding to these images show that $\Delta y$ remains constant as function of $n_0$. However, the distribution along $x$, which begins with a single mode at $n_0 = 28$, clearly widens and splits to a degree that grows with increasing initial principal quantum number.

## Spatial Distribution of Charge in the Ultracold Plasma as a Function of Rydberg Gas Density

Reference to Figure 10.7 shows that, with a laser pulse energy of 1.75 $\mu$J, the plasma formed from a Rydberg gas for which $n_0 = 58$ bifurcates in $x$ to show a slight bimodal character. Rotating the polarizer in $10°$ steps to reduce its de-alignment with $\omega_1$, increases the $\omega_1$ pulse energy and changes the spatial distribution for $n_0 = 58$. As shown in Figure 10.8, the distribution along $x$ develops distinct modes, and these separate with increasing $\omega_1$ pulse energy from 1.75 $\mu$J to 4.24 $\mu$J. The highest pulse energy approaches the point of
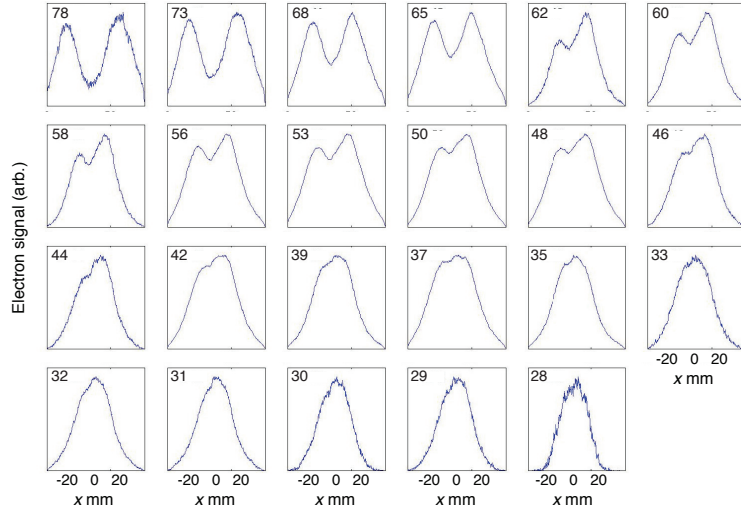
Figure 10.7: **Normalized distributions of** $y, z$ **integrated electron density** as function of $x$, collected using a an $\omega_1$ pulse energy of 1.75 $\mu$J with long flight path for selected initial principal quantum numbers, $n_0 f(2)$, in the range from 78 to 28.

saturating the $\omega_1$ transition. For an $\omega_1$ energy of 3.74 $\mu$J, the separation evident here for $n_0 = 58$ exceeds that observed for $n_0 = 78$ at 1.75 $\mu$J.
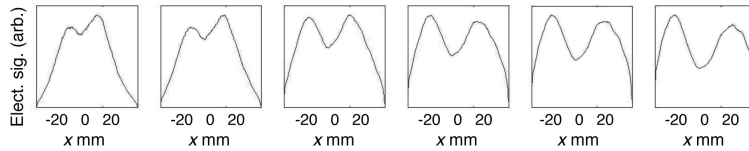


Figure 10.8: $x, y$ **plasma images** collected using a long flight path with a single initial $n_0 f(2)$ principal quantum number of 58 and varying laser pulse energies from 1.75 $\mu$J to 4.24 $\mu$J.

155

**Discussion:**

**Electron Impact Avalanche and the Evolution to Plasma**

The volume of Rydberg gas formed by double-resonant excitation evolves to plasma in two steps. Within the time of the $\omega_2$ laser pulse, pairs of Rydberg molecules that happen to form within a critical intermolecular separation, $r_c$, Penning ionize to yield an ion plus free electron and a deactivated Rydberg molecule. This initial ionization forms a space charge that traps the majority of electrons. These electrons collide with the remaining Rydberg molecules in the charged volume. Electron-Rydberg collisions drive transitions in the Rydberg manifold, and after a time that depends on the density of Penning electrons, $\rho_e$, an electron-impact avalanche begins. This avalanche quickly forms an ultracold plasma quasi-equilibrium of ions, electrons and Rydberg molecules.

The density of promptly formed Penning electrons, $\rho_e$, depends on the initial density of the Rydberg gas, $\rho_0$, and the selected initial principal quantum number, $n_0$, to a degree determined by the Erlang distribution function of nearest-neighbour distances, integrated from 0 to the critical value, $r_c$.

$$\rho_e(n_0, \rho_0) = \frac{0.9}{2} 4\pi\rho_0^2 \int_0^{r_c} r^2 e^{-\frac{4\pi}{3}\rho_0 r^3} \mathrm{d}r \qquad (10.1)$$

The plasma formation mechanism was discussed in detail in Part III of this thesis.

**Dynamics of plasma expansion in the plane perpendicular to laser propagation**

The plasma formed by electron impact avalanche at lower values of $n_0$ and lower $\omega_1$ laser pulse energy grows in major and minor axis dimensions at a rate that exceeds the divergence of the molecular beam by about a factor of two. In the previous chapter, I have analyzed the electron signal waveform obtained by collecting the integrated charge in successive $x, y$ planes as the plasma volume transits a perpendicular grid to gauge the rate of expansion along the short axis aligned with the molecular beam propagation direction,

156

$z$. This expansion conforms with the hydrodynamics of an ambipolar expansion driven by the pressure of an electron gas with a temperature in the range of $\sim 2$ K.

For all values of $n_0$ and $\omega_1$ laser pulse energy, the expansion rate in the short axis dimension, $y$, measured crudely here by the difference between the image widths in $y$ for short and long flight times, accords with observations of $z$ expansion seen both in earlier experiments, and for present conditions in the oscilloscope traces at the bottom of Figures 10.6. This short axis expansion does not vary significantly, either with increasing principal quantum number or increasing $\omega_1$ laser pulse energy.

## Dynamics of plasma expansion in the direction of laser propagation

In contrast with the unvarying short-axis expansion dynamics observed here and in previous experiments, the cross-beam, long-axis dimension of the plasma volume evolves dramatically, bifurcating to form separating lobes of charge density. Inspecting Figures 10.7 and 10.8, we see that the velocity of separation, $\check{v}_x$, grows with either an increase in the level of Rydberg excitation or initial laser pulse energy.

In separate experiments, we have studied the saturation of the NO A-state population as a function of the $\omega_1$ energy. These studies show that the interval of $\omega_1$ intensities used in the present experiment fall in the upper end of the regime of linear absorption. Under conditions of NO A-state saturation, we estimate a Rydberg gas density $\rho_0 \approx 1 \times 10^{12}$ cm$^{-3}$ [74].

For lower laser powers, in the linear regime, we associate $\omega_1$ laser pulse energies with Rydberg gas density as shown in Figure 10.9. Thus, assuming a near-saturation density of $7 \times 10^{11}$ cm$^{-3}$ for the Rydberg gas prepared using an $\omega_1$ laser pulse energy of 4 $\mu$J, we can estimate a Rydberg gas density of $3 \times 10^{11}$ cm$^{-3}$ in the first frame of Figure 10.8, and all of the measurements shown in Figure 10.7, which were obtained at laser pulse energy of 1.75 mJ.

The experimental images provide striking evidence that the ellipsoidal plasma volume forms repelling plasma volumes. In the top frames of Figure
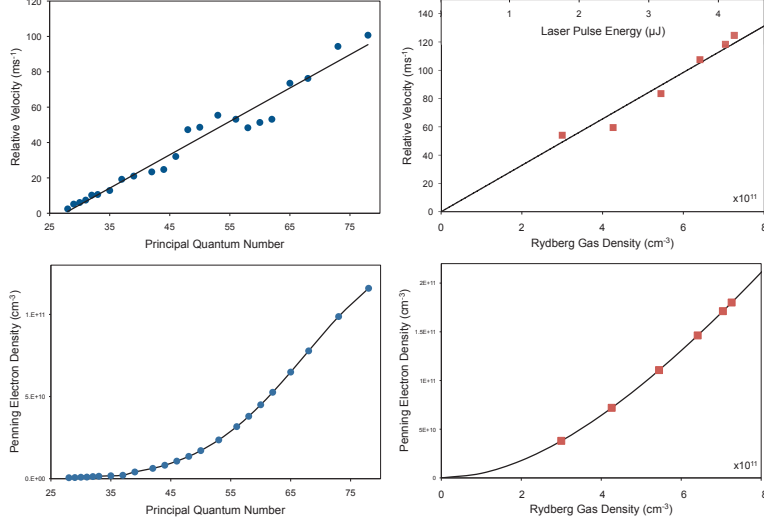
Figure 10.9: **Top:** Relative velocity, $\check{v}_x$, with which mesoscopic volume elements of the plasma charge distribution separate along $x$ as a function of Rydberg gas initial principal quantum number at constant density of $3 \times 10^{11}$ cm$^{-3}$, and as a function of Rydberg gas density at a constant principal quantum number of $n_0 = 58$. **Bottom:** Penning fraction as a function of Rydberg gas initial principal quantum number at constant density of $3 \times 10^{11}$ cm$^{-3}$, and as a function of Rydberg gas density at a constant principal quantum number of $n_0 = 58$, as determined by Eq. (10.1).

10.9, we see clearly that the recoil velocity of these separating lobes grows linearly with an increase in Rydberg gas initial principal quantum number, or initial Rydberg gas density.

Raising $n_0$, increases the orbital radius of the excited NO molecules in the Rydberg gas. Increasing the density decreases the average distance between Rydberg molecules, and more importantly, increases the fraction of nearest neighbour distances that fall within a particular radius.

The question now remains, whether a single property of the Rydberg gas varies with a change in orbital radius (depends on $n_0$) or a change in average inter particle distance (depends on $\rho_0$) in such as way as to cause this uniform variation in $\check{v}_x$.

Referring to Eq. (10.1), we note that pairs of NO Rydberg molecules with nearest-neighbour separations that fall within a critical distance instantaneously interact to form a population of Penning electrons. The density of this population, $\rho_e$, rises both with $n_0$ and with $\rho_0$. The lower frames of Figure 10.9 draw upon Eq. (10.1) to plot the variation of $\rho_e$ with $n_0$, for a fixed Rydberg gas density of $\rho_0 = 3 \times 10^{11}$ cm$^{-3}$, and the variation of $\rho_e$ with $\rho_0$ for a fixed principal quantum number of $n_0 = 58$.

Referring to this information, we can recast recoil velocities observed as functions of $n_0$ and $\rho_0$ into a universal form that represents the variation in $v_x$ with a change in the Penning electron density, $\rho_e$. Figure 10.10 shows that the simple, self-consistent choice of $3 \times 10^{11}$ cm$^{-3}$ as the Rydberg gas density produced by double-resonant excitation using an $\omega_1$ pulse energy of 1.75 $\mu$J, linearly relates $\check{v}_x$ to $\rho_e$ over a factor of three in recoil velocity and more than an order of magnitude in Penning electron density.
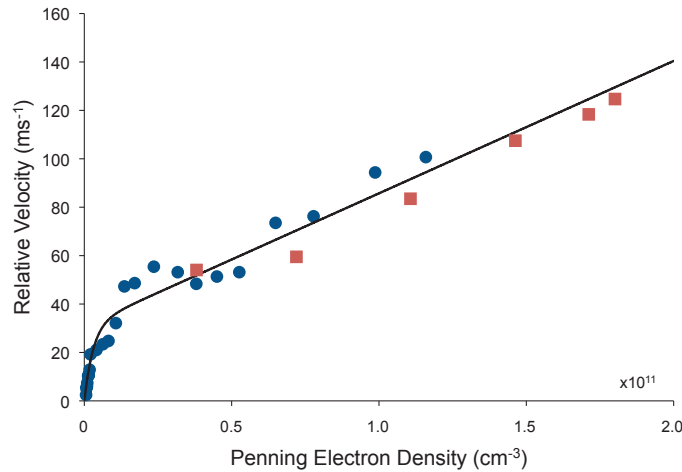


Figure 10.10: **Relative velocity, $\check{v}_x$, with which lobes of the charge distributions separate** along $x$ as a function of Penning electron density, for plasmas formed both at constant $\omega_1$ pulse energy with varying principal quantum number, $n_0$ (circles) and at constant quantum number with varying $\omega_1$ pulse energy (squares).

**Plasma recoil velocity as a function of Penning electron density**

Whether increased by raising the initial principal quantum number or increasing the initial Rydberg density, we see that, $\breve{v}_x$, the recoil velocity of plasma segments separating along the long-axis dimension, $x$, scales uniformly with Penning electron density, $\rho_e$. This quantity reflects the population of electrons and ions that appears instantaneously on the timescale of the plasma frequency.

We represent $\rho_e$ in Figures 10.9 and 10.10 by its average value in the Rydberg gas volume, as determined by the orbital radius ($n_0^2 a_0$) taken together with the average spacing ($[3/4\pi\rho_0]^{1/3}$). But, while double-resonant excitation selects a uniform value of $n_0$ in the Rydberg gas, the laser-crossed molecular beam illumination forms a non-uniform excited state density distribution. The charge distributions pictured in Figure 10.5 for $n_0 = 32$ with a short flight path and lower $\omega_1$ pulse energy clearly show that the ellipsoidal Rydberg gas produced by the intersection of a Gaussian $\omega_1$ laser beam and Gaussian molecular beam peaks decidedly in the centre. This affects the distribution of plasma electrons that forms on the timescale of the laser pulse.

## 10.2.2 Ultracold plasma hydrodynamics in three dimensions

The last section introduced the concept of plasma bifurcation as a means to convert core electron thermal energy into mesoscopic recoil. In this section, I wish to further discuss the process that facilitates this energy transfer process and propose a qualitative mechanism leading to plasma bifurcation.

**Plasma expansion as a measure of electron temperature**

Electron temperature values exceeding 100 K represent a signature feature of avalanche ionization to form a dense ultracold plasma. In a freely expanding plasma, the ambipolar pressure of this electron gas causes a radial acceleration of the ions. The Vlasov equations describe this acceleration analytically
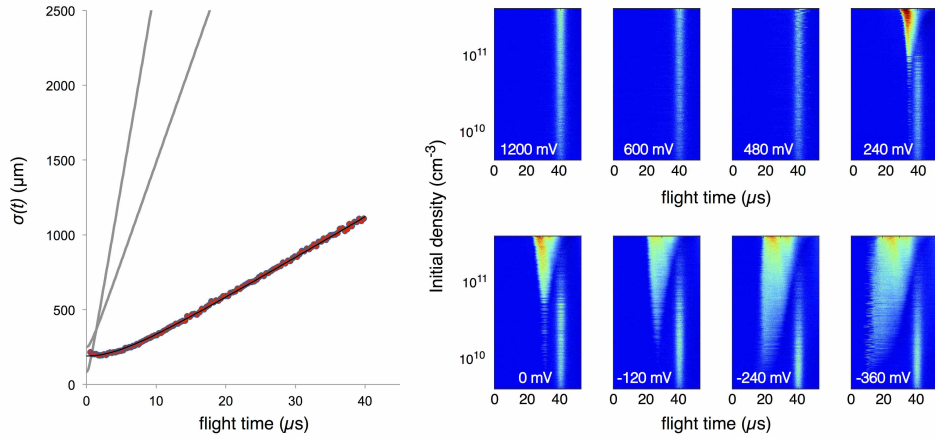
Figure 10.11: **Left:** Self-similar expansion of Gaussian ultracold plasmas: (grey lines) Ambipolar expansion of a model Gaussian plasma core ellipsoid of cold ions and $T_e = 180$ K electrons with $\sigma_y(0) = \sigma_z(0) = 83$ $\mu$m and $\sigma_x(0) = 250$ $\mu$m. Ions rapidly attain ballistic velocities, $\partial_t \sigma_y = \partial_t \sigma_z = 272$ m s$^{-1}$ and $\partial_t \sigma_x = 132$ m s$^{-1}$. (blue line with red data points) Experimental measure of $\partial_t \sigma_z(t)$ fit by Vlasov model for a Gaussian spherical expansion for $T_e = 5$ K. **Right:** Electron signal as a function of flight time to G2 observed in the moving grid apparatus diagrammed in Figure 9.2 with a constant reverse bias on G1 of 1.20, 0.60, 0.48 and 0.24 V (top row), and forward bias of 0.0, $-0.12$, $-0.24$ and $-0.36$ V (bottom row), all with a flight distance to G2 of 56 mm. The Rydberg gas was prepared at $n_0 = 50$.

for the self-similar expansion of a spherical Gaussian plasma. We and others have extended these hydrodynamics both analytically and numerically to non-spherical plasma distributions (see Part III of this thesis).

In the limit of saturated $\omega_1$ excitation, laser-crossed molecular beam illumination creates an ellipsoidal volume of Rydberg gas with a peak density as high as $\sim 10^{12}$ cm$^{-3}$. A coupled rate-equation model (c.f. Figures 7.2 and 7.3) predicts avalanche in a regime of this density on a nanosecond timescale to form an electron gas with an initial temperature, $T_e(0) = 180$ K. The pressure of this electron gas drives the expansion of the ions. The steeper charge-density gradient in the $y, z$ coordinate directions causes the rate of radial expansion in the short axis plane to substantially exceed that along the cross-beam $x$ axis of the ellipsoid.

Grey curves in Figure 10.11 diagram the self-similar ambipolar expansion of a Gaussian plasma ellipsoid of initially cold ions and $T_e = 180$ K electrons in a subspace with $\sigma_y(0) = \sigma_z(0) = 83$ $\mu$m and $\sigma_x(0) = 250$ $\mu$m. In a Vlasov model, electrons of this temperature accelerate the distribution of NO$^+$ ions to a $z$ expansion rate, $\partial_t \sigma_z$, of 272 m s$^{-1}$. This radial velocity, which approaches 20% of the laboratory speed of the molecular beam, greatly exceeds the observed expansion rate of the ultracold plasma in $z$ determined experimentally by the growing widths of waveforms such as those displayed in Figure 9.7. A typical set of late-peak Gaussian widths yields values of $\sigma_z(t)$ plotted as the red data points in Figure 10.11.

Clearly, the system travelling with the velocity of the supersonic beam has little in common with this hot plasma predicted by rate-equation models. The employment of our moving-grid detector at a fixed G1 to G2 distance of 56 mm, while varying the potential on G1, yields new insights. Data displayed in the right frame of Figure 10.11 provides clear evidence for the presence of two distinct domains of ultracold plasma evolution. The forward bias between G1 and G2 reveals points toward an avalanche of a high-density Rydberg gas that produces a diffuse, rapidly expanding plasma of energetic ions and electrons. A reverse bias of 480 mV cm$^{-1}$ or more sweeps these electrons away, isolating the slowly expanding waveform of the ultracold

plasma. But, the signal of electrons in advance of the late peak waveform persists up to a reverse bias as great as 250 mV cm$^{-1}$, signifying an initial fast-component $T_e$ of 200 K.[21]

How does the observation of a rapidly expanding plasma domain of energetic electrons and ions figure into the process of plasma bifurcation?

**Plasma evolution in a Rydberg gas of non-uniform density**

We propose the following process for ensemble bifurcation: Laser-crossed molecular beam excitation forms an ellipsoidal Rydberg gas in which density distributes differently in $x, y$ and $z$. The local density of ground-state NO does not vary in the molecular beam propagation direction, $z$. Thus, the Rydberg gas density distribution in this coordinate simply reflects the narrow Gaussian intensity profile of the laser beam. The Rydberg gas has the broader Gaussian width of the molecular beam in the $x$ coordinate direction, defined by the propagation of the laser. The profiles of the laser beam and molecular beam combine to form a steeper gradient of Rydberg gas density in $y$, determined by the product of these Gaussians.

The superimposed distributions of laser intensity and molecular beam number density create a Gaussian ellipsoid of NO* Rydberg molecules. The density distribution peaks at the core of this volume. There, rate-equation simulations predict avalanche on a nanosecond timescale, forming a local population of free electrons in a quasi equilibrium with initial temperature $T_e(0)$ as high as 180 K. Such a high electron temperature must drive plasma expansion.

For the purposes of a conceptual model, we represent the density distribution of this core plasma by means of a set of concentric ellipsoidal shells. To simplify, we will neglect both the thermal motion of the ions and any process that leads to neutralization, such as dissociative or three-body recombination, so that the number of charged particles in each shell remains constant.

---

[21]This experiment was performed by my colleague Rafael Haenel. My thanks to him for allowing me to use his data in my thesis.

In the quasi-neutral approximation, an electric potential gradient represents a force, $-e\nabla\phi_{k,j}(t)$, which accelerates the ions in shell $j$ in direction $k$ according to (see Chapter 8):

$$-\frac{e}{m'}\nabla\phi_{k,j}(t) = \frac{\partial u_{k,j}(t)}{\partial t}$$
$$= \frac{k_B T_e(t)}{m'\rho_j(t)} \frac{\rho_{j+1}(t) - \rho_j(t)}{r_{k,j+1}(t) - r_{k,j}(t)} \quad (10.2)$$

The instantaneous velocity, $u_{k,j}(t)$ determines the change in the radial coordinates of each shell, $r_{k,j}(t)$,

$$\frac{\partial r_{k,j}(t)}{\partial t} = u_{k,j}(t) = \gamma_{k,j}(t)r_{k,j}(t) \quad (10.3)$$

which in turn determines the shell volume and thus its density, $\rho_j(t)$.

The electron temperature supplies the thermal energy that drives this ambipolar expansion. Ions accelerate and $T_e$ falls according to:

$$\frac{3k_B}{2}\frac{\partial T_e(t)}{\partial t} = -\frac{m'}{\sum_j N_j}\sum_{k,j} N_j u_{k,j}(t)\frac{\partial u_{k,j}(t)}{\partial t} \quad (10.4)$$

where we have defined an effective ion mass that recognizes the redistribution of ion momentum by free-electron-mediated resonant ion-Rydberg charge exchange, which occurs with a very large cross section [62]:

$$m' = \left(1 + \frac{\rho_j^*(t)}{\rho_j(t)}\right)m \quad (10.5)$$

The initial avalanche in the high-density core of the ellipsoid leaves few Rydberg molecules, so this term has little initial effect. Rydberg molecules predominate in the lower-density wings. There momentum sharing by charge exchange assumes greater importance.

As indicated by the high-temperature expansion curves in Figure 10.11, core ions reach ballistic velocities in just a few hundred nanoseconds. This quenches electron temperature. After expanding less than 50 $\mu$m, the motion of the core ellipsoid becomes a flux of ballistic ions and very cold electrons.

Much of this population streams out of the Rydberg gas volume in the $y$ and $z$ directions to produce the early signal pictured in Figure 10.11. But, a substantial fraction of these expanding ions and electrons remain in the volume of Rydberg gas, streaming in $\pm x$. Here, ion-Rydberg charge exchange has two important consequences:

(1) A rapid sequence of electron transfer processes act to redistribute the directed momentum of the ions over the entire population of Rydberg molecules and ions [6]. The heavy particles relax to correlated positions [72], and the two volumes stream as a whole in opposite directions.

(2) Charge exchange increases the effective inertial mass of the ions, which acts to retard the ambipolar expansion of the plasma forming in the bifurcated volumes.

### 10.2.3  Recent work

In the following, I include two recent experiments and their qualitative discussion. These experiments serve as proof of concept for my discussion thus far and identify families of experiments in which we plan to conduct major work in the future.

**Experiment 1:**

**Experimental:** Figure 10.12 displays data obtained with the 3D-imaging detector in configuration a). Here, we have tuned our lasers to prepare Rydberg molecules at PQN 64. Our detector voltages were set to the following values: MCP input = +7V, MCP output = 1.6 kV and Screen = 3.5 kV. The positive input on the MCP is unusual as we tend to set this potential either to ground or slightly negative to achieve a better signal-to-noise ratio. We record 100 single images and corresponding oscilloscope traces with constant experimental conditions.

The bottom left image in Figure 10.12 displays the pixel average of these 100 shots. We observe strong bifurcation of the plasma ellipsoid and note two peculiarities in the image. The first is a strong charge particle impact between 10 and 11 o'clock in the image. The second peculiarity is an asym-

metry in signal strength between the two bifurcated volumes. The top signal trace in Figure 10.12 displays the corresponding oscilloscope measurement.

**Discussion:** I define two distinct measurement areas in image and oscilloscope trace. Henceforth, signal A refers to particles travelling with the velocity of the molecular beam. These particles impact on the detector between 200 and 250 $\mu$s after laser excitation and light up the phosphor within the central measurement area. I have discussed signal A, the arrested subcomponent, at length in the last section. Signal B appears $\sim$170 $\mu$s prior to signal A and corresponds to particle impact on the top-left corner of the phosphor screen.

What is the origin of signal B? In the current configuration, our detector has a positive input face and repels positive charges. I can rule out ion impact. We observe that the variation of potentials on the MCP input face, between +7 V and +25 V, moves signal B on a line from the observed position to the image centre.[22] Examining the electric field environment within the vacuum chamber gives me further insights. The high voltage vacuum feedthroughs which apply potential to our detector are located, as seen by the camera, in positions 11 o'clock (screen) and 10 o'clock (MCP out). At the time of this measurement, these feedthroughs were not shielded.[23] Interplay between the large MCP input area and these connectors creates an inhomogeneous field, channeling negative charges emitted by the evolving Rydberg volume toward the top-left corner of the detector. This inhomogeneous field is also responsible for the asymmetry between the left-hand and right-hand bifurcating volumes.

We observe an interesting correlation between signal B and the mag-

---

[22]I claim correspondence between signals B on the oscilloscope and screen based on circumstantial evidence. Varying the voltage on the MCP input face, I can move signal B off the screen, which results in it's disappearance on the scope.

[23]Usually, we install a shield which screens these potentials.
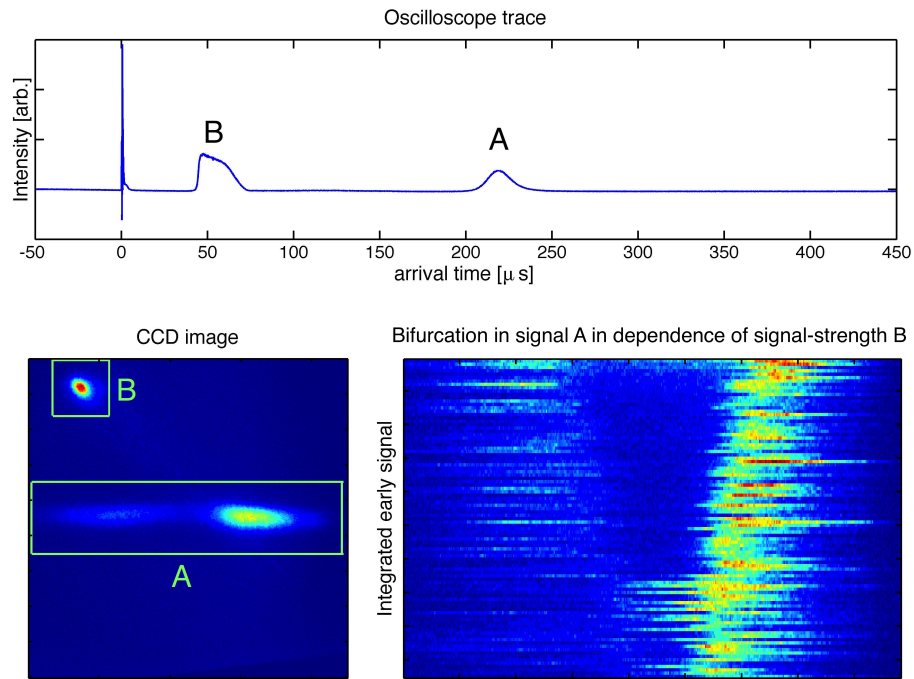
Figure 10.12: **Detector response in configuration a)** - Our system is prepared at n=64. MCP input is at +7 V, MCP output at 1.6 kV and Screen at 3.5 kV. We record 100 single images and corresponding oscilloscope traces. Top: Averaged oscilloscope traces. Bottom left: Averaged CCD image and definition of top-corner and centre measurement areas. Bottom right: For each of the 100 images, I sum over the total pixel response of area B and sort the images accordingly. I then integrate pixel in the centre area A in the vertical and stack the obtained traces. The obtained graph highlights the fact that the stronger signal B the stronger bifurcation in signal A.

nitude of bifurcation. For this, I consider each of the 100 measurements individually. For each image, I extract the total pixel count of the top-left measurement area (displayed in Figure 10.12) as well as a signal trace, obtained by integrating signal A in dimension y. I next sort the signal traces in dependence of signal B and display my findings in the bottom-right of Figure 10.12. I learn that the extent of bifurcation is intimately linked to the magnitude of signal B. The stronger signal B the more bifurcation is observed. This result fits well into the concept of ballistic core ions streaming into the distribution wings.

**Outlook:** At present, we are planing a systematic study of signal B. For this, we need a better characterization and control of the field environment in our experiment. At what point in time is B polarized? How high is the required field? Signal B appears to behave very much like the plasmas observed in MOT experiments for direct ionization (not via Rydberg manifold). Does our system become all B for higher photon energies, as suggested by Figure 9.4?

**Experiment 2:**

**Experimental:** We prepare our Rydberg ensemble at $n_0$=57. Our detector is in configuration c) and we set detector voltages to: G1=1.2 V / G2=grnd. / P1=20 V / P2=500 V / C1=grnd. / C2=2 kV / C3=50 V / MCPin=200 V / MCPout= 1.5 kV / Screen=3 kV. Our molecular beam is illuminated ~1.7 cm before grid G2. We record 100 single images and the corresponding oscilloscope traces. A 'by eye' analysis of the images shows that we can classify these images into three categories. The first category of images display a cigar shaped volume transiting imaging plane G2. It is possible to discern eight to ten vertical grid lines and one horizontal line in the images. This allows us to estimate the volume size at G2 to 4mm to 5mm in x-width and about 1mm in y-hight (grid spacing .5mm). We find that 36 out of 100 images fit this first category. The second category shows the same volume, but with a distinct hole of varying size in the distribution. This

hole is located predominantly towards the centre of the volume. We find 32 images in this category. The third category displays images similar to category two, but with a distinct signal appearance at the centre of the hole. We recognize that our detection grid G2 imprints its shape onto this hole-centre-signal. The oscilloscope signal corresponding to category three tells us that the hole-centre-signal appears $0.5\mu s$ prior to the rest of the cigar shaped volume. For the other two categories, the scope trace was purely Gaussian. 32 images fit this last category.

Figure 10.13 displays examples of category one in the first row, examples of category two in the second row and examples of category three in the third and fourth rows. The bottom left subfigure shows the oscilloscope response for figures of the last category.

**Discussion:** Grids G1 and G2 are separated by a distance of 20.75 mm. A voltage of +1.2 V on G1 yields a field of 0.58 V/cm (G2 at ground). Loosely bound electrons are pulled away from detection grid G2. Positive ions can reach G2 but not the positively charged input face of the MCP. Our plasma forms in this environment.

Viewing the first row (category) of images in Figure 10.13, we recognize the ellipsoidal shape of our illuminated volume. The corresponding oscilloscope trace shows that this signal travels with the velocity of the molecular beam to arrive at the detector after $\sim$12.5 $\mu s$. The shape of the detected volume does not seem to be perturbed by the small external field. We recognize plasma state A from experiment 1.

Images of category 2 (second row) display a distinct hole at the centre of the ellipsoidal distribution. Possible reasons for this observation are: a) The core has decayed/dissociated to neutrals which cannot be field ionized by the potential between G2 and P2. b) The core has developed into a state where it can be polarized by the small external field. Electrons are pulled away from G2 toward G1.

Images of category 3 seem to support the latter hypothesis. Here, we observe a strong signal originating at the location of the missing core in

169
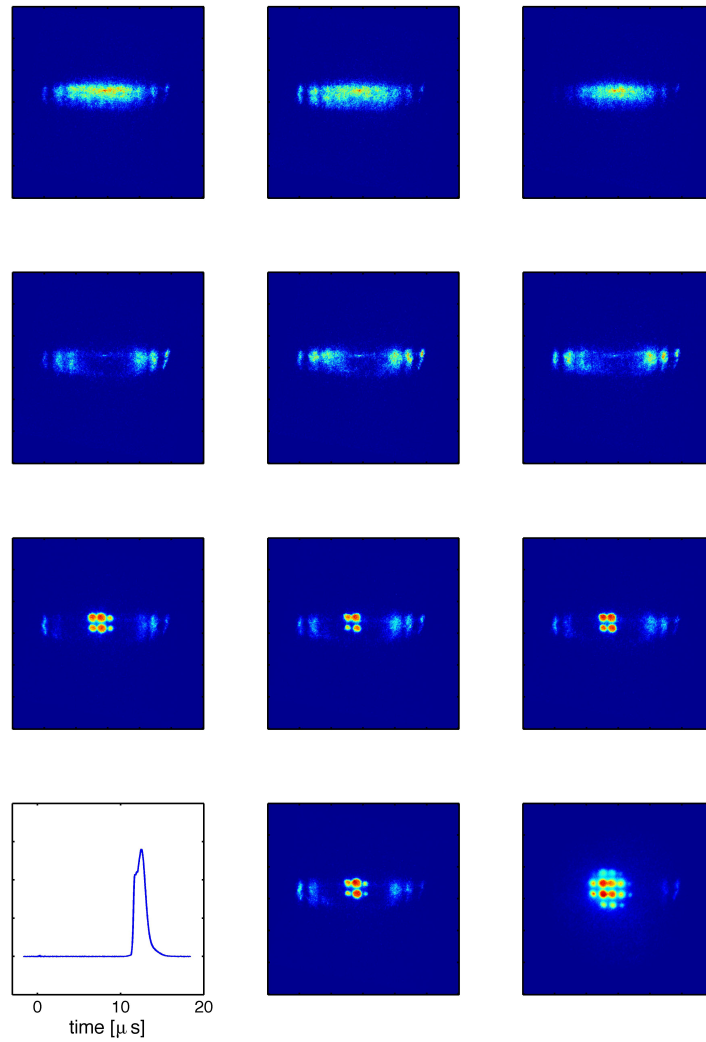
Figure 10.13: **Detector response in configuration c) -** Our system is prepared at $n_0$=57. Out of 100 single shot images, I display example captures of 3 families of CCD camera responses (1st line / 2nd line / 3er & 4th line). The bottom left oscilloscope trace corresponds to the 3rd family. Discussion in text.

category 2. Note, that this core-signal completely disappears for voltages on G1 higher than 2V. This core signal differs distinctly from the images of distributed charge. The oscilloscope trace for category 3 images tells us that this signal arrives up to 500 ns earlier at the detector. This can be explained via two mechanisms: 1) Particles responsible for this signal have excess kinetic energy compared to the molecular beam. They are faster and arrive earlier. 2) The polarizing field between G2 and P2 does not abruptly begin at G2 but reaches a small distance through the G2 mesh into the region between G1 and G2. Detection through polarization takes place earlier.

Likely is that both mechanisms are present. The round shape of the observed core-signal pores, as opposed to the quadratic shape of the grid, can be explained via mechanism 2. At the same time, the bottom-right image shows this core-signal extending beyond the original hight of the ellipsoid in $y$, suggesting the presence of excess kinetic energy. It stands to reason that this core-signal corresponds to plasma state B in experiment 1. We confirm that, for a yet unknown reason, our plasma develops into two distinct macroscopic regions.

**Outlook:** The characterization of the nature of the arrested component lies at the centre of our current work. Our new 3D detector in configuration c) allows us to study the early time behaviour of our system. Is a microscopic system variable or perhaps a race-condition responsible for the macroscopic boundary between regions A and B? Systematic experiments, similar to the above, might lead us to understand this boundary, which in turn allows us to understand the observed state of arrest.

## 10.3   Chapter summary

Imaging of our ensemble density distribution at long evolution times show that the ellipsoidal ultracold plasma formed in a supersonic beam by avalanche ionization in a Rydberg gas of nitric oxide can spontaneously break symmetry, to channel a substantial fraction of its excess energy into the cross-beam laboratory motion of opposing plasma volumes. As discussed in Section
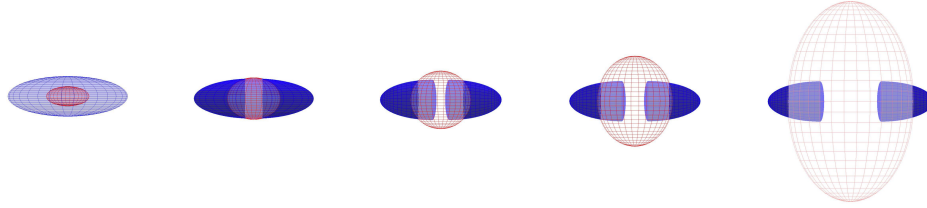
Figure 10.14: **Time sequence of plasma bifurcation -** At the core of the Rydberg ellipsoid, plasma self-assembles into a hot state, distinct from the surrounding outer layers. Ambipolar expansion quenches electron kinetic energy and accelerates the core as a shock though the outer layers, causing bifurcation via ion-ion collisions and resonant charge exchange.

10.2.1, the dynamics of this process can be controlled by selecting the initial density and principal quantum number of the Rydberg gas. These observations point to a new physics of ultracold plasma relaxation, in which the thermal energy of avalanche-heated electrons transforms first into radial motion of electrons and ions, and then into the recoil energy of plasma lobes.

Section 10.2.2 discussed the observation of two plasma components, one hot and one cold. Based on this observation, I proposed a qualitative mechanism explaining plasma bifurcation. Here, core avalanche produces a cloud of initially hot electrons and cold ions. Ambipolar expansion quenches electron kinetic energy and accelerates core ions to velocities of as much as one-fifth the laboratory speed of the molecular beam. These ions stream in the $\pm x$ direction, into the wings of the Rydberg gas. There, recurring reactions that exchange charge between $NO^+$ ions and $NO^*$ Rydberg molecules equilibrate velocities and change ion motion within the gas to $\pm x$ motion of gas volumes in the laboratory. In the wings, momentum redistribution owing to continuing charge transfer with the residual high-Rydberg population retards axial expansion. By redirecting electron energy from ambipolar acceleration to $\pm x$ plasma motion, $NO^+$ to $NO^*$ charge exchange dissipates electron thermal energy and preserves density. This sequence of events leading to plasma bifurcation is shown in Figure 10.14.

Lastly, I introduced two recent experiments and discussed my qualitative findings. These are summarized in the following:

- I confirm the development/self-assembly of our system into 2 macroscopic states (A and B), observed as early as 12 $\mu$s into system evolution. These two states are distinguished by their appearance time on the oscilloscope as well as their impact location on the phosphor screen.

- We know about state A that it:

  - Is quasi-neutral and travels with the velocity of the molecular beam.
  - It survives field pulses exceeding 100 V/cm, applied 500 ns after $\omega_2$ [51].
  - Does not show signs of decay after evolution times of 5-10 $\mu$s (cf. Section 9.2.3).
  - Makes up the bifurcated wings.

- We know about state B that it:

  - Reacts much stronger to electric fields.
  - Appears to be polarizable a few microseconds into its evolution by fields as low as 0.5 V/cm.
  - Appears to have excess kinetic energy.

- We confirmed that bifurcation acts as a link between system states A and B. The larger the observation of state B the more bifurcation.

Overall, experiments 1 & 2 seem to confirm our current concept on plasma formation. That our Rydberg system is able to develop two distinct macroscopic domains which are linked through bifurcation. Future work in our group will focus on the detailed study of the interplay of domains A and B.

In the concluding remarks of the last chapter, I stated three fundamental question which have for years been at the centre of our work: 1) Why does

our plasma signal vanish completely prior to reaching the IP? 2) Why don't we observe indirect effects of hot electrons? 3) Why does the signal decay shut off? Based on the findings of this chapter, I can explain the first two points in the following:

- The Rydberg scan displayed in Figure 9.4 captures the transit of the long-lived plasma component through detection grid G2. For high PQNs, this component bifurcates and develops a macroscopic recoil velocity. At some point, further increase in PQN pushes these bifurcated volumes out of the detection aperture of our detector, resulting in the observed disappearance of the signal. The question remains, whether a long-lived plasma component even exists at $\omega_2$-energies near the IP.

- We do observe indirect effects of hot electrons. However, other than expected these effects manifest through bifurcation rather than ambipolar expansion in $z$.

Our observation of two distinct domains of plasma is of fundamental importance. Two questions naturally arise: What aspect of the Rydberg gas relaxation dynamics distinguishes these two domains, which separate so evidently in the molecular beam propagation direction, $z$? How do these dynamics shut off signal decay in a highly unstable system?

# Chapter 11

# Arrested relaxation

In previous chapters of my thesis, up to Section 10.2.3, I have discussed established and for the most part published and reviewed material. In the following chapter, my last chapter, I will break with this narrative and discuss up-to-date research topics, which still raise controversy within our research community. At the heart of the following discussion lies our observation of the shut-off of signal decay within the long-lived plasma component which travels with the velocity of the molecular beam. I will quantify our observations with regard to this phenomenon and speculate on the corresponding microscopic system state.

## 11.1 Comparison of model calculations and experiment

Part III of this thesis represents a toolbox which allows predictions of our Rydberg ensemble evolution within idealized theory models. In the following, I will select experimental data from the previous chapter, and predict ensemble evolution based on initial experimental conditions. Comparison of simulation and experimental results will highlight shortcomings of our current computational model as well as understanding.

**Initial conditions**

For the following, I will select experimental data discussed in Section 10.2.1, more specifically the dataset discussed on the left-hand side of Figure 10.6. Here, I prepared our Rydberg system in PQN 32 and probe its density distribution after 225 and 421 $\mu$s evolution in 3 dimensions. I choose this dataset

due to the lack of apparent bifurcation. The initial conditions at which this system was prepared are collected from Section 10.2.1 and summarized in Table 11.1. I adjust the initial Rydberg gas peak density to reflect my findings in Section 9.2.2.

Table 11.1: Initial conditions corresponding to experimental data discussed in Figure 10.6 (left-hand side).

| Rydberg ensemble initial conditions | |
|---|---:|
| $\text{FWHM}_x$ | $\sim$3.2 mm |
| $\text{FWHM}_y$ | $\sim$1 mm |
| $\text{FWHM}_z$ | $\sim$1 mm |
| $\rho_{Ry}$ | $\sim 2.7 \cdot 10^{11}$ cm$^{-3}$ |
| $n_0$ | 32 |

**Evolution according to model calculations**

Chapter 7 developed a plasma formation model by which a uniform-density Rydberg gas undergoes Penning ionization to yield a seed density of quasi-free electrons. Subsequent electron-Rydberg collisions model the avalanche process turning the Rydberg ensemble to plasma. Computation results by this model for densities of 100%, 80%, ... , 20% of $\rho_{Ry} = 2.7 \cdot 10^{11}$ cm$^{-3}$ and initial PQN of 32 are summarized in Table 11.2.

Table 11.2: Plasma rise-time calculations for uniform density Rydberg systems. Density in [$10^{11}$ cm$^{-3}$].

| % [$\rho_{Ry}^0$] | $\rho_{Ry}$ | $t_{rise}$ [ns] | $T_e(2 \cdot t_{rise})$ [K] | $\rho(2 \cdot t_{rise})$ |
|---:|---:|---:|---:|---:|
| 100 | 2.7 | $\sim$160 | $\sim$200 | 2.1 |
| 80 | 2.16 | $\sim$214 | $\sim$200 | 1.7 |
| 60 | 1.62 | $\sim$308 | $\sim$200 | 1.27 |
| 40 | 1.08 | $\sim$514 | $\sim$200 | 0.85 |
| 20 | 0.54 | $\sim$1200 | $\sim$200 | 0.43 |
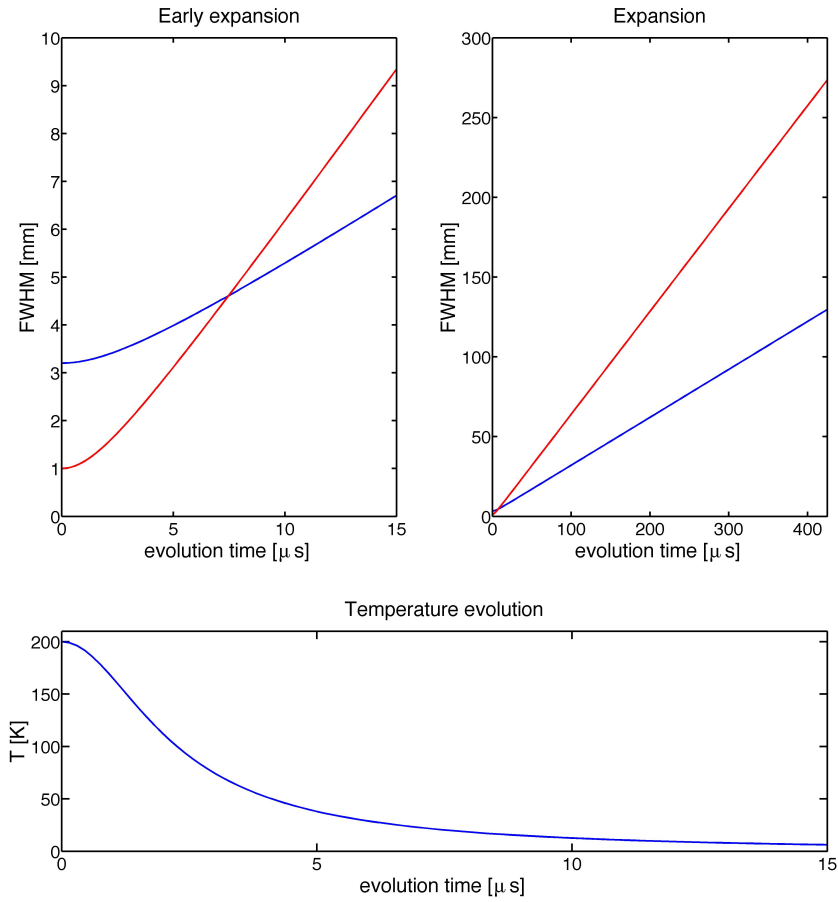
Figure 11.1: **Self-similar ambipolar expansion of a 200 K plasma -** Initial condition according to Table 11.1 with $T_e(t = 0) = 200$ K. Top: Evolution of plasma width according to self-similar model. Dimensions x and y,z are colour-coded blue and red. Bottom: Evolution of electron temperature.

Note that plasma formation for this $n_0 = 32$ system is much delayed (compared with higher PQN systems) due to the small Rydberg orbital size, yielding a much lower initial Penning density. Nonetheless, this system is predicted to transition to plasma with $\sim$ 200 K hot quasi-free electrons on a microsecond timescale.

In the following, I will take system dimensions from Table 11.1 and assume an electron temperature of 200 K as plasma initial conditions. Section 8.1 provided a set of differential equations, solving self-similar plasma expansion in the absence of dissociative recombination.[24] Figure 11.1 plots results obtained though this model. This simulation shows how, over the first 10 $\mu$s, $\sim$90% of electron thermal energy is transformed into ion hydrodynamic motion. The density gradient plays an important role in this energy redistribution process and acceleration along y/z exceeds that along x. As a result, the system turns from prolate, via spherical shape after $\sim$ 7.5 $\mu$s, to oblate. After 425 $\mu$s evolution, the simulated system exhibits a size of $\sim$125x275x275 mm FWHM, exceeding the size of our experiment chamber.

**Observed experimental expansion**

Our molecular Rydberg ensemble, formed via 2-photon resonant transitions in nitric oxide, is prepared far from thermal equilibrium. Each Rydberg molecule receives over 9 eV excess energy through photon absorption. Model calculations, supported by experimental observations (cf. Section 9.2.2), show the transition of this ensemble to plasma. Our calculations predict that a substantial fraction of the Rydberg excess energy flows into electron thermal motion which subsequently drives ambipolar expansion. Our experimental observations, however, do not confirm this prediction.

---

[24] At 200 K electron temperature, electrons travel very fast resulting in weak electron-ion recombination. This allows me to employ the simple modal from Section 8.1. The initial thermal as well as hydrodynamic motion of the ions is a result of the $<$ 1 K thermal motion of supersonic beam molecules at the point of skimming. I neglect this residual motion in comparison with the initial electron temperature.
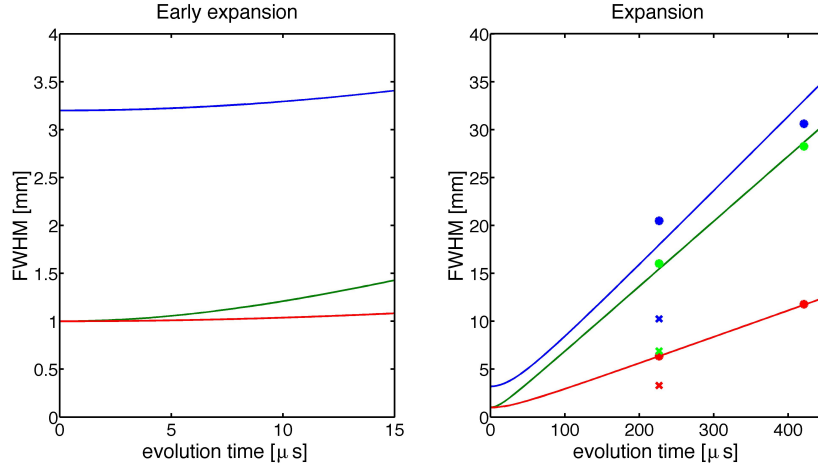
Figure 11.2: **Extrapolation of ensemble expansion based on experimental data from Table 10.2 -** Dimensions x,y,z are colour-coded blue, red, green. Dots represent experimentally measured distribution widths at 225 $\mu$s and 421 $\mu$s evolution. The lines represent fits of ambipolar expansion curves to the respective two data points in each dimensions. X marker plot the expected thermal width-evolution of a non-interacting 'marked' expansion.

Figure 11.2 plots the measured ensemble width after 225 and 421 $\mu$s for a system prepared at PQN 32. X marker predict the ensemble width at 225 $\mu$s, assuming that the $\omega_1$-laser simply 'marked' the beam distribution, which subsequently evolves only according to the unperturbed thermal and hydrodynamic particle trajectories (cf. Section 6.2). Our experiment clearly shows that some energy ($\sim$1 K) has been channelled into hydrodynamic expansion. This value, however, falls $\sim$99.5% short of the prediction from the last subsection and represents a clear discrepancy between simulation and observation. It conforms precisely with the very slow rates of expansion, determined for short times of flight in our moving grid machine (data from Figure 9.8). The slow expansion rate of this component in all three spatial dimensions and over its entire trajectory puts a significant limit on the

final kinetic energy of the excited molecules or ions.[25] Expansion models in the ellipsoidal geometry of the system call for initial temperatures (Rydbergs/ions plus electrons) no more than 2 degrees Kelvin. If not channeled into expansion, where are the ~9 eV excess energy per molecule?

**Experimental evidence for the arrest of decay channels**

Figure 9.8 traces the number of signal generating particles as a function of flight time observed for an ultracold plasma produced in a beam of NO seeded in helium. Here, a system with initial Rydberg gas density of $\sim 3 \cdot 10^{11}$ cm$^{-3}$ falls with the loss of its hot component and dissociative recombination after 10 $\mu$s to ~40% of its initial particle number. Thereafter, the loss of signal apparently stops, and the number of extracted electrons remains constant for as long as we can observe it in the moving grid apparatus.[26] The $z$ waveforms in Figure 10.6 show that the longer flight-path imaging apparatus forms an anode waveform at 421 $\mu$s with comparable area than the one we observe with the detector positioned for a time of flight of 225 $\mu$s. The persistent magnitude of this signal suggests that the corresponding Rydberg $-$ NO$^+-$ electron system lives a millisecond or more.

Thus, our bifurcated domain exhibits remarkable chemical stability with respect to neutral fragmentation on a millisecond timescale. Charge separation persists, despite ultrafast predissociation channels that exist for nitric oxide molecular Rydberg states with lower angular momentum at all principal quantum numbers, and efficient electron Rydberg inelastic collisions that rapidly scramble populations in $n$ and $\ell$. Our long-time observations of nitric oxide molecular ultracold plasma evolution, thus appear to indicate a state of arrested relaxation.

---

[25]In this formulation, I am being purposefully vague. As previously mentioned, our detector does not differ between a plasma electron and a high-Rydberg electron as long as it can be extracted from the ensemble to create a cascade in the MCP pores.

[26]In similar fashion, after an initial period of dissipation, the evolving NO-Rydberg ensemble entrained in a slower beam of argon survives undiminished out to 180 $\mu$s [31].

## 11.2    The inadequacy of 'classic' models

Our experiment clearly establishes the existence of a cold, durable component that forms from an elliptical Rydberg gas as it evolves to plasma. We have observed this durable component in cigar shape, morphing into two bifurcated volumes with a $\pm x$ recoil velocity that depends systematically on the initial density of the Rydberg gas, $\rho_0$, and its selected principal quantum number, $n_0$ (see Section 10.2.1). Rates of expansion suggest ensemble temperatures comparable to disorder induced heating. Rydberg/ion radial velocities reflect little more kinetic energy than might be available through spatial correlation (cf. Section 4.3.3). This durable component exhibits remarkable chemical stability with respect to neutral fragmentation on a millisecond timescale.

It remains now to speculate on a final state that best accounts for the properties of this system. I consider four possible quasi-stationary states precedented by our current understanding of Rydberg gas – ultracold plasma dynamics:

**A 'hot' classical plasma:** This is the most logical system state and confirms with predictions by model calculations in Chapter 7 of this thesis. Our SFI experiments (Figure 9.2.2) support this scenario. The evolution of our Rydberg ensemble to plasma, however, must be accompanied by electron heating to temperatures exceeding 100 K (cf. Table 11.2). Fast electrons, in turn, should drive plasma expansion as discussed for example in Section 11.1. Based on the observed lack of system expansion, we must dismiss this scenario.

**A 'cold' classical plasma:** As a thought experiment, let's consider the premise of a 'cold' plasma despite the *lack of concept* on how such a system might emerge. Early in its flight path from $z = 0$ to 600 mm, a classical plasma with the properties suggested by our long-time system behaviour would exist in a regime of strong coupling with respect to both ions and electrons. Efficient three-body recombination and Rydberg relaxation would consume ions, heat electrons and drive the system to exhibit a *fast expansion*, which we do not see. Furthermore, Section 9.2.3 considered the *shape-shift*

181

of the distribution due to high-order density dependent decay channels and found that such mechanism should be apparent in our probing of the density distribution. Thus, we identify three inconsistencies in this scenario.

**A quenched system of long-lived high-Rydberg states:** Such a quasi-stationary state accords with selective field ionization measurements that collect the entirety of the electron signal at exceedingly low voltage. Let's derive an estimate of the peak density of the experimental system considered in Section 11.1. Figure 11.2 fits expansion curves through the data points derived experimentally. After 15 $\mu$s evolution, the fitted curves suggest a system size of $FWHM_x$=3.42 mm, $FWHM_y$=1.07 mm and $FWHM_z$ =1.4 mm. Assuming an initial peak density of $\rho_{Ry}^0 = 2.7 \cdot 10^{11}$ cm$^{-3}$ and accounting for a signal loss of 60% (cf. Section 11.1) over the first 15 $\mu$s evolution, I predict a remaining peak density of,

$$\rho(15\mu s) = \frac{\sigma_x^0 \sigma_y^0 \sigma_z^0}{\sigma_x' \sigma_y' \sigma_z'} \cdot \rho_{Ry}^0 \cdot \text{loss factor} = 6.7 \cdot 10^{10} \text{ cm}^{-3}, \qquad (11.1)$$

where $\sigma_k$ represents the distribution width along dimension $k$. Under comparable conditions in a MOT, Penning interactions [68] and interatomic Coulomb decay [2] drive electron-impact avalanche on a timescale no slower than tens of microseconds [89]. Conventional relaxation would again heat electrons and produce an expansion that fails to materialize in our experimental observations. Even after 100 $\mu$s evolution, above argument yields a remaining peak density of $\rho(100\mu s) = 2.2 \cdot 10^9$ cm$^{-3}$, which, according to the model from Chapter 7 and assuming a PQN of 90 turns plasma within a microsecond.

**A relaxed system of deeply bound Rydberg states:** Such a system might resist Penning ionization on the observation timescale so-far employed in our bifurcated plasma experiments. However, studies show that NO Rydberg states of low principal quantum number predissociate on a nanosecond timescale (see Table 3.3). Our volumes show no evidence of such dissipation. Moreover, Rydberg molecules with deep binding energies would show a characteristic SFI spectrum not seen in our experiments.

The process of elimination suggests unconventional or 'new' physics as responsible for the arrest of relaxation dynamics. The apparent experimental condition of arrested relaxation in our experiment naturally raises the question whether many-body and/or quantum mechanical coupling somehow constrains the transport of matter and energy. An incoherent mechanism may yet emerge, but our experimental observations substantially narrow the possibilities that can rely on conventional kinetics.

## 11.3 Future work

This thesis does not intend to solve the open question, which microscopic state might explain our macroscopically observed system behaviour. Nonetheless, the following section will introduce avenues of research which our group currently pursues.

### How & when does arrest emerge?

Part II of this thesis went to great length to describe the initial state of our experiment. Which mechanism could facilitate the transition of our initial system state into the arrested domain? What can we learn through this question?

### Hypothesis 1: Bifurcation as quench?

The results of selective field ionization experiments, such as those pictured in Figure 9.5, suggest that the state of the bifurcated plasma in its early evolution is one of high-Rydberg molecules and electrons weakly bound to a space charge of $NO^+$ ions. We observe the prompt expansion of electrons and accelerated ions that initiates the process of bifurcation (see Chapter 10). On simple electrodynamics grounds, these initial ions reach ballistic velocities in a few hundred nanoseconds, after travelling only a few tens of micrometers. This ambipolar transfer of the thermal energy of the electrons to the radial energy of the ions quenches $T_e$ to the order of $T_i$.

Ballistic ions with velocity components in $\pm x$ expand into the wings of the elliptical Rydberg gas. Resonant charge exchange transfers ion momentum to Rydberg molecules. This process recurs, creating a uniform $\pm x$ velocity field in which ions, cold electrons and Rydberg molecules all stream together. For higher principal quantum numbers at higher Rydberg gas densities, the observed recoil velocity of bifurcating plasma volumes approaches half the initial radial velocity of the ambipolar accelerated core ions. This suggests a medial expansion of ions and electrons that advances to meet an approximately equal density of cold Rydberg molecules.

Internal energy of the system in all coordinates flows to the relative motion of bifurcating volumes, quenching the internal state of the plasma. As their relative velocities approach zero, ions and Rydberg molecules naturally move to positions of minimum potential energy. These spatial correlations deplete the leading and trailing edges of the initially random distribution of nearest neighbours in the Rydberg gas [72], forming a random, three-dimensional network in which the distribution of $NO^+/NO^+$ distances, $r$, (referring both to Rydberg molecules and bare ions) peaks sharply at a Wigner-Seitz radius. We can thus imagine that the plasma self-assembles to form a correlated spatial distribution of intermolecular distances dictated entirely by internal forces. Thus, bifurcation quenches the ensemble of ions and electrons to an annealed domain of low energy, perhaps to an ultracold regime.

Hypothesis 1 favours the notion of ballistic ions streaming into a Rydberg gas based on an argument of conservation of momentum along dimension $x$. Ions, streaming along dimension $x$ into a Rydberg gas, undergoing resonant charge exchange, are able to contain a large fraction of their momentum in $x$. This is not true for ballistic ions streaming into stationary ions, where a majority of collisions result in large angle deflections, transferring momentum from dimension $x$ into $y$. Table 10.2 shows that the bifurcated plasma is as narrow or even more narrow in $y$ as the non-bifurcated one. Thus, the ensemble wings must predominantly contain Rydberg molecules in order to

contain the momentum along $x$.[27]

In recent work, we have identified two inconsistencies between above model and our experimental observations: 1) In Figure 10.5, we observe our arrested volume (prepared at $n_0$=32) after 420 $\mu$s in ellipsoidal shape. Above model requires the flow of ballistic ions into a Rydberg gas, leading to bifurcation as quench. Why do we observe arrest in a non-bifurcated system? 2) In order for ballistic core ions to stream into Rydberg wings, these ions must overtake the plasma-formation in the wings. Table 11.3 considers the plasma formation times of our system and computes a velocity for a 'plasma-formation front' travelling outward though our Rydberg volume. I find that this velocity exceeds that of the ballistic ions ($v_{ion} \approx 200$m/s) by at least an order of magnitude, which represents an inconsistency to above model.

The first inconsistency could be circumvented through postulation of a much smaller core streaming into the surrounding Rydberg gas, leading to arrest without causing bifurcation. We have plans to study this issue further by gating our 3D detector to obtain sliced images of our density distribution. A solution to inconsistency two, however, would require much delayed avalanche times in the system wings. This in turn leads to problems as Rydberg predissociation lifetimes only extend to hundreds of nanoseconds. Overall, this suggests that either the information pertaining to arrested relaxation travels faster than the ballistic ions, or that we should consider arrest as a mechanism that occurs independent from the bifurcating core.

**Hypothesis 2: Density dependent self-assembly?**

High Rydberg systems have been widely studied in the context of light-matter interactions governed by exceedingly strong dipole-dipole interactions [35, 60]. Laser excitation to Rydberg states gives rise to a num-

---

[27]A solid state nature of the arrested plasma, i.e. the formation of a macroscopic lattice, could also explain the observed observation of momentum conservation along $x$, but also leads us further into the realm of speculation.

Table 11.3: I consider a spherical Rydberg volume with peak density, $\rho_0 = 2.7 \cdot 10^{11}$ cm$^{-3}$, and FWHM of 3.2 mm. I model the system through ten non-interacting shells with densities $\rho_0$, $0.9 \cdot \rho_0$, $0.8 \cdot rho_0$,...,$0.1 \cdot \rho_0$. I calculate each shell centre position, $x$, and divide by the computed avalanche time for each shell, $t$ (cf. Chapter 7) to find the velocity of the 'plasma-formation front', $v$.

| shell | % [$\rho_0$] | $\rho$ [$10^{11}$ cm$^{-3}$] | $x$ [mm] | $t$ [ns] | $v$ [m/s] |
|---|---|---|---|---|---|
| 1 | 1 | 2.7 | 0 | 16 | 0 |
| 2 | 0.9 | 2.43 | 0.62 | 19 | 208100 |
| 3 | 0.8 | 2.16 | 0.91 | 22 | 94784 |
| 4 | 0.7 | 1.89 | 1.15 | 27 | 48022 |
| 5 | 0.6 | 1.62 | 1.38 | 33 | 37665 |
| 6 | 0.5 | 1.35 | 1.60 | 45 | 18886 |
| 7 | 0.4 | 1.08 | 1.84 | 61 | 14987 |
| 8 | 0.3 | 0.81 | 2.11 | 91 | 8977 |
| 9 | 0.2 | 0.54 | 2.44 | 170 | 4172 |
| 10 | 0.1 | 0.27 | 2.92 | 410 | 1994 |

ber of important phenomena of current interest in quantum optics and many-body quantum dynamics, including entanglement, dipole blockade and electromagnetic-induced transparency [8, 27, 36, 75], as well as coherent energy transport, optical bistability and directed percolation [5, 14, 47, 48].

We speculate, that under our conditions, each Rydberg molecule undergoes an excitonic interaction with its nearest neighbour [20, 58, 86], either a Rydberg molecule in a different high-$n$, high-$\ell$ electronic state or an ion in the field formed by the quasi-continuum of electrons bound to multiple charge centres. Importantly, every such interaction in the bifurcated ensemble randomly pairs two molecules in *different* excited states to define a unique, resonant close-coupled interaction.

The question arises whether the quasi-particles defined by these pairwise interactions can constrain the global evolution of the system in its spatial or energetic coordinates. Modelling many-body ensembles of resonant spins, Yao and coworkers [90] argue that, in three dimensions, $1/r^3$ dipole-dipole

interactions give rise to sub-diffusive transport. We speculate that a comparable mechanism might be responsible for the observed arrest of relaxation channels.

Thus, as an alternative to hypothesis 1, I consider a Rydberg system which develops an arrested state independent of bifurcation but based on the ratio between the size of the Rydberg molecules and the average distance between Rydberg cores. The hypothesis is simple. In order for arrest to develop, Rydberg molecules must have orbital diameters comparable to the inter-particle spacing, but without a significant overlap of orbitals. If the Rydberg gas density is too low, the molecules are too far apart. If the density is too high, Rydberg molecule overlap is too large, shutting off arrest.

Within the framework of hypothesis 2, I can envision the following mechanism forming the two observed domains: In the core of our Rydberg ensemble, density is highest and a significant number of molecules have overlapping orbitals, leading to Penning ionization (ICD). Similar to the ordering in a Rydberg blockaded gas, the Penning process constitutes an ordering of the plasma ions and remaining Rydberg molecules, by removing nearest neighbours from the respective distribution [71]. Thus, the randomness of our Rydberg ensemble is lowest at its core and highest in the outer layers. This, combined with the well know fact that localization, whether classical or quantum in nature, is highly dependent on disorder (randomness) could lead to an explanation of the observed system behaviour. Randomness might constitute a boundary between delocalized and localized transport within our Rydberg ensemble, leading to the suppression of avalanche to plasma within the ensemble wings.

Questions clearly remain: Can our system truly self-assemble to form a glass or localize, at least in the coordinates of electron binding energy? Does the relaxation of varying systems to a common density signify a universal macroscopic physics? Does a network of quantum mechanical interactions explain the slow dynamics of the nitric oxide molecular ultracold plasma?

Hypothesis 2, much like hypothesis 1, is pure speculation. It has entered my considerations because it solves the two inconsistencies of hypothesis 1 - yet different issues arise. Clearly, at this point in time, further systematic experiments as well as computation models are necessary to proof, disprove or develop above hypotheses.

## Chapter summary

In the context of my findings in Chapters 2 through 10, this last thesis chapter compared experimentally observed and 'expected' ensemble evolution to derive an inconsistency, highlighted by the arrest of relaxation channels. I speculated on the nature as well as formation process of the arrested domain. Based on a process of elimination, Section 11.2 called for new physics to explain the arrest of relaxation pathways. The ensuing discussion proposed two hypotheses for the transition of the Rydberg ensemble to the state of arrest: Bifurcation as quench and density dependent self-assembly. I discussed pros and cons of each hypothesis.

# Summary and Outlook

Over the course of this thesis, I have given a comprehensive account of the work in our research group. The complexity of the system under study, together with the fact that the field of ultracold molecular plasmas is still young, motivated a first principal discussion. Part I, *Fundamentals*, introduced the spectroscopic character of nitric oxide, our molecular ion, and followed with a review of Rydberg physics. Next, I discussed the fundamental assumptions of 'established' plasma theory and motivated the theoretical and experimental study of correlated plasma, due to the breakdown of said assumptions in a regime of Coulomb correlation.

Part II, *Formation of a molecular Rydberg ensemble*, began by introducing our experimental setup. I described how the convolution of two laser pulses with the cold molecular beam drives resonant transitions in NO, resulting in the preparation of a Gaussian ellipsoidal Rydberg ensemble. Here, the study of well established methods to describe supersonic beam expansions allowed for the characterization of the nitric oxide distribution and subsequently of the Rydberg molecule distribution in a moving-frame phase-space representation.

Part III, *Theory work*, discussed the microscopic evolution of this Rydberg ensemble to plasma, via Penning ionization, electron-Rydberg collisional heating as well as ionization avalanche, on a nanosecond timescale. This was followed by a discussion of macroscopic plasma evolution, incorporating plasma expansion and decay, on a microsecond timescale. The qualitative discussions in Part III were aided by computation results of rate-equation model calculations.

Part IV, *Experimental work*, introduced our methods of plasma detection. I discussed various experimental datasets within the context of previ-

ous chapters. My analysis showed, that (under certain conditions) our Rydberg ensemble unexpectedly develops two distinct macroscopic domains. These domains are distinguished by their polarizability as well as their locality within the plasma. The first domain appears at the system core and displays a character similar to that of plasma discussed in Part III. The second domain travels with the velocity of the supersonic beam and is distinguished through the apparent arrest of microscopic relaxation channels. I found that both domains are linked via the process of plasma bifurcation. Part IV concludes with speculations on the nature of the arrested domain as well as its mechanism of formation.

My hope is that this thesis provides a strong theoretical foundation to our area of research and helps to establish this young field of ultracold molecular plasmas. In proving a fundamental knowledge of the plasma precursor, the underlying Rydberg ensemble, I aim to attract the interest of other researchers into our work and gain support with the theoretical difficulties we are facing.

We believe that the molecular beam environment, introducing higher densities and additional evolution channels, causes a distinction between the fields of ultracold molecular plasma and ultracold atomic plasma. The analog computer in our laboratory, the studied Rydberg ensemble, solves our well defined many-body system in a way we do not yet understand. The discrepancy between our conceptual understanding of this many-body system and our observation of nature provides us with the motivation as well as the justification for our continued work. Based on the process of elimination, led up to over the course of this thesis and discussed in Chapter 11, we consider new physics to describe the evolution of our system, drawing from quantum mechanics as well as the immature field of correlated plasma physics. An incoherent mechanism may yet emerge, but our experimental observations substantially narrow the possibilities that can rely on conventional kinetics.

There is a great deal left to discover. At present, we are working on maximizing our control of the electric field environment within our experiment chamber. The observed polarizability of the non-arrested plasma domain allows for a systematic study of this state, which may lead to an improved understanding of the macroscopic boundary condition between the two domains. This, in turn, leads to a better understanding of the arrested domain.

Our electronic lens aided 3D imaging system, the 'plasma-TV' in configuration c), has only recently come online. Initial results with this new detector, discussed in Section 10.2.3, hint on the vast research possibilities of this machine. A systematic mapping of the boundary between the arrested and non-arrested domains will certainly yield new insight. Furthermore, a gating of this detector through voltage pulses on P2 or the MCPs allows us to record sliced images of the plasma density distribution. We have already begun experimenting with this tool. Lastly, the reconfiguration of the plasma-TV detector for velocity-map-imaging of the plasma domains is conceivable.

In addition to our present detection methods, we plan to develop a moving phosphor screen detector, merging the capabilities of the plasma-TV in configurations a)/b) with those of the moving-grid detector.

More up to date, we are working to employ different carrier gases than helium or different molecules than nitric oxide in our experiment. We can change beam parameters like pressure, gas mixture, skimmer area and laser geometry (i.e. crossed laser pathways), in order to create specific Rydberg phase-space distributions. These represent rich experimental tools in our continued work.

Naturally, we will continue to develop our computational capabilities. Here, my discussions in Chapter 11 has made it necessary to develop the plasma formation model discussed in Chapter 7 to allow for different evolution times within the layered shells.

# Bibliography

[1] Nist standard reference database 69: Nist chemistry webbook, nitric oxide, 2011.

[2] T Amthor, J Denskat, C Giese, N N Bezuglov, A Ekers, L S Cederbaum, and M Weidemüller. Autoionization of an ultracold Rydberg gas through resonant dipole coupling. *The European Physical Journal D*, 53(3):329–335, June 2009.

[3] J. B. Anderson. Molecular beams from nozzle sources. Technical report, 1974.

[4] H. Askenas and C. K. Sherman. Rarified gas dynamics. In J.H. de Leeuw, editor, *Proc. 4th Symposium on Rarified Gas Dynamics*, volume 2, pages 84 – 105, New York, 1966. Academic Press.

[5] Daniel Barredo, Henning Labuhn, Sylvain Ravets, Thierry Lahaye, Antoine Browaeys, and Charles S Adams. Coherent Excitation Transfer in a Spin Chain of Three Rydberg Atoms. *Physical Review Letters*, 114(11):113002, March 2015.

[6] R L Becker and A D MacKellar. Theoretical initial l dependence of ion-Rydberg-atom collision cross sections. *J Phys B*, 17(19):3923–3942, January 1999.

[7] Paul M. Bellan. *Fundamentals of Plasma Physics*. Cambridge University Press, 2006.

[8] I I Beterov and M Saffman. Rydberg blockade, Förster resonances, and quantum state measurements with different atomic species. *Physical Review A*, 92(4):042710, October 2015.

[9] G. W. Bethke. Oscillator strength in the far ultraviolet. i. nitric oxide. *J. Chem. Phys.*, 31(3), 1959.

[10] B.J. Bichsel, M.A. Morrison, N. Shafer-Ray, and E.R.I. Abraham. Experimental and theoretical investigation of the stark effect for manipulating cold molecules: Application to nitric oxide. *Phys. Rev. A*, 75:023410, Feb 2007.

[11] M. Bixon and J. Jortner. The dynamics of predissociating high rydberg states of no. *J. Chem. Phys.*, 105,4:1363, 1996.

[12] T. L. Brown, H. E. Lemay, B.E. Bursten, and C.J. Murphy. *Chemistry: The Central Science, 11th ed.* Prentice Hall, 2009.

[13] R. J. Campbell. Gas phase energy transfer processes. *J. Chem. Ed.*, 45(3):156 – 162, 1968.

[14] C Carr, R Ritter, C G Wade, C S Adams, and K J Weatherill. Nonequilibrium Phase Transition in a Dilute Rydberg Ensemble. *Phys Rev Lett*, 111(11):113901, September 2013.

[15] F. F. Chen. *Introduction to plasma physics and controlled fusion.* Plenum Press, New York, 1984.

[16] J. H. Chu and I.-C. Lin. Direct observation of coulomb crystals and liquids in strongly coupled rf dusty plasmas. *Phys. Rev. Lett.*, 72(25):4009–4012, 1994.

[17] D. Comparat, T. Vogt, N. Zahzam, M. Mudrich, and P. Pillet. Star cluster dynamics in a laboratory: electrons in an ultracold plasma. *Mon. Not. R. Astron. Soc.*, 361:1227 – 1242, 2005.

[18] E.A. Cummings, J.E. Daily, D.S. Durfee, and S.D. Bergeson. Fluorescence measurements of expanding strongly-coupled neutral plasma. *Phys. Rev. Lett.*, 95:235001, 2005.

[19] A.S. Davydov. *Quantum Mechanics.* Pergamon Press, 2nd edition edition, 1976.

[20] Johannes Deiglmayr. Long-range interactions between Rydberg atoms. *Physica Scripta*, 91:104007, October 2016.

[21] J. F. Delpech and J. C. Gauthier. Electron-ion recombination in cryogenic helium plasmas. *Phys. Rev. A*, 6(5):1932–1939, 1972.

[22] S.N. Dixit, D.L. Lynch, V. McKoy, and W.M. Huo. Rotational branching ratios in (1+1) resonant-enhanced multiphoton ionization of no via the a $^2\sigma^+$ state. *Phys. Rev. A*, 32(2), 1985.

[23] D. Dorozhkina and V. Semenov. Exact solution of the problem of quasineutral expansion into vacuum of a localized collisionless plasma with cold ions. *JETP Letters*, 67(8):573–578, 1998.

[24] D. Dorozhkina and V. Semenov. Exact solution of vlasov equations for quasineutral expansion of plasma bunch into vacuum. *Phys. Rev. Lett.*, 81(13):2691–2694, 1998.

[25] Daniel Dubin. First-order anharmonic correction to the free energy of a coulomb crystal in periodic boundary conditions. *Phys. Rev. A*, 42(8):4972–4982, 1990.

[26] Hossein Sadeghi Esfahani. *Strongly correlated ultracold plasma*. PhD thesis, The University of British Columbia, October 2016.

[27] O Firstenberg, C S Adams, and S Hofferberth. Nonlinear quantum optics mediated by Rydberg interactions. *Journal of Physics B: Atomic, Molecular and Optical Physics*, 49(15):152003, June 2016.

[28] T.F. Gallagher. *Rydberg Atoms*. Cambridge University Press, 2005.

[29] R. J. Goldston and P. H. Rutherford. *Introduction to Plasma Physics*. IOP Publishing Ltd, 1995.

[30] R. Schmiedl H. Zacharias and K. H. Welge. State selective step-wise photoionization of no with mass spectroscopic ion detection. *J. Appl. Phys.*, 21:127, 1980.

[31] R Haenel, M Aghigh, and E R Grant. Long-time dynamics of ultracold plasma expansion and decay. *to be published*, (2017).

[32] G. Herzberg. *Spectra of Diatomic Molecules*. Van Nostrand Reinhold Company, 2 edition, 1950.

[33] T. L. Hill. *An introduction to Statistical Thermodynamics*. Addison-Wesley, Reading, MA, pp. 135, 466, 1960.

[34] Michael Hippler and Josef Pfab. Detection and probing of nitric oxide (no) by two-colour laser photoionisation (rempi) spectroscopy on the a - x transition. *Chem. Phys. Lett.*, 243(5-6):500–505, 1995.

[35] C S Hofmann, G Günter, H Schempp, N L M Müller, A Faber, H Busche, M Robert-de Saint-Vincent, S Whitlock, and M Weidemüller. An experimental approach for investigating many-body phenomena in Rydberg-interacting quantum systems. *Frontiers of Physics*, 9(5):571–586, November 2013.

[36] C S Hofmann, G Günter, H Schempp, M Robert-de Saint-Vincent, M Gärttner, J Evers, S Whitlock, and M Weidemüller. Sub-Poissonian Statistics of Rydberg-Interacting Dark-State Polaritons. *Physical Review Letters*, 110(20):203601, May 2013.

[37] J Hung, H Sadeghi, M Schulz-Weiling, and E R Grant. Evolution from Rydberg gas to ultracold plasma in a supersonic atomic beam of Xe. *J. Phys. B: At. Mol. Opt. Phys*, 47(15):155301, July 2014.

[38] J. Hung, H. Sadeghi, M. Schulz-Weiling, and E.R. Grant. The evolution from rydberg gas to ultracold plasma in a supersonic atomic beam of xe. *J. Phys. B*, 47:155301, 2014.

[39] Setsuo Ichimaru. Strongly coupled plasmas: high-density classical plasmas and degenerate electron liquids. *Rev. Mod. Phys.*, 54(4):1017–1059, 1982.

[40] D. C. Jacobs, R. J. Madix, and R. N. Zare. Reduction of 1+1 Resonance Enhanced MPI Spectra to Population Distributions: Application to the NO A $^2\Sigma^+ -$ X $^2\Pi$ System. *J. Chem. Phys.*, 85(10):5469–5479, 1986.

[41] Glenn Joyce, Martin Lampe, Steven P. Slinker, and Wallace M. Manheimer. Electrostatic particle-in-cell simulation technique for quasineutral plasma. *Journal of Computational Physics*, 138(2):540 – 562, 1997.

[42] T. C. Killian, S. Kulin, S. D. Bergeson, L. A. Orozco, C. Orzel, and S. L. Rolston. Creation of an ultracold neutral plasma. *Phys. Rev. Lett.*, 83(23):4776–4779, 1999.

[43] T.C. Killian, T. Pattard, T. Pohl, and J. Rost. Ultracold neutral plasmas. *Phys. Rept.*, 449:77–130, 2007.

[44] S.G. Kuzmin and T.M. O'Neil. Numerical simulation of ultracold plasmas: How rapid intrinsic heating limits the development of correlation. *Phys. Rev. Lett.*, 88(6):065003, 2002.

[45] XinPei Lu, ZhongHe Jiang, Quing Xiong, ZhiYuan Tang, and Yuan Pan. A single electron room-temperature plasma jet device for biomedical applications. *Appl. Phys. Lett.*, 92(15), 2008.

[46] P. Mansbach and J. Keck. Monte carlo trajectory calculations of atomic excitation and ionization by thermal electrons. *Phys. Rev.*, 181:275–289, 1969.

[47] M Marcuzzi, J Schick, B Olmos, and I Lesanovsky. Effective dynamics of strongly dissipative Rydberg gases. *J Phys.A*, 47:482001, 2014.

[48] Matteo Marcuzzi, Michael Buchhold, Sebastian Diehl, and Igor Lesanovsky. Absorbing State Phase Transition with Competing Quantum and Classical Fluctuations. *Physical Review Letters*, 116(24):245701, June 2016.

[49] J. P. Morrison. *Correlated Molecular Plasmas*. PhD thesis, The University of British Columbia, May 2013.

[50] J. P. Morrison, C. J. Rennick, J. S. Keller, and E. R. Grant. Evolution from a molecular rydberg gas to an ultracold plasma in a seeded supersonic expansion of no. *Phys. Rev. Lett.*, 101(20), 2008.

[51] J P Morrison, C J Rennick, J S Keller, and E R Grant. Evolution from a molecular rydberg gas to an ultracold plasma in a seeded supersonic expansion of no. *Phys. Rev. Lett.*, 101:205005, 2008.

[52] J. P. Morrison, N. Saquet, and E. R. Grant. Classical scaling and the correspondence between the coupled rate equation and molecular dynamics models for the evolution of ultracold neutral plasma. *J. Phys. B*, 45:025701, 2012.

[53] E. Murgu, J.D.D. Martin, and T.F. Gallagher. Stabilization of predissociating nitric oxide rydberg molecules using microwave and radio-frequency fields. *J. Chem. Phys.*, 115:7032–7040, 2001.

[54] M. S. Murillo. Strongly coupled plasma physics and high energy-density matter. *Physics of Plasmas*, 11(5):2964 – 2971, 2004.

[55] S.B. Nagel, C.E. Simien, S.Laha, P. Gupta, V.S. Ashoka, and T. C. Killian. Magnetic trapping of metastable 3p2 atomic strontium. *Phys. Rev. A*, 67:011401, 2003.

[56] A.P. Nefedov, O.F. Petrov, V.I. Molotkov, and V.E. Fortov. Formation of liquidlike and crystalline structures in dusty plasmas. *JETP Letters*, 72(4):218–226, 2000.

[57] P. L. Owen and C. K. Thornhill. The flow in an axially symmetric supersonic jet from a nearly sonic orifice into a vaccum. Technical Report 30/48, Ministry of Supply Armament Res. Establishment (British), Sept 1948.

[58] Hyunwook Park, T F Gallagher, and P Pillet. Microwave pump-probe spectroscopy of the dipole-dipole interaction in a cold Rydberg gas. *Phys Rev A*, 93(5):052501, May 2016.

[59] L. Pedemonte and G. Bracco. Study of he flow properties to test he dimer potentials. *J. Chem. Phys.*, 119(3):1433–1441, 2003.

[60] Pierre Pillet and Daniel Comparat. Dipole blockade in a cold Rydberg atomic sample. *JOSA B*, 27(6):A208–A232, January 6.

[61] T. Pohl. *Relaxation dynamics of ultracold neutral plasmas*. PhD thesis, Technical University of Dresden, 2005.

[62] T Pohl, T. Pattard, and J M Rost. Kinetic modeling and molecular dynamics simulation of ultracold neutral plasmas including ionic correlations. *Phys Rev A*, 70:033416, 2004.

[63] T. Pohl, T. Pattard, and J.M. Rost. Kinetic modelling and molecular dynamics simulation of ultracold neutral plasmas including ionic correlations. *Phys. Rev. A*, 70(3):033416, 2004.

[64] T. Pohl, D. Vrinceanu, and H.R. Sadeghpour. Rydberg atom formation in ultracold plasmas: Small energy transfer with large consequences. *Phys. Rev. Lett.*, 100:223201, 2008.

[65] G. Reiser and K. Mueller-Dethlefs. Rotationally resolved zero kinetic energy photoelectron spectroscopy of nitric oxide. *J. Chem. Phys.*, 96:9–12, 1992.

[66] C. J. Rennick, N. Saquet, J. P. Morrison, J. Ortega-Arroyo, P. Godin, L. Fu, M. Schulz-Weiling, and E. R. Grant. Dissociative recombination and the decay of a molecular ultracold plasma. *J. Phys. Conf. Ser.*, 300:012005, January 2011.

[67] F. Robicheaux. Ionization due to the interaction between two rydberg atoms. *J. Phys. B*, 38(2):333 – 342, 2005.

[68] F Robicheaux. Ionization due to the interaction between two rydberg atoms. *J Phys B*, 38:S333–S342, 2005.

[69] M.P. Robinson, B.L. Tolra, M.W. Noel, and T.F. Gallagher. Spontaneous evolution of rydberg atoms into an ultracold plasma. *Phys. Rev. Lett.*, 85(21):4466, 2000.

[70] H. Sadeghi and E. R. Grant. Dissociative recombination slows the expansion of a molecular ultracold plasma. *Phys. Rev. A*, 86(052701), 2012.

[71] H Sadeghi, A Kruyen, J Hung, J H Gurian, J P Morrison, M Schulz-Weiling, N Saquet, C J Rennick, and E R Grant. Dissociation and the Development of Spatial Correlation in a Molecular Ultracold Plasma. *Physical Review Letters*, 112(7):075001, February 2014.

[72] H Sadeghi, A Kruyen, J Hung, J H Gurian, J P Morrison, M Schulz-Weiling, N Saquet, C J Rennick, and E R Grant. Dissociation and the development of spatial correlation in a molecular ultracold plasma. *Phys Rev Lett*, 112:075001, 2014.

[73] H. Sadeghi, M. Schulz-Weiling, J. P. Morrison, J. C. H. Yui, N. Saquet, C. J. Rennick, and E. R. Grant. Molecular ion-electron recombination in an expanding ultracold neutral plasma of no+. *PCCP*, 13:18872–18879, 2011.

[74] Hossein Sadeghi, Markus Schulz-Weiling, Jonathan P Morrison, Julian C H Yiu, Nicolas Saquet, Christopher J Rennick, and Edward Grant. Molecular ion–electron recombination in an expanding ultracold neutral plasma of $NO^+$. *Phys Chem Chem Phys*, 13:18872, 2011.

[75] M Saffman. Quantum computing with atomic qubits and Rydberg interactions: progress and challenges. *Journal of Physics B: Atomic, Molecular and Optical Physics*, 49(20):202001, October 2016.

[76] Giovanni Sanna and Giuseppe Tomassetti. *Introduction to molecular beams gas dynamics*. Inperial College Press, 2005.

[77] N. Saquet, J. P. Morrison, and E. R. Grant. Recombinative dissoci-
ation and the evolution of a molecular ultracold plasma. *J. Phys. B*,
45(175302), 2012.

[78] N. Saquet, J. P. Morrison, M. Schulz-Weiling, H. Sadeghi, J. Yiu, C. J.
Rennick, and E. R. Grant. On the formation and decay of a molecular
ultracold plasma. *J. Phys. B*, 44(184015), February 2011.

[79] Nicolas Saquet, Jonathan P Morrison, and Edward Grant. Recombina-
tive dissociation and the evolution of a molecular ultracold plasma. *J.
Phys. B: At. Mol. Opt. Phys*, 45(17):175302, August 2012.

[80] M Schluz-Weiling, J Sous, H Sadeghi, M Aghigh, L Melo, R Haenel,
J S Keller, and E R Grant. Arrested relaxation in an isolated molecular
ultracold plasma. *submitted to Phys. Rev. A*, 2017.

[81] I. F. Schneider, I. Rabadán, L. Carata, L. H. Andersen, A. Suzor-
Weiner, and J. Tennyson. Dissociative recombination of $NO^+$: calcula-
tions and comparison with experiment. *J. Phys. B*, 33:4849, 2000.

[82] Markus Schulz-Weiling and Edward Grant. Three-dimensional imaging
of the ultracold plasma formed in a supersonic molecular beam. *AIP
Conf Proc*, 1668(050002), 2015.

[83] Giacinto Scoles, editor. *Atomic and Molecular Beam Methods*, vol-
ume 1. Oxford University Press, 1988.

[84] A. H. Shapiro. *Compressible Fluid Flow*. Ronald Press, New York,
1953.

[85] C.E. Simien, Y.C. Chen, P. Gupta, S. Laha, Y.N. Martinez, P.G. Mick-
elson, S.B. Nagel, and T. C. Killian. Using absorption imaging to
study ion dynamics in an ultracold neutral plasma. *Phys. Rev. Lett.*,
92:143001, 2004.

[86] B Sun and F Robicheaux. Spectral linewidth broadening from pair fluc-
tuations in a frozen Rydberg gas. *Phys Rev A*, 78(4):040701, October
2008.

[87] M.J.J. Vrakking and Y.T. Lee. Enhancements in the lifetimes of no rydberg states in dc electric fields: Implications for zero-electron-kinetic-energy photoelectron spectroscopy experiments. *Phys. Rev. A*, 51(2), 1995.

[88] A. Walz-Flannigan, J.P. Guest, J.-H. Choi, and G. Raithel. Cold-rydberg-gas dynamics. *Phys. Rev. A*, 69:63405, 2004.

[89] A Walz-Flannigan, JR Guest, JH Choi, and G Raithel. Cold rydberg-gas dynamics. *Phys Rev A*, 69:063405, 2004.

[90] N Y Yao, C R Laumann, S Gopalakrishnan, M Knap, M Müller, E A Demler, and M D Lukin. Many-Body Localization in Dipolar Systems. *Phys Rev Lett*, 113(24):243002, December 2014.

[91] M. Zucrow and J. Hoffman. *Gas Dynamics, Vols. I and II*. Wiley, New York, 1976.

# Appendix A

# Hardware

Appendix A of my PhD thesis is meant to give a detailed description of our hardware implementation. Within my first year of working in our research group, I took on the task to build up a new experimental setup, beginning with the moving and connecting of three empty optical tables. Since then, I have made countless decisions with respect to the experimental setup, like choosing one electronic part, method or technical realization over another. The following will be a valuable toolset for someone with interest in joining the field of molecular ultracold plasma in an experimental capacity.

Our group currently works with two independent experimental setups. These setups only differ slightly in manufacturer or generation of the equipment. In both systems, we form an ultracold molecular plasma within a supersonic beam expansion. The main difference between our two setups is the way of detection. The older setup is hosting what we call the 'movable grid detector' (Sec. 9.1) while the new setup I've build makes up the 'PlasmaTV experiment' (Sec. 10.1), referring to a tomographic plasma imaging system. For the purposes of this thesis, I will only describe the new setup as well as the new generation detector in detail. For more information on the older setup, including ZEKE and moving-grid detectors, please refer to older theses from our group [26, 49].

## A.1   Overview

Figure A.1 gives a schematic overview of the components on the optical tables that make up the PlasmaTV experiment. The PlasmaTV setup consists of three optical tables. The tables are bolted together to minimize relative movement. The bottom table is 3 by 10 foot and holds two laser sources.

Detector (variable)

Beam stop

Chamber

Skimmer

Nozzle

Dichroic

Spatial filter

Polarizer

~327.5nm

Color filter

Frequency
doubling

~226
nm

ω1

ω2

655nm
output

452nm
output

532nm
output

Periscope

Photo diode

Gas mixture

Scanmate YAG+dye laser

Laser control monitor

ND 6000 dye laser

Powerlite DLS YAG laser
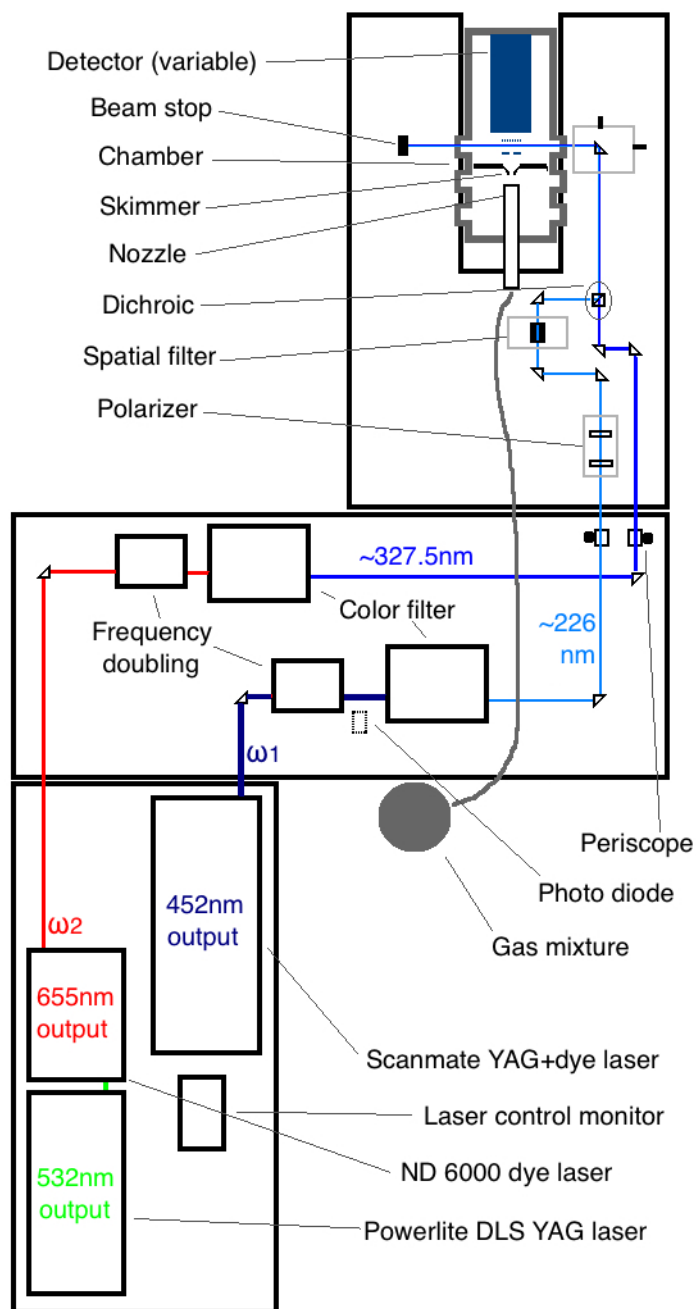
Figure A.1: **Birdview-schematic of the experimental setup**

We differ between two light-paths, $\omega_1$ and $\omega_2$. On the middle table, also 3 by 10 foot, we frequency double and color filter our laser pulses. A photo diode records accurate timing information on $\omega_1$ for triggering purposes. Two periscopes raise the laser beams to final hight for transit though our vacuum chamber. The last table, the detector table, is 4 by 10 feet with a 16 inch by 5 feet central cut-out which holds the vacuum chamber, housing molecular beam and detector. Prior to transit through this chamber, laser beam $\omega_1$ is attenuated, spatially cleaned and merged with $\omega_2$. A translation stage supporting the last 90 degree prism before the chamber allows us to move the light pulses horizontally across the diameter of our viewport.

Further measurement equipment like oscilloscope, timing unit, mol. beam control unit and measurement PC are sitting in racks above and below the optical tables. The individual component descriptions follow.

## A.2 Laser and optics

Figure A.1 shows a schematic of the optical layout on our laser table. The setup realizes two laser pathways, $\omega_1$ and $\omega_2$. The unfocused beams overlap within the experimental section of our vacuum chamber.

### A.2.1 Pump- and dye-lasers

The $\omega_1$-beam originates within a *Scanmate Pro C-400* laser by Coherent Lambda Physik. This system incorporates both, pump and dye laser, in a compact setup. The pump laser is a Brilliant b Nd:YAG system by Quantel, operated in pulsed mode. Part of the beam, at 1064 nm, is doubled and subsequently mixed with the fundamental to generate the third harmonic, which is split form the background of the first and second fundamental. This assembly yields an output beam of $\sim$ 180 mJ/pulse at a wavelength of 355 nm. This beam pumps the dye cavity of the ScamMate system. We use Coumarin 460 in methanol as a dye solution to generate a tuneable laser output at $\sim$ 452 nm with a power of $\sim$ 11 mJ/pulse.

$\omega_2$ follows the same concept, except it originates in the second harmonic of a *Continuum Powerlite 8000 DLS* Nd:YAG laser. The used dye in the second step is DCM in a *Continuum ND6000* dye laser. The respective laser intensities and wavelengths are $\sim$ 640 mJ/pulse at 532 nm after the YAG, allowing for $\sim$ 200 mJ/pulse at $\sim$ 652 nm after the dye laser. We typically attenuate the pump laser by means of a flash-lamp/Q-switch delay to limit our dye laser output to $\sim$ 100 mJ/pulse in order to protect subsequent optics.

### A.2.2   Frequency-doubling and colour filtering

Both dye-laser output beams are frequency doubled in a single-pass *Inrad Autotracker III* unit and subsequently pass through a 4-prism colour filter which only allows the doubled light through. At this point, the beam power of $\omega_1$ at $\sim$ 226 nm is less than 2 mJ/pulse. $\omega_2$ at $\sim$ 326 nm retains a power of $\sim$ 20 mJ/pulse.

### A.2.3   Additional optics

- We further reduce the $\omega_1$-beam by a set of **Glan-Thompson polarizing crystals**, which are rotated with respect to the laser polarization axis. Typical $\omega_1$ powers used in our experiments vary between 1.5 and $15\mu$J.

- Before merging our laser beams, we send $\omega_1$ through a **spatial filter** model KT310 by the manufacturer *Thorlabs*. The filter mounts a $50\mu$m pinhole to produce a clean, spatially uniform, Gaussian beam.

- We merge our laser beams using a **dichroic filter**.

- In some experiments we utilize an UV lens **Galilean telescope** to collimate our $\omega_1$-beam after the spatial filter and before the merging.

## A.3  The vacuum chamber

### A.3.1  Chamber dimensions
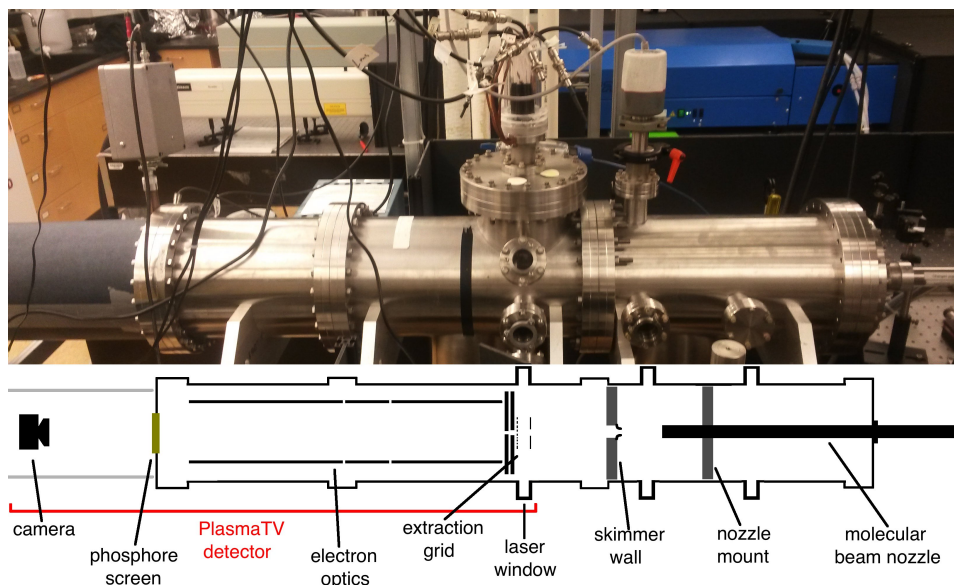


Figure A.2: **Schematic of the vacuum chamber**

Our vacuum chamber is a 10 inch diameter chamber separated by the skimmer wall into two compartments, the source chamber and the experimental chamber. The horizontal chamber dimensions of the three connected stainless steel segments, as illustrated in Figure A.2, are 11inch, 16inch and 15inch. The skimmer wall mounts a nickel electro-formed molecular beam skimmer with an orifice diameter of 1mm, supplied by *BEAM DYNAMICS, INC.*.

The experimental chamber allows the access of laser beams through fused silica view port windows. Pumping access for our turbo molecular vacuum pups is via two 8" ports below the chamber. The top of our chamber allows electrical access to the experiment chamber via a vacuum feedthrough passing 8 SHV connectors into the chamber. We use the access port above the source chamber to monitor our vacuum pressure.

### A.3.2 Mu-metal shielding

Our vacuum chamber incorporates magnetic shielding via 1mm thick mu-metal plates, fitted to the inside wall of the experiment chamber. In configuration c), a shield-cap of 7.25" diameter with a 2.66" diameter hole sits on the hight of G2 and closes the shield towards the source chamber. 20 mm diameter pores above the pump port allow for pump access through the shield. This creates a cylindrical shield, closed to one end. The mu-metal sheets were cut and vacuum annealed by *Magnetic-Shield Corporation*. We rolled the sheets after delivery.

### A.3.3 Vacuum

Both, our source and experimental chamber, are differentially pumped by a combination of a *PFEIFFER VACUUM HiPace 700* turbo pump and a *Welch 1397 Duo-Seal* roughing pump. We monitor our source chamber pressure via a BOC Edwards WRG-SL gauge using Pirani technology for the upper pressure range, with a seamless switch over to an inverted magnetron for the lower range. We typically achieve vacuum pressure in the range of $10^{-9}$torr. This pressure drops by two orders of magnitude when we run our beam valve.

### A.3.4 The supersonic beam

A *General Valve Series 9* nozzle with a 0.5 mm diameter orifice creates a supersonic jet of nitric oxide, seeded at 10% in helium, that expands into the experimental vacuum. The nozzle has an opening interval of $350\mu$s at a 10Hz pulse count. The gas mixture is a commercial product from *Paraxiar Distribution Inc.* with a certified gas ratio of 9.97% and an analytical accuracy of $\pm 2\%$.

The beam cools by progressively converting thermal energy into directional kinetic energy. It traverses the source chamber and its core encounters a skimmer wall with a 1 mm diameter skimmer at a distance of 25 to 35 mm downstream of the nozzle. The coldest part of the particle jet enters the experimental chamber.

## A.4 The PlasmaTV detector

The PlasmaTV detector was introduced in Chapter 10. It consists of a Chevron Model 3075FM detector assembly by *BURLE ELECTRO-OPTICS INCORPORATED*, integrated into our experiment in one of three configurations (cf. Figure 10.1). In the following, I will discuss subcomponents of this detector in more detail.

### A.4.1 The chevron detector

Manufacturer specifications: "The Chevron Model 3075FM detector assembly contains two Imaging Quality Extended Dynamic Range Long-Life Microchannel Plates and a fiberoptic phosphor screen with P20 phosphor mounted to an 8.0" vacuum flange. The fiberoptic is frit sealed into the flange to form a vacuum seal that is tight to a leak rate of 10-10 cc/sec of helium. The detector assembly is mounted in stainless steel hardware which is bakeable to 300 °C. The vacuum feedthroughs are mounted radially on the flange to facilitate viewing and access to the fiberoptic phosphor screen. The flange mounted assembly is equipped with one BSHV vacuum feedthrough rated up to 7.5 kV (for the phosphor screen) and three SHV vacuum feedthroughs rated up to 5 kV (two for the MCPs and one spare)."

The MCPs are further characterized by a quality diameter of 75 mm, centre-to-centre spacing of 32 $\mu$m, pore size of 25 $\mu$m and 8 degree bias angle. A 0.1 $\mu$m thick gold coating is applied to the input and output face. At 2 kV potential applied over the MCPs, electron gain is a minimum of $4 \cdot 10^6$.

### A.4.2 The lens element

The purpose and function of the electronic lens element has been discussed in Section 10.1. Figure A.3 displays the dimensionality in z of the PlasmaTV detector in configuration c). The different lens elements are stacked onto three 1/2 inch stainless steal rods, which are heat shrunk into a 10 to 8 inch zero length adapter. The different lens elements are isolated from each

other as well as the mounting rods via 1mm thick non-conducting spacers. Plates P1 and P2 have 4mm and 5mm thickness and a hole diameter of 10mm and 8mm, respectively. Grid plate G2 has 2.5" diameter with 4 holes, each 0.125" diameter on a 1.061" radius. The integrated mesh has 90% transparency and measures 50 lines per inch, stainless steel. G1 has the same dimensions without a mesh. Both plates, G1 and G2, were supplied by *Jordan TOF Products, Inc.*.
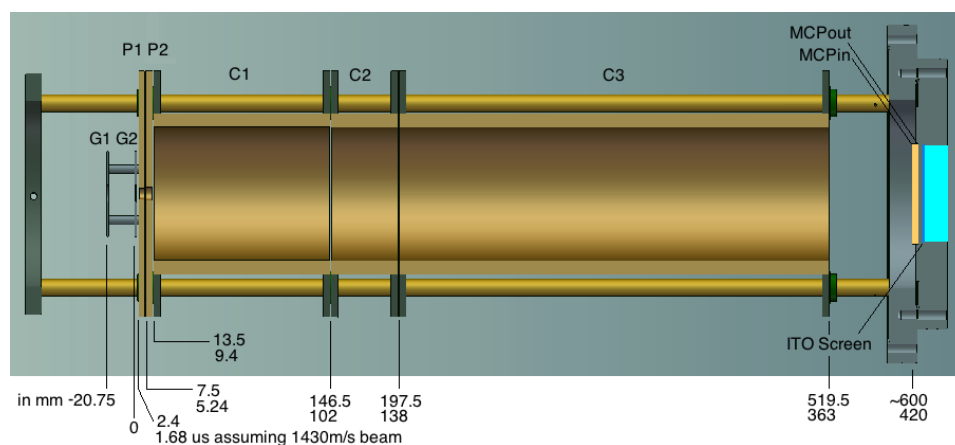


Figure A.3: **Dimensionality of the PlasmaTV detector in configuration c) along the z-axis**

## A.5 Electronics

### A.5.1 PlasmaTV voltage supply and output coupler

We set voltage potentials on our PlasmaTV lens element as well as the MCP input via an in-house build variable voltage supply. To supply MCP output and anode/screen potentials to the chevron detector, we use a *Burle Model PF1054 Dual Output Power Supply* with a voltage range 0 to 3kV and 0 to 8kV and up to $500\mu A$ current for both outputs.

Figure A.4 shows a schematic of our signal output coupler. The displayed

box is connected directly to the BSHV vacuum feedthrough of the chevron detector. The detector anode/screen is charged though a low-pass filter which blocks high-frequency components originating in the power supply. Particle impact on the charged chevron detector creates a high frequency signal which passes though our high-pass filter to be viewed with an oscilloscope. We employ this dual-filter scheme to protect our oscilloscope line from voltages spikes (e.g. power outage) on the HV in line.[28]
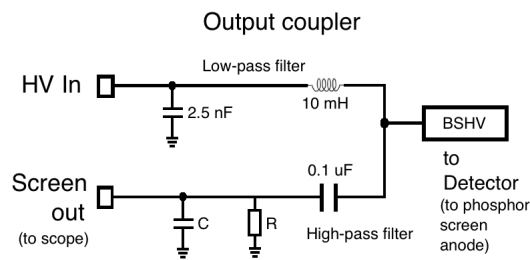
Figure A.4: **Layout of the PlasmaTV output coupler**

### A.5.2 Oscilloscope

We use a *Agilent Technologies DSO5052A Oscilloscope* with a bandwidth of 500 $MHz$ and 4 $GSa/s$ to view the detector signal. We typically trigger via a photo diode, located after the *Continuum ND6000* dye laser.

### A.5.3 Timing

Both pulsed laser beams are synchronized and overlap temporally and spatially in the experimental chamber where they intersect with a particle jet.

The timing of the flash lamps and Q-switches of both laser units, as well as of the nozzle and camera, are performed by a *BNC - Model 575*

---

[28]Please note that the anode/screen does not represent a 50$\Omega$ input impedance. Thus, our detection circuit incorporates an impedance mismatch which leads to strong 'ringing' especially for brief (nanosecond) signal bursts. The plasma impact, however, is a microsecond event and we obtain a well-defined impact characteristic.

*pulse/delay generator.*

### A.5.4 Camera

In order to capture the lighting-up of our phosphor screen, we employ a *UEye UI-224xSE-M Camera* with the following specifications: sensor type - CCD monochrome; exposure mode - electronic global shutter; resolution - 1280 x 1024 pixel; pixel clock range - 5 - 30 MHz; frame rate in trigger mode with 1ms exposure time - 14 fps. We reset the active area to 1024 x 1024 pixel and software bin to 512 x 512 pixel size images stored in unsigned 8-bit integers.

We have designed an aluminum camera mount that attaches to the chevron detector. The camera is adjusted to focus on the edges of the fiberoptic window. Detector and camera are surrounded by a blackout screen.

# Appendix B

# Computation source-code

In the following, I will publish the Matlab source-code I developed, discussed and applied in Part III of my thesis. Once more, I'd like to acknowledge the contributions of my coworkers, Nicolas Saquet, Jonathan Morrison, Hossein Sadeghi and Jachin Hung, who were kind enough to share their code so I would not have to start from scratch.

## B.1   Early-time dynamics model

```matlab
%% This function evaluates the plasma rise time for a given Ry density, n0
% I set n_min as lower decay boundry. States reaching levels <= n_min
% are considered to decay immediately via PD

% den0     = Ry atom density [um^-3] or [1e12 cm^-3]
% n0       = initial PQN
% t_final  = final computation time [ns]

% Use like: [t,nden,eden,aden,Te,~]=msw_runplasmasim_atom(0.3,50,500)

function [t,nden,eden,deac,Te,y0]=msw_runplasmasim_atom(den0,n0,t_final)

%%%%%%%%%%%%%%%%%%%%
% Penning fraction %
%%%%%%%%%%%%%%%%%%%%%

    % This function calculates the inital seed electrons

    % n are initial PQN-levels before Penning ionization
    % den is Ry-atom density in 10^12 pcc
```

```matlab
21
22      % eden is the # of electrons produced
23      % rden are the remaining PQN-levels after Penning ionization
24
25  function [PenningFraction eden rden]=penningfraction(n0,den0)
26
27      a0=5.2917721092e-5;      % bohr radius in um
28      Rn0=n0.^2*a0;
29       % radius of Rydb. atom by bohr model using semi-classical method
30      Rmax=1.8*(Rn0*2);
31       % Robicheaux paper, within this distance, 90% penning ionize (~15ns)
32
33      PenningFraction=zeros(length(n0),1);
34
35      % Calculates number of Penning partners based on Erlang distribution:
36      for i=1:length(n0)
37       % proportion between 0 and Rmax - integral is solved analytically
38      PenningFraction(i)=1-exp(-4*pi*den0*Rmax.^3/3);
39      end
40
41      % 90% ionization within certain time (assume rest non-interactive)
42      eden=PenningFraction/2*den0*.9;
43       % the dens. of electrons produced is half
44      rden=(1-PenningFraction*0.9)*den0;
45       % this is remaining density of rydbergs
46
47  end
48
49  %%%%%%%%%%%%%%%%%%%%%%
50  % Initial conditions %
51  %%%%%%%%%%%%%%%%%%%%%%
52
53  % Set constants and lower cut-off for PQN distribution:
54  kB = 1.3806504e-23;                 % #m2 kg s-2 K-1;J K-1; 8.62e-5 #eV K-1,
55  Ry = 2.179872e-18;                  % #J: Rydberg energy in J
56
57  firstn=1;
58  n_min=10;
59  numlev=100;      % this is the number of n levels initially considered
60  deac=0;                             % start with all Rydberg states
```

213

```
61   nl=(firstn:firstn+numlev−1)';         % array of accessible n levels
62
63   tspan=linspace(0,t_final,500);
64
65   % Sets initial conditions for electron and n—level distributions:
66   % no initial electrons —> calc. Penning seed electrons (Robicheaux)
67
68       [PF,eden,rden]=penningfraction(n0,den0);
69
70       % Redistributes the Penning partners over lower n's:
71       f=@(x)5.95*x.^5;
72        % This is the penning fraction distribution
73       np=firstn:fix(n0/sqrt(2));
74        % Array of n states allowed after Penn ion
75       ind=1:length(np);
76        % This is the distribution of penning fraction
77       nden=nl*0;
78       nden(ind)=eden*f(np/n0)/sum(f(np/n0));
79        % dividing by the sum normalizes the function
80
81       nden(nl==n0)=rden;                 % set n0 to rden
82
83       deac=sum(nden(1:n_min));           % allow n<=n_min to decay to aden
84       nden(1:n_min)=zeros(n_min,1);
85
86   % Set initial temperature:    (Robicheaux 2005 JPhysB)
87
88       T_penning=(−Ry*den0/n0^2 + Ry*rden/n0^2 + ...
89               Ry*sum(nden(ind)./nl(ind).^2) )*1/(3/2*kB*eden);
90        % set according to energy conservation
91
92
93   %%%%%%%%%%%%%%
94   % rate coeffs %
95   %%%%%%%%%%%%%%%
96
97   function [ni,nf,II,minn,maxn,diffsn]=buildns(nl)
98
99       % Is needed to reevaluate the rate coeff.
100      a=length(nl);
```

```
101     II=ones(a,a); % will be matrix of ij=1 and ii=0
102     ni=zeros(a,a);
103     nf=zeros(a,a);
104     minn=zeros(a,a);
105     maxn=zeros(a,a);
106     for i=1:a
107         for j=1:a
108             ni(i,j)=nl(i); % an array of initial states
109             nf(i,j)=nl(j); % an array of final state
110             minn(i,j)=min(ni(i,j),nf(i,j));
111              %find min of init and final state potential problem
112             maxn(i,j)=max(ni(i,j),nf(i,j));
113              %find max of init and final state
114             if i==j
115             II(i,j)=0; % set to 0 for same ini and final states
116             end
117         end
118     end
119     diffsn=abs(1./ni.^2-1./nf.^2);
120      % difference in energy between the 2 states (no units)
121
122 end
123
124 function ktbr=kTBR(n,T)     % three-body-recombination
125
126     % TBR rates output units in um^6 ns-1
127     kB = 1.3806504e-23;% #m2 kg s-2 K-1;J K-1; 8.62e-5 #eV K-1,
128     emass = 9.1093822e-31;% #kg
129     h = 6.6260690e-34;% #m2 kg / s 4.13e-15 #eV s
130     Rydhc = 2.179872e-18;% #J: Ryd [cm-1] --> [J]
131
132     epsi=Rydhc./(power(n,2.0)*kB*T);
133     lmbd=1e6*h./sqrt(2.0*pi*emass*kB*T);
134
135     ktbr=kION(n,T).*power(n,2.0).*power(lmbd,3.0).*exp(epsi);
136      % unit um^6 ns-1
137     ktbr(isnan(ktbr))=0;
138      % take care of computation error for values matlab
139      % sees as too small and turns NaN
140     ktbr(~isfinite(ktbr))=0;
```

215

```matlab
141        % take care of computation error for values matlab
142        % sees as too large and turns inf
143
144  end
145
146  function kion=kION(n,T) % ionizing collisions
147
148      % output unit is um^3
149      kB = 1.3806504e-23;% #m2 kg s-2 K-1;J K-1; 8.62e-5 #eV K-1,
150      Rydhc = 2.179872e-18;% #J: Ryd [cm-1] --> [J]
151      epsi=Rydhc./(power(n,2)*kB*T); % find reduced initial energy
152      kion=11*sqrt(Rydhc./(kB*T)).*kNOT(T).*exp(-epsi)./...
153            (power(epsi,2.33)+4.38*power(epsi,1.72)+1.32*epsi);
154
155  end
156
157  function out=knnp(ni,nf,II,minn,maxn,diffsn,T) % rate for n to n'
158
159      % output units is um^3 ns^-1
160      % use in conjunction with [ni,nf,II,minn,maxn,diffsn]=buildns(nl);
161
162      kB = 1.3806504e-23;% #m2 kg s-2 K-1;J K-1; 8.62e-5 #eV K-1,
163      Rydhc = 2.179872e-18;% #J: Ryd [cm-1] --> [J]
164
165      eps_i=Rydhc./(power(ni,2.0)*kB*T);
166      eps_f=Rydhc./(power(nf,2.0)*kB*T);
167      max_eps_i=Rydhc./(power(minn,2)*kB*T);
168      min_eps_i=Rydhc./(power(maxn,2)*kB*T);
169
170      diffs=Rydhc.*diffsn./(kB*T); % scale dffsn properly
171
172      out=II.*(kNOT(T).*power(eps_i,5/2).*power(eps_f,3/2)./...
173            power(max_eps_i,5/2))...
174            .*exp(-(eps_i-min_eps_i)).*((22./(power(max_eps_i+0.9,7/3)))...
175            +(4.5./(power(max_eps_i,2.5).*power(diffs+1-II,4/3))));
176
177  end
178
179
180  %%%%%%%%%%%%%%%%
```

```
181  % Calculations %
182  %%%%%%%%%%%%%%%
183
184  y0=[nden;eden;deac;T_penning]; % set initial value for ODE
185
186  ncrit=@(T)round(sqrt(Ry/(kB*T)));  % to calculate n-max
187
188  [ni,nf,II,minn,maxn,diffsn]=buildns(nl);
189   % is needed to calculate the rate coeffs
190
191  progress = waitbar(0,'Progress...'); % shows progress of computation
192
193  function dy=eqrateode(t,y)
194
195
196      % Select valiables:
197      nden=y(1:numlev);        % pick out density over distribution of n
198      eden=y(numlev+1);        % pick out electron density
199      deac=y(numlev+2);        % pick out density of radiatively decayed atoms
200      T=y(numlev+3);           % pick out temperature
201
202      nc=ncrit(T);             % calculates n max with this temperature
203
204      % Adjusts max allowed n:
205      if nc>=nl(1) && nc<nl(end)
206          index=find(nl==ncrit(T));
207      elseif nc<nl(1)
208          index=1;
209      else
210          index=numlev;
211      end
212
213
214      % Evaluate the updated rate terms:
215
216          d_tbr=zeros(numlev,1);
217          d_tbr(1:index)=kTBR(nl(1:index),T)*eden^3; % units [um^-3 ns^-1]
218
219          d_ion=kION(nl,T).*nden*eden; % units [um^-3 ns^-1]
220
```

```
221          % rate for transfer from n to n', units [um^3 ns^-1]
222          k_n_np=knnp(ni,nf,II,minn,maxn,diffsn,T);
223          d_n_np=sum(k_n_np,2).*nden*eden;
224
225          % rate for transfer from n' to n, units [ns^-1]
226          k_np_n=zeros(numlev,numlev);
227          for i=1:index % only to levels <= nc
228              k_np_n(i,1:numlev)=k_n_np(1:numlev,i).*(nden(1:numlev));
229          end
230          d_np_n=sum(k_np_n,2)*eden;          % units [um^-3 ns^-1]
231
232          % transfer from n's above ncrit(T) to eden
233          k_n_npion=zeros(numlev,1);
234          if index<=numlev
235              k_n_npion(1:index)=sum(k_n_np(1:index,index+1:numlev),2)...
236                                 .*nden(1:index); % units [ns^-1]
237          end
238          d_n_npion=sum(k_n_npion)*eden;      % units [um^-3 ns^-1]
239
240      % Evaluate time derivatives:
241
242          d_eden=sum(d_ion-d_tbr)+d_n_npion;
243
244          d_nden=d_tbr-d_ion-d_n_np+d_np_n;
245
246          dT=(Ry*sum(d_nden./nl.^2)-1.5*kB*T*d_eden)/(1.5*kB*eden);
247
248          % Implements PD for levels n <= n_min:
249          d_deac=sum(d_nden(1:n_min));
250           % deac is the number of Ry's predissociated
251          d_nden(1:n_min)=zeros(n_min,1);
252
253
254      dy=[d_nden;d_eden;d_deac;dT];
255
256      waitbar(t/t_final);
257
258  end
259
260  %%%%%%%
```

```
261  % ODE %
262  %%%%%%
263
264  options=odeset('reltol',1e−8);
265  [t,y]=ode23(@(t,y)eqrateode(t,y),tspan,y0);
266
267  nden=y(:,1:numlev);
268  eden=y(:,numlev+1);
269  deac=y(:,numlev+2);
270  Te=y(:,numlev+3);
271
272  close(progress);
273
274  end
```

## B.2   Long-time dynamics model

```
1   %% This function evaluates plsma evolution within the 3D shell model
2   % The input is collected in array in.* (see below)
3   % Output: [N; R_x; R_y; R_z; u_x; u_y; u_z; Ti_x; Ti_y; Ti_z; Te]
4   % spatial dimensions are in [um]
5   % time dimensions are in [us]
6
7   function [yout] = msw_expansionmodel_3D_ion(in)
8
9
10  %%%%%%%%%%%%%%%%%%%%%
11  % Initial conditions %
12  %%%%%%%%%%%%%%%%%%%%%%
13
14  % Define input:
15      sig0_x=in.rx;                % initial plasma width in um (sigma0_x)
16      sig0_y=in.ry;                % initial plasma width in um (sigma0_y)
17      sig0_z=in.rz;                % initial plasma width in um (sigma0_z)
18      Te0=in.Te0;                  % initial electron temperature in K
19      shells=in.shells;
20       % total number of shells used to evaluate gaussian profile
21      Ccut_x=in.distance_x;
22       % the final x−boundary of plasma usually 5 times initial width
```

219

```
23      Ccut_y=in.distance_y;
24       % the final y-boundary of plasma usually 5 times initial width
25      Ccut_z=in.distance_z;
26       % the final z-boundary of plasma usually 5 times initial width
27      tspan=in.tspan';
28       % the time array which will be used to evaluate time integration of ODE
29      rho0=in.n0;                    % peak density of plasma in [um^3]
30      kB=1.3806488e-23;              % kB Boltzmann constant SI unit
31      mi=4.982629691838400e-26;      % mi Mass of one molecule of NO in Kg
32      kBm=kB/mi;
33       % save time on calculation of kB/mi in ODE loop
34      kDR1kelvin=in.kDR1kelvin;      % DR constant at 1 kelvin in um^3/us
35      kDRpower=in.kDRpower;
36       % power of DR temperature dependence [unitless]
37      gamma0_x=in.u0_x;              % HD velocity x in um/us
38      gamma0_y=in.u0_y;              % HD velocity y in um/us
39      gamma0_z=in.u0_z;              % HD velocity z in um/us
40      Ti_x0=in.Ti_x;                % initial ion temperature in x
41      Ti_y0=in.Ti_y;                % initial ion temperature in y
42      Ti_z0=in.Ti_z;                % initial ion temperature in z
43
44      % Create shells:
45          % array of initial k-shell radius between 0 to 5 * r0
46          % divided to number of shells
47          % avoiding zero shell radius by shifting the array
48          R0_x=linspace(0,Ccut_x,shells)';
49          R0_x=R0_x+R0_x(2)-R0_x(1);
50          R0_y=linspace(0,Ccut_y,shells)';
51          R0_y=R0_y+R0_y(2)-R0_y(1);
52          R0_z=linspace(0,Ccut_z,shells)';
53          R0_z=R0_z+R0_z(2)-R0_z(1);
54
55          rho=rho0*exp(-R0_x.^2/(2*sig0_x^2));
56           % rho is array of density at x-axis shell boundry
57
58      % Find array of initial HD velocity:
59           % array that initialized the velocity (um/us) of ions at each shell
60          u0_x=R0_x.*gamma0_x;
61          u0_y=R0_y.*gamma0_y;
62          u0_z=R0_z.*gamma0_z;
```

220

```
63
64       % this function calculates the volume between each shell.
65       function [volume]=volume3D(x,y,z)
66
67        xm1=[0;x(1:end-1)];
68        ym1=[0;y(1:end-1)];
69        zm1=[0;z(1:end-1)];
70        volume = 4/3*pi*((x.*y.*z) - (xm1.*ym1.*zm1));      % area of ellipsoid
71
72       end
73
74       % Find shell info:
75           vol=volume3D(R0_x,R0_y,R0_z);
76           N=rho.*vol;
77
78       % Define ion temperature:
79           Ti0_x=Ti_x0*ones(shells,1);
80           Ti0_y=Ti_y0*ones(shells,1);
81           Ti0_z=Ti_z0*ones(shells,1);
82
83   %%%%%%%%%%%%%%%
84   % Calculations %
85   %%%%%%%%%%%%%%%%
86
87       % Define initial conditions:
88           y0=[N; R0_x; R0_y; R0_z; u0_x; u0_y; u0_z; Ti0_x; Ti0_y; Ti0_z; Te0];
89
90       % Define fit parameter:
91           fo = fitoptions('method','SmoothingSpline','SmoothingParam',1e-1);
92           ft = fittype('smoothingspline');
93
94   % Define inner function:
95       function [dy du]=expansionmodelinnerfunction(t,y)
96           % this function takes time and ODE variable and calculates dy/dt
97           % (called dy) and du/dt (optional: called du)
98           % this format is used by mode ODE integratores
99
100          % fprintf('%f\n',t); % uncomment to see the progress of ODE
101
102      % Give proper name to variables from the VERCAT y
```

```
103        N=y(1:shells);
104        R_x=y(shells*1+1:shells*2);
105        R_y=y(shells*2+1:shells*3);
106        R_z=y(shells*3+1:shells*4);
107        u_x=y(shells*4+1:shells*5);
108        u_y=y(shells*5+1:shells*6);
109        u_z=y(shells*6+1:shells*7);
110        Ti_x=y(shells*7+1:shells*8);
111        Ti_y=y(shells*8+1:shells*9);
112        Ti_z=y(shells*9+1:shells*10);
113        Te=y(shells*10+1);
114
115    % Calculate some parameters base on the updated values
116        vol=volume3D(R_x,R_y,R_z);
117        rho=N./vol;
118        kDR=kDR1kelvin*(Te^(-kDRpower));
119
120    % Change in N due to DR
121        dN=-kDR*rho.^2.*vol;
122
123    % Calculating expansion force along x:
124        rxnp=[-flipud(R_x); R_x];
125        nnp=[flipud(rho); rho];
126         % building up a density profile on either side of r=0
127         % to get a symmetric fit
128
129        cfx=fit(rxnp,nnp,ft,fo);
130         % fit density over distance, in order to calculate expansion force
131
132        fx=-differentiate(cfx,R_x)./rho;
133         % part of expansion force that is calculated from density profile
134
135        du_x=(kBm*(Te+Ti_x)).*fx;
136
137        dR_x=u_x;
138
139    % Calculating expansion force along y:
140        rynp=[-flipud(R_y); R_y];
141
142        cfy=fit(rynp,nnp,ft,fo);
```

```
143
144          fy=−differentiate(cfy,R_y)./rho;
145
146          du_y=(kBm*(Te+Ti_y)).*fy;
147
148          dR_y=u_y;
149
150      % Calculating expansion force along z:
151          rznp=[−flipud(R_z); R_z];
152
153          cfz=fit(rznp,nnp,ft,fo);
154
155          fz=−differentiate(cfz,R_z)./rho;
156
157          du_z=(kBm*(Te+Ti_z)).*fz;
158
159          dR_z=u_z;
160
161      % Update Te and Ti in terms of transfer of thermal
162      % to directional kinetic energy:
163          % Change in total temp:
164          dT_x=−2*(u_x.*du_x)/(3*kBm);
165          dT_y=−2*(u_y.*du_y)/(3*kBm);
166          dT_z=−2*(u_z.*du_z)/(3*kBm);
167
168          % Change in ion temp:
169          dTi_x=Ti_x./(Te+Ti_x).*dT_x;
170          dTi_y=Ti_y./(Te+Ti_y).*dT_y;
171          dTi_z=Ti_z./(Te+Ti_z).*dT_z;
172
173          Ti_mean=sum(N.*(Ti_x+Ti_y+Ti_z))/(3*sum(N));
174
175          dTe=Te/(Te+Ti_mean)*sum(N.*(dT_x+dT_y+dT_z))/(3*sum(N));
176          % change in el. temp.
177          % has to be scaled by particle number per shell
178
179      % Update y
180          dy=[dN; dR_x; dR_y; dR_z; du_x; du_y; du_z; dTi_x; dTi_y; dTi_z; dTe];
181
182      end
```

```matlab
183
184  odeoptions=odeset('RelTol',1e−13);
185  handler=@(t,y)expansionmodelinnerfunction(t,y);
186
187  %%%%%%
188  % ODE %
189  %%%%%%
190
191  % Solve ODE:
192  [˜,yout]=ode113(handler,tspan,y0,odeoptions);
193
194
195  % To have matlab check if electron temp. evolution is ok:
196  for j=(shells*7+1):(shells*10+1)
197
198      T=yout(1,j);
199      for i=2:length(tspan)
200          Tp1=yout(i,j);
201          if Tp1 > (T+0.01)
202      sprintf('Error in the evolution of temperature! row: %i column: %i',i,j)
203          break
204          end
205          T=yout(i−1,j);
206      end
207  end
208
209
210  end
```

## B.3   Simulate detector response to 3D Gaussian ellipsoid

```matlab
1  % This function simulates detector response for the shell model plasma.
2  % It takes the output of msw_expansionmodel_3D_ion and simulates the
3  % response of our detector for a given plasma. The output of this function
4  % is equivalent to plasma observed in our detector!
5
6  % Input: ([N; Rx; Ry; Rz; ux; uy; uz; Tix; Tiy; Tiz; Te],timestep)
```

```
7  % timestep: select (solution) in OutExpMod3D for which to simulate response
8
9
10 function [graph_out,sig,peak] = SimDetecResp3D_ion(OutExpMod3D,timestep)
11
12 % Extract parameters of output msw_expansionmodel_3D_ion:
13
14         [rows,columns]=size(OutExpMod3D);
15         shells=(columns-1)/10;
16
17         N=OutExpMod3D(timestep,1:shells)';
18         R_x=OutExpMod3D(timestep,shells*1+1:shells*2)';
19         R_y=OutExpMod3D(timestep,shells*2+1:shells*3)';
20         R_z=OutExpMod3D(timestep,shells*3+1:shells*4)';
21
22         % takes function from within msw_expansionmodel_3D_ion:
23         vol=volume3D(R_x,R_y,R_z);
24
25         % Find rho with reduced computational error:
26         rho=N./vol;
27         rho=[flipud(rho);rho]*1e6;
28
29         % Define fit parameter and turn shell
30         % model to continuous distribution:
31         fo = fitoptions('method','SmoothingSpline','SmoothingParam',1e-1);
32         ft = fittype('smoothingspline');
33
34         dens_profile_x=fit([-flipud(R_x);R_x],rho,ft,fo);
35         dens_profile_y=fit([-flipud(R_y);R_y],rho,ft,fo);
36         dens_profile_z=fit([-flipud(R_z);R_z],rho,ft,fo);
37
38
39 %       We'll slice up the plasma and count the particles per
40 %       slice as the system traverses the detection grid:
41
42
43    % Calculate geometies:
44
45
46         % Find new z shells:
```

```matlab
47          bin_pos_z=0:15:R_z(end);
48          new_dens=dens_profile_z(bin_pos_z);
49          bin_number=size(bin_pos_z);
50          bin_number=bin_number(2);
51
52          % Find new y shells:
53          shell_pos_y=zeros(1,bin_number);
54
55          for i=2:bin_number                  % shells start at 2nd index
56              desiredValue = new_dens(i);
57              objective = @(pos) dens_profile_y(pos) - desiredValue;
58              desiredPos = fzero(objective, bin_pos_z(i));
59
60              shell_pos_y(i)=abs(desiredPos);
61              % because of sym. sometimes finds neg. value
62          end
63
64          lookforerror=max(find(isnan(shell_pos_y)));
65          if isempty(lookforerror) == 0; n=1:lookforerror; shell_pos_y(n)=0;
66              fprintf('NaN error at y=%i\n',max(n));
67          end
68
69          % Find new x shells:
70          shell_pos_x=zeros(1,bin_number);
71
72          for i=2:bin_number                  % shells start at 2nd index
73              desiredValue = new_dens(i);
74              objective = @(pos) dens_profile_x(pos) - desiredValue;
75              desiredPos = fzero(objective, bin_pos_z(i));
76
77              shell_pos_x(i)=abs(desiredPos);
78              % because of sym. sometimes finds neg. value
79          end
80
81          lookforerror=max(find(isnan(shell_pos_x)));
82          if isempty(lookforerror) == 0; n=1:lookforerror; shell_pos_x(n)=0;
83              fprintf('NaN error at x=%i\n',max(n));
84          end
85
86
```

```matlab
87          % Do integration (bin count):
88
89
90          response=zeros(bin_number,2);
91
92          response(:,1)=bin_pos_z;
93          dRz=bin_pos_z(2);              % bins are equal distance
94
95          for i=2:bin_number
96              Rz=bin_pos_z(i-1);
97              correction=1-(Rz^2./bin_pos_z(i:end).^2);
98              % takes care of ellipsodal geometries
99
100             % Define 2D ellipse corrected for z:
101             Rx=sqrt(correction.*shell_pos_x(i:end).^2);
102             Rxm1=[0,Rx(1:end-1)];
103             Ry=sqrt(correction.*shell_pos_y(i:end).^2);
104             Rym1=[0,Ry(1:end-1)];
105
106
107             % gives area of ellipse shells
108             Area=pi*(Rx.*Ry-Rxm1.*Rym1);
109
110             % gives # of particles per shell
111             Number_shell=dRz*Area'.*new_dens(i:end);
112
113             % gives # of particles for whole bin
114             Number=sum(Number_shell);
115             response(i-1,2)=Number;
116         end
117
118
119         x=[-flipud(response(:,1));response(:,1)];
120         y=[flipud(response(:,2));response(:,2)];
121         grapth_out=[x,y];
122
123         GaussFit=fit(x,y,'gauss1');
124         coeff=coeffvalues(GaussFit);
125         ci = confint(GaussFit,0.95);
126
```

```
127          sig=coeff(3)/sqrt(2);
128          sig_up=ci(5)/sqrt(2);
129          sig_down=ci(6)/sqrt(2);
130
131          peak=coeff(1);
132
133          sprintf('sigma = %.6f (%.6f - %.6f) us',sig,sig_up,sig_down)
134
135   end
```